الجمهورية الجزائرية الديمقراطية الشعبية
République Algérienne Démocratique et Populaire
وزارة التعليم العالي و البحث العلمي
Ministère de l'Enseignement Supérieur et de la Recherche Scientifique

المدرسة الوطنية المتعددة التقنيات
Ecole Nationale Polytechnique

ÉCOLE NATIONALE POLYTECHNIQUE
Département d'automatique

Laboratoire de Commande des Processus

مخبر التحكم في العمليات التصنيعية
Laboratoire de Commande des Processus

PhD THESIS

Presented by :

Fatma Zohra HADJAIDJI

Engineer and Master's Degree in Automatic Control from ENP

For the degree of
Doctor
in Automatic
Discipline : Electrical Engineering - Automatic Control of Industrial Systems

Thesis title

Investigations on modern control techniques for multi-source energy conversion systems connected to microgrids

Defended on December 18, 2025, before the committee members :

President	MAHMOUDI Mohand Oulhadj	Professor	ENP, Algiers
Supervisor	BOUKHETALA Djamel	Professor	ENP, Algiers
Co-Supervisor	BARBOT Jean-Pierre	Professor	ENSEA, Paris
Examiners	BOUDJEMA Farès	Professor	ENP, Algiers
	TADJINE Mohamed	Professor	ENP, Algiers
	RAHMANI Lazhar	Professor	Univ. Setif
	BENMANSOUR Khalifa	Professor	ESDAT, Algiers

ENP 2025

Thesis prepared at the Laboratoire de Commande des Processus (LCP) - École Nationale Polytechnique (ENP)
10, Avenue des Frères Oudek, Hassen Badi, BP. 182, 16200 El Harrach, Algiers, Algeria
In collaboration with the QUARTZ Laboratory, N°EA 7393, Voie 6 avenue de ponceau, 95014 CERGY-PONTOISE, France.

الجمهورية الجزائرية الديمقراطية الشعبية
République Algérienne Démocratique et Populaire
وزارة التعليم العالي و البحث العلمي
Ministère de l'Enseignement Supérieur et de la Recherche Scientifique

المدرسة الوطنية المتعددة التقنيات
Ecole Nationale Polytechnique

ÉCOLE NATIONALE POLYTECHNIQUE
Département d'automatique

Laboratoire de Commande des Processus

Laboratoire de Commande des Processus

PhD THESIS

Presented by :

Fatma Zohra HADJAIDJI

Engineer and Master's Degree in Automatic Control from ENP

For the degree of
Doctor
in Automatic
Discipline : Electrical Engineering - Automatic Control of Industrial Systems

Thesis title

Investigations on modern control techniques for multi-source energy conversion systems connected to microgrids

Defended on December 18, 2025, before the committee members :

President	MAHMOUDI Mohand Oulhadj	Professor	ENP, Algiers
Supervisor	BOUKHETALA Djamel	Professor	ENP, Algiers
Co-Supervisor	BARBOT Jean-Pierre	Professor	ENSEA, Paris
Examiners	BOUDJEMA Farès	Professor	ENP, Algiers
	TADJINE Mohamed	Professor	ENP, Algiers
	RAHMANI Lazhar	Professor	Univ. Setif
	BENMANSOUR Khalifa	Professor	ESDAT, Algiers

ENP 2025

Thesis prepared at the Laboratoire de Commande des Processus (LCP) - École Nationale Polytechnique (ENP)
10, Avenue des Frères Oudek, Hassen Badi, BP. 182, 16200 El Harrach, Algiers, Algeria
In collaboration with the QUARTZ Laboratory, N°EA 7393, Voie 6 avenue de ponceau, 95014 CERGY-PONTOISE, France.

الجمهورية الجزائرية الديمقراطية الشعبية
République Algérienne Démocratique et Populaire
وزارة التعليم العالي و البحث العلمي
Ministère de l'Enseignement Supérieur et de la Recherche Scientifique

المدرسة الوطنية المتعددة التقنيات
Ecole Nationale Polytechnique

ÉCOLE NATIONALE POLYTECHNIQUE
Département d'Automatique

Laboratoire de Commande des Processus

Laboratoire de Commande des Processus

THÈSE DE DOCTORAT

Présentée par :

Fatma Zohra HADJAIDJI

Ingénieur et Master en Automatique de l'ENP

En vue de l'obtention du titre de
Docteur
en Automatique
Discipline : Génie Électrique - Automatique des Systèmes Industriels

Thème

Investigations sur les techniques de commande modernes dédiées aux systèmes de conversion d'énergie multi sources connectés aux microgrids

Soutenue le 18 décembre 2025 devant les membres du jury :

Président	MAHMOUDI Mohand Oulhadj	Professeur	ENP, Alger
Directeur	BOUKHETALA Djamel	Professeur	ENP, Alger
Co-Directeur	BARBOT Jean-Pierre	Professeur	ENSEA, Paris
Examinateurs	BOUDJEMA Farès	Professeur	ENP, Alger
	TADJINE Mohamed	Professeur	ENP, Alger
	RAHMANI Lazhar	Professeur	Univ. Sétif
	BENMANSOUR Khalifa	Professeur	ESDAT, Alger

ENP 2025

Thèse préparée au Laboratoire de Commande des Processus (LCP) - École Nationale Polytechnique (ENP)
10, Avenue des Frères Oudek, Hassen Badi, BP. 182, 16200 El Harrach, Alger, Algérie
En collaboration avec le Laboratoire :Laboratoire QUARTZ, N°EA 7393, Voie 6 avenue de ponceau, 95014 CERGY-PONTOISE, France.

ملخص ـ الميكرو شبكات هي شبكات كهربائية صغيرة الحجم تدمج بين مصادر الطاقة المتجددة، والمولدات الموزعة، بالإضافة إلى الأحمال المحلية. تم تصميمها لتوفير إمداد كهربائي موثوق وعالي الجودة في أوضاع تشغيل مختلفة، سواء كانت معزولة أو متصلة بالشبكة الكهربائية الرئيسية، مع ضمان انتقال سلس بين هذه الأوضاع. هذا النوع من الأنظمة يواجه العديد من المشاكل التقنية المرتبطة بطبيعة الأحمال، والانقطاعات في مصادر الطاقة، والترابط بين مكونات ذات طبيعة مختلفة، مما يؤثر على جودة الطاقة المقدمة والاستقرار العام للميكرو شبكة. ومع ظهور محولات إلكترونيات الطاقة الحديثة وأجهزة التحكم المتطورة، أصبح من الممكن تجاوز جزء كبير من هذه التحديات. العمل المنجز في إطار هذه الأطروحة يدخل في هذا السياق. وبناءً على الأداء القوي لأنظمة التحكم الحديثة، بما في ذلك أنظمة التحكم ذات الأس الكسري، التحكم الإنزلاقي والتحكم عن طريق المنطق الضبابي، قمنا بتطوير استراتيجيات وأدوات تحكم جديدة للميكرو شبكة. تم إدماج أنواع حديثة من محولات الجهد، تعرف بمحولات مصدر Z ومحولات شبه مصدر Z ، والتي تسمح، من خلال تصميمها واستراتيجية التحكم المعتمدة، بإضافة وظيفة تعزيز الجهد المدخل. وبفضل التعديلات التي أجريت على التحكم الشامل في التوازن، تم تصميم هيكل هرمي محسن و بنية لامركزية جديدة لإدارة عدة محولات مصدر جهد موصلة بالتوازي. تم اقتراح استراتيجية التحكم اللامركزي كحل لإدارة أوضاع التشغيل المختلفة للميكرو شبكة دون الحاجة إلى خطوط اتصال. وهذا يسمح بتجنب عيوب التحكم الثانوي المركزي المتضمن في البنية الهرمية، مثل التأخير أو فقدان البيانات، مما قد يؤدي إلى انهيار النظام بأكمله. علاوة على ذلك، تم اعتماد خوارزميات ميتايورستية حديثة لتحديد القيم المثلى لمعاملات التحكم بناءً على معايير دقيقة.

كلمات مفتاحية ـ ميكرو شبكة مرنة، عاكسات مصدر جهد متوازي، عاكس مصدر Z ، التحكم في الانحدار الشامل، التحكم بالترتيب الكسري، التحكم الانزلاقي فائق الالتواء، التحكم اللامركزي، التحكم الهرمي، التحسين الميتايورستي.

Résumé—Les microgrids sont des réseaux électriques de petite taille intégrant des sources d'énergie renouvelable, des générateurs distribués, ainsi que des charges locales. Ils sont conçus pour fournir un approvisionnement électrique fiable et de meilleure qualité dans différents modes de fonctionnement, qu'ils soient isolés ou connectés au réseau principal, tout en assurant une transition douce entre ces modes. Ce type de système est confronté à de nombreux problèmes techniques liés à la nature des charges, aux interruptions des sources d'énergie, et à l'interconnexion de multiples composants de nature différente, ce qui impacte la qualité de l'énergie fournie et la stabilité globale du microgrid. Avec l'émergence des convertisseurs de l'électronique de puissance et des dispositifs de commande modernes, il est désormais possible de résoudre un grand nombre de ces problèmes. Le travail réalisé dans le cadre de cette thèse rentre dans ce contexte. En conséquence, et compte tenu des performances robustes des commandes modernes, y compris la commande par ordre fractionnaire, la commande par mode glissant et la commande logique flou, nous avons développé de nouvelles stratégies et outils de commande pour les microgrids. De récents types d'onduleurs à source de tension, appelés onduleurs Z-source et onduleurs quasi-Z-source, sont incorporés. Grâce à leur conception et à la stratégie de commande adoptée, une fonction supplémentaire d'augmentation de la tension d'entrée est incluse. En apportant des ajustements au commande universelle du statisme, une structure hiérarchique améliorée et une nouvelle structure décentralisée ont été conçues pour gérer plusieurs onduleurs à source de tension connectés en parallèle. La stratégie de commande décentralisée a été proposée comme solution pour gérer les différents modes de fonctionnement du microgrid sans recours à des lignes de communication. Cela permet d'éviter les limitations de la commande secondaire centralisée incluse dans la structure hiérarchique, telles que les retards ou les pertes de données, qui pourraient entraîner l'effondrement complet du système. Différents algorithmes métaheuristiques modernes ont été adoptés pour déterminer les valeurs optimales des paramètres des commandes proposée.

Mots-clés : Microgrid flexible, Onduleurs de source de tension parallèles, Onduleur Z-source, Commande universelle du statisme, Commande par ordre fractionnaire, Commande par mode glissant super twisting, Commande décentralisée, Commande hiérarchisée, Optimisation métaheuristique.

Abstract—Microgrids are small-scale electrical networks integrating renewable energy sources, distributed generators, and local loads. They are designed to provide reliable and high-quality power supply in various operating modes, whether islanded or connected to the main grid, ensuring a seamless transition between these two modes. This type of system faces numerous technical challenges related to the nature of the loads, interruptions in energy sources, and the interconnection of components with different characteristics, which can impact the quality of the supplied power and the overall stability of the microgrid. With the emergence of modern power electronics converters and advanced control devices, a large part of these challenges can be solved. The work conducted as part of this thesis aligns with this context. Based on the robust performance of modern control systems, including fractional-order control, sliding mode control, and fuzzy logic control, we have developed new strategies and control tools for microgrids. Modern types of voltage source inverters, called Z-source and quasi-Z-source inverters, have been integrated. Through their design and adopted control strategies, an input voltage boosting function is enabled. Thanks to modifications in universal droop control, an improved hierarchical structure and a new decentralized structure were designed for managing multiple voltage-source inverters connected in parallel. The decentralized control strategy was proposed as a solution to manage the various operating modes of the microgrid without the need for communication lines. This approach avoids the drawbacks of centralized secondary control in hierarchical structures, such as delays or data loss, which could lead to a complete system failure. Furthermore, modern metaheuristic algorithms were employed to determine the optimal values for control parameters.

Keywords : Flexible microgrid, parallel voltage source inverters, Z-source inverter, Universal droop control, Fractional-order control, Super-twisting sliding mode control, Decentralized control, Hierarchical control, Metaheuristic optimization.

Acknowledgements

This doctoral research was carried out at the Laboratoire de Commande des Processus (LCP) of the École Nationale Polytechnique (ENP), in collaboration with the QUARTZ Laboratory in Cergy-Pontoise, France.

I would like to sincerely thank my supervisor, Pr. Djamel BOUKHETALA, for his invaluable support and guidance, which, after God's help, enabled me to complete this dissertation. His confidence in me, insightful advice, and constant encouragement helped me overcome challenges and stay focused throughout this journey. I am truly grateful and offer him my sincere thanks and deep respect. I would also like to express my heartfelt thanks to my co-supervisor, Pr. Jean-Pierre BARBOT, for graciously agreeing to contribute to my supervision. Despite his many commitments and busy schedule, he made an effort to offer his support, which I truly appreciate.

I would also like to express my sincere gratitude to the president of the jury, Pr. Mohand Oulhadj MAHMOUDI, as well as the members of the jury : Pr. Fares BOUDJEMA, Pr. Mohamed TADJINE, Pr. Lazhar RAHMANI, and Pr. Khalifa BENMANSOUR. I deeply appreciate their acceptance to serve on the reading committee and their constructive analysis of my work.

I am deeply thankful to my family and friends for their continuous support, encouragement, and presence throughout my studies. I also wish to extend my warm appreciation to all my colleagues from the LCP laboratory at ENP for their kindness and collaboration. Likewise, I express my sincere gratitude to all the professors of the Automatic Department at ENP, without exception, for the knowledge and guidance they provided along my academic journey.

Fatma-Zohra Hadjaidji
2025

Table of contents

Nomenclature

AC	Alternative-current
ANN	Artificial neural network
BESS	Battery energy storage system
C-YSGA	Chaotic yellow saddle goatfish algorithm
CC-VSI	Current-controlled VSI
DC	Direct-current
DG	Distributed generation
DPC	Direct power control
EMS	Energy management system
FLC	Fuzzy logic control
FOPID	Fractional-order proportional-integral-derivative
FOTSTA	Fractional-order terminal super-twisting algorithm
FSMC	Fuzzy sliding mode control
GA	Genetic algorithm
GWO	Grey wolf optimization
IC	Incremental conductance
ISMC	Integral sliding mode control
MG	Microgrid
MGCC	Microgrid centralized controller
MGDC	Microgrid decentralized controller
MPC	Model predictive control
MPPT	Maximum power point tracking
P&O	Perturb and observe
PID	Proportional-integral-derivative
PSO	Particle swarm optimization
PV	Photovoltaic
qZSI	Quasi-Z-source inverter
RES	Renewable energy source
SLPSO	Self-learning particle swarm optimizer
SMC	Sliding mode control
SOC	State of charge
SS	Static switch
SSMC	Synergetic sliding mode controller
SSE	Steady-state error
SSTA	Simplified super-twisting algorithm
SSSTA	Synergetic simplified super-twisting algorithm
STA	Super-twisting algorithm
SVPWM	Space vector pulse width modulation
THD	Total harmonic distortion
UDC	Universal droop control
VC-VSI	Voltage-controlled VSI
VSI	Voltage source inverter
ZSI	Z-source inverter

List of figures

List of tables

General Introduction

For several decades, electrical energy has been produced from hydraulic, thermal or nuclear stations. Located in areas far from centers of consumption, the central stations require a very powerful process of generation with a vast transmission and distribution network to feed electricity on a large scale. This model is based on a unidirectional power flow, circulating from high voltage levels to low voltages. However, this mode of centralized electricity production faces significant economic and environmental challenges, including ever-increasing global electricity consumption, pollution of the environment by rejecting CO2 under the generation process, the gradual depletion of fossil and fissile resources, and significant energy losses during transmission and distribution. To face these challenges, energy-productive companies have adopted a more flexible and localized mode of production : decentralized or distributed generation [1, 2].

In decentralized production, electrical energy is generated locally and near the consumers, using a variety of distributed-generation (DG) sources such as photovoltaic panels, wind turbines, microturbines, and fuel cells. Some of these technologies offer dual production of heat and electricity, known as cogeneration systems. This model offers a number of advantages, including reduced greenhouse gas emissions, lower energy losses during transmission, and lower infrastructure construction and maintenance costs [3–6]. However, due to the intermittent nature of some sources and the emergence of new types of electrical loads, the isolated integration of a DG units into a network can generate voltage and frequency fluctuations, as well as power line overloads that can exceed thresholds set by international standards. These disturbances compromise the quality of the energy distributed. To overcome these constraints and ensure stable grid operation, the microgrid concept was introduced [7, 8].

In fact, microgrids ensure a reliable, cost-effective power supply, guaranteeing better power quality for critical loads. Thanks to the integration of DGs, the microgrids enhance grid stability, offering greater flexibility and resilience. They can operate either in standalone mode or connected to the main grid. This concept optimizes electricity management and distribution. From the point of view of the electrical distribution network, the microgrid can be considered as a load or a generator according to the amount of power generated by the DG units or the power required from loads [9].

A microgrid has a different architecture and operation from a conventional electrical network, giving it additional advantages and challenges. Indeed, the operation of mi-

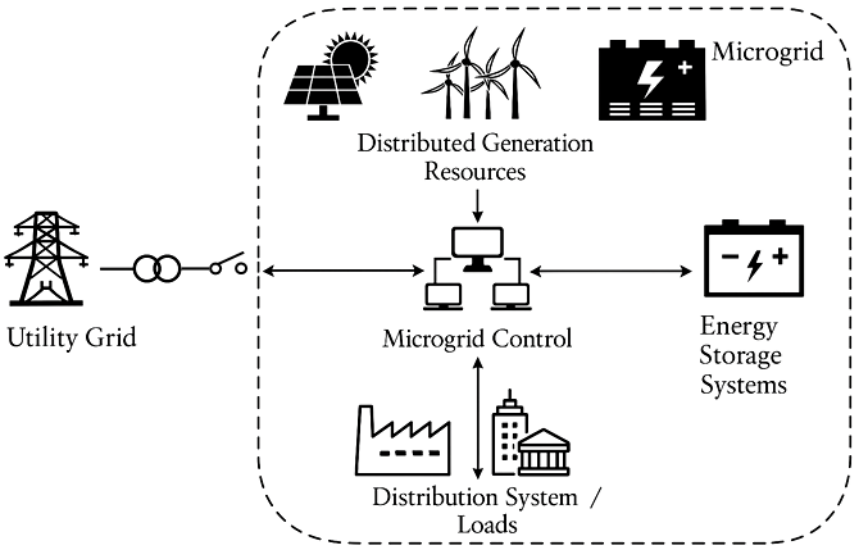

Figure 1 – Smart Hybrid Microgrid Architecture

crogrids is affected by several disturbances related to weather conditions, the nature of electrical loads, and the transition between different operating modes [10]. This generates instabilities, frequency and voltage variations, and the presence of harmonic currents. Indeed, this requires special protection equipment taking into account the bidirectional energy flow as well as the sharing of active and reactive power between all the DGs which must be guaranteed [11]. To face all these challenges and to ensure a reliable, sustainable, and uninterrupted power supply, microgrids require advanced control strategies and intelligent management to ensure local balance and improve their economic performance. Microgrid control must fulfill several essential roles :

— Operate as a single entity in front of the main grid
— Limit power exchanges according to defined thresholds
— Maintain frequency and voltage within standards
— Distribute resources to achieve energy balance
— Reconnect and synchronize the microgrid securely

Moreover, most DGs are not compatible with each other. Power converters are therefore crucial to ensure the interface between them [12]. As an example, photovoltaic panels and batteries produce DC power, while wind turbines generate AC power that needs an improvement in its quality in terms of voltage and frequency. Thus, Power converters play a key role in the integration and management of DGs. They ensure the conversion of the energy produced in order to make it compatible with the microgrid. By adapting the voltage, frequency, and shape of the current, they guarantee a stable and quality power supply, facilitating the control of energy flows, optimizing the use of available resources, and contributing to the stability of the whole system.

To ensure efficient conversion of energy from DGs, different types of power converters are used depending on the characteristics of each source. In the case of photovoltaic (PV) energy, a boost converter is generally used to increase the DC voltage from the solar panels. This process is optimized by the maximum power point tracking (MPPT) technique, which also facilitates the exploitation of the energy produced by the PV cells.

Once the voltage is adjusted, a DC/AC converter is necessary to transform this energy into AC nature in order to supply the AC loads of the microgrid or to inject the energy into the main grid.

For DC/AC conversion, the VSIs are widely utilized as power electronics interfaces where they can operate as voltage-controlled-VSI (VC-VSI) or current-controlled-VSI (CC-VSI) [13]. The VC-VSI is used to stabilize the microgrid voltage at the point-of-common-coupling (PCC), where the loads are connected. The CC-VSI is adopted to exploit the maximum power of the RESs to the local grid under all operating conditions and modes. In fact, the hybridization between CC-VSIs and VC-VSIs provides better reliability of local supply to the household user when connected to the regional microgrid. On the other hand, conventional VSIs have some limitations, particularly in terms of adapting to variations in RESs. To overcome these constraints, the Z-source inverter (ZSI or ZSVSI) has been introduced as a high-performance alternative [14, 15]. Thanks to its ability to operate in boost or buck mode without the need for an additional conversion stage, the ZSI improves the reliability and efficiency of power systems.

Power converter control is crucial for ensuring the stability and performance of microgrids, which increasingly integrate intermittent renewable energy sources and complex loads. The scientific literature explores a broad spectrum of strategies to meet this challenge [16]. Classical techniques, such as proportional-integral (PI), proportional-integral-derivative (PID) controllers, and vector control, while established, may struggle to deliver optimal performance given the fast dynamics and nonlinearities of modern electrical systems [17–19]. In response, advanced, intelligent, and robust approaches have been developed. Among these are various nonlinear strategies, fuzzy logic control (FLC), which can handle imprecision and uncertainty without requiring an exact mathematical model of the system , and model predictive control (MPC), particularly its finite-set variant (FS-MPC) [20–23]. MPC is valued for its ability to optimize control actions considering constraints and future system predictions, thereby improving waveform quality and dynamic response [24]. Proportional-resonant (PR) controllers are effective for regulating alternating currents [25], while fractional-order robust control (CRONE) aims for enhanced robustness [26, 27]. Sliding mode control (SMC) and its derivatives, like higher-order SMC (HOSMC) or terminal SMC (TSMC), are recognized for their inherent robustness against disturbances and parametric uncertainties [28–33]. Hybridization of these techniques is a strong trend, combining, for instance, fuzzy logic and sliding mode control (Fuzzy-SMC) to improve robustness and mitigate undesirable oscillations [21, 34, 35], or integrating artificial neural networks (ANN) into adaptive control schemes to enhance voltage regulation and harmonic reduction [36]. Another promising avenue is the use of metaheuristic optimization algorithms (e.g., genetic algorithms, particle swarm optimizer, simulated annealing) to fine-tune controller parameters (PI, PID, SMC, etc.) or to optimize the overall energy management within the microgrid. This allows for improvements in efficiency, stability, and system resilience under variable and complex operating conditions [19, 37, 38]. These advanced approaches collectively aim to enhance the dynamic response of converters, optimize power injection to the grid or local loads, minimize harmonic distortions, and ensure better microgrid resilience against disturbances.

In microgrids, also known as small-scale smart grids, the integration of multiple

distributed power sources requires efficient management and coordination. Parallel connection of VSIs improves the reliability and efficiency of power generation by allowing multiple isolated inverters to share demand, balance fluctuations, and provide redundancy [39, 40]. This configuration ensures a more stable output power, thereby reducing the risk of overload or failure of individual VSIs. However, to ensure smooth operation and avoid problems such as voltage or current imbalances, special control strategies are required. Several strategies have been proposed in the literature for controlling parallel VSIs in isolated mode, namely centralized control, distributed control, and decentralized control [41, 42]. Based only on the local information without requiring communication links between different VSIs, the droop control method regulates voltage magnitude and frequency by ensuring accurate sharing of active and reactive power, among DG-VSIs that are connected in parallel and proportional to their nominal power values, but on the conditions that they have the same output impedance. Furthermore, the scheduled active and reactive power is injected when the microgrid is connected to the main grid.

The decentralized structure of the droop control technique offers desirable properties such as extensibility, modularity, and flexibility. This is what encourages researchers to develop it to overcome challenges and improve its performance, to be robust and more flexible during various operating modes. In [43], a robust universal droop control controller is developed to operate in islanded mode regardless of the output impedance of the DG-VSIs. However, deviation in islanded microgrid voltages may occur due to the droop characteristics [44]. In addition, although the UDC can also operate in grid-connected mode as in islanded mode, it remains unable to transfer its operating mode from islanded to grid-connected operation due to the lack of synchronization between microgrid and utility grid voltages. For these reasons, the UDC is improved via a hierarchical control structure where an ameliorated UDC represents the primary control [45, 46]. microgrid-centralized-controller (MGCC) is adopted in the secondary level to restore the islanded microgrid voltage and ensure a smooth transition to the connected mode by correcting the phase angle error between both the grid and PCC voltage. Because of the MGCC process, microgrid control loses its decentralization advantage. Besides, the hierarchical control scheme is often unable to handle the fast-varying conditions due to its slow dynamic response. Afterward, a new local re-synchronization mechanism for the UDC, inspired by the self-synchronized UDC [47], has been introduced in [48]. It achieves a seamless transition to reconnect the microgrid to the grid, after the loss of connection without requiring another synchronization control loop.

In this context, this thesis focuses on the advanced control of distributed renewable energy systems and their integration into microgrids. First, it explores different control techniques applied to grid-connected PV systems, including MPPT control based on the proposed fractional-order super-twisting algorithm and the use of advanced correctors such as P-DPC-SVM for the grid-connected VSI. Then, the study focuses on stand-alone PV systems, addressing energy management, operating modes, and control strategies such as the proposed SSSTA control. Particular attention is carried to the integration of ZSI and qZSI inverters into these systems, exploring specific control techniques such as PR regulation, STA control, and FOPID control.

Furthermore, this thesis focuses on the hierarchical control of parallel DGs in mi-

crogrids, by successively studying the decentralized improved primary control, the centralized secondary control, and the proposed tertiary control. The primary control is addressed through the implementation of an enhanced fractional order universal droop controller, while the secondary control aims to restore the voltage and frequency of the island microgrid and to ensure a smooth synchronization process during transition mode. The proposed tertiary control, on the other hand, plays a key role in the overall flexibility and stability of the microgrid. Simulations are studied to validate these strategies, including a flexible microgrid based on parallel VSIs and a hybrid PV/battery microgrid integrating parallel ZSIs.

Finally, the thesis highlights the proposed decentralized control strategy, based on a universal droop controller, for DGs in microgrids, focusing on autonomous and local mechanisms such as self-restoration and self-synchronization based on fuzzy logic. A global decentralized control strategy is proposed to ensure efficient management of the flexible microgrid, with specific applications to the hybridization between VC-VSI and CC-VSI in a system based on a qZSI photovoltaic generator.

After selecting the overall control scheme for the studied topology, the main challenge in designing control laws lies in the lack of systematic methods for accurate parameter selection, particularly in interconnected non-linear systems such as multi-source energy conversion systems connected to microgrids. The design and synthesis of control laws often relies on human expertise and empirical testing, making the process time-consuming and imprecise. To overcome this drawback, metaheuristic optimization techniques : such as particle swarm optimization (PSO), self-learning PSO (SLPSO), grey wolf optimizer (GWO), and yellow saddle goatfish algorithm (YSGA), are used, to find optimal values for controller gains, taking into account the desired performance, guaranteeing robustness in the face of variations in operating conditions, and offering solutions adapted to non-linear and highly coupled systems. They also considerably reduce the need for trial and error by automating parameter optimization.

Based on the previous objectives, this thesis is structured as follows :

— **Chapter 1** presents a descriptive study of multi-source microgrid systems, introducing fundamental concepts of energy conversion and distributed generation. It provides an overview of microgrid architectures, operating modes, and typical PV-based structures, and reviews the main power electronic interfaces, including DC–DC converters, VSIs, and impedance-source inverters. The chapter also introduces relevant standards and basic microgrid control concepts, with emphasis on decentralized droop control and the introduction of hierarchical control structures.

— **Chapter 2** discusses recent solvers for the optimization problem based on metaheuristic algorithms such as PSO, SLPSO, GWO, and YSGA, which are used to tune the optimal parameters of the developed control structures according to specific criteria.

— **Chapter 3** investigates advanced control techniques, including the development of enhanced MPPT algorithms, VSI control strategies, and the integration of ZSI/qZSI within various PV system configurations.

— **Chapter 4** addresses hierarchical control for parallel distributed generation inverters, detailing enhanced decentralized primary droop control, centralized secon-

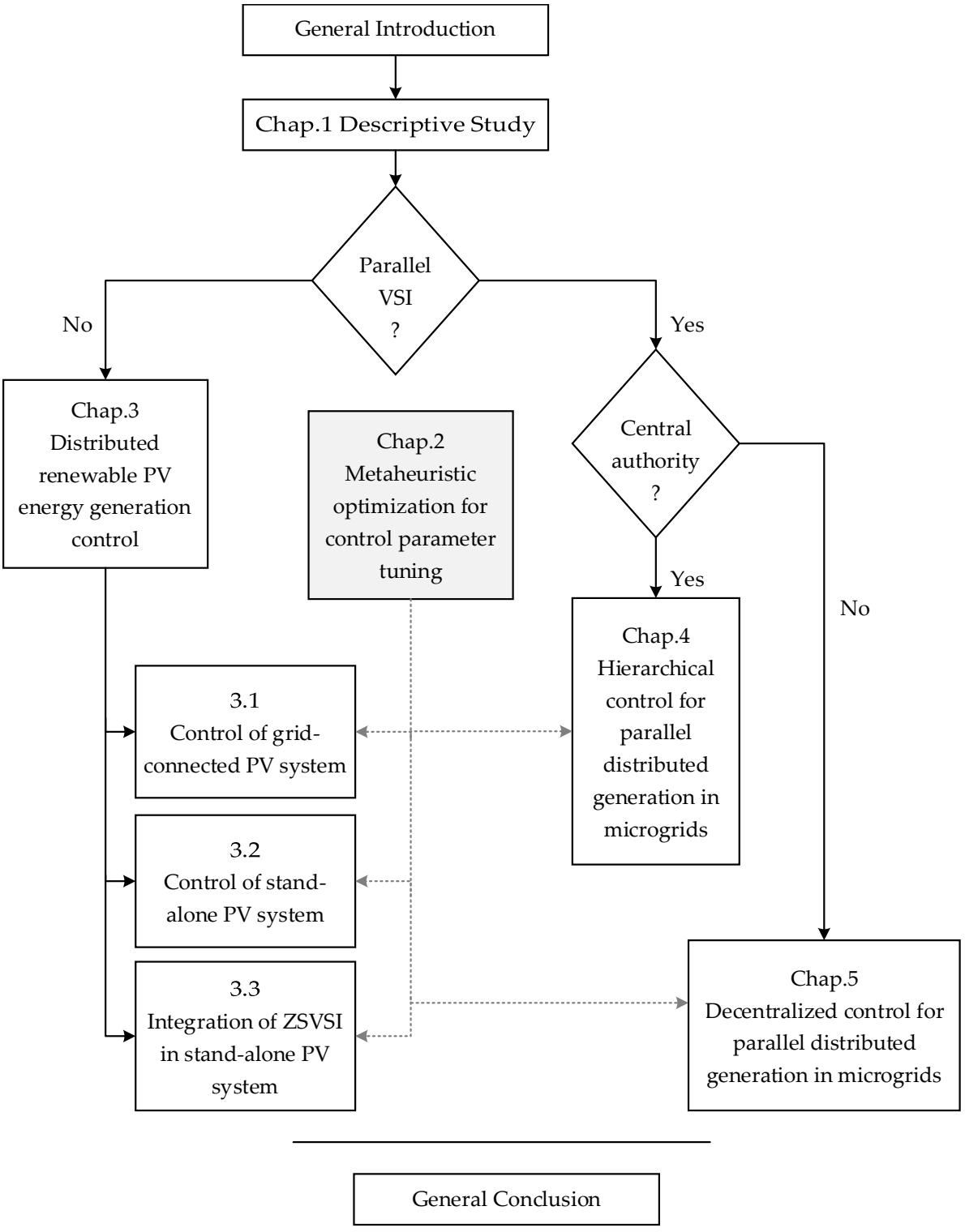

Figure 2 – Thesis reading guide diagram

dary voltage restoration and synchronization, and a proposed tertiary controller.

— **Chapter 5** develops an overall decentralized control strategy based on self-restoration and self-synchronization mechanisms, specifically tailored for the parallel inverters configuration.

Finally, the thesis concludes with a general summary and directions for future research perspectives. Figure. 2 provides a reading guide for this thesis.

Chapter 1

Descriptive study of multi-source microgrid systems

1.1 Introduction

In order to enable power grids to meet the new challenges posed by the depletion of traditional energy resources, the increase in global electricity consumption, and power quality issues, the concept of microgrids has been introduced as a promising solution. This concept facilitates the integration of renewable energy resources and their optimal use. In this chapter, after studying multi-source conversion systems and the integration of distributed generators, we explore the definitions of microgrid, its operating modes, advantages, and challenges. We also present the current standards and the control strategies necessary to ensure the reliable operation of the microgrid [49, 50].

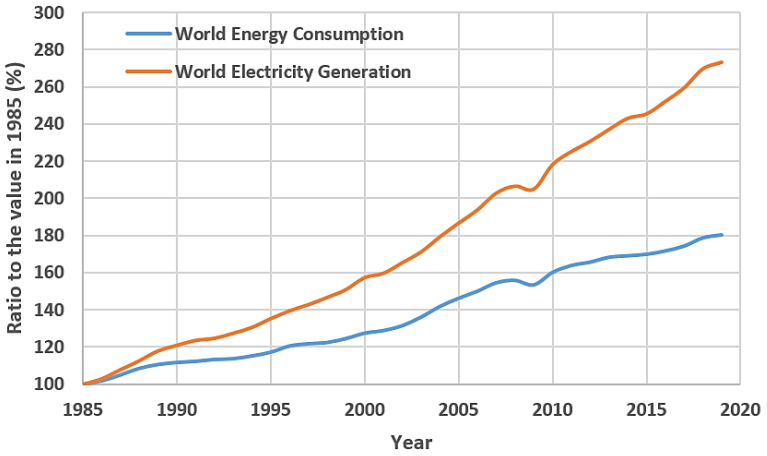

Figure 1.1 – The increase in global energy consumption in the world

1.2 Multi-source energy conversion systems

1.2.1 Energy conversion concepts

Conversion of energy to electrical energy is essential to transform different forms of energy into electricity. For example, in solar panels, light energy is converted directly into

electricity through the photovoltaic effect [51, 52]. Similarly, in wind turbines, the kinetic energy of the wind is transformed into mechanical energy by a turbine, which in turn drives a generator to produce electricity. In thermal power plants, the chemical energy of fuels (gas, coal) is first converted into thermal energy, which generates steam to turn a turbine, and this mechanical energy is then converted into electricity by an alternator. Turbines, generators, and alternators are the key devices for this transformation [53–55].

On the other hand, when discussing the conversion of the nature of electrical energy, it is about transforming electricity from one form to another to adapt it to the needs of users or systems [56]. Regarding power electronics converters, these devices play a fundamental role in the management of electrical energy. They allow the control and adaptation of the shape nature, frequency and voltage of electricity to optimize it in different contexts [57]. A typical example is the conversion DC/AC in systems such as solar installations, where the energy produced by photovoltaic panels is in DC. To make this energy compatible with household appliances and electrical networks, inverters are used, which convert DC to AC. Conversely, a rectifier is used to transform AC into DC, as in power supplies for electronic devices. As in battery systems or electrical applications for electric vehicles, a DC/DC converter is used to adjust the DC voltage [58].

In summary, the conversion of energy to electrical energy and the conversion of the nature of electrical energy are made possible by specific devices such as PV cells, turbines, generators, and alternators, as well as power electronics converters such as inverters, rectifiers, and DC/DC converters, which not only ensure the transformation of energy but also the adaptation of voltage and frequency to meet the varied needs of modern electrical systems.

1.2.2 Multi-source systems

Multi-source systems are energy systems that integrate multiple energy sources to optimize energy production and management [59]. For example, a multi-source system can combine solar, wind, and thermal energy to ensure a stable and reliable supply, even when production fluctuates [60]. This diversification helps to overcome the limitations of each individual source. For example, solar energy may be insufficient at night or on cloudy days, while wind energy may be less available during quiet periods. A multi-source system therefore helps to balance these variations and ensure continuity of service by combining the advantages of each source [61]. These systems are increasingly used in microgrids and smart grids, where they can improve energy efficiency and grid resilience.

1.2.3 Distributed energy generation

Distributed generation (DG) refers to small-scale power generation, often located close to the point of consumption. unlike centralized generation systems, where power is produced in large facilities and transmitted over long distances, distributed generation allows power to be produced directly at the site of use, such as residential solar panels or small wind turbines [62]. This model offers several advantages, including reducing power losses associated with transmission and achieving greater power autonomy for consumers

[63, 64]. Furthermore, the DG is often associated with the exploiting of renewable energy sources (RES)s, which helps reduce the carbon footprint and encourages an energy transition towards a more sustainable and decentralized system. It also allows users to actively participate in the management of their energy consumption.

1.3 Overview of microgrids

1.3.1 Definition

Microgrids are small-scale autonomous energy systems that provide electricity to an isolated area. By integrating DGs and enabling intelligent management of energy flows, these systems contribute to creating more flexible, sustainable and decentralized energy networks. To facilitate the integration of DGs and optimize their operation, it is necessary to combine loads and distributed energy storage systems via power converters equipped with advanced control of electrical quantities such as voltage, frequency, active and reactive power.

1.3.2 Operating modes

Microgrid operation may depend on conflicting interests between the various players involved in energy supply, such as grid operators, owners of distributed generators, energy suppliers, etc., as well as customers. The optimal operation of the microgrid is based on economic, technical, and environmental aspects. Four operating modes have been identified by the IEEE 1547 standard : grid-connected mode, transition mode, islanded mode, and reconnection mode [65, 66].

In grid-connected mode, the microgrid is connected to the main grid via the common coupling point (PCC), allowing power exchange. If local production is insufficient, the grid compensates for the deficit, and conversely, excess power is injected into the grid. This mode imposes voltage and frequency constraints defined by the main grid.

In islanded mode (isolated or autonomous), the microgrid operates autonomously after disconnection from the main grid, whether voluntarily (maintenance, protection) or involuntarily (faults, incidents). A stable power supply must then be ensured through local voltage and frequency management.

A smooth transition between these modes is crucial to avoid overvoltages and current peaks, thus ensuring the stability, flexibility, and continuity of microgrid operation and power supply. In fact, the PCC plays a key role in this management ensuring precise control of critical variables [67].

1.3.3 AC and DC microgrids

Microgrids can be designed to operate in alternating current (AC) or direct current (DC), depending on the nature of the distribution lines [68, 69]. There are also hybrid microgrids combining these two types. Each configuration has advantages and disadvantages.

AC microgrids use single-phase or three-phase alternating current, facilitating their integration into existing electrical networks with a few modifications. They allow simple adjustment of voltage levels and offer a wide choice of protection equipment. Moreover, their development cost is reduced thanks to the maturity of the technology. However, the AC microgrids require synchronization of the DG units with the network and control of reactive power, which can cause losses in transmission lines.

In the DC microgrids, the current is continuous, which is particularly well-suited to the majority of the DG sources, such as solar panels, batteries, and fuel cells, as well as to DC loads (LED lighting, variable speed drives, etc.). This configuration reduces DC/AC conversions, thus limiting energy losses. In addition, it requires neither synchronization with the main grid or reactive power management. However, the implementation of DC microgrids implies major modifications to existing infrastructures, generating high costs. Protection technologies are still under development and remain expensive.

The hybrid microgrid systems combine AC and DC technologies, allowing optimized integration of equipment by minimizing the number of conversions. This reduces power losses and simplifies the control of the different devices by connecting them directly to their adapted bus. However, the management of hybrid microgrids is more complex due to the coexistence of two types of configurations and necessary control strategies.

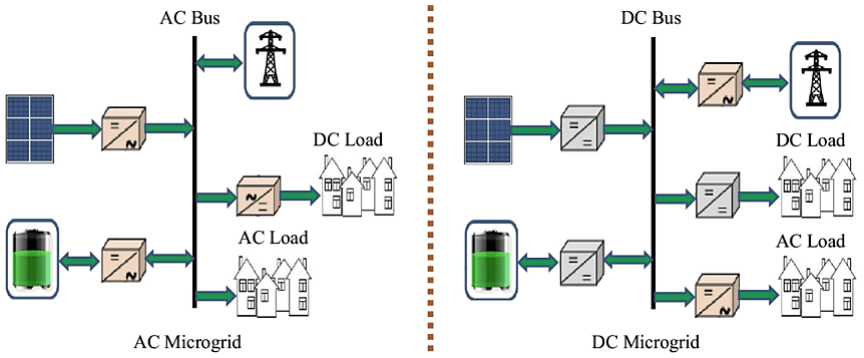

Figure 1.2 – AC and DC microgrids

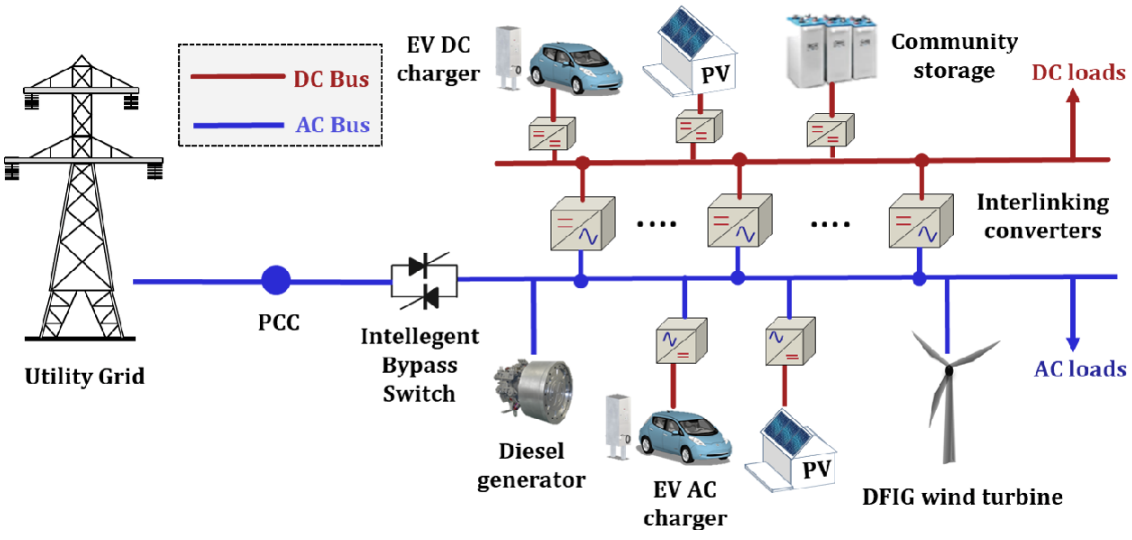

Figure 1.3 – Example of a hybrid microgrid

1.3.4 Typical PV-based microgrid architecture

Solar energy is widely available over the entire surface of the Earth. Despite a considerable decrease when crossing the atmosphere, the quantity reaching the ground remains quite significant. In temperate zones, the peak power reaches about $1000W/m^2$ and can rise to $1400W/m^2$ under favorable atmospheric conditions. This abundance makes solar energy one of the most accessible renewable resources. Photovoltaic (PV) generation has experienced rapid growth in recent decades due to its direct conversion of solar energy into electricity, absence of fuel consumption, low environmental impact, and modular structure [70]. According to the International Energy Agency, solar energy represented about 5.5% of total global electricity production in 2023. Considering that renewables accounted for roughly 30% of global electricity generation, solar energy contributed approximately 18.3% of renewable electricity generation, ranking third in terms of generation growth rate after hydropower and wind.

Beyond its abundance, photovoltaic generation is particularly well suited for microgrids due to its modularity, scalability, and decentralized nature, which allow flexible integration, local energy production, and reduced transmission losses. Its compatibility with AC, DC, and hybrid microgrid structures further enhances its adaptability, making solar energy a preferred and dominant renewable resource and a cornerstone for sustainable, reliable, and locally managed microgrid systems.

Overview of photovoltaic systems

PV systems are divided into three categories : stand-alone, grid-connected, and hybrid [71–73]. Grid-connected or grid-interactive systems operate in parallel with the grid, with their inverter converting the DC power produced by the panels into AC power that complies with grid standards. In the event of a power outage, the power supply is automatically interrupted. These systems reduce the consumption of electricity from the grid and, in some cases, reinject excess energy. They ensure efficient and high-quality energy production close to the point of consumption, thus limiting losses related to transmission and distribution. Stand-alone systems, on the other hand, operate independently of the electrical grid, supplying DC and/or AC electrical loads, and are generally sized according to specific energy needs. Since energy demand fluctuates and does not always match solar production, batteries are recommended as energy storage systems (ESS)s to ensure a stable supply [74]. Finally, hybrid systems combine solar PV with other generation sources, such as diesel, gas, or wind generators, to optimize energy supply based on needs and available conditions.

A photovoltaic solar system consists of several elements interconnected with each other [75, 76]. It consists of solar panels, which in turn are formed by assembling several solar modules. Each module consists of a group of solar cells, round or square, electrically connected in series or parallel and encapsulated to ensure their protection and performance. When a solar cell is exposed to sunlight, free-charge carriers are generated. The amount of charge is directly proportional to the intensity of the incident radiation, such as the photocurrent flowing inside the cell. Thus, an ideal photovoltaic cell can be created by an electrical circuit consisting of a diode representing a P-N junction, and a constant

current source whose intensity depends on the received radiation. Adding two resistors, one in series and one in parallel, allows to assimilate the real behavior of the cell.

Thus, a PV cell can be represented by the following equivalent electrical circuit :

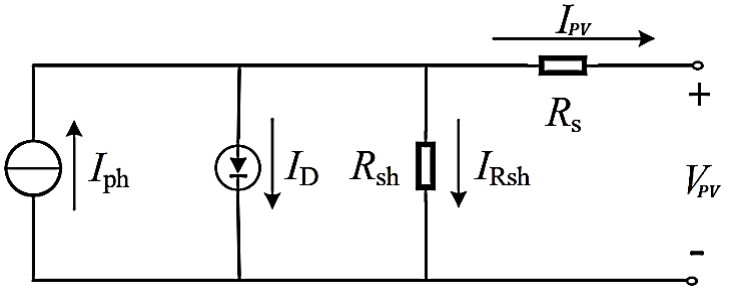

Figure 1.4 – Equivalent circuit of a photovoltaic solar cell

According to Kirchhoff's law [77], the PV cell can be modeled as follows :

$$I_{pv} = I_{ph} - I_s \left(\exp\left(\frac{q}{\gamma k T} (V_{pv} + R_s I_{pv}) \right) - 1 \right) - \frac{V_{pv} + I_{pv} R_s}{R_{sh}} \tag{1.1}$$

where I_{pv} and V_{pv} are the output current and voltage of the PV module, I_{ph} is the photo-generating current and I_s the reverse bias current of the diode saturation. R_s and R_{sh} are series and shunt resistors, respectively. γ is the ideality factor of the PN junction (1 *to* 2), T is the operating temperature of the cell in Kelvin, q is the electron charge ($1,602 \times 10^{-19}\ C$) and K is the Boltzmann's constant ($1.3806 \times 10^{-23}\ J/K$).

To obtain a more accurate modeling of the PV cell, the effect of both sunlight level and temperature must be considered. Thus, for a temperature T and a solar radiance G, the currents I_{ph} and I_s can be obtained using the following system of equations :

$$\begin{cases} I_{ph} = \dfrac{G}{G_{\text{STD}}} \left(I_{sc,\text{STD}} + \mu_{sc} (T - T_{\text{STD}}) \right) \\ I_s = I_{s,\text{STD}} \left(\dfrac{T}{T_{\text{STD}}} \right)^3 \exp\left(\dfrac{q E_{bg}}{\gamma K} \left(\dfrac{1}{T_{\text{STD}}} - \dfrac{1}{T} \right) \right) \end{cases} \tag{1.2}$$

where, $I_{sc,STD}$ and $I_{s,STD}$ are the short-circuit and saturation currents under standard conditions ($T_{STD} = 298\ K$ and $G_{STD} = 1000\ W/m^2$). μ_{sc} is the temperature coefficient of the cell short-circuiting current. E_{bg} is the bandgap energy of the silicon solar cell.

Indeed, a single PV cell cannot provide enough power to supply the load. It is therefore advisable to combine the cells together to provide more power. A series association will increase the output voltage of the solar panel while a parallel association will increase the current supplied to the load. For this purpose, a PV panel combining N_s series cells and N_p parallel cells can be presented by the following expression :

$$I_{pv} = N_p I_{ph} - N_p I_s \left(\exp\left(\frac{q}{N_s K \gamma T} \left(V_{pv} + \frac{N_s}{N_p} R_s I_{pv} \right) \right) - 1 \right) - N_p \left(\frac{V_{pv} + \frac{N_s}{N_p} R_s I_{pv}}{\frac{N_s}{N_p} R_{sh}} \right) \tag{1.3}$$

Maximizing PV power generation

As shown in Figure. 1.5, the MPP position varies depending on the climatic conditions.

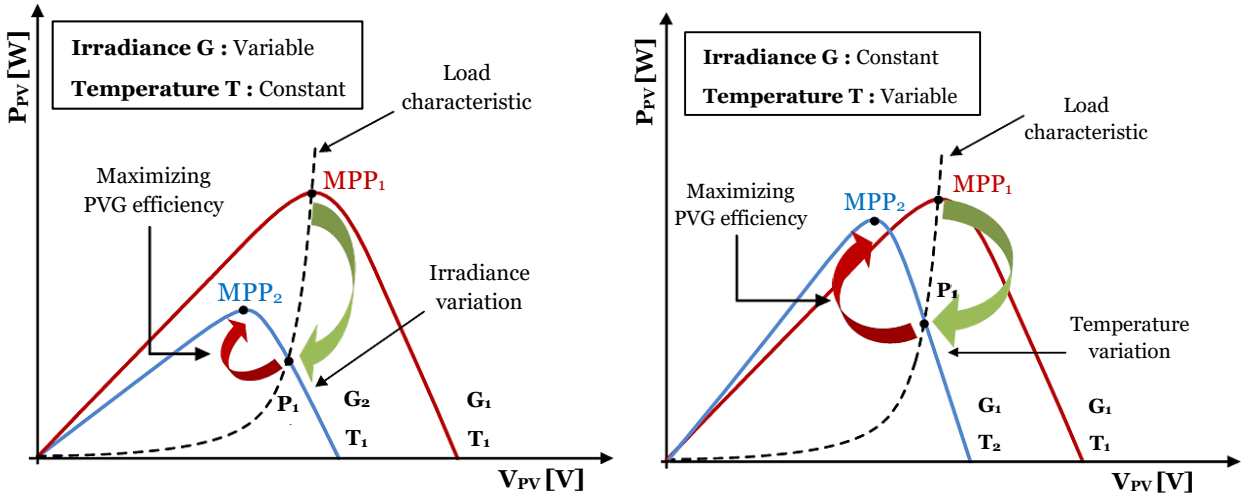

Figure 1.5 – MPP variation, depending on solar irradiance and panel temperature

The mathematical definition of the optimum function corresponds to the point at which its derivative with respect to a given variable is zero. This principle is the basis of all the algorithms for tracking the maximum power point. Some of these algorithms require precise knowledge of the mathematical model of the photovoltaic generator to estimate this point, while others do not. In the latter cases, the maximum power point is determined by measuring the PV power on two successive samples, then calculating the slope of the power as a function of the voltage [78, 79].

Numerous algorithms and techniques are discussed in the literature allowing efficient tracking of the maximum power point (MPPT). These controls can be classified according to their operating principle. According to the most common classification, MPPT methods can be split into two categories, conventional and intelligent methods [80, 81]. In the first category, the well-known incremental conductance (IC) and perturb and observe (P&O) are the most popular algorithms due to their intuitive understanding, simple implementation, and relatively good performance [82]. The second category relies on advanced artificial intelligence techniques, such as metaheuristic algorithms and fuzzy logic. Thanks to their adaptive and learning capabilities, these methods allow more efficient monitoring of the MPP position, even in the presence of crucial variations in environmental conditions. However, their implementation requires significant computational complexity, which may be a barrier to their adoption in some embedded or low-cost systems.

To combine high performance with ease of implementation, hybrid techniques have been developed. These approaches are based on advanced strategies derived from automatic control theory, particularly nonlinear and robust methods. They are designed to enhance energy efficiency while striving to minimize implementation complexity. Their main objective is to overcome the limits of conventional and intelligent techniques by ensuring a fast and precise response to variations in the nonlinear characteristics of PV generators, while remaining accessible in terms of hardware and software implementation.

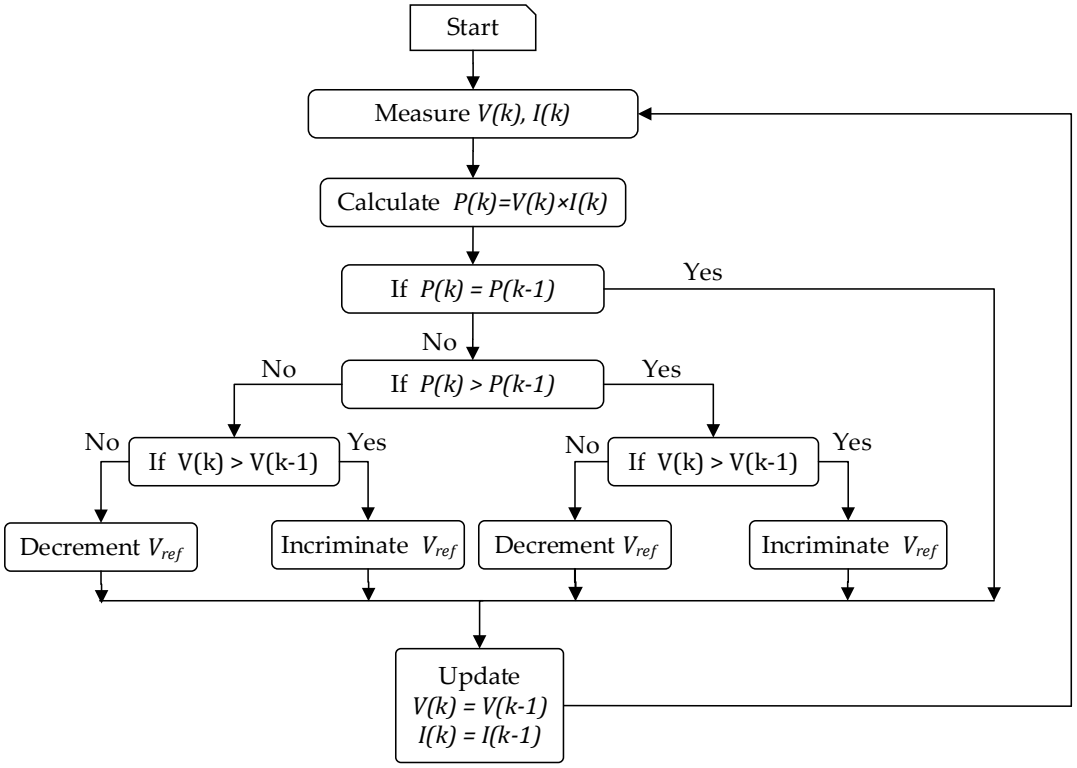

Figure 1.6 – Flowchart of the P&O MPPT algorithm

1.4 Power electronic interfaces in microgrids

Electrical energy from distributed energy resources (DER), in particular renewable energy sources (RES), presents a variability that requires specific adaptation steps to ensure efficient use and high-quality transmission [83]. This is particularly the case for PV energy, whose production depends directly on sunshine and weather conditions, leading to voltage and current fluctuations that must be regulated for optimal operation. The integration of these energies into electrical networks or stand-alone systems is based on the use of power converters adapted to the conversion and conditioning of the electricity produced [84]. These converters are divided into several categories depending on the nature of the conversion carried out : DC/DC, DC/AC, AC/DC, and AC/AC. Each of these devices plays an essential role depending on the energy source's characteristics and the connected loads' requirements.

In the specific case of photovoltaic systems, only DC/DC and DC/AC converters are used [85–88]. DC/DC converters, such as boost and bidirectional converters, are used to adapt the output voltage of solar panels to optimize energy extraction via the maximum power point tracking (MPPT) technique and make it compatible with storage devices [89–91]. In addition, DC/AC converters, mainly voltage source inverters (VSIs), are used to convert direct current electricity from solar panels into alternating current that complies with grid standards or is suitable for the supplied loads. Thanks to these adaptation steps, photovoltaic energy can be optimally exploited, with efficient regulation of production and power transmission ensuring the stability and quality required for different applications [91, 92].

1.4.1 DC–DC conversion for PV-based microgrids

Boost converter

In the PV system. The boost converter is used not only to adapt the PV generator but also to track the operating MPP by introducing an appropriate control of the converter [93]. As clarified in Figure. 1.7, the boost converter's performance can be expressed by two states, ON and OF, depending on the state of its power switch. Therefore, the mathematical representation of this system is given as follows :

$$\begin{cases} \dfrac{dV_{pv}}{dt} = \dfrac{1}{C_{pv}} i_{pv} - \dfrac{1}{C_{pv}} i_L \\ \dfrac{di_L}{dt} = \dfrac{1}{L} V_{pv} - \dfrac{1}{L}(1-D)V_{dc} \end{cases} \tag{1.4}$$

where V_{dc} is the voltage across the DC-bus capacitor C_{dc}, L is the boost inductance and D is the duty cycle which represents the control signal. A DC filter capacitor C_{pv} is placed at the output of the PV power generation source, to protect the system from the effect of ripple content, and convert the PVG from a current source I_{pv} to a voltage source V_{pv}.

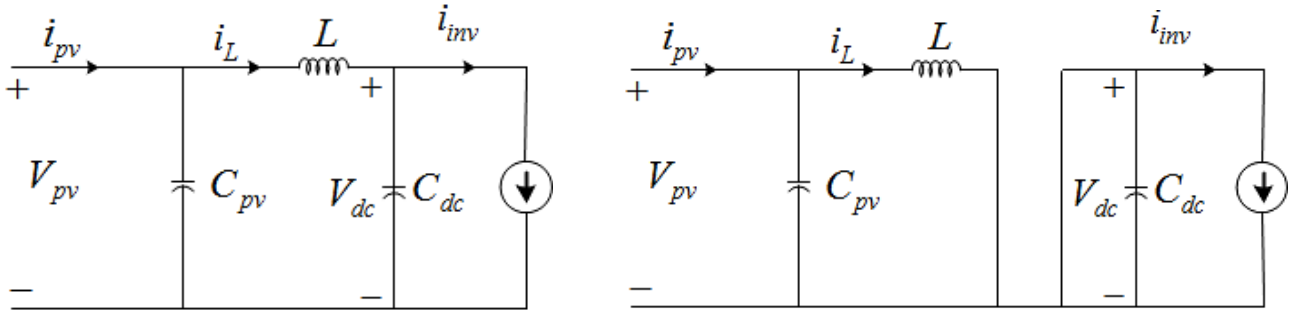

Figure 1.7 – Schematic of the boost power converter : (a) OFF state, (b) ON

Bidirectional converter

Because of the unpredictability of solar energy, the battery energy storage system (BESS) is used to maintain the energy balance in the PV system. The BESS is linked to the DC-bus through a DC-DC-bidirectional converter [94–96]. From the circuit diagram shown in Figure. 1.8, the model of the bidirectional converter can be introduced by the following equations system :

$$\begin{cases} \dfrac{di_b}{dt} = \dfrac{V_b - D_b V_{dc}}{L_b} \\ \dfrac{dV_{dc}}{dt} = \dfrac{1}{C_{dc}} i_{dc} \end{cases} \tag{1.5}$$

where, V_b is BESS output voltage, i_b is the stream through the internal inductance L_b, V_{dc} is the DC bus capacitance-voltage and i_{dc} its stream. D_b the duty cycle of the converter.

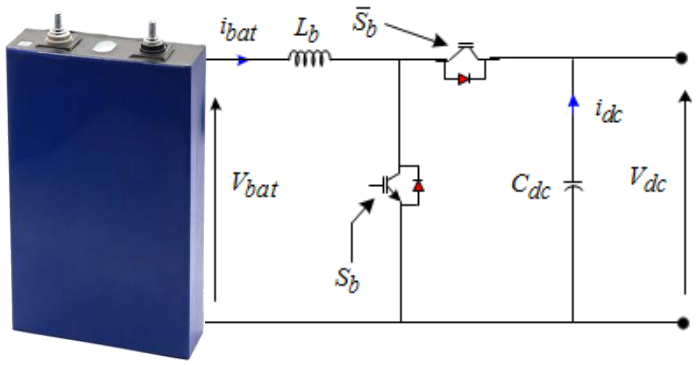

Figure 1.8 – Schematic of the Bidirectional DC-DC Converter Integrated with BESS

1.4.2 Three-phase voltage source inverter (VSI)

The three-phase VSI plays a key role in photovoltaic systems by converting the continuous power produced by the solar panels into usable alternative energy. Its operation can be done in grid-connected mode, where it ensures the synchronization and efficient injection of energy, or in stand-alone mode, guaranteeing the energy autonomy of local AC loads. To improve the quality of the output signal, the use of RL filters in the connected mode allows to reduce harmonics and ensure better integration with the grid, while the LC filters in isolated mode ensure a stable sinusoidal voltage.

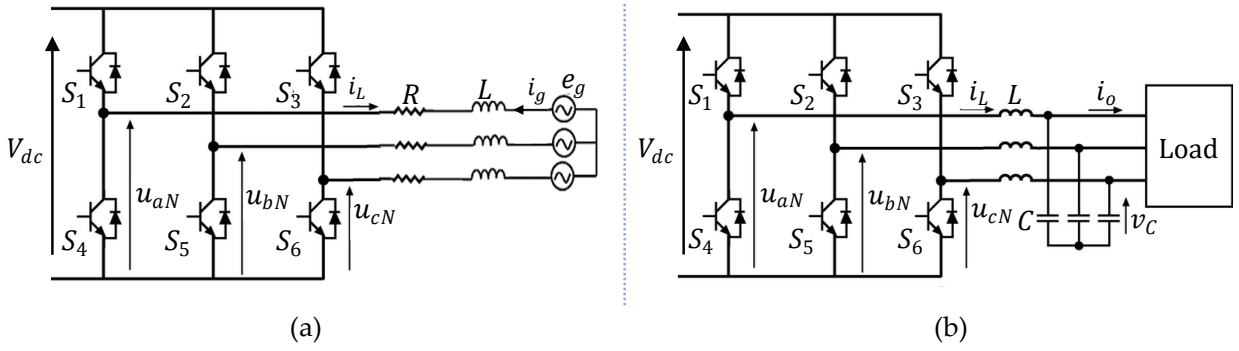

Figure 1.9 – Three-phase VSI (a) grid-connected (b) stand-alone

In addition, the $(\alpha\beta)$ and (dq) transformations are essential to simplify the analysis and control of the inverter, thus facilitating the optimization of performance and the regulation of the system. The Clarke transformation projects the three voltages or currents (abc) into a fixed frame $(\alpha\beta)$, where the components remain alternating and independent. In contrast, the Park transformation converts these components $(\alpha\beta)$ into a synchronized rotating frame (dq) , making the signals linear but introducing a coupling between the d and q components.

Grid-connected VSI with RL filter

The circuit of the grid-connected VSI with RL filter is illustrated in Figure. 1.9a. Applying the Clarke transformation, this system can be modeled by the following expression :

$$L\frac{di_{g,\alpha\beta}}{dt} = -Ri_{g,\alpha\beta} + e_{g,\alpha\beta} - u_{\alpha\beta} \tag{1.6}$$

Where $i_{g,\alpha\beta}$, $e_{g,\alpha\beta}$ are the line current and the grid voltage in the stationary reference frame ($\alpha\beta$), respectively. R and L are the RL filter parameters.

Then, the instantaneous inverter outputs, active and reactive power p_s and q_s, injected into the main grid can be expressed in the reference frame ($\alpha\beta$) as follows :

$$\begin{cases} p_s = \frac{3}{2}\left(e_{g,\alpha}i_{g,\alpha} + e_{g,\beta}i_{g,\beta}\right) \\ q_s = \frac{3}{2}\left(e_{g,\beta}i_{g,\alpha} - e_{g,\alpha}i_{g,\beta}\right) \end{cases} \tag{1.7}$$

Stand-alone VSI with LC filter

In the stationary reference frame ($\alpha\beta$), the stand-alone VSI associated with the LC filter shown in Figure. 1.9b can be presented by the following model :

$$\begin{cases} C\frac{dv_{C,\alpha\beta}}{dt} = i_{L,\alpha\beta} - i_{o,\alpha\beta} \\ L\frac{di_{L,\alpha\beta}}{dt} = -v_{C,\alpha\beta} - ri_{L,abc} + u_{\alpha\beta} \end{cases} \tag{1.8}$$

Where C, L, and r are the LC filter capacitance, inductance, and its internal resistance, respectively. v_C and i_L are their voltage and current. u is the output voltage of the VSI.

The output quantities can also be transformed into continuous and coupled quantities in the reference frame (dq), which rotates synchronously with the angular velocity ω of the inverter output voltage. Using the Park transformation, we can obtain :

$$\begin{cases} C\frac{dv_{C_d}}{dt} = i_{L_d} - i_{o_d} + \omega C v_{C_q} \\ C\frac{dv_{C_q}}{dt} = i_{L_q} - i_{o_q} - \omega C v_{C_d} \\ L\frac{di_{L_d}}{dt} = -v_{C_d} - ri_{L_d} + \omega L i_{L_q} + u_d \\ L\frac{di_{L_q}}{dt} = -v_{C_q} - ri_{L_q} - \omega L i_{L_d} + u_q \end{cases} \tag{1.9}$$

1.4.3 Impedance source inverters (ISI)s

As a DC–AC converter, conventional VSI requires strict conditions to be respected when adopted in a PV system. A proactive DC–DC conversion level is mainly needed to achieve MPPT tracking despite critical changes in climate conditions [97]. Furthermore, switches on the same arm cannot operate simultaneously. Therefore, it is necessary to have a dead time to block these two switches to avoid the shoot-through state of the voltage source. This leads to distortion of electrical signals and a significant decrease in reliability. In contrast, the cost of both power and control circuits increases. The strict requirements

of traditional PV–VSIs have encouraged researchers to design a new type called the impedance source inverter (ISI) that overcomes these challenges. Thanks to the additional impedance network, the ISI is not only an alternative topology capable of providing two-stage power conversion (DC/DC and DC/AC) but is also able to include the extra shoot-through zero state as an additional switching state. This increases reliability and reduces the harmonic distortion rate of the AC output signals.

Z-source inverter (ZSI) topology

The Z-source inverter (ZSI) is the classical and basic topology of impedance source inverters (ISIs). It consists of energy storage inductances L_{z1}, L_{z2}, energy storage capacitances C_{z1}, C_{z2} connected in X shape and diode D, forming a Z-network to couple the inverter's main circuit to the DC power supply. In addition to the six active states and the two zero states of the traditional VSI, the Z-source one has an additional state located only in the zero states, without affecting the active state. This state is called the shoot-through state, which is forbidden in the traditional VSIs. This new state is used to boost the output DC-bus voltage. The structure of the ZSI is shown in Figure. 1.10.

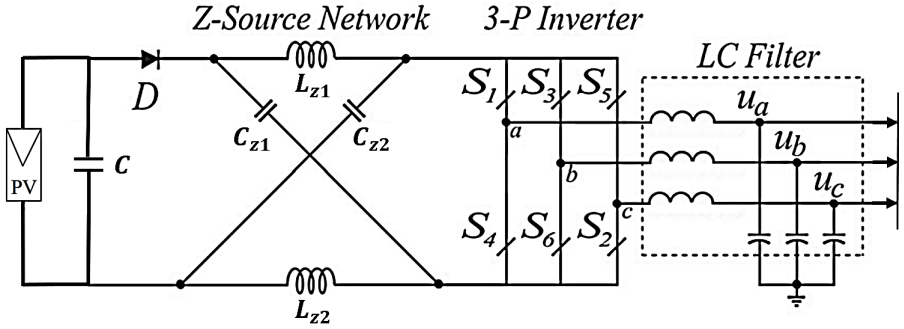

Figure 1.10 – The topological structure of the Z-source/ PV inverter

The three different modes of the Z-source inverter are summarized in Figure. 1.11.

Using the average state-space model, the combination of shoot-through and non-shoot-through states can be expressed as follows :

$$\begin{cases} \dfrac{dV_{pv}}{dt} = -\dfrac{1}{C_{pv}} i_{Lz} + \dfrac{1}{C_{pv}} \left(i_{pv} - i_{cz}\right) \\ \dfrac{di_{Lz}}{dt} = \dfrac{1}{L_z} \left[V_{cz} + (1-d)(V_{pv} - 2V_{cz}) - r_{Lz} i_{Lz}\right] \end{cases} \tag{1.10}$$

where V_{pv} and i_{pv} are the input voltage and input current from the PVG, respectively. i_{Lz} is the Z-inductance current. C_{pv} is the DC filter, L_z is the Z-source inductance, and r_{Lz} is its parasitic resistor. i_{Cz} is the Z-source capacitor current, and d is the duty cycle of the shoot-through state, i.e. $d = T_o/T_s$ where $T_o \in [0, T_s]$ is the shoot-through time and T_s is the switching cycle.

In steady-state operation, the average inductor voltage over the complete switching period T_s can be considered to be zero. Therefore, the relationship between the DC quantities of the impedance network is given by :

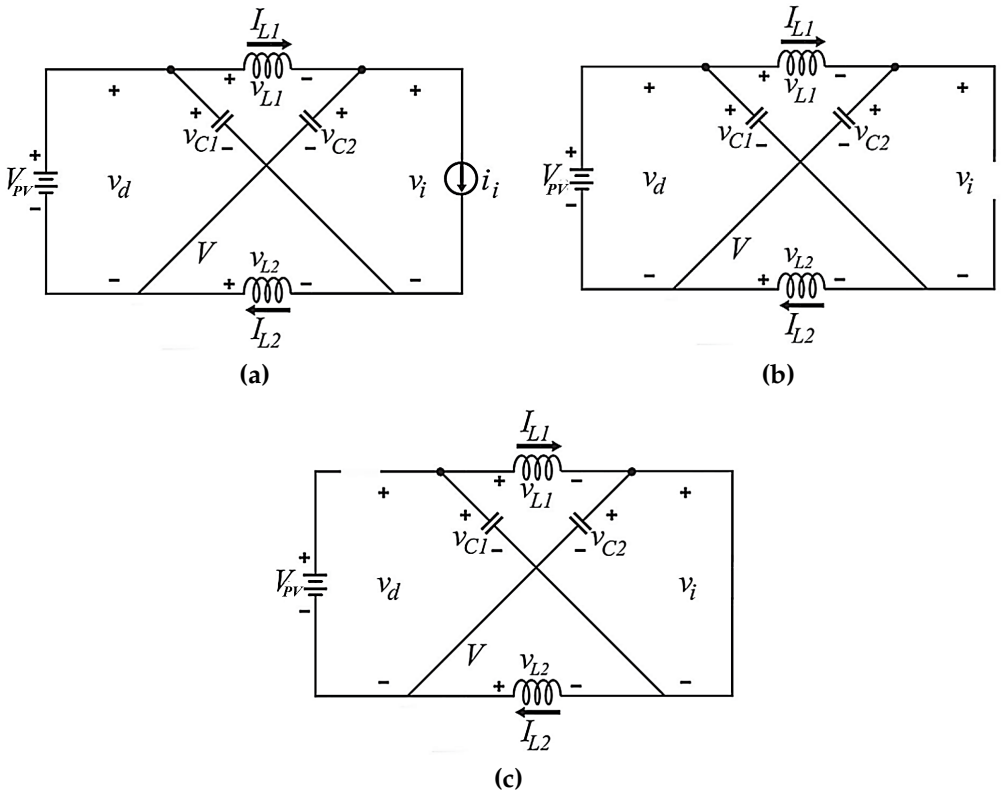

Figure 1.11 – (a) active voltage mode (b) zero voltage mode (c) shoot-through state

$$\begin{cases} V_{C1} = V_{C2} = V_{Cz} = \dfrac{1-d}{1-2d} V_{PV} \\ V_i = \dfrac{1}{1-2d} V_{PV} = B V_{PV} \quad \text{(non shoot-through state)} \\ V_i = 0 \quad \text{(shoot-through state)} \end{cases} \tag{1.11}$$

where V_i is the Z-source DC-chain output voltage. V_Cz is the voltage of the ZSI capacitors. B is the boost factor of the ZSI.

As for the AC side of the ZSI, it is similar to the traditional VSI.

Being M the modulation ratio, the output voltage amplitude V_m of the ZSI can be expressed as follows :

$$V_m = M \times B \frac{V_{pv}}{2} \tag{1.12}$$

Quasi-Z-source inverter (qZSI) topology

Several topologies derived from the classical Z-source inverter (ZSI) have been proposed in the literature. Among these, the quasi-Z-source inverter (qZSI) is the most recommended for PV power generation systems. Compared to the ZSI, it features a continuous input current, reduced size of passive network components, and lower source stress [15].

The qZSI impedance network (DC side) also consists of two inductors, two capacitors,

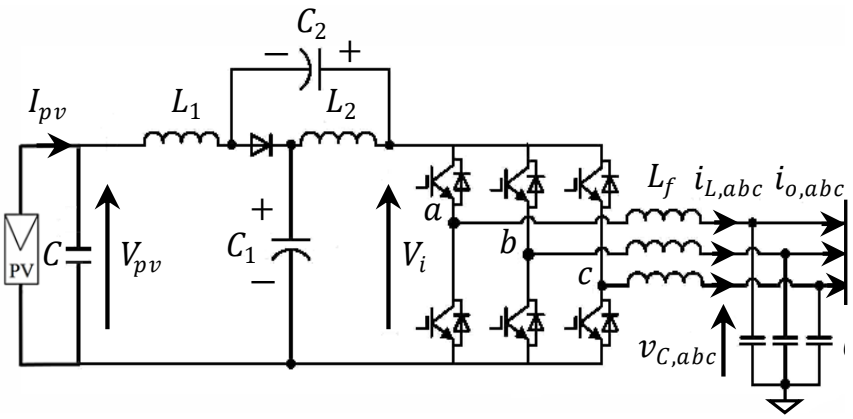

Figure 1.12 – The topological structure of quasi-Z-source/ PV inverter

and a diode connected between them as shown in Figure. 1.12. The relationship between the DC quantities of the qZS-impedance network at steady state can be described as :

$$\begin{cases} V_{C1} = \dfrac{1-d}{1-2d} V_{pv} \\ V_{C2} = \dfrac{d}{1-2d} V_{pv} \\ V_i = \dfrac{1}{1-2d} V_{pv} = B V_{pv} \end{cases} \tag{1.13}$$

1.5 Norms and Standards

Connecting DG resources to power grids poses engineering, safety, and reliability challenges, particularly due to the traditional radial structure of the grids, which does not allow for a bidirectional energy flow. This paradigm shift requires robust standardization to ensure grid stability, reliability, and interoperability.

A pivotal development in this context is the IEEE 1547 series of standards, which provide a comprehensive framework for the interconnection of DGs with electric power systems [98]. Although the initial IEEE P1547 standard did not explicitly refer to microgrids, it introduced the concept of a Local Electric Energy System (LEES), which effectively encompasses networks of safety, testing, and maintenance for DG-grid interconnection, aiming to establish universally applicable technical criteria [99].

Subsequent developments in the series, such as IEEE P1547.3, address the methodologies for monitoring, information exchange, and control of DGs, while IEEE 1547.4 focuses specifically on the planning and operation of microgrids in islanded mode, an essential capability for enhancing grid resilience and autonomy.

Among the key technical requirements and operational provisions defined by IEEE 1547 standards are :

— Ensuring that the grounding of a LEES does not introduce overvoltage or disrupt ground fault protection in the main grid
— Maintaining voltage fluctuations within ±5% at the PCC, and limiting flicker

acceptable levels
- Prohibiting the energization of a de-energized grid by DGs
- Requiring DG units rated at 250 kVA or more to include monitoring devices for connection status, real and reactive power, and voltage
- Mandating isolation devices with visible disconnection where applicable, and adherence to electromagnetic compatibility and overvoltage standards
- Allowing reconnection to the grid only after a minimum of 5 minutes once the voltage and frequency are within permissible limits
- Permitting intentional islanding under agreed conditions by relevant stakeholders

Beyond interconnection, the quality of the power remains a critical concern. International standards such as IEC 61000, IEEE Std 1159, and EN50160 define thresholds and limits for power quality disturbances, including voltage sags, overvoltages, and current harmonics. These standards are vital for ensuring stable and high-quality power delivery in DG-rich environments [98, 100].

Control and communication within microgrids are addressed by IEC 61850, which standardizes data exchange, protection, automation, and control protocols among DG components. Additionally, IEEE 2030.7 specifies requirements for microgrid Energy Management Systems (EMS), supporting both grid-connected and islanded operations through autonomous control functions [101]. More recently, IEEE 2030.12-2025 provides detailed guidance on protection system design, including the coordination and selection of protective devices in different operating modes.

For mission-critical and specialized contexts, such as military installations, the Tactical Microgrid Standard (TMS) has been developed [102]. It introduces control and communication interfaces tailored to tactical microgrids, prioritizing resilience, adaptability, and compatibility with emerging technologies. This is particularly significant for ensuring an independent and reliable power supply during grid outages or disruptions.

Collectively, these evolving standards play a key role in achieving the safe, reliable, and efficient integration of DGs and microgrids, thereby supporting the transition toward more flexible and resilient energy systems.

1.6 Microgrid control

At the first level, power converters enable and improve the integration and control of DGs. In AC microgrids, VSIs are widely used as DC/AC power electronics interfaces where they can operate as VC-VSI or CC-VSI. The main objectives of VSI control are :

- Achieve low total harmonic distortion (THD) of output quantities.
- Ensure a good dynamic performance of the power supply, with minimum ripples and low overshoot.
- Maintain output current within safe limits.
- Improve disturbance rejection.

On the other hand, the parallel connection of VSIs improves the reliability and efficiency of power generation by allowing multiple isolated inverters to share demand, balance

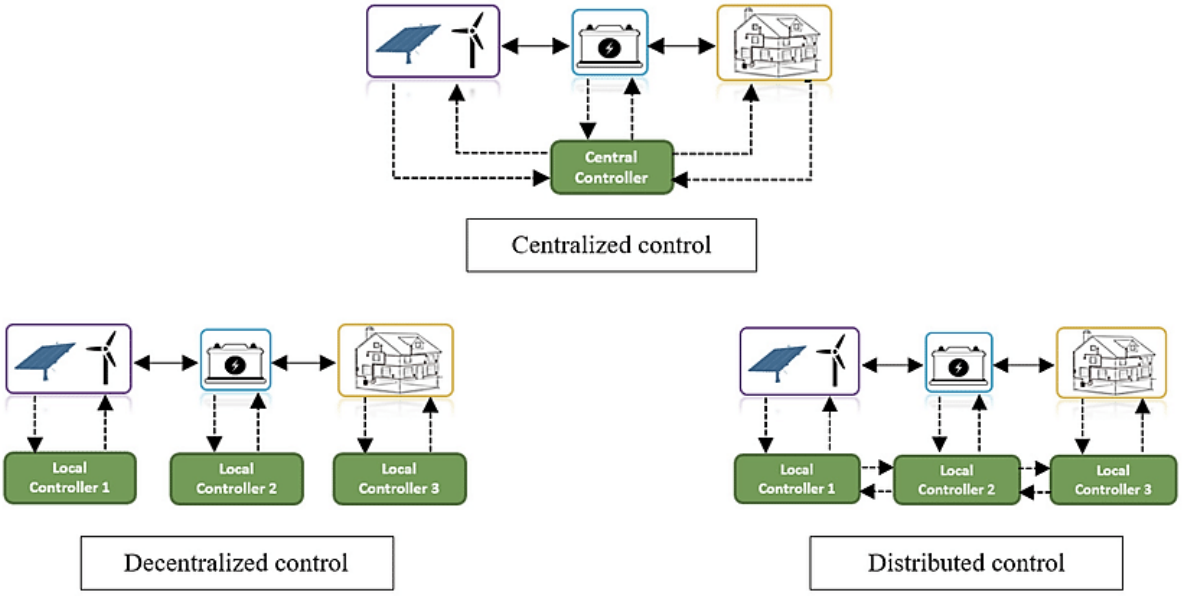

Figure 1.13 – Representation of centralized, distributed, and decentralized control structure

fluctuations, and provide redundancy. This configuration ensures more stable output power, reducing the risk of overload or failure of individual VSIs. However, to ensure smooth operation and avoid problems such as voltage or current imbalances, special control strategies are required. Several strategies have been proposed in the literature for the control of parallel VSIs in isolated mode namely centralized control, distributed control and decentralized control [103–106].

In the centralized control strategy, all the information is collected by a specific central regulator which performs the necessary calculations and determines the corrective actions for the other units of the microgrid, then the commands are sent. Current sharing is guaranteed at all times, even during the transient regime and other VSIs can be connected without changing the control structure. The main disadvantage of this strategy is the single point of failure ; if the central controller fails, the rest of the system malfunctions. Furthermore, this strategy requires high-bandwidth communication links between the subsystems and the centralized control unit. This system is also sensitive to nonlinear loads.

The distributed control strategy can only be used in balanced systems. Current and power sharing is ensured and the currents flowing between the parallel VSIs are reduced. It uses a communication link with a narrower bandwidth.

Decentralized control relies only on local information without the need for communication links between the different VSIs. This technique is often used when the distance between the parallel VSIs is long. It is usually based on the droop control technique. The basic idea is to regulate the voltage and frequency by regulating the reactive power and active power respectively, which can be measured locally.

However, droop control has inherent limitations. In islanded mode, it causes voltage and frequency deviations from their nominal values, which can degrade power quality. It also does not ensure a smooth transition to the grid-connected mode, creating potential

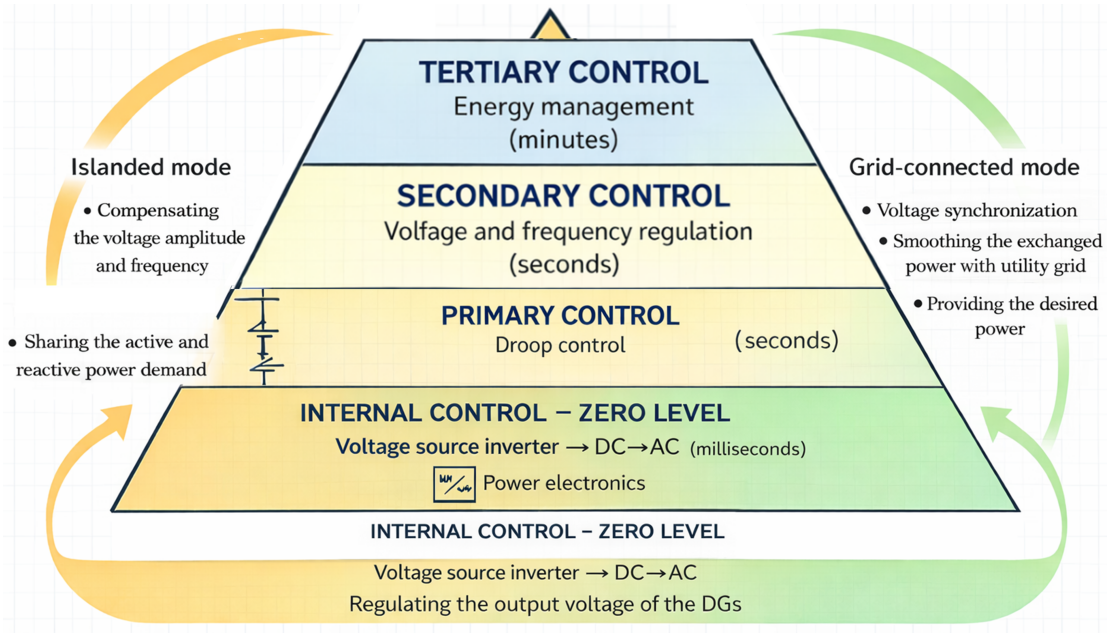

Figure 1.14 – Microgrid hierarchical control structure

stability risks. To address these challenges, the hierarchical control concept is introduced [45, 46, 107]. This multi-level framework consists of : a primary level, where droop control ensures immediate stability and proportional power sharing while generating references for the inner VSI voltage and current loops ; and a secondary level, which compensates for droop-induced deviations in islanded mode and synchronizes the microgrid with the main grid, enabling a smooth and stable transition to the connected mode. Higher levels can also be incorporated to enhance system flexibility, provide supervision, and perform energy management across the microgrid.

1.7 Conclusion

A microgrid is a system composed of several DG sources with various loads and storage systems, including with internal control mechanism to ensure stable and reliable operation, both in grid-connected and stand-alone modes. Microgrids offer power generation with a strong integration of intermittent renewable resources, thus ensuring a reliable and efficient power supply. However, it faces several challenges, including the stability of electrical quantities and power quality requirements. In the rest of this thesis, we provide solutions to problems that affect the optimal operation of microgrids.

Chapter 2

Metaheuristic optimization for control parameter tuning

2.1 Introduction

Solving optimization problems is currently a major research focus for several research teams, given its crucial importance in our daily lives. This field of research involves mathematical and computational methods [108, 109]. The solution of an optimization problem consists of searching for a solution of sufficient quality among a set of solutions with regard to a given criteria(s) and the objectives to be satisfied. It consists of maximizing or minimizing one or a set of objective functions while respecting the problem's constraints. In the literature, there are several optimization algorithms. This chapter describes the bio-inspired meta-heuristics : particle swarm optimization (PSO), self-learning PSO (SLPSO), grey wolf optimization (GWO), and chaotic yellow saddle goatfish algorithm (C-YSGA) to be used to solve the optimization problem of finding optimal parameters for advanced control laws designed for multi-source power conversion systems connected to microgrids, achieving optimal performance.

2.2 Overview of metaheuristic optimization

Metaheuristic algorithms represent a powerful class of optimization methods, often drawing inspiration from natural, biological, or physical phenomena to navigate complex search spaces effectively [110, 111]. Their application spans a wide array of classical optimization challenges, including logistical planning, the traveling salesman problem, task allocation, and machine learning tasks such as neural network training [112, 113]. Beyond these, they have found specialized utility in diverse fields like reactive power and voltage control in power systems, biomedical image registration, and even computational creativity in areas like musical composition [114–116]. In recent years, metaheuristics have become particularly favored for tackling multi-objective and dynamic optimization problems, offering robust and efficient solution pathways for intricate, interconnected systems where traditional methods may falter [117–119]. Early pioneering work demonstrated their potential ; for instance, Particle Swarm Optimization (PSO), inspired by social

flocking behavior, was employed by Eberhart and Kennedy not only for general optimization but also explored as an alternative to traditional backpropagation for training multilayer perceptrons, potentially offering faster convergence [120, 121]. PSO and its variants remain widely applied, including for Maximum Power Point Tracking (MPPT) in photovoltaic systems [122, 123]. Similarly, the Grey Wolf Optimizer (GWO), which mimics the leadership hierarchy and hunting mechanism of grey wolves, has shown significant promise in various engineering problems [124]. GWO is increasingly utilized for control system applications, particularly for the optimal tuning of controller parameters, such as those in PID or fuzzy PID controllers, to enhance system performance and robustness [125, 126]. Researchers continually propose and adapt novel metaheuristics ; for example, algorithms inspired by other animal behaviors, like the Yellow Saddle Goatfish Algorithm (YSGA), have also been investigated for MPPT [127] and adapted using techniques like chaotic mapping (C-YSGA) to enhance robustness when tuning controllers such as Fractional-Order PID (FOPID) [128, 129]. Furthermore, advanced PSO variants like self-learning PSO (SLPSO) have been applied to optimize parameters within hierarchical control structures for microgrids [45]. Crucially, the application of these diverse metaheuristic algorithms has proven particularly effective for robust control tuning optimization, enabling engineers to systematically find controller parameters (e.g., for PID, FOPID, H∞ controllers) that ensure stability and high performance despite system uncertainties and disturbances, a critical requirement in many complex engineering systems [130, 131].

In the context of dynamic system control, metaheuristic algorithms enable the parameters of control laws to be optimally determined by minimizing an optimization problem based on one or more criteria. The main challenge in designing control laws lies in the lack of systematic methods for accurate parameter selection, particularly in interconnected non-linear systems such as multi-source energy conversion systems connected to microgrids. The design and synthesis of control laws often relies on human expertise and empirical testing, making the process time-consuming and imprecise. To overcome this drawback, metaheuristic optimization techniques can be used to find optimal values for controller gains, taking into account the desired performance, guaranteeing robustness in the face of variations in operating conditions, and offering solutions adapted to non-linear and highly coupled systems. They also considerably reduce the need for trial and error by automating parameter optimization.

The optimization of control parameters plays a key role in microgrid management, where the integration of renewable energy sources and storage systems requires advanced control strategies. Metaheuristics have been widely used for optimizing energy management controllers, tuning MPPT controller parameters, managing energy storage, and dynamically distributing energy flows. For this reason, PSO, SLPSO, YSGA, and C-YSGA have been applied to ensure better dynamic system response, minimize energy losses, and improve overall network stability. By integrating these optimization algorithms, microgrid control becomes more efficient, guaranteeing greater stability, optimization of available energy resources, and improved system reliability.

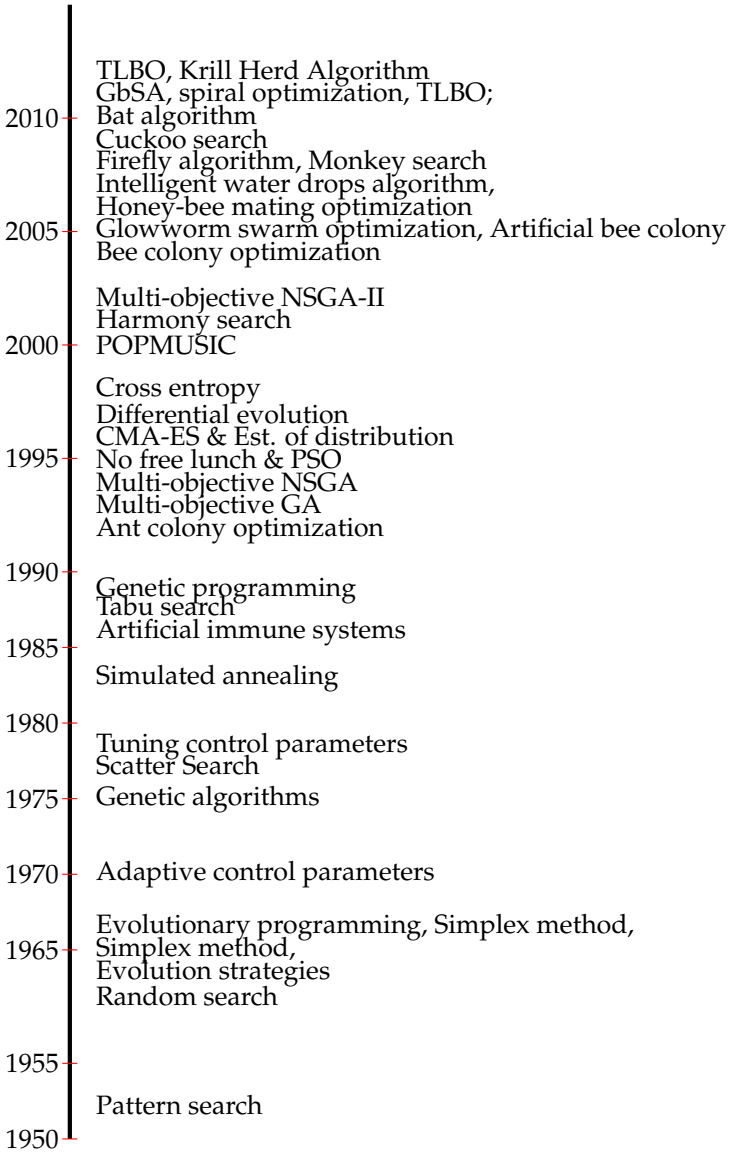

Figure 2.1 – A history of metaheuristics

2.3 Metaheuristic algorithms

2.3.1 Particle swarm optimization (PSO)

Particle Swarm Optimization (PSO) is an optimization technique developed by Russel Eberhart and James Kennedy in 1995 [120]. It is inspired by the collective behavior of bird swarms or schools of fish. Each particle represents a potential solution and moves through the search space, adjusting its position and speed according to its own experience (best position found) and that of its neighborhood (best position found collectively). Thanks to this cooperation, the algorithm efficiently explores the solution space and generally converges towards a global or local optimum. Simple to implement, PSO is widely used to solve optimization problems in a variety of fields.

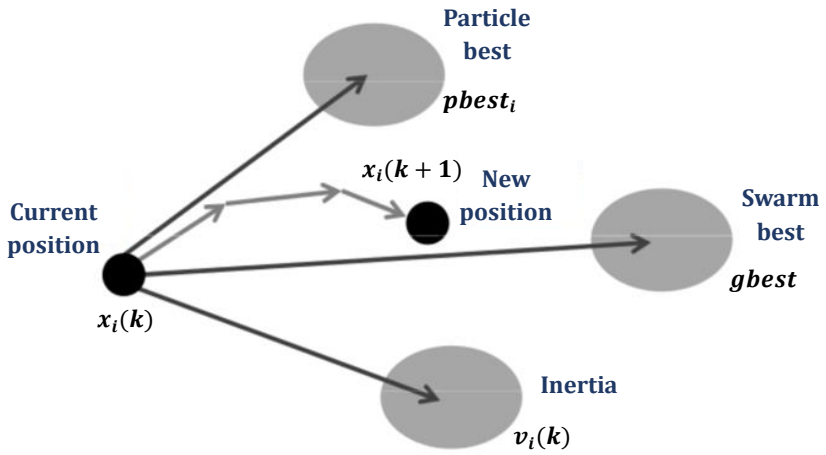

Figure 2.2 – Displacement of a particle

Each particle has a memory that stores two essential pieces of information : its best visited position (called best personal position, noted b_{best}) and the best position reached by its neighbors (called best global position, noted g_{best}). These references directly influence the evolution of the particle, which adjusts its movement according to its individual experience and that of the group.

Particle movement is defined by a velocity, which is updated at each iteration according to a formula that takes three components into account :

- **Inertia :** this retains part of the previous speed, to avoid abrupt changes
- **Attraction to the best personal position (b_{best}) :** this encourages the particle to return to the solutions that gave it the best results
- **Attraction towards the best global position (g_{best}) :** this guides the particle towards the best solution found by the group as a whole, thus promoting convergence

To move to the next step, each particle combines the following three tendencies : following its own velocity, returning to its best performance, and moving towards the best performance of its informants. Once the best informant has been detected, the change in velocity becomes a simple linear combination of these three tendencies. The strategy for moving a particle is illustrated in Figure. 2.2.

We consider a set of n particles (size of the population) and an objective function f that we wish to minimize in a search space D. The particle i is characterized by a position vector $x_i = [x_i^1, x_i^2, ..., x_i^D]$ and a velocity vector $v_i = [v_i^1, v_i^2, ..., v_i^D]$. The quality of its position is evaluated according to the value of the objective function f at each iteration. This particle memorizes the best position it has encountered, noted $pbest_i = (pbest_i^1, pbest_i^2, \ldots, pbest_i^D)$. Furthermore, $gbest = (gbest^1, gbest^2, \ldots, gbest^D)$ represents the best position found by all the particles in the swarm. In the global version of PSO, all particles are considered neighbors of each other, which justifies the notation $gbest$ (global best position).

The algorithm initializes by distributing particles randomly or regularly in the search space. Subsequently, at each iteration $(k+1)$, each particle updates its position and velocity based on its history and the information shared by the swarm. The equations

used for these updates are given by expressions 2.1 and 2.2, respectively :

$$v_i^d(k+1) = \omega v_i^d(k) + c_1 r_i^d \left(pbest_i^d - x_i^d(k) \right) + c_2 r_i^d \left(gbest^d - x_i^d(k) \right) \tag{2.1}$$

$$x_i^d(k+1) = x_i^d(k) + v_i^d(k+1) \tag{2.2}$$

where ω is the inertia factor, it is used to control the influence of the direction of movement on the future movement. c_1 and c_2 are positive constants, called respectively the cognitive factor and the social factor allowing the control of the individual and collective behavior of each particle. r_1 and r_2 are random numbers distributed uniformly in the interval $[0, 1]$ for each dimension d and each iteration k.

Algorithm 1 Particle Swarm Optimization

Random initialization of n particles : position x_i and velocity v_i
repeat
— Evaluation of the position of each particle i, according to the objective value
— Update of the local best position of each particle i
— Update of the global best position of the whole swarm
— Displacement of particles according to equations 2.1 and 2.2
— Evaluation of particle positions
until the stopping condition is met

2.3.2 Self-learning particle swarm optimization (SLPSO)

In most cases, PSO algorithms apply a single learning model to all particles [132]. This means that all particles in a swarm follow the same learning strategy, which limits their ability to handle complex and diverse environments. However, in the face of fitness landscape challenges, it is preferable to adopt an intelligent system with differentiated characteristics rather than a uniform training model.

This section introduces a PSO-inspired algorithm, called self-learning PSO (SLPSO), aimed at enriching the knowledge of individual particles. Its operation is based on several key aspects. First, four distinct learning strategies are implemented to help particles better adapt to the different characteristics of fitness landscapes. Then, an adaptive learning system is integrated to allow each particle to select the most appropriate strategy according to its local environment. In addition, an information update mechanism is defined to identify and extract useful knowledge from the improved particles. A monitoring system is also designed to accurately detect whether a particle has converged. Furthermore, a restart mechanism is implemented to generate new swarms by separating some particles from old groups, thus promoting diversity. Finally, a generalized parameter tuning approach is adopted to address various types of problems. In addition, different population management methods are used to encourage particles to explore unexplored areas of the fitness landscape. It is therefore a question of structuring these components coherently to ensure their optimal functioning.

The concept of division of labor is applied in SLPSO by assigning specific roles to particles based on the local fitness landscape. Each particle can either converge to the global best, exploit its own best position, explore new promising areas, or escape from local optima. The assignment of these roles is based on an intelligent assessment of the context in which each particle evolves.

The algorithm uses four learning techniques, based on different sources of information : the particle archive gbest (*abest*), the personal position *pbest*, the position pbest of a random particle ranked higher (*pbestrand*), and a random position prand nearby. Each of these strategies plays a specific role :

1. **Exploitation** (strategy a) : the particle adjusts its speed according to its personal best position (*pbest*), favoring stability and local improvement

$$v_k^d = \omega v_k^d + \eta r_k^d (pbest_k^d - x_k^d) \tag{2.3}$$

2. **Random jump** (strategy b) : A nearby random position is used to increase diversity and avoid premature trapping

$$x_i^d = x_i^d + v_{\text{avg}}^d \cdot \mathcal{N}(0,1) \tag{2.4}$$

3. **Exploration** (strategy c) : the particle learns from another random particle with a better position *pbest*, thus improving the exploration of the fitness landscape

$$v_i^d = \omega v_i^d + \eta r_i^d (pbest_{\text{nearest}}^d - x_i^d) \tag{2.5}$$

4. **Convergence** (strategy d) : learning is guided by the archive of the best global particles (*abest*), favoring convergence towards an optimal solution

$$v_i^d = \omega v_i^d + \eta r_i^d (abest^d - x_i^d) \tag{2.6}$$

Thanks to these strategies, each particle adapts its behavior according to its environment and the evolution of the search, ensuring an effective balance between local exploitation and global exploration to improve the performance of the algorithm.

2.3.3 Grey Wolf Optimization (GWO)

The Grey Wolf Optimizer (GWO) algorithm is a metaheuristic inspired by the social behavior and hunting techniques of gray wolves. Developed by Mirjalili in 2014, it mimics the social hierarchy and prey pursuit strategies observed in a wolf pack [124]. Its operation is based on a structured organization of wolves into four categories :

— Alpha (α) : the leader of the pack, representing the best solution found
— Beta (β) : the second-best wolf, helping the alpha guide the pack
— Delta (δ) : the third best wolf, obeying the leaders' instructions
— Omega (ω) : the other members of the pack who explore the search space and follow the instructions of the first three

The algorithm is based on three key behaviors of gray wolves :

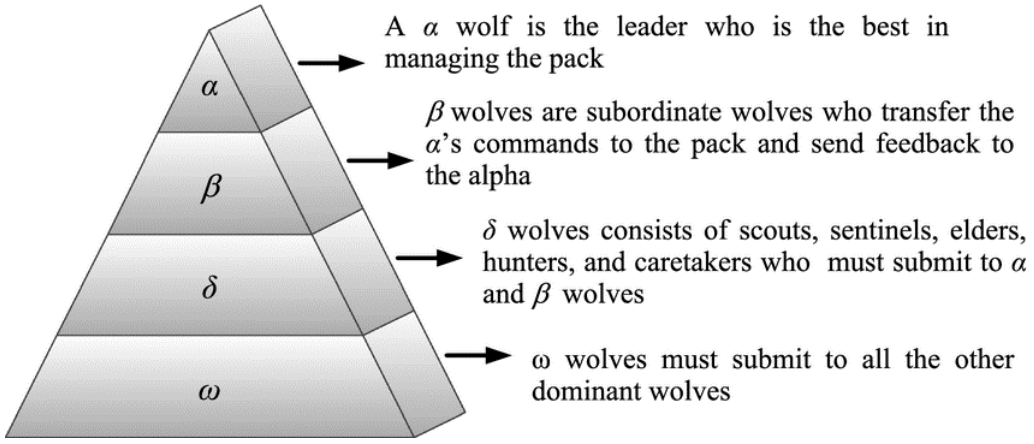

Figure 2.3 – The leadership hierarchy of wolves

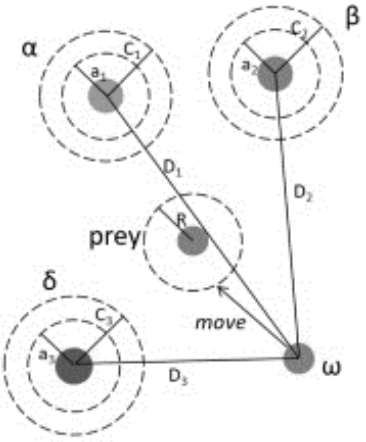

Figure 2.4 – The hunting behavior of wolves

1. **Prey Encirclement :** All wolves adapt their position according to the three best individuals (α, β, δ). This encirclement is modeled by the following equations :

$$\vec{D} = \left| \vec{C} \cdot \vec{X}_{leader} - \vec{X} \right| \tag{2.7}$$

$$\vec{X}_{new} = \vec{X}_{leader} - \vec{A} \cdot \vec{D} \tag{2.8}$$

where $\vec{X}_{leader}$ is the position of the leaders (α, β, δ), $\vec{X}$ the current position of a wolf, and $\vec{A}$ and $\vec{C}$ are dynamic coefficients influencing exploration and exploitation.

2. **Prey Tracking :** Wolves adjust their trajectories based on the position of the top three individuals. The update is done according to :

$$\vec{X}(t+1) = \frac{1}{3}\left(\vec{X}_{\alpha} + \vec{X}_{\beta} + \vec{X}_{\delta}\right) \tag{2.9}$$

This approach allows solutions to converge towards promising areas while maintaining diversity in the research space.

3. **Prey attack :** As the algorithm progresses, the parameter A decreases linearly, which reduces the amplitude of the movements and promotes finer exploitation around the best solution. The attack results in a progressive rapprochement of the

wolves around the best-identified position

4. **Territory exploration :** To avoid falling into local optima, the algorithm introduces perturbations via the parameter C, which influences the diversity of movements. When A is greater than 1 or less than -1, the wolves move away from the dominant solutions, thus improving their exploration capacity

The algorithm follows a simple but efficient process :

— Initialization of the positions of the wolves in the search space
— Evaluation of the objective function to identify the three best individuals (α, β, δ)
— Update of the positions of the other wolves according to the leaders
— Repetition of the process until a stopping criterion (number of iterations or convergence)

Algorithm 2 Grey Wolf Optimizer (GWO)

1: Initialize the grey wolf population (random positions)
2: Evaluate the objective function of each wolf
3: Identify the three best wolves : α (best), β (second), δ (third)
4: Repeat until reaching the stopping criterion :
   a. Update coefficients A and C
   b. Update the wolf positions based on α, β, and δ
   c. Evaluate the objective function of each wolf
   d. Update α, β, and δ if better solutions are found
5: Return the best solution (α)

2.3.4 Chaotic yellow saddle goatfish algorithm (C-YSGA)

The yellow saddle goatfish algorithm (YSGA) is inspired by the hunting behavior of these fish, as described in [133]. In this approach, the total population is subdivided into several subgroups. Each subpopulation has one fish designated as a chaser while the others act as blockers. The search space of the solutions to be optimized is assimilated to the hunting area of the goatfish. The first phase of the YSGA consists of initializing the population. Assuming a population P of m goatfish ($P = \{p_1,\ p_2,\ \ldots,\ p_m\}$), each individual is randomly generated between the lower bound (b_l) and the upper bound (b_u) of $D-$dimensional search space :

$$p_i^d = r \cdot (b_u^d - b_l^d) + b_l^d\ , \quad i = 1, 2, \ldots, m\ ; \quad d = 1, 2, \ldots, D \tag{2.10}$$

where r is random numbers distributed uniformly in the interval $[0, 1]$.

The random initialization of the YSGA algorithm does not always guarantee a good starting point, which affects the optimization performance. To address this problem, several studies have explored the incorporation of chaotic maps to replace the random parameters. Among the most promising approaches, the use of populations generated by chaotic maps, such as logistic, cubic, or sinusoidal maps, has been studied. Comparisons

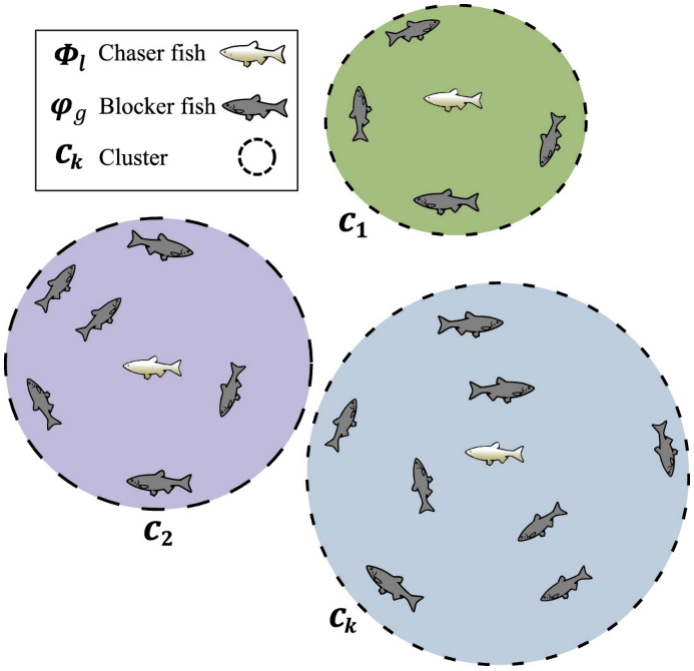

Figure 2.5 – The partitions of a goatfish population

[134–136] show that the logistic map stands out for its efficiency and computational simplicity.

Based on the previous analysis, [128] proposed an improvement of the population initialization in the YSGA algorithm by replacing the random approach with a chaotic logistic mapping. This method generates vectors Y according to :

$$Y_1^d = r, \quad Y_{i+1}^d = \mu \cdot Y_i^d \cdot (1 - Y_i^d) \tag{2.11}$$

where r rand is a random number in $[0,1]$ and $\mu = 4$ to guarantee chaotic behavior. The initialization of positions in C-YSGA is then defined by :

$$p_i^d = Y_i^d \cdot (b_u^d - b_l^d) + b_l^d \,, \quad i = 1,2,\ldots,m \,; \quad d = 1,2,\ldots,D \tag{2.12}$$

Before the hunting process begins, the population is segmented into subgroups via the K-means clustering algorithm, where each cluster contains one chaser fish Φ_l responsible for the hunt and a number of blocker fish φ_g responsible for encircling the prey, as shown in Figure. 2.5.

In each cluster, the chaser fish is identified as the one with the best fitness value. The hunting process begins by updating its position. Denoting the current position $\Phi_l(k)$, the new position $\Phi_l(k+1)$, and the best chaser fish among all clusters $\Phi_{best}(k)$, the update rule is defined as :

$$\Phi_l(k+1) = \Phi_l(k) + \alpha \cdot \left(\frac{u}{|v|^{1/\beta}} \right) (\Phi_l(k) - \Phi_{\text{best}}(k)) \tag{2.13}$$

where α represents the update step (set to 1 in this study).

However, to update the position of the best chaser fish, the following equation is used

instead of 2.13.

$$\Phi_{\text{best}}(k+1) = \Phi_{\text{best}}(k) + \alpha \cdot \left(\frac{u}{|v|^{1/\beta}} \right) \tag{2.14}$$

The parameters u and v used in the position update are defined by :

$$u \sim \mathcal{N}(0, \sigma_u^2), \quad \text{where} \quad \sigma_u = \left(\frac{\Gamma(1+\beta) \cdot \sin\left(\frac{\pi\beta}{2}\right)}{\Gamma\left(\frac{1+\beta}{2}\right) \cdot \beta \cdot 2^{\frac{\beta-1}{2}}} \right)^{1/\beta} \tag{2.15}$$

$$v \sim \mathcal{N}(0, \sigma_v^2), \quad \text{where} \quad \sigma_v = 1 \tag{2.16}$$

Being k_{max} the maximum number of iterations k, the Lévy flight index β, which influences the displacement, is calculated as follows :

$$\beta = 1.99 + 0.01 \cdot \frac{k}{k_{\max}} \tag{2.17}$$

Then, updating the positions of the blocker fish is the next step in the optimization process. The new position of a blocker fish is determined by :

$$\varphi_g\,(k+1) = \left| r.\Phi_l\,(k) - \varphi_g\,(k) \right| .\exp\,(b.\rho).\cos\,(2\pi\rho) + \Phi_l\,(k) \tag{2.18}$$

where ρ is a random number in the interval $[a, 1]$, and b is a constant set to 1. The exploitation factor a decreases linearly from -1 to -2 over the iterations.

During optimization, a role swap may occur : if the blocker fish obtains a better fitness value than the chaser, they will swap roles in the next iteration.

Each group of fish performs its prey search autonomously, allowing parallel local exploration by all clusters. When a cluster has explored its entire search area without improvement, it moves to the area of the best group. This behavior is modeled by the following equation :

$$p_g(k+1) = \frac{\Phi_{\text{best}} + p_g(k)}{2} \tag{2.19}$$

where $p_g(k+1)$ is the new position of the goatfish, whether it is a hunter or a blocker. This process is repeated until the maximum number of iterations is reached.

2.4 Motivation for metaheuristic selection in control design

In the development of advanced control strategies for multi-source energy conversion systems, tuning controller parameters plays a critical role in ensuring dynamic system performance, robustness, and adaptability. For this reason, a set of metaheuristic optimization algorithms has been progressively employed, each selected according to the increasing complexity of the control tasks, limitations, and constraints in prior stages based on the literature review.

In the first part of the implementation, the PSO algorithm has been used to calculate the initial controllers. Inspired by the social behavior of bird flocks, the PSO algorithm

boasts a simple structure and rapid convergence in the early search stages. It was suitable for initial controller designs for the following reasons :

— Good initial performance in smooth and low-dimensional search spaces
— Easy implementation and low computational complexity
— Rapid convergence in early iterations

However, as the controller designs became more complex and nonlinear, the PSO algorithm began to exhibit weaknesses, particularly concerning local optima entrapment and reduced exploration capability. To address this end, the second part introduced the self-learning PSO algorithm (SLPSO), which extends the capabilities of PSO by incorporating a learning mechanism that allows particles to explore beyond their local and global best positions, improving their overall diversity and swarm adaptability. SLPSO was recommended in the second phase due to :

— Enabling improved exploration/exploitation balance of the search space
— Reducing the risk of premature convergence through self-learning components
— Improving robustness in more complex, time-varying environments

However, despite its performance advantages, SLPSO also showed a higher level of algorithmic complexity, which led to greater computational demands. This is why, the GWO algorithm has been introduced in the third phase to address more complex control problems involving nonlinear dynamics and interacting subsystems. GWO simulates the cooperative hunting behavior and social hierarchy of grey wolves, providing a well-structured yet adaptive search mechanism. It was particularly suitable for optimizing systems with strong nonlinear coupling and interdependent variables. The decision to employ GWO was based on :

— Its ability to maintain a good balance between global search and local refinement
— Natural convergence mechanism in complex objective landscapes
— Minimal sensitivity to parameter tuning

Compared to SLPSO, GWO offered a simpler structure with reduced computational cost while still providing competitive or superior optimization performance in many practical cases.

For the final and most complex fitness landscapes, the chaotic-YSGA was employed in the last stage to address the limitations of previous methods and handle the most demanding control scenarios. By integrating chaotic dynamics into the YSGA structure, C-YSGA enhances global search behavior and avoids stagnation more effectively than traditional metaheuristics. It was particularly effective for fine-tuning control systems requiring high precision and adaptability. The choice of C-YSGA was justified by :

— Strong global search capability through chaotic sequences
— Fast and reliable convergence even in complex, multi-modal spaces
— Improved final solution quality and response smoothness

In summary, the progressive application of PSO, SLPSO, GWO, and C-YSGA was not arbitrary but rather the result of a careful evaluation of algorithmic capabilities regarding system complexity (see Figure. 2.6). Each algorithm was introduced to address specific

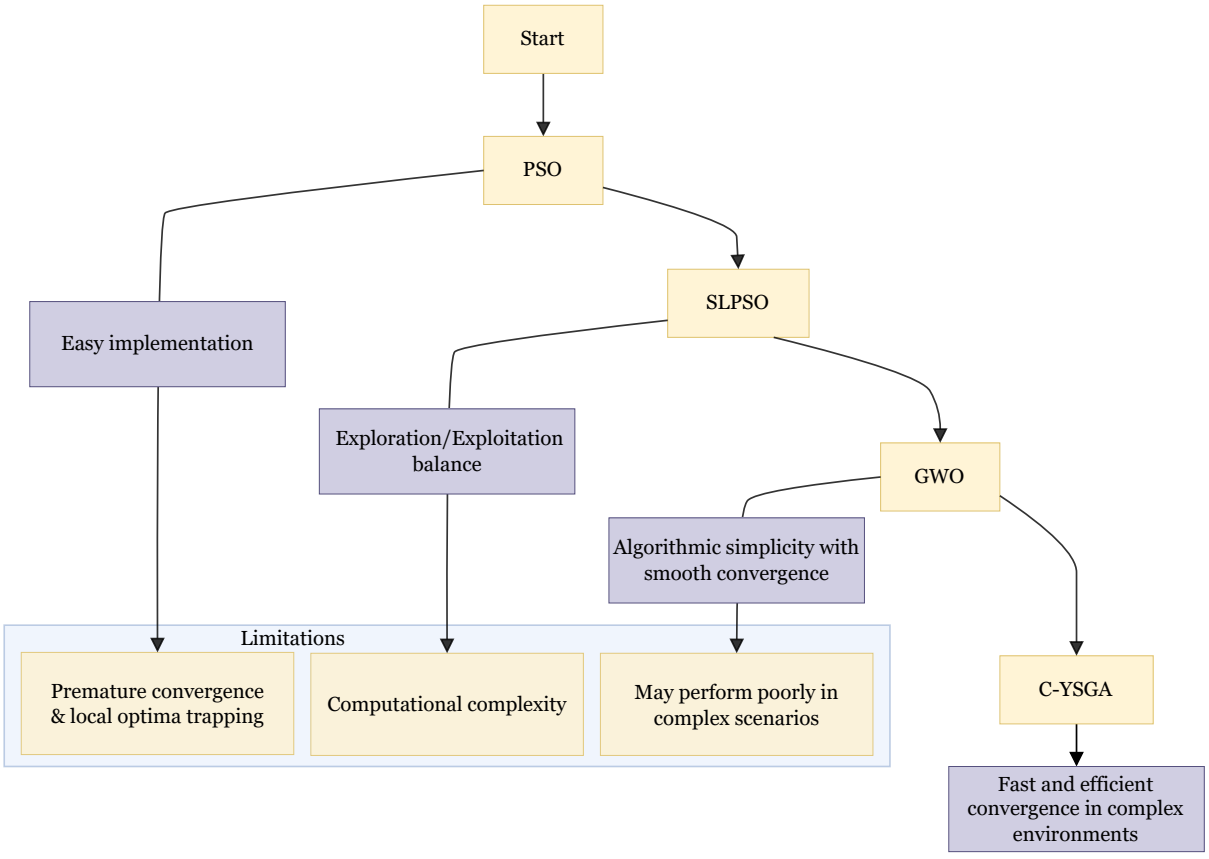

Figure 2.6 – Metaheuristic Progression for Tuning

optimization challenges encountered with its predecessor, ensuring that the control design process remained both efficient and adaptive. This strategic sequence contributed significantly to the overall effectiveness of the control techniques developed in this work.

2.5 Conclusion

This chapter has introduced the fundamentals of the metaheuristic optimization algorithms PSO, SLPSO, GWO, and C-YSGA, highlighting their exploration and exploitation strategies for finding optimal solutions. Each of these algorithms, inspired by natural phenomena, offers various approaches to improve the efficiency and speed of convergence in complex optimization problems.

In the context of energy conversion system control studied in the present work, these methods allow to efficiently adjust the control parameters taking into account different operating conditions. Their application guarantees an optimization adapted to the system requirements, thus contributing to improve its performance and stability. This theoretical framework will serve as a basis for the implementation and analysis of these algorithms in the following chapters.

Chapter 3

Distributed renewable energy generation control

3.1 Introduction

The increasing penetration of distributed renewable energy sources, particularly photovoltaic (PV) systems, requires advanced control strategies to ensure efficient, stable, and reliable operation. Effective control must address challenges such as variable solar irradiance, power flow management, and coordination with energy storage systems and loads. This chapter presents a comprehensive study of control techniques for both grid-connected and stand-alone PV systems, including maximum power point tracking (MPPT), voltage-source inverter regulation, and energy management strategies. Special attention is given to modern approaches, such as fractional-order, supertwisting, and Z-source inverter-based controls, which enhance system flexibility, robustness, and performance. The following sections detail the modeling, controller design, and implementation of these techniques, providing a structured framework for distributed PV generation control.

3.2 Control of grid-connected PV system

3.2.1 Fractional-order terminal super twisting algorithm (FOTSTA)-based MPPT

Efficiently managing boost converters holds significant importance, given their frequent use in power supply applications where energy efficiency is of paramount importance. The command system's role is to minimize power losses and ensure that the grid receives the precise power it requires through the adjustment of the converter's output voltage and current, as shown in Figure. 3.1. In this study, the proposed FOTSTA approach is used for the MPPT process regulating the boost converter.

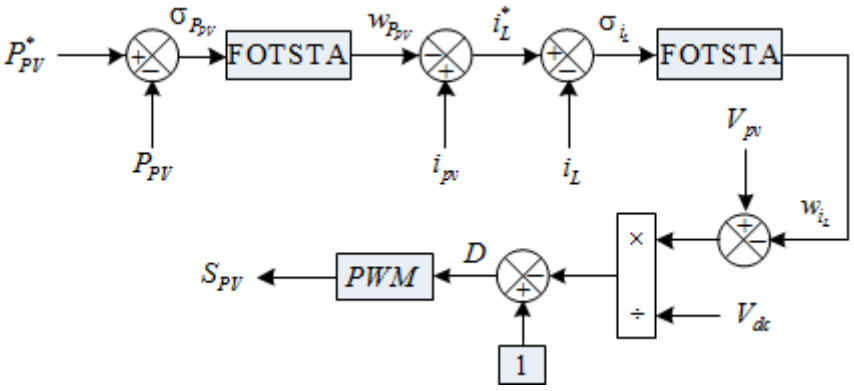

Figure 3.1 – Control scheme of boost converter

Proposed FOTSTA controller

The SMC approach is renowned for its popularity, wide applicability, and robustness as a prominent nonlinear approach rooted in variable structure systems. Nevertheless, it faces a significant challenge in the form of oscillations, commonly referred to as chattering [137]. This issue stands out as a major drawback of the usual SMC approach. In the literature, numerous approaches have been proposed to mitigate chattering phenomena. Among these, the high-order SMC approach stands out as a particularly effective option for reducing chattering. Specifically, the second-order variants of high-order SMC approaches, such as the twisting approach, suboptimal approach, and super twisting algorithm (STA), aim to establish a SMC involving both the sliding surface and its time derivative within a finite period [70, 138]. In our study, we have opted for the STA due to its distinct advantages. Unlike the first two methods (twisting and suboptimal), the STA exclusively relies on the sliding surface without necessitating its derivative. However, it's worth noting that STA is solely applicable to systems with a relative level of one, where command action affects the first derivative of the sliding surface.

The law governing the STA approach is articulated as follows :

$$\begin{cases} u_n = -k\sqrt{|S|}\,\mathrm{sign}(S) + u_1 \\ \dot{u}_1 = -\beta\,\mathrm{sign}(S) \end{cases} \tag{3.1}$$

where $S = x^* - x$, the linear sliding surface and β, k positive coefficients. x and x^* are the signal to be controlled and its reference, respectively.

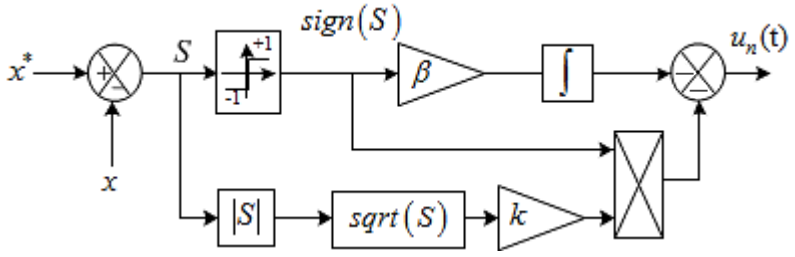

Figure 3.2 – Traditional STA controller

In the classical STA control approach, a linear sliding surface is traditionally employed, which results in the system state not converging to zero within the specified time frame. To address this challenge, we have introduced the utilization of a nonlinear sliding surface or a terminal sliding surface. This innovation has led to the development of a novel command approach named the terminal STA (TSTA). This strategy boasts a straightforward structure and bears a resemblance to the usual STA method. However, the key distinction between TSTA and the usual STA method lies in the type of sliding surface employed. TSTA introduces nonlinear functions into the design of the manifold, creating a TSTA hyperplane. Tracking errors on this hyperplane will effectively converge to zero within a finite time.

The fundamental concept behind the TSTA approach can be expressed as follows :

$$w = -k\sqrt{|\sigma|}\,\mathrm{sign}(\sigma) - \beta \int \mathrm{sign}(\sigma)\, d\tau \tag{3.2}$$

σ is the terminal sliding function.

The terminal sliding surface can be represented using the following equation :

$$\sigma = \dot{S} + \alpha S^{\mu} \tag{3.3}$$

Where, α represents a positive constant and μ is a positive value.

The TSTA approach is capable of compelling the system states to reach zero within a finite duration. The TSTA principle can be illustrated by the following equation :

$$w(t) = -k\sqrt{|\dot{S} + \alpha S^{\mu}|}\,\mathrm{sign}(\dot{S} + \alpha S^{\mu}) - \beta \int \mathrm{sign}(\dot{S} + \alpha S^{\mu})\, d\tau \tag{3.4}$$

Figure. 3.3 shows the proposed TSTA controller structure.

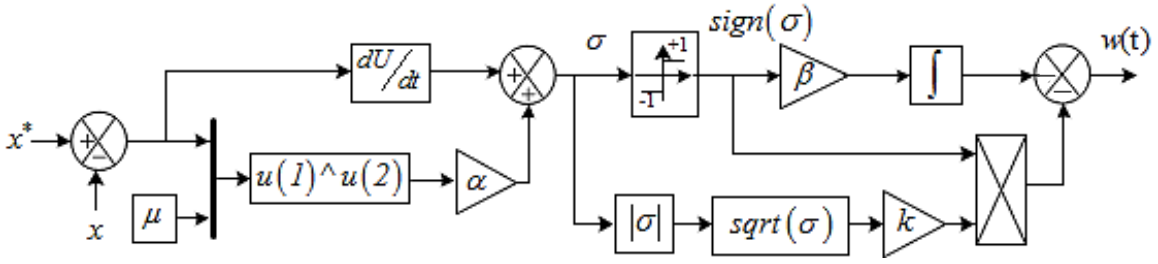

Figure 3.3 – TSTA controller structure

Considering the robust performance of fractional-order control, in [139], we have introduced a novel command approach called fractional-order TSTA (FOTSTA), which generalizes the TSTA method using an extra fractional term and outperforms conventional STA controllers, especially in systems exhibiting non-linear dynamics. In summary, the FOTSTA method provides a more adaptable and robust command system capable of enhancing performance and stability across a broad spectrum of applications, particularly in systems characterized by non-linear dynamics and model uncertainties. Figure. 3.4 illustrates that the FOTSTA approach developed is user-friendly, versatile, and straightforward. Furthermore, the designed method facilitates the straightforward implementation

of complex systems, as expressed in the following equation :

$$w(t) = \left[-k\sqrt{|\dot{S} + \alpha S^{\mu}|}\,\mathrm{sign}(\dot{S} + \alpha S^{\mu}) - \beta \int \mathrm{sign}(\dot{S} + \alpha S^{\mu})\, d\tau \right]^{\lambda} \tag{3.5}$$

Where λ is the extra non-integer parameter of the proposed fractional order control ($\lambda \in \mathbb{R}^{+}$, with $0 < \lambda < 2$).

The FOTSTA approach presented in Figure. 3.4 exhibits simplicity, straightforwardness, ease of adjustment, and straightforward implementation. Furthermore, this method is readily applicable to intricate systems.

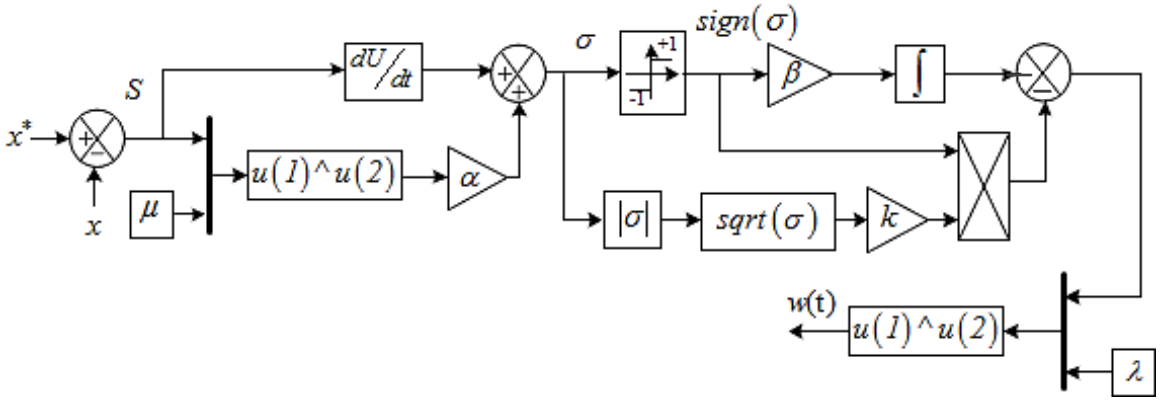

Figure 3.4 – Proposed FOTSTA controller

PV power control

Defining the sliding surface constitutes a crucial initial phase in governing the SMC. Furthermore, in the context of PV power control, the terminal sliding surface is specified as follows :

$$\sigma_{P_{\mathrm{pv}}} = \dot{S}_{P_{\mathrm{pv}}} + \alpha_{P_{\mathrm{pv}}} S^{\mu_{P_{\mathrm{pv}}}} \tag{3.6}$$

Being $\tilde{P}_{\mathrm{pv}}$ the PV power derivative $\left(\partial P_{\mathrm{pv}}/\partial V_{\mathrm{pv}}\right)$ and $\tilde{P}^{*}_{\mathrm{PV}}$ its reference, the linear sliding surface for PV power can be expressed as $S_{P_{\mathrm{pv}}} = \tilde{P}_{\mathrm{pv}} - \tilde{P}^{*}_{\mathrm{pv}}$.

$$S_{P_{pv}} = \tilde{P}^{*}_{pv} - \tilde{P}_{pv} \tag{3.7}$$

where

$$\tilde{P}_{pv} = \frac{\partial P_{pv}}{\partial V_{pv}} = \frac{\partial (V_{pv} \times i_{pv})}{\partial V_{pv}} = V_{pv} \times \frac{\partial i_{pv}}{\partial V_{pv}} + i_{pv} \tag{3.8}$$

According to the (P-V) characteristics, $\tilde{P}^{*}_{pv}$ is set to zero to keep the PV system operating point at the MPP position, i.e., $\tilde{P}^{*}_{pv} = 0$.

The FOTSTA approach law for PV power regulator can be given as follows :

$$w_{P_{pv}}(t) = \left[-k_{P_{pv}}\sqrt{|\sigma_{P_{pv}}|}\,\mathrm{sign}(\sigma_{P_{pv}}) - \beta_{P_{pv}}\int \mathrm{sign}(\sigma_{P_{pv}})\,d\tau\right]^{\lambda_{P_{pv}}} \tag{3.9}$$

The compensation-enhanced PV power command loop provides the reference current.

$$i_L = i_{pv} - \left[-k_{P_{pv}}\sqrt{|\sigma_{P_{pv}}|}\,\mathrm{sign}(\sigma_{P_{pv}}) - \beta_{P_{pv}}\int \mathrm{sign}(\sigma_{P_{pv}})\,d\tau\right]^{\lambda_{P_{pv}}} \tag{3.10}$$

Inductor stream control design

The terminal sliding surface for the inductor stream can be written as :

$$\sigma_{i_L} = \dot{S}_{i_L} + \alpha_{i_L} S^{\mu_{i_L}} \tag{3.11}$$

where

$$S_{i_L} = i_L^* - i_L \tag{3.12}$$

S_{i_L} is the linear sliding surface for the inductor current

The FOTSTA approach law for the inductor stream regulator can be given as

$$w_{i_L}(t) = \left[-k_{i_L}\sqrt{|\sigma_{i_L}|}\,\mathrm{sign}(\sigma_{i_L}) - \beta_{i_L}\int \mathrm{sign}(\sigma_{i_L})\,d\tau\right]^{\lambda_{i_L}} \tag{3.13}$$

The control loop for inductor current (i_L) determines the duty cycle of the DC-DC boost converter through :

$$D = 1 - \frac{V_{pv} - \left[-k_{i_L}\sqrt{|\sigma_{i_L}|}\,\mathrm{sign}(\sigma_{i_L}) - \beta_{i_L}\int \mathrm{sign}(\sigma_{i_L})\,d\tau\right]^{\lambda_{i_L}}}{V_{dc}} \tag{3.14}$$

Stability Analysis

In order to ensure that the quantities to be controlled are attracted towards their reference values, the stability of the control law must be evaluated [139]. For this reason, the following Lyapunov function are defined :

$$V_x = \frac{1}{2}\sigma_x^2 \quad \text{where} \quad x = [P_{pv}, i_L] \quad \text{and} \quad \sigma_x = \dot{S}_x + \alpha_x S_x^{\mu_x} \tag{3.15}$$

Stability is guaranteed only when its derivative is negative, i.e.,

$$\dot{V}_x = \sigma_x \dot{\sigma}_x < 0 \tag{3.16}$$

Substituting the value of $\dot{\sigma}_{P_{pv}}$ and $\dot{\sigma}_{i_L}$ from Eqs 3.6 and 3.11, respectively, gives

$$\dot{V}_x = \begin{cases} \dot{V}_{P_{pv}} = \sigma_{P_{pv}}\left(\ddot{S}_{P_{pv}} + \alpha_{P_{pv}}\dot{S}^{\mu_{P_{pv}}}\right) \\ \dot{V}_{i_L} = \sigma_{i_L}\left(\ddot{S}_{i_L} + \alpha_{i_L}\dot{S}^{\mu_{i_L}}\right) \end{cases} \tag{3.17}$$

where

$$S_{P_{pv}} = \tilde{P}^*_{pv} - \tilde{P}_{pv} \quad \text{and} \quad S_{i_L} = i^*_L - i_L \tag{3.18}$$

Considering $\tilde{P}^*_{pv} = 0$ and substituting both equations from the system 1.4 in the derivative of 3.18 yields :

$$\dot{S}_x = \begin{cases} \dot{S}_{P_{pv}} = \dot{\tilde{P}}_{PV} = \dfrac{1}{C_{pv}} \left(2\dfrac{\partial I_{pv}}{\partial V_{pv}} + V_{pv} \dfrac{\partial^2 I_{pv}}{\partial V^2_{pv}} \right) (i_{PV} - i_L) \\ \dot{S}_{i_L} = \dot{i}^*_L - \dot{i}_L = \dot{i}^*_L - \dfrac{1}{L} \left(V_{pv} - (1-D)V_{dc} \right) \end{cases} \tag{3.19}$$

Now by putting the value of the TSTA control law, we can get the following :

$$\dot{V}_x = \begin{cases} \dot{V}_{P_{pv}} = \sigma_{P_{pv}} \left(-k_{P_{pv}} \sqrt{|\sigma_{P_{pv}}|}\, \text{sign}(\sigma_{P_{pv}}) - \beta_{P_{pv}} \int \text{sign}(\sigma_{P_{pv}})\, d\tau \right) \\ \dot{V}_{i_L} = \sigma_{i_L} \left(-k_{i_L} \sqrt{|\sigma_{i_L}|}\, \text{sign}(\sigma_{i_L}) - \beta_{i_L} \int \text{sign}(\sigma_{i_L})\, d\tau \right) \end{cases} \tag{3.20}$$

Simplification of Eqs 3.20 gives the following expressions :

$$\dot{V}_x = \begin{cases} \dot{V}_{P_{pv}} = -k_{P_{pv}} |\sigma_{P_{pv}}|^{1.5} - \beta_{P_{pv}} \sigma_{P_{pv}} \int \text{sign}(\sigma_{P_{pv}})\, d\tau \\ \dot{V}_{i_L} = -k_{i_L} |\sigma_{i_L}|^{1.5} - \beta_{i_L} \sigma_{i_L} \int \text{sign}(\sigma_{i_L})\, d\tau \end{cases} \tag{3.21}$$

Therefore, due to the definite negativity of the derivative of the Lyapunov function, the global asymptotic stability of the proposed controller can be guaranteed.

3.2.2 P-DPC-SVM-based grid-connected VSI control

Recently, a robust control method has caught the attention of researchers which is called the model predictive command (MPC)[140–142]. The MPC approach is an advanced nonlinear controller that is characterized by its ability to handle different command objectives in one command law named the cost function. Thanks to its simple and intuitive implementation and fast dynamic, the MPC has been widely used to command power converters [143, 144]. Within the MPC classes, finite command set-MPC (FCS-MPC) is developed to produce the command decision directly for converter switches without using any modulation devices. Despite its features, the latter technique suffers from the disability of variable and high switching frequency [145, 146]. Because of that, a predictive direct power control (P–DPC) associated with the space vector modulation technique (SVM) is proposed for the grid-connected inverter control stage, ensuring a constant switching frequency through the SVM method as illustrated in Figure. 3.5. In the P–DPC–SVM approach, the control decision is determined by minimizing the cost function to provide the optimal command vector to the SVM modulation stage for the next sampling time. Using the switching states (Sa, Sb, Sc) given by the SVM block, a minimum error is guaranteed between the controller active and reactive powers P_s and

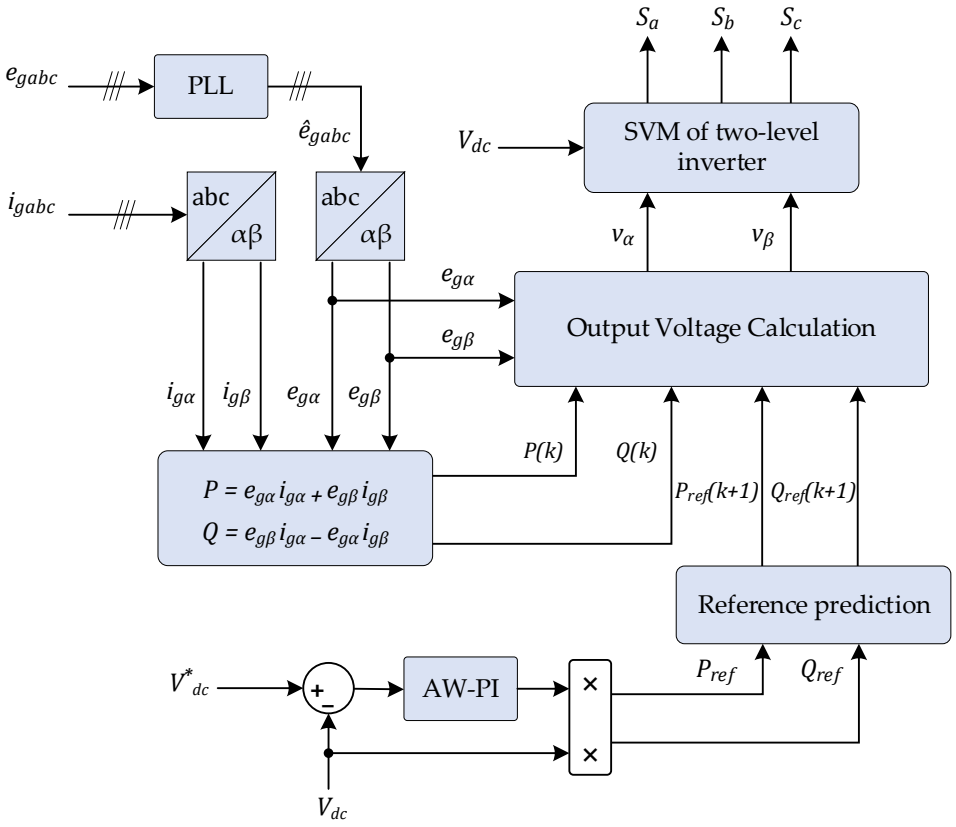

Figure 3.5 – The P–DPC–SVM approach

Q_s, and their references which are generated by the outer loop of the DC link voltage via an anti-windup PI controller, mitigating unwanted harmonic components within the grid current [139]. This minimization is accomplished using a robust phase-locked loop (PLL) shown in Figure. 3.6.

The variation of the P_s and Q_s between two successive sampling instants can be expressed as follows :

$$\begin{bmatrix} P(k+1) - P(k) \\ Q(k+1) - Q(k) \end{bmatrix} = \begin{bmatrix} e_{g\alpha}(k) & e_{g\beta}(k) \\ e_{g\beta}(k) & -e_{g\alpha}(k) \end{bmatrix} \begin{bmatrix} i_{g\alpha}(k+1) - i_{g\alpha}(k) \\ i_{g\beta}(k+1) - i_{g\beta}(k) \end{bmatrix} \tag{3.22}$$

Furthermore, by neglecting the effect of the resistance of the network, the evolution of the stream vector is governed by a first-order differential equation :

$$\begin{bmatrix} i_{g\alpha}(k+1) - i_{g\alpha}(k) \\ i_{g\beta}(k+1) - i_{g\beta}(k) \end{bmatrix} = \frac{T_s}{L_g} \left(\begin{bmatrix} e_{g\alpha}(k) \\ e_{g\beta}(k) \end{bmatrix} - \begin{bmatrix} v_\alpha(k) \\ v_\beta(k) \end{bmatrix} \right) \tag{3.23}$$

By using the Forward Euler approach, it is possible to discretization the grid stream in the $(\alpha\beta)$ reference frame which is given by the following expression :

$$\frac{d}{dt} \begin{bmatrix} i_{g\alpha} \\ i_{g\beta} \end{bmatrix} = \frac{1}{L_g} \left(\begin{bmatrix} e_{g\alpha} \\ e_{g\beta} \end{bmatrix} - \begin{bmatrix} v_\alpha \\ v_\beta \end{bmatrix} \right) \tag{3.24}$$

Substituting Equation 3.23 into Equation 3.22, variation of P_s and Q_s during one

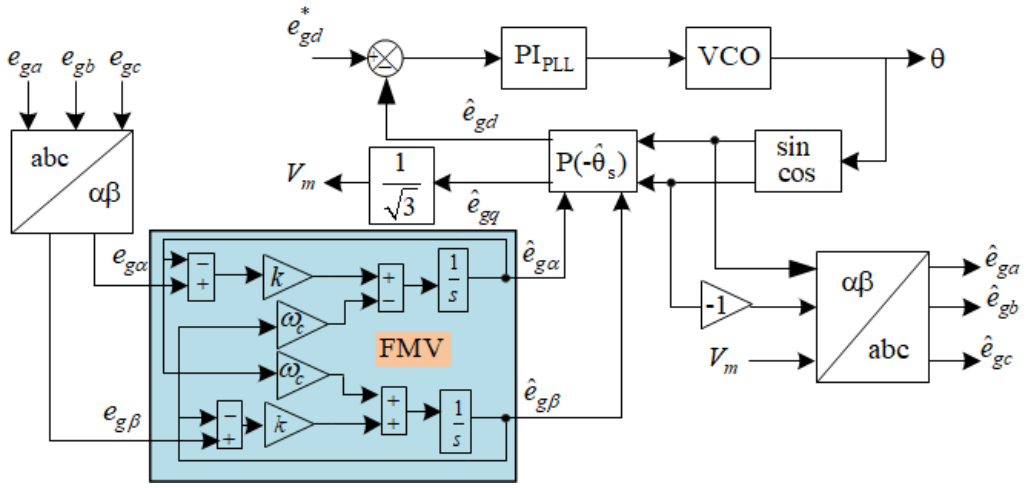

Figure 3.6 – PLL technique with MVF

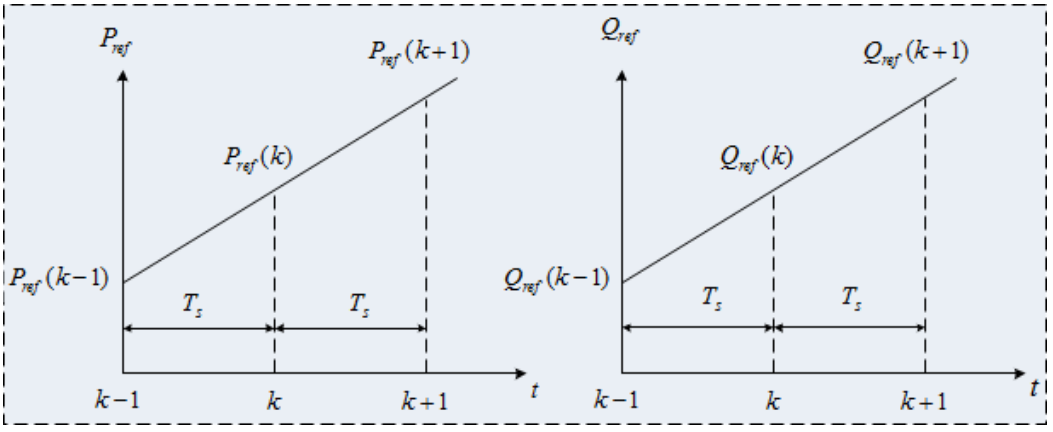

Figure 3.7 – Predictive value estimation of reference power

switching period T_s is given as follows

$$\begin{bmatrix} P(k+1)-P(k) \\ Q(k+1)-Q(k) \end{bmatrix} = \frac{T_s}{L_g} \begin{bmatrix} e_{g\alpha}(k) & e_{g\beta}(k) \\ e_{g\beta}(k) & -e_{g\alpha}(k) \end{bmatrix} \left(\begin{bmatrix} e_{g\alpha}(k) \\ e_{g\beta}(k) \end{bmatrix} - \begin{bmatrix} v_\alpha(k) \\ v_\beta(k) \end{bmatrix} \right) \tag{3.25}$$

Taking this account, the objective of the predictive command is to make the output P_s and Q_s track the relevant reference energies :

$$\begin{cases} \varepsilon_P = P_{\text{ref}}(k+1) - P(k+1) \\ \varepsilon_Q = Q_{\text{ref}}(k+1) - Q(k+1) \end{cases} \tag{3.26}$$

For an optimal convergence toward the desired energy values, the following equation must be verified.

$$\begin{cases} P_{\text{ref}}(k+1) = P(k+1) \\ Q_{\text{ref}}(k+1) = Q(k+1) \end{cases} \tag{3.27}$$

A graphical illustration of these predictions is represented in Figure. 3.7.

The predicted reference values $P_{ref}(k+1)$ and $Q_{ref}(k+1)$ are computed as follows :

$$\begin{cases} P_{\text{ref}}(k+1) = 2P_{\text{ref}}(k) - P_{\text{ref}}(k-1) \\ Q_{\text{ref}}(k+1) = Q_{\text{ref}}(k) \end{cases} \tag{3.28}$$

Putting Equation 3.28 into Equation 3.25, and solving the equation, the output voltage components of the control can be listed as :

$$\begin{bmatrix} v_\alpha(k) \\ v_\beta(k) \end{bmatrix} = \begin{bmatrix} e_{g\alpha}(k) \\ e_{g\beta}(k) \end{bmatrix} - \frac{L_g}{T_s\left(e_{g\alpha}^2 + e_{g\beta}^2\right)} \begin{bmatrix} e_{g\alpha}(k) & e_{g\beta}(k) \\ e_{g\beta}(k) & -e_{g\alpha}(k) \end{bmatrix} \begin{bmatrix} 2P_{\text{ref}}(k) - P_{\text{ref}}(k-1) - P(k) \\ Q_{\text{ref}}(k) - Q(k) \end{bmatrix} \tag{3.29}$$

3.2.3 Anti-windup PI controller

In order to mitigate fluctuations and instability in the DC link voltage, a PI controller with anti-windup compensation is suggested for DC link voltage regulation, as depicted in Figure. 3.8, this regulator operates by utilizing a proportional gain (k_p) to enhance system dynamics and an integral component with a gain (k_i) for accurate steady-state tracking. To prevent the regulator output from saturating due to noise amplification, an anti-windup loop is introduced, incorporating a second integral term with a high loop gain ($1/Tu$), which has no adverse impact on the desired system performance [139]. To determine the appropriate values for the regulator gains, the transfer function of the system is initially defined first [146].

The equation describing the dynamic behavior of the DC link voltage is as follows :

$$C_{dc}\frac{dV_{dc}}{dt} = i_{PVS} - i_{dc} \tag{3.30}$$

The DC link voltage is regulated through adjustment of the inverter stream on the DC side, which is regarded as an external disturbance.

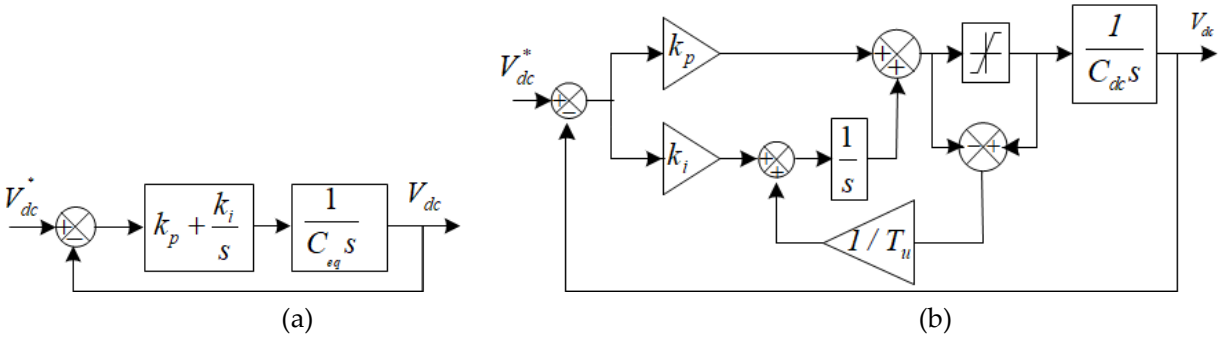

Figure 3.8 – Link voltage command ; (a) : PI control, (b) : anti-windup PI regulator

The determination of the controller gains k_p and k_i involves placing the poles of the closed-loop system directly, and it can be expressed as follows :

$$\frac{V_{dc}}{V_{dc}^*} = \frac{k_p s + k_i}{C_{dc}s^2 + k_p s + k_i} \tag{3.31}$$

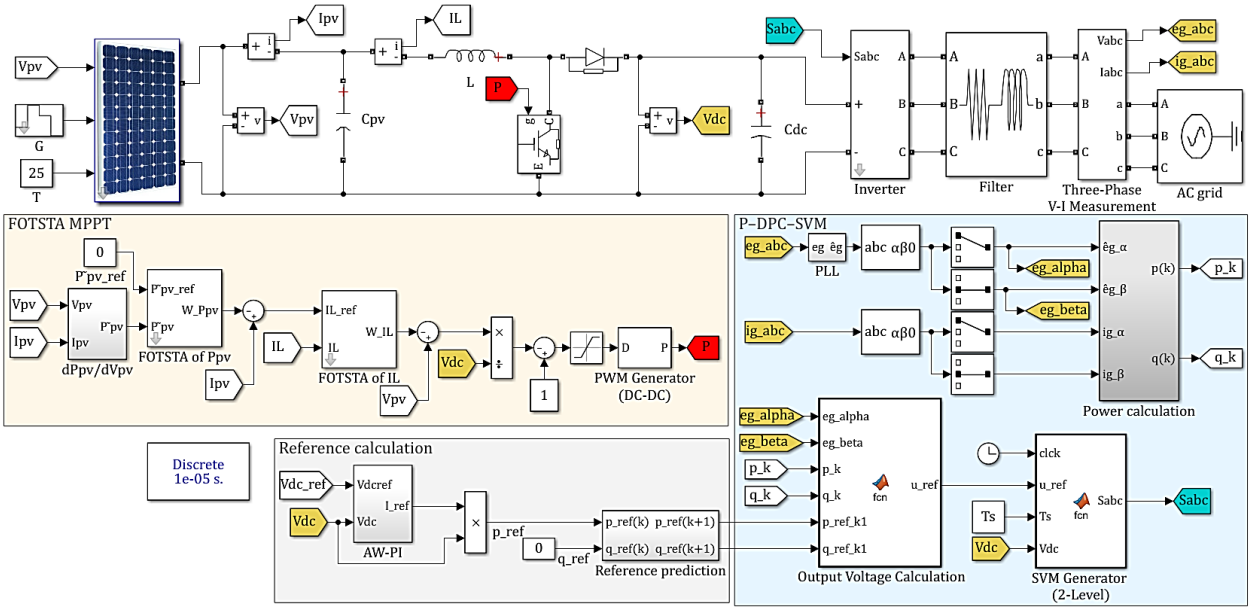

Figure 3.9 – Presentation of the overall command scheme in MATLAB/Simulink

As seen in 3.31, it is evident that the characteristic polynomial of the closed-loop system takes the form of a second-order canonical equation :

$$s^2 + 2\xi\omega_n s + \omega_n^2 \tag{3.32}$$

where ω_n is the natural frequency, and ξ is the damping coefficient.

By matching 3.31 and 3.32 and selecting an optimal damping coefficient, the regulator gains are determined as follows :

$$\begin{pmatrix} k_p = 2\xi\omega_n C_{dc} \\ k_i = C_{dc}\omega_n^2 \end{pmatrix} \tag{3.33}$$

Hence, the reference power value is deduced as :

$$P_{ref} = V_{dc} i_{dc} \tag{3.34}$$

Table 3.1 – Physical parameters of the grid-connected PV system

DC-DC converter parameters				Grid-connected inverter parameters				
C_{pv}	L	C_{dc}	f_s	V_{dc}^*	R_g	L_g	e_g	f
200 μF	10 mH	2000 μF	20 kHz	800 V	0.34 Ω	0.15 mH	220 V	50 Hz

Table 3.2 – Control parameters of MPPT-FOTSTA and AW-PI

PV Power FOTSTA controller				Inductor current FOTSTA controller				AW-PI controller	
k_{Ppv}	β_{Ppv}	μ_{Ppv}	λ_{Ppv}	k_{iL}	β_{iL}	μ_{iL}	λ_{iL}	k_p	k_i
11	36	1.5	0.7	240	360	1.5	0.8	16	0.3

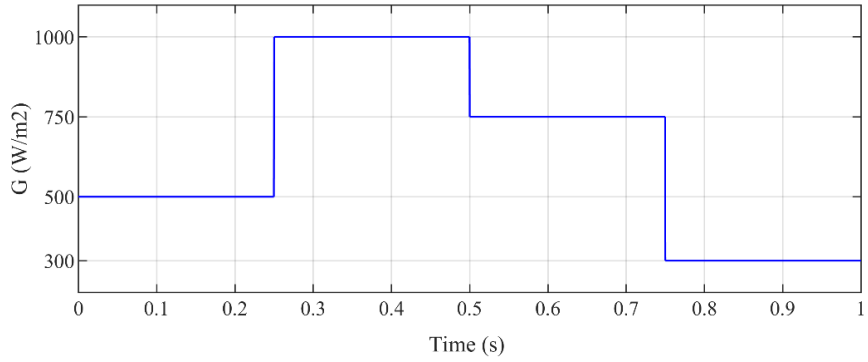

Figure 3.10 – Irradiance profile

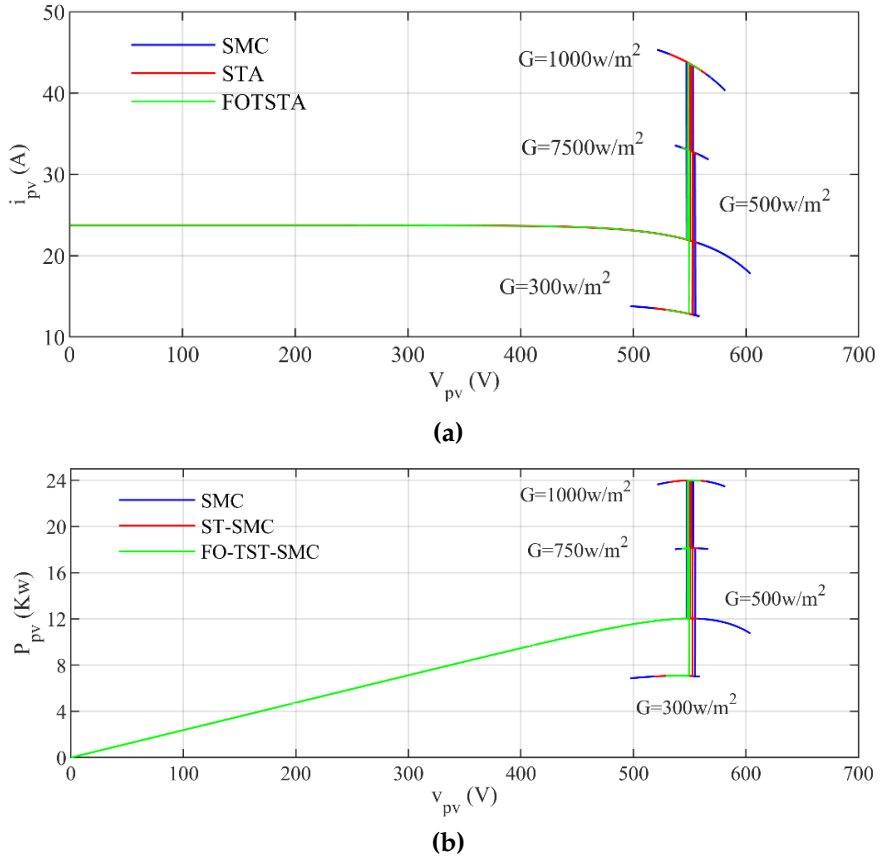

Figure 3.11 – Characteristics of PV solar for different irradiation (a) I-V and (b) P-V

3.2.4 Results and discussion

In this section, A two-stage grid-connected PV system is simulated using MATLAB. For this purpose, we test different nonlinear control functions for both control stages, DC-DC-BC command and P_s and Q_s management of the grid-connected inverter stage. The competence of the proposed FOTSTA is evaluated for the first stage and compared with the well-known conventional SMC and STA techniques, considering the P–DPC–SVM method for the second stage. Figure. 3.9 shows an illustration of the overall system in which the BM SX150S solar panel model is used.

In the present study, the optimal control parameters are calculated by using the metaheuristic algorithm so-called particle swarm optimizer (PSO), which is based on

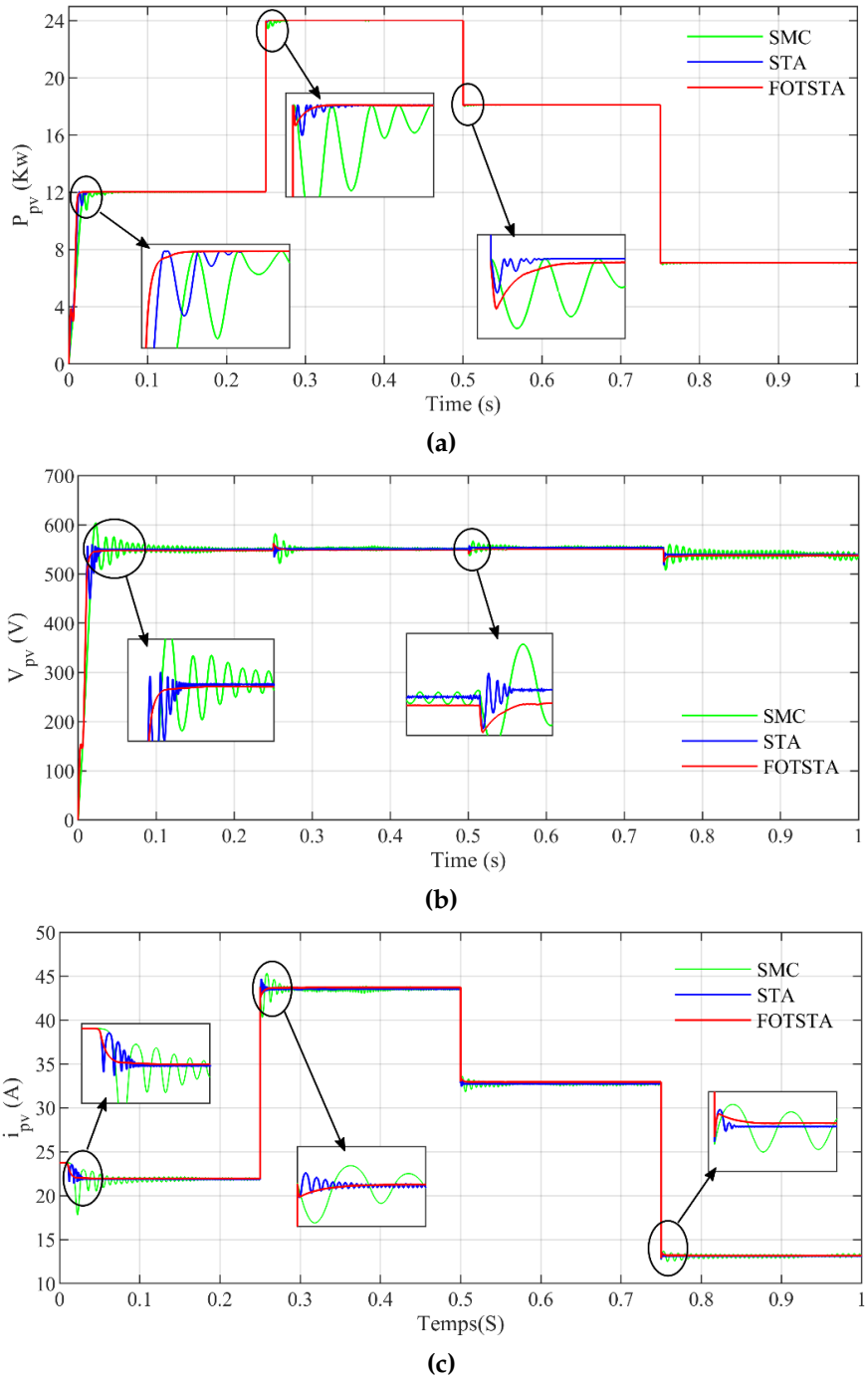

Figure 3.12 – PV module (a) Output energy (b) Output voltage (c) Output current

the minimization of a specific objective function. The control parameters of both DC controllers, FOTSTA and AW-PI controllers, are given respectively by $\theta_{FOTSTA} = [k, \beta, \lambda]^T$ and $\theta_{AW-PI} = [k_p, k_i]^T$. Being e_k is the error of the k^{th} sample between the actual and the desired output, the objective function is expressed as :

$$\mathrm{OF}_{\mathrm{DC}}(\theta) = \sum_{k=0}^{N} k \left| e_k(\theta) \right| \tag{3.35}$$

Using the physical parameters presented in Table 3.1, the optimal control parameters

Table 3.3 – Tracking performance indicators of MPPT : FOTSTA, STA, and SMC

Performances	MPPT Methods		
	SMC	*STA*	*FOTSTA*
Tracking accuracy η (%)	99.1 %	99.71 %	99.83 %
Power ripple (Rip) (%)	3.82 %	0.55 %	0.33 %
Overshoot/Undershoot (%)	1.66 %	0.58 %	0.29 %
Tracking Time (s)	0.0176 s	0.0134 s	0.0117 s

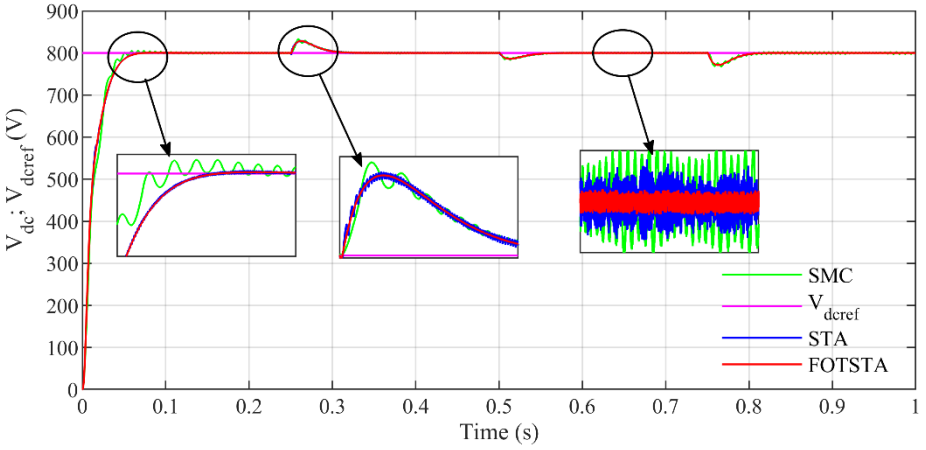

Figure 3.13 – DC link voltage

are calculated and given in Table 3.2, where the sampling time for both MPPT and P–DPC–SVM algorithms is set to $0.1ms$.

According to P-V characteristics, temperature has a non-significant effect on the MPP position, while irradiation level changes have an important impact on its performance. For this reason, the solar irradiance change scenario is adopted to visualize the overall competence and compare the results of the applied control approaches. In this scenario, the performance comparison of the MPPT-FOTSTA with SMC and STA is performed under the dynamic behavior of irradiation and constant temperature, considering the P–DPC–SVM technique for the AC side. The results are verified under four different irradiation levels. Figure. 3.10 shows the different irradiation patterns with a sudden change after every $0.25s$.

Firstly, the results of comparative study of three DC-DC boost converter control techniques in terms of tracking performance are presented in Figure. 3.11 and Figure. 3.12. $I_{pv} - V_{pv}$, $P_{pv} - V_{pv}$ curves can be seen in Figure. 3.11 and PV energy, voltage and stream in Figure. 3.12. The objective of this study is to test the ability of different non-linear control techniques including the proposed one to achieve the MPPT with rapid convergence, superior quality and robust disturbance rejection in the face of irradiation variation which has a significant effect on the MPP position of the PV generator.

The results clearly show that all the tested algorithms are able to correctly follow the behavior of irradiation to achieve the MPPT. The augment in irradiation implies an augment in PV energy created and vice versa. Therefore, the MPP moves to reach the new maximum point corresponding to the irradiation change thanks to the MPPT algorithm

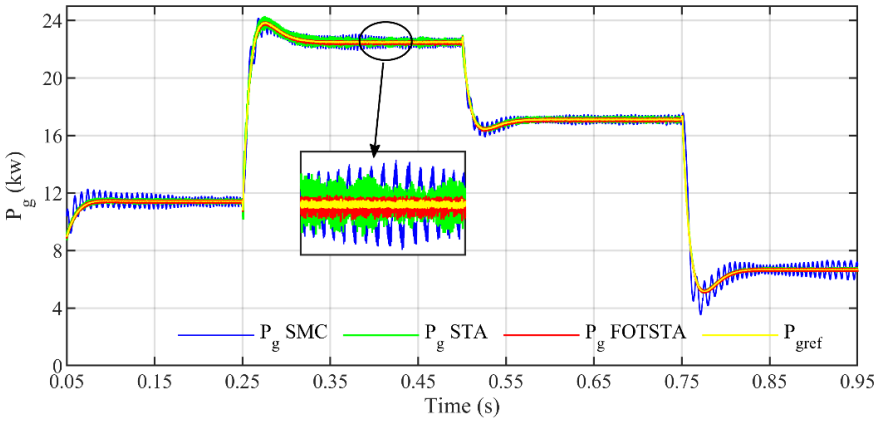

(a)

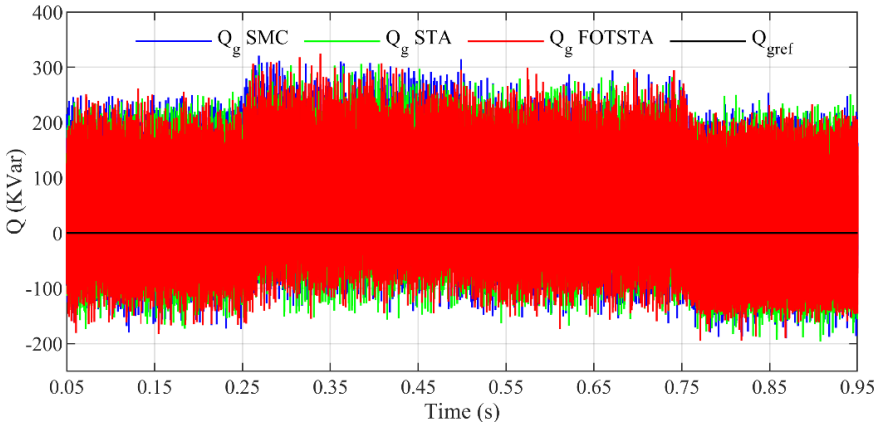

(b)

Figure 3.14 – (a) Grid active power (b) Grid reactive power

which continually determines the optimal voltage to give maximum power. The voltage varies slightly, contrary to the PV current which changes following irradiation. However, the conventional SMC and STA introduce undesirable transient responses and ripples to reach the MPP point that are considered a serious drawback of the PV system, while the FOTSTA delivers faster and higher quality MPP tracking, lower overshoot and ignored ripples which make its dynamic performance better than that of SMC and STA in terms of competence, quality and durability. When the solar irradiation suddenly decreases, high-precision convergence can be observed under the STA control which proves its strength, but looking at the overall performance, we can clearly observe the superiority of the proposed FOTSTA especially in enhancing the transient response and reducing the ripples which negatively affect the performance, durability and sustainability of the system, especially in real application.

To further demonstrate the enhancement of the designed approach compared to the usual method regarding the first stage performance, the efficiency characteristics of three control techniques are presented in Table 3.3. It is obvious that the fineness of energy delivered by the PV generator using FOTSTA is better than other conventional ones. The proposed method achieves an extreme performance enhancement in terms of quality, accuracy, convergence speed, and robustness.

Considering that the P-DPC-SVM technique is used to regulate the grid power to its

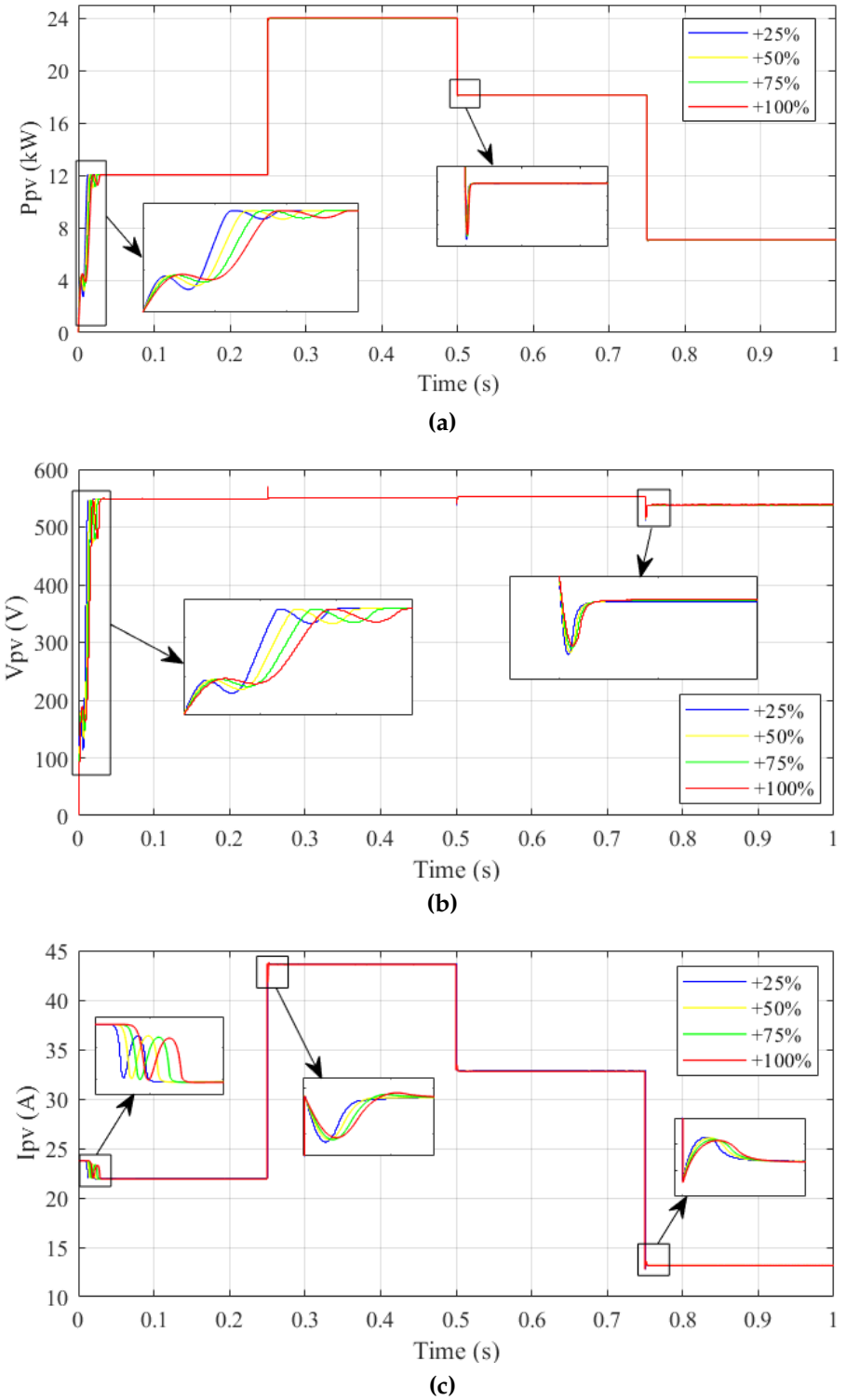

Figure 3.15 – Durability test (a) PV power (b) PV voltage (c) PV current

reference value provided by the outer loop of the DC link voltage via an anti-windup PI, the behavior of the DC-link voltage, grid P_s and Q_s given by the above MPPT control algorithms are shown in Figure. 3.13 and Figure. 3.14, respectively. From the results of the first two figures, it is evident that the FOTSTA gives the highest tracking speed, the least overshoot and steady-state oscillations, in contrast to the SMC method, which gives

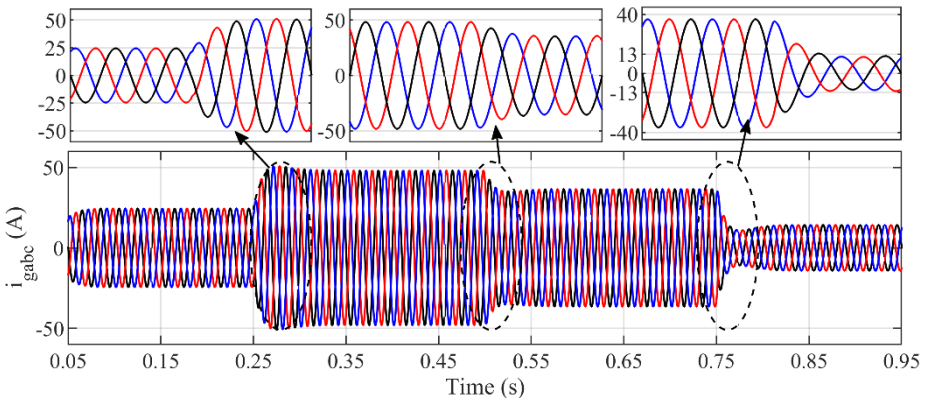

Figure 3.16 – Three-phase grid current using the proposed P–DPC–SVM associated with MPPT FOTSTA controller

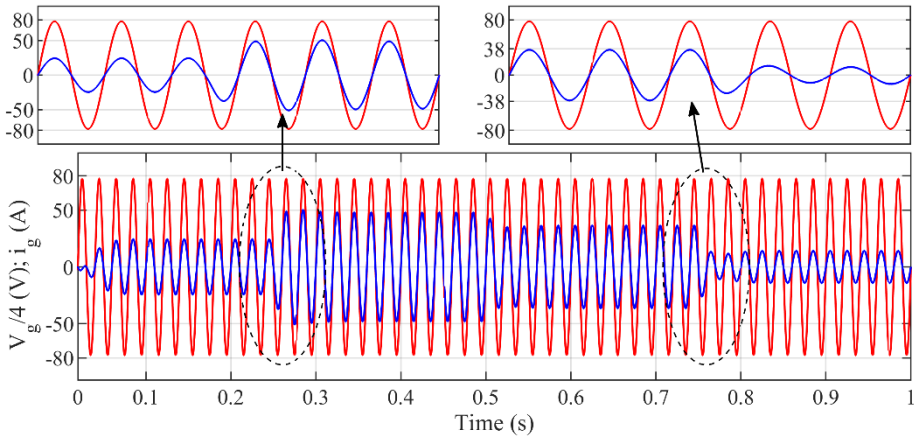

Figure 3.17 – Phase-a grid current and voltage using P–DPC–SVM associated with MPPT FOTSTA controller

the most oscillations due to the chattering phenomena. On the other hand, the Q_s band is almost zero which corresponds to unitary power factor operation for all MPPT algorithms studied.

Then, in order to test the durability of the proposed FOTSTA controlled, simulations are performed under different values of the physical parameters X such that they vary as follows :

$$X = X + \Delta X \tag{3.36}$$

where

$$X = \{C_{pv}, L, C_{dc}\} \tag{3.37}$$

And

$$\Delta X = X \cdot \ [25\% \ 50\% \ 75\% \ 100\%]^T \tag{3.38}$$

Figure. 3.15 shows the dynamic behavior of electrical quantities : PV power, PV voltage, and PV current as a function of four-step change conditions in solar irradiance. Again,

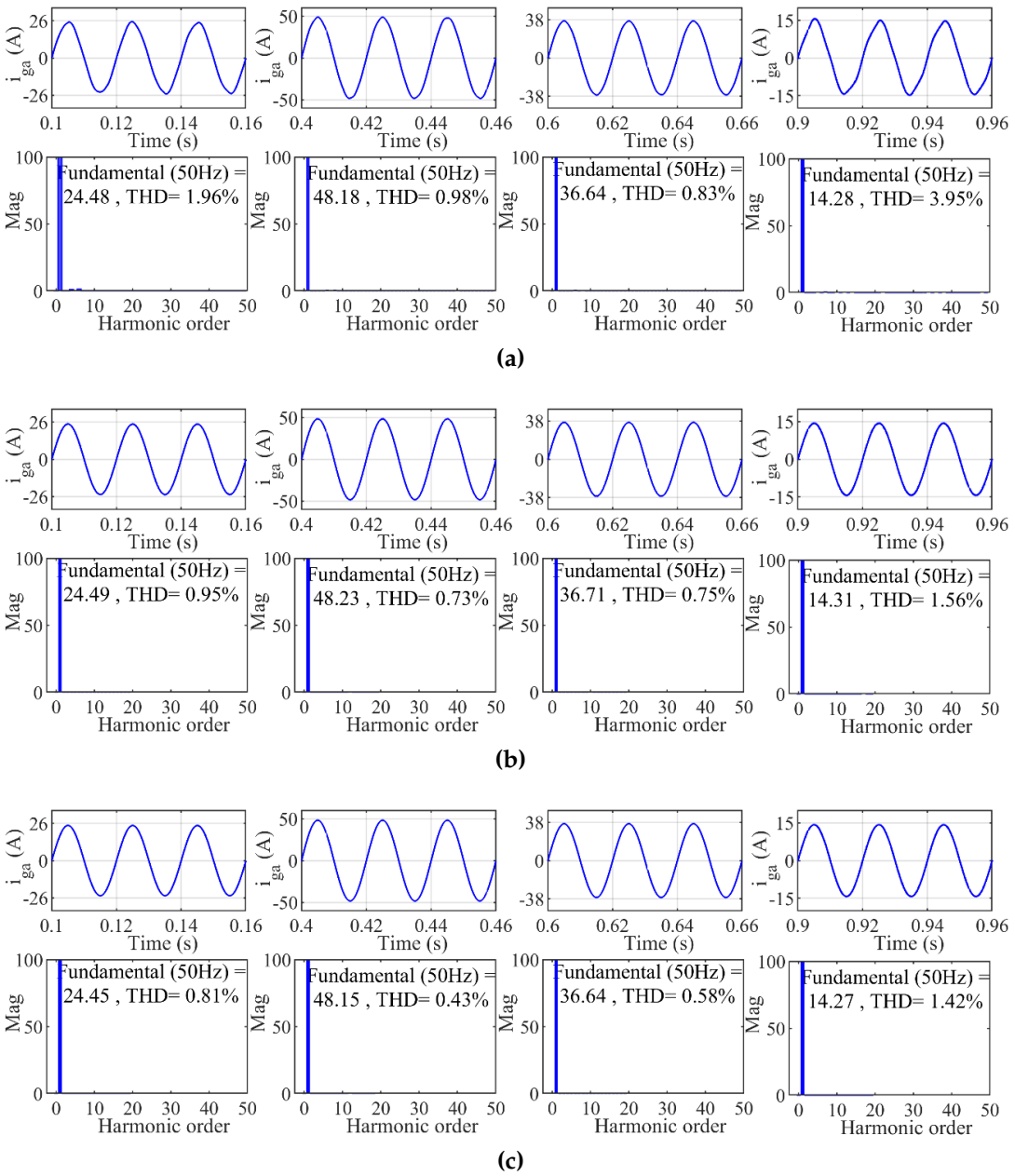

Figure 3.18 – Grid current with FFT using P–DPC–SVM associated with MPPT (a) SMC (b) STA (c) proposed FOTSTA

the findings demonstrate the high durability and robust performance of the proposed FOTSTA controller.

The output current and output voltage received by the grid are depicted in Figure. 3.16 and Figure. 3.17, respectively. We can see that the phase difference between the voltage and the current is zero ($\varphi \approx 0$) which indicates that operation at unity energy factor is almost achieved ($\cos\varphi \approx 1$). Because the power grid voltage is kept constant, the trace of variation in grid current is very clearly visible respecting the variation of the irradiation.

Figure. 3.18 shows the Fast Fourier Transform (FFT) analysis of the output stream using the three MPPT controllers tested, from where the THD values are extracted and presented in Table 3.4 for different irradiation conditions. Thanks to their robust performance, the

Table 3.4 – Grid current THD under, FOTSTA, STA, and SMC

THD (%)	MPPT techniques		
	SMC	*STA*	*FOTSTA*
$G = 300\ (W/m^2)$	3.95 %	1.56 %	1.42 %
$G = 500\ (W/m^2)$	1.96 %	0.95 %	0.81 %
$G = 750\ (W/m^2)$	0.83 %	0.75 %	0.58 %
$G = 1000\ (W/m^2)$	0.98 %	0.73 %	0.43 %

Table 3.5 – Grid current THD analysis : proposed FOTSTA vs. recent MPPT techniques

MPPT techniques	THD (%)	References
Finite-set model predictive control	1.31	[147]
fuzzy SMC	2.48	[148]
Integral backstepping approach	1.15	[149]
Third-order SMC	0.91	[150]
Model predictive control	4.82	[143]
Adaptive STA	3.48	[138]
Second-order SMC	1.38	[70]
Fractional order controller	1.24	[151]
Model-free controller	2.48	[152]
Proposed FOTSTA control	0.43	[139]

Table 3.6 – Overall performance comparison of various MPPT techniques

Features	MPPT Techniques					
	P&O	*INC*	*FS-MPCC*	*SMC*	*STA*	*FOTSTA*
Transient fluctuations	High	High	minimal	Medium	Low	minimal
Steady-state oscillation	High	High	Low	High	Low	minimal
Dynamic response	Low	Medium	High	Medium	High	High
Convergence speed	Low	Low	High	High	High	Extreme
Control accuracy	Low	High	High	High	High	High
Injected power quality	Low	Low	High	Medium	High	Extreme
Algorithm complexity	Low	Low	High	Medium	Medium	Medium
Overall effectiveness	Medium	Medium	High	High	High	High

simulation result reveals that all algorithms give good THD values which remain below 5% as recommended by IEC and IEEE (THD). Nevertheless, the proposed FOTSTA can maintain the least THD value compared to SMC and STA algorithms even after each solar irradiation transition.

In essence, a comparison is made between the approaches specified in different sources and the approach used to assess the current THD. Table 3.5 presents the contrasting results. Analysis of this table demonstrates that when compared to several other methods, FOTSTA produced more favorable outcomes regarding THD. This thorough comparison supports the competence of the suggested approach in machinery command and the field of renewable energies.

Table 3.6 briefly summarizes the comparison between the simulation results of different MPPT approaches previously studied, including the proposed FOTSTA. According to the simulation and comparative study results, the MPPT-FOTSTA has better control performance under irradiation change conditions. This is because FOTSTA can offer a fast convergence speed, less oscillations, and power ripples, better transient response, and high quality of power injected into the grid. The outstanding performance coupled with the simplicity of the algorithm makes the proposed FOTSTA recommended for application in machinery command and the field of renewable energies compared to other techniques.

3.3 Control of a stand-alone PV system

In a stand-alone PV system, the solar PV module is the main source of power generation. However, the output voltage of the PV module is not only unreliable but also insufficient. As a solution, a DC/DC boost converter is used to synchronize the output voltage of the PV unit with the standard voltage of the common DC bus and ensure that the solar panels operate at their MPP point to maximize energy extraction. Despite this adjustment, the intermittent nature of the solar PV unit makes it difficult to maintain a constant voltage level on the DC bus. To mitigate this problem, the BESS is connected to the common DC bus via a bidirectional DC/DC converter. The aim is to effectively regulate power imbalances within the stand-alone PV system and provide a DC load.

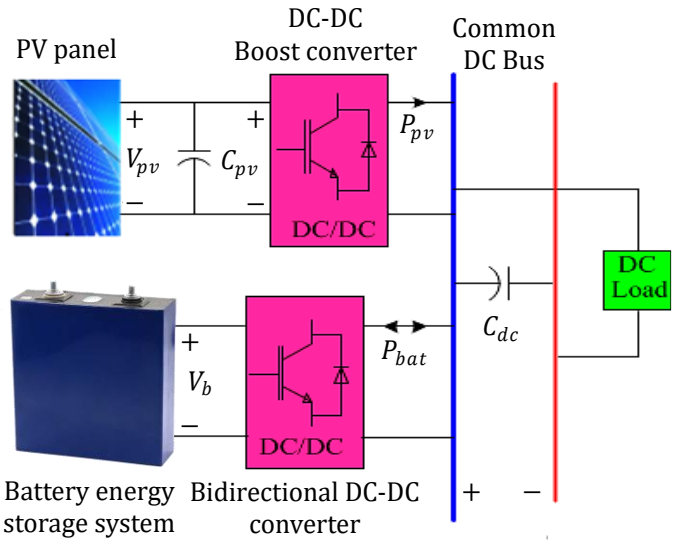

Figure 3.19 – Presentation of DC stand-alone PV system

In order to ensure stable and optimal operation of the entire DC stand-alone PV system, power optimization, control, and management are required [153, 154]. The adopted control strategy consists of two stages. The first stage is used to optimize the GPV power efficiency under various irradiation conditions via a boost converter. The second controller stabilizes the common DC bus voltage to maintain the power balance between the PV power source and the DC load demand through a battery (BESS) connected to the common DC bus via a bidirectional DC/DC converter.

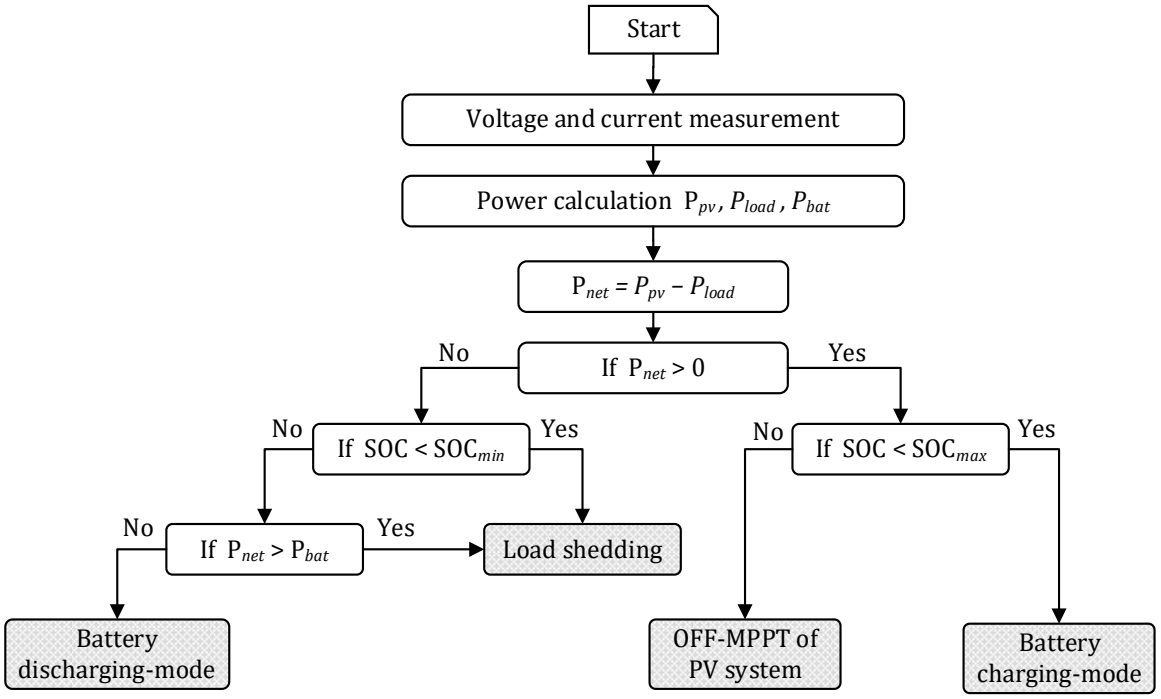

Figure 3.20 – Power management strategy for standalone PV/BESS

3.3.1 Power management and operational modes

In the present topology, the primary energy source will be the solar PV unit, with a BESS utilized to manage power equilibrium. The BESS will store excess power during low-demand periods and provide additional power during peak demand, ensuring stability on the DC bus. Consequently, the net power can be represented as follows :

$$P_{net} = P_{pv} - P_{load} - P_{loss} \pm P_{bat} \tag{3.39}$$

where P_{bat} is the BESS output power, which is positive during discharging mode and negative during charging mode, P_{load} is the power consumed by DC loads, P_{net} is the net power, P_{pv} is the SPV output power and P_{loss} is the power loss.

It is frequently acknowledged that the maintenance of power equilibrium in the studied DC system requires a steady voltage across the DC-bus capacitor C_{dc}. Consequently, the dynamic of the DC-bus voltage can be articulated depending on the net power :

$$C_{dc} V_{dc} \frac{dV_{dc}}{dt} = P_{net} \tag{3.40}$$

However, any rise or fall in the DC-bus voltage indicates an excess or shortfall of power within the system. Through regulation of the BESS power flow, the controller proposed in this study aims to preserve the state of charge (SOC) of the BESS within a secure operational range while ensuring a consistent DC-bus voltage. Operational modes determined by power balance are elaborated upon in the subsequent section.

The flow chart depicting the proposed Energy management system (EMS) is illustrated in Figure. 3.20. Based on this EMS, this study assesses four primary operating modes

aimed at sustaining power equilibrium. These modes are elaborated upon in further detail below :

Mode I : In this mode ($P_{pv} > P_{load}$ and $SOC < SOC_{max}$), the generated PV power exceeds the load demand, enabling the battery to absorb the surplus power. The PV system operates at its MPP, while the battery ensures the DC bus voltage remains steady at its nominal value.

Mode II : ($P_{pv} < P_{load}$ and $SOC > SOC_{min}$), the PV power falls short of meeting the load demand. Consequently, the battery discharges to supplement the additional load. Like Mode I, the PV operates at its MPP, and the battery controls the voltage of the DC bus.

Mode III : ($P_{pv} > P_{load}$ and $SOC \geq SOC_{max}$), in this scenario, when the battery is at full charge and the PV power surpasses the load demand, the battery's current is adjusted to zero to prevent overcharging. Additionally, the excess PV power is limited through power curtailment, accomplished by adjusting the PV operation to maintain the DC bus voltage at its nominal level.

Mode IV : ($P_{pv} = 0$ and $SOC \geq SOC_{min}$), in conditions such as cloudy weather or nighttime, when solar PV power is unavailable, the PV system is disconnected. In this mode, the battery takes charge of regulating the DC bus voltage to fulfill the load demand.

Whenever : ($P_{pv} < P_{load}$ and $SOC \leq SOC_{min}$), the battery needs to halt its power supply, and any surplus non-critical loads should be disconnected from the system. However, it's important to note that the operational mode involving load shedding is not addressed within the scope of this study.

3.3.2 Synergetic simplified supertwisting algorithm (SSSTA) control

The simplified super twisting algorithm control (SSTA) stands out as one of the most prevalent nonlinear approaches in electrical machine control, prized for its robustness and straightforward implementation [155]. Its integration into automated systems significantly enhances the performance and efficiency of electrical machines. Notably, the SSTA algorithm falls under the umbrella of sliding mode control (SMC) techniques, distinguished by its effectiveness in mitigating chattering issues compared to traditional SMC methods and STA. Expression 3.41 outlines the core principles of the SSTA algorithm.

$$u = -k\sqrt{|S|} \cdot \text{sign}(S) \tag{3.41}$$

where S the error or linear sliding surface, and $k \neq 0$ are positive values.

$$S = x^* - x \tag{3.42}$$

The sliding control (SC) approach constrains the system trajectories to evolve within a predefined manifold by appropriately shaping a macro variable in accordance with the control objectives. To this end, a first-order linear differential equation is imposed on the sliding variable to regulate the system behavior once the manifold is reached. The conventional SC formulation is expressed as

$$T\,\dot{S}(X) + S(X) = 0, \tag{3.43}$$

where $T > 0$ denotes the convergence rate of the sliding surfaces toward the intersection defined by $S = 0$. The stability of the SC scheme is guaranteed provided that the sliding variable satisfies $S(0) = 0$ and $S(x)\,x > 0$ for all $x \neq 0$. Solving 3.43 yields an exponential evolution of the sliding variable given by :

$$S(t) = S_0 e^{-t/T}, \tag{3.44}$$

which ensures asymptotic convergence of the system trajectories toward the sliding manifold.

The proposed Synergetic Simplified Super-Twisting Algorithm (SSSTA) combines the smoothness and robustness of synergetic control with the finite-time convergence properties of the simplified super-twisting algorithm. This hybrid approach aims to enhance the convergence speed while significantly reducing chattering effects. A synergetic sliding surface $S(t)$ is defined based on the system tracking error and its dynamics. The control objective is to force the system trajectories to converge toward and remain on the surface $S(t) = 0$, thereby ensuring the desired closed-loop behavior.

The command input of the proposed SSSTA controller is given by :

$$u(t) = -k\sqrt{|S(t)|}\,\mathrm{sign}(S(t)) - T\frac{d}{dt}\big(S(t)\big) - S(t) \tag{3.45}$$

where $k > 0$ and $T > 0$ are tuning parameters. The nonlinear term ensures fast and finite-time convergence, while the synergetic terms provide smooth control action and mitigate the chattering phenomenon.

As shown in Figure. 3.21, the sliding surface from the tracking error is processed through derivative (T), nonlinear super-twisting (k), and linear stabilizing branches to form the control signal.

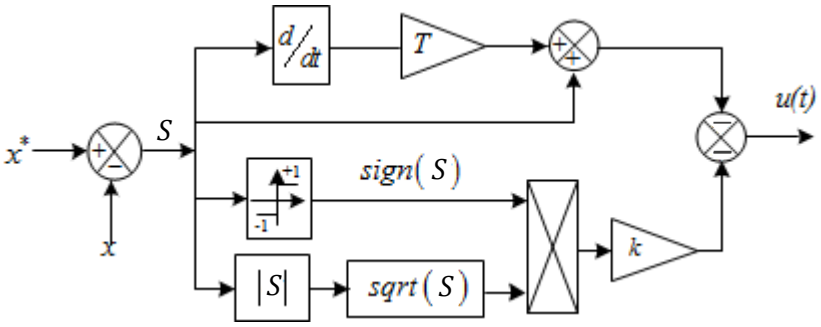

Figure 3.21 – SSSTA controller structure

To establish stability, a Lyapunov candidate function is selected as :

$$V_x = \frac{1}{2}S_x^2 \tag{3.46}$$

which is positive definite for all $S_x \neq 0$.

The sliding surface is selected according to the system constraints, where the proposed SSSTA approach forces the state trajectories to evolve toward and remain on the surface $S_x = 0$. To guarantee this behavior, the time derivative of the Lyapunov function must be

negative, i.e.,

$$\dot{V}_x = S_x \cdot \dot{S}_x < -\eta |S_x| \tag{3.47}$$

where $\eta > 0$ is a design gain.

If $S_x(0) > 0$, then $S_x(t) \leq S_x(0) - \eta t$; if $S_x(0) < 0$, then $S_x(t) \geq S_x(0) + \eta t$. Consequently, the sliding variable reaches the surface $S_x = 0$ in a finite time bounded by $|S_x(0)|/\eta$.

For $S_x(0) \neq 0$, the reaching dynamics of the sliding surface are imposed as :

$$\dot{S}_x = -TS_x - k\sqrt{|S_x|} \cdot \text{sign}(S_x) \tag{3.48}$$

Starting from the above reaching law, the corresponding SSSTA control input is designed to enforce the surface dynamics and is expressed as :

$$u(t) = -TS_x - k\sqrt{|S_x|} \cdot \text{sign}(S_x) \tag{3.49}$$

Equation 3.49 is satisfied provided that the gains k and T are positive, which ensures the convergence of the sliding variable toward the surface.

Consequently, the sliding surface satisfies the inequality 3.47.

Boost converter control for MPPT

A nonlinear SSSTA is used in the PV current and voltage loops to extract maximum and consistent power from the PV system. The first SSSTA loop regulates the PV voltage and produces the reference current for the inductor, while the second SSSTA loop controls the inductor current with minimal steady-state error and determines the duty cycle for the DC/DC boost converter.

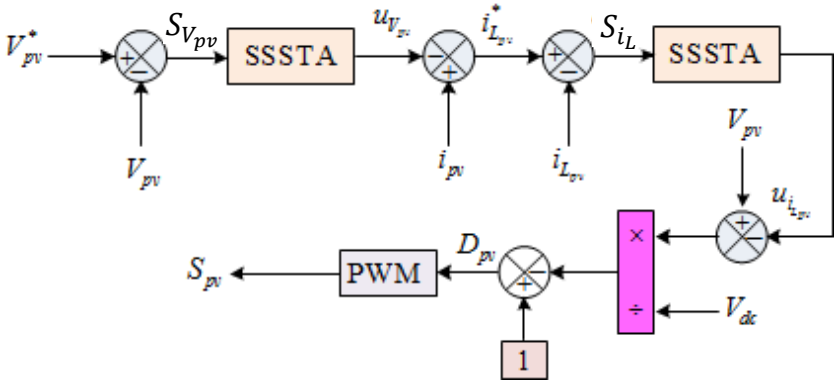

Figure 3.22 – Scheme SSSTA control of PV system

a) PV voltage Control

Defining the sliding surface is a critical first step in controlling the SSSTA. In the realm of PV power control, the sliding surface is defined as follows :

$$S_{V_{pv}} = V^*_{pv} - V_{pv} \tag{3.50}$$

The SSSTA control law for the PV voltage controller can be expressed as :

$$u_{V_{pv}} = k_{V_{pv}} \sqrt{|S_{V_{pv}}|} \cdot \text{sign}(S_{V_{pv}}) + T_{V_{pv}} \frac{dS_{V_{pv}}}{dt} + S_{V_{pv}} \tag{3.51}$$

The compensated PV voltage control loop provides the reference current of the boost converter inductor as follows :

$$i_L^* = i_{pv} - \left[k_{V_{pv}} \sqrt{|S_{V_{pv}}|} \cdot \text{sign}(S_{V_{pv}}) + T_{V_{pv}} \frac{dS_{V_{pv}}}{dt} + S_{V_{pv}} \right] \tag{3.52}$$

b) Boost inductor current control

The sliding surface for the inductor current is defined as follows :

$$S_{i_L} = i_L^* - i_L \tag{3.53}$$

The SSSTA control law for the inductor current controller can be defined as follows :

$$u_{i_L} = k_{i_L} \sqrt{|S_{i_L}|} \cdot \text{sign}(S_{i_L}) + T_{i_L} \frac{dS_{i_L}}{dt} + S_{i_L} \tag{3.54}$$

The inductor current control loop determines the duty cycle of the boost converter as :

$$D_{pv} = 1 - \frac{V_{pv} - \left[k_{i_L} \sqrt{|S_{i_L}|} \cdot \text{sign}(S_{i_L}) + T_{i_L} \frac{dS_{i_L}}{dt} + S_{i_L} \right]}{V_{dc}} \tag{3.55}$$

Bidirectional converter control for BESS system

The SSSTA control strategy is implemented in the bidirectional DC/DC converter to ensure optimal management of the DC microgrid. Two SSSTA controllers are employed : one to regulate the DC bus voltage and the other to manage the battery current. The voltage control process adjusts the DC bus voltage of the bidirectional DC-DC converter to follow its reference. The output of the voltage loop regulator provides the reference for the battery current to the internal loop current regulator. Ultimately, the current control loop determines the duty cycle of the bidirectional DC-DC converter.

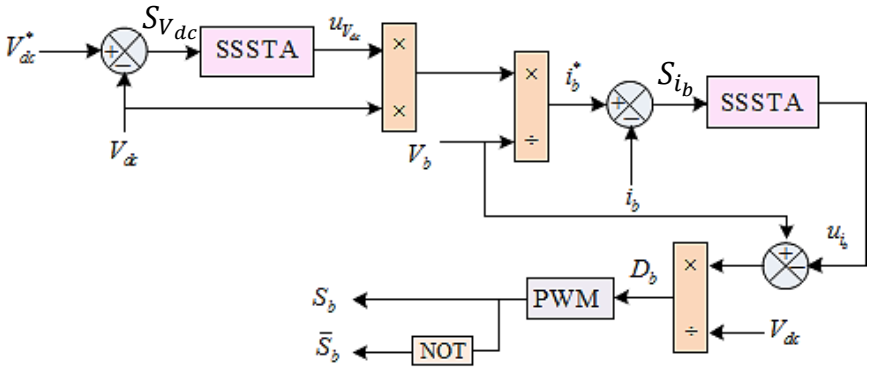

Figure 3.23 – SSSTA Control of the BESS

a) DC Bus Voltage Control

First, the sliding surface of the DC bus voltage can be defined as the difference between the reference value and the actual value, which can be expressed as follows :

$$S_{V_{dc}} = V_{dc}^{*} - V_{dc} \tag{3.56}$$

The switching control law is designed based on the SSSTA as follows :

$$u_{V_{dc}} = k_{V_{dc}} \sqrt{|S_{V_{dc}}|} \cdot \text{sign}(S_{V_{dc}}) + T_{V_{dc}} \frac{dS_{V_{dc}}}{dt} + S_{V_{dc}} \tag{3.57}$$

The power of the bus voltage can be expressed by multiplying the current by the DC bus voltage, as follows :

$$P_{BESS} = V_{dc} \left[u_{V_{dc}} = k_{V_{dc}} \sqrt{|S_{V_{dc}}|} \cdot \text{sign}(S_{V_{dc}}) + T_{V_{dc}} \frac{dS_{V_{dc}}}{dt} + S_{V_{dc}} \right] \tag{3.58}$$

b) Battery Current Control

Stabilizing the dc-bus voltage, the reference current of the battery can be expressed by dividing by the battery voltage as follows :

$$i_b^{*} = \frac{P_{BESS}}{V_b} \tag{3.59}$$

The sliding surface of the battery current (i_b) is given as

$$S_{i_b} = i_b^{*} - i_b \tag{3.60}$$

The SSSTA control law for the bidirectional inductor current controller can be defined as follows :

$$u_{i_b} = k_{i_b} \sqrt{|S_{i_b}|} \cdot \text{sign}(S_{i_b}) + T_{i_b} \frac{dS_{i_b}}{dt} + S_{i_b} \tag{3.61}$$

Using Equation 3.61, the switching control signal of the BESS is as follows :

$$D_b = \frac{V_b - \left[k_{i_b} \sqrt{|S_{i_b}|} \cdot \text{sign}(S_{i_b}) + T_{i_b} \frac{dS_{i_b}}{dt} + S_{i_b} \right]}{V_{dc}} \tag{3.62}$$

3.3.3 Results and discussion

The performance of the proposed SSSTA-based control strategy is evaluated in terms of accuracy, robustness, and adaptability. The control parameters were optimally tuned using the Particle Swarm Optimization (PSO) algorithm by minimizing the objective function defined in expression 3.35. The effectiveness of the PSO-optimized SSSTA controller is assessed under various operating conditions, including fluctuations in climatic variables and changes in load demand, and compared against a conventional control approach. The physical parameters of the overall PV-battery system used in the simulations are listed in Table 3.7.

Table 3.7 – Simulated system parameters of the stand-alone PV system

Parameter	Value
G_{ref}	1000 W/m^2
T_{ref}	25°C
V_{oc}	43.5 V
I_{sc}	4.75 A
V_{mp}	34.5 V
I_{mp}	4.35 A
MPP of P_{PV}	36 kW
Parameter of BESS (Lithium Ion Battery)	
Q	100 Ah
Battery converter inductance	1 mH
Battery converter capacitance	4000 μF
Parameter of DC-bus	
V_{dc}	800 V
C_{dc}	5.5e-3 F

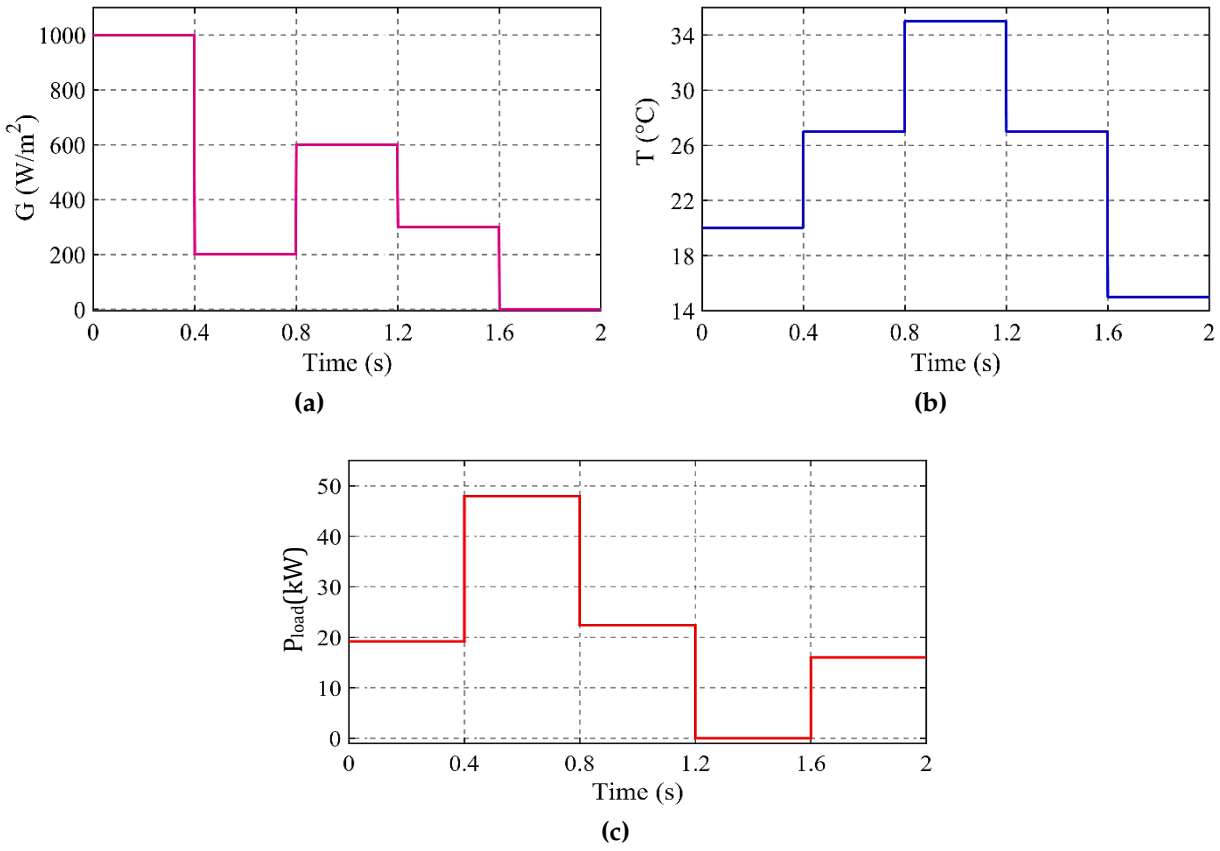

Figure 3.24 – (a) Irradiance profile, (b) Temperature profile, and (c) Load demand profile

Figure. 3.24 shows the patterns of different previous conditions with a sudden change after every 0.5 s. Figure. 3.25 illustrates the dynamic behavior of electrical quantities of the DC stand-alone PV system as a function of five-step change conditions of irradiance,

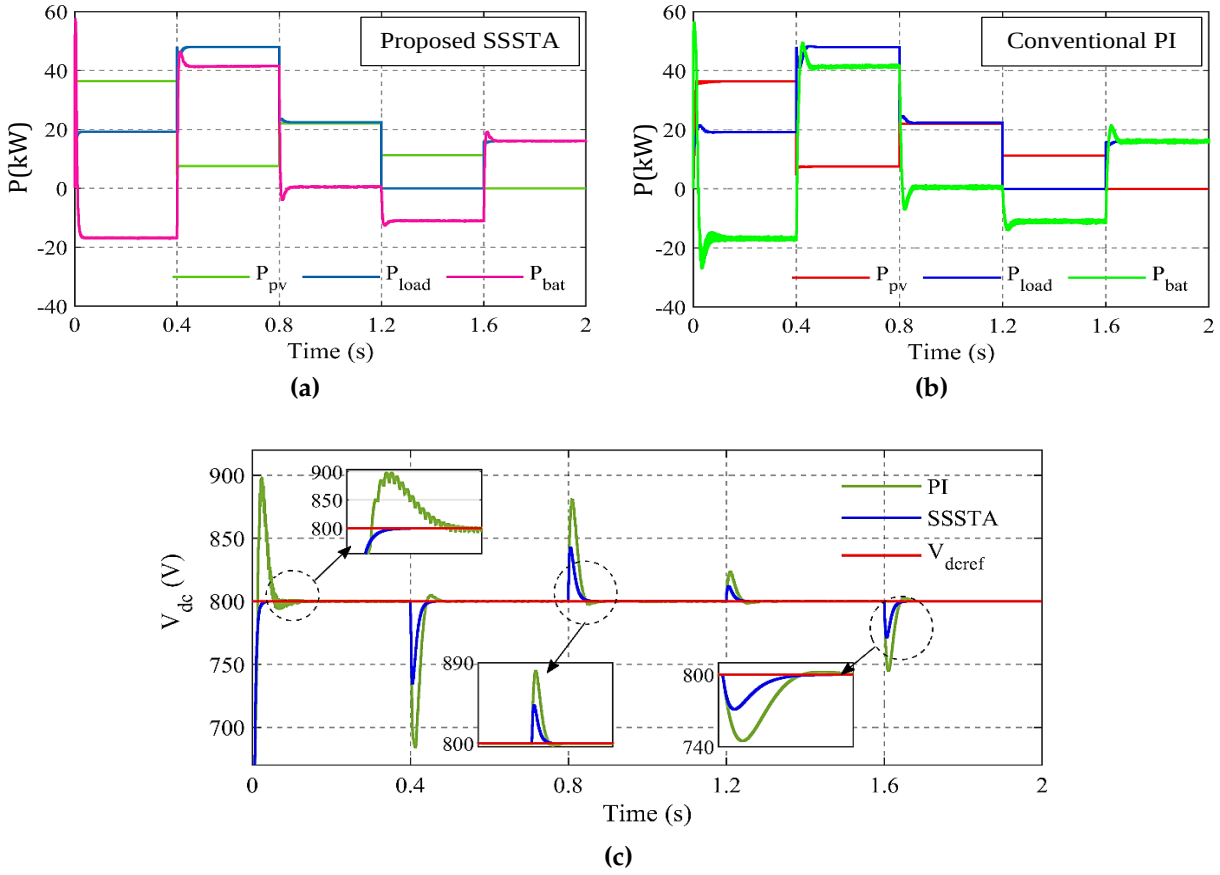

Figure 3.25 – Performance of the SSSTA compared to the conventional PI regulator (a) Power balancing (SSSTA), (b) Power balancing (PI), and (c) DC bus voltage

temperature, and power demand. Meanwhile, the energy quality of the PV panel, battery, and DC load is investigated through Figure. 3.26 under step fluctuation in irradiance and ambient temperature for both the designed SSSTA and the conventional PI regulator. From Figure. 3.25a and b, we can observe that the energy balance between the PV power source, battery, and load is correctly achieved for both the SSSTA and the PI regulator. The battery bank provides the energy difference between the load and the PV generator or absorbs excess energy during climatic conditions fluctuations or load demand changes. When the power produced by the PV generator is greater than the load consumption, the battery charges the excess power which is indicated by the negative sign of the battery energy curve. In contrast, when the PV generator provides lower energy than that of the load, a discharge mode is imposed on the battery to compensate for the missed demand i.e. the battery energy curve becomes in the positive zone. As for the zero energy of the battery, this indicates that the amount of energy generated by the PV panel is equal to that required by the load. In other words, the main objective of a battery converter is to keep the voltage across the DC bus stable at a reference value (see Figure. 3.25c). Although both the SSSTA and PI command units are capable of handling power balance and DC bus stability, obvious oscillations and large overshoot can be observed under PI command compared to the SSSTA technology, which provides a fast response and ideal energy quality in terms of tracking accuracy, reducing overshoot and lack of ripples.

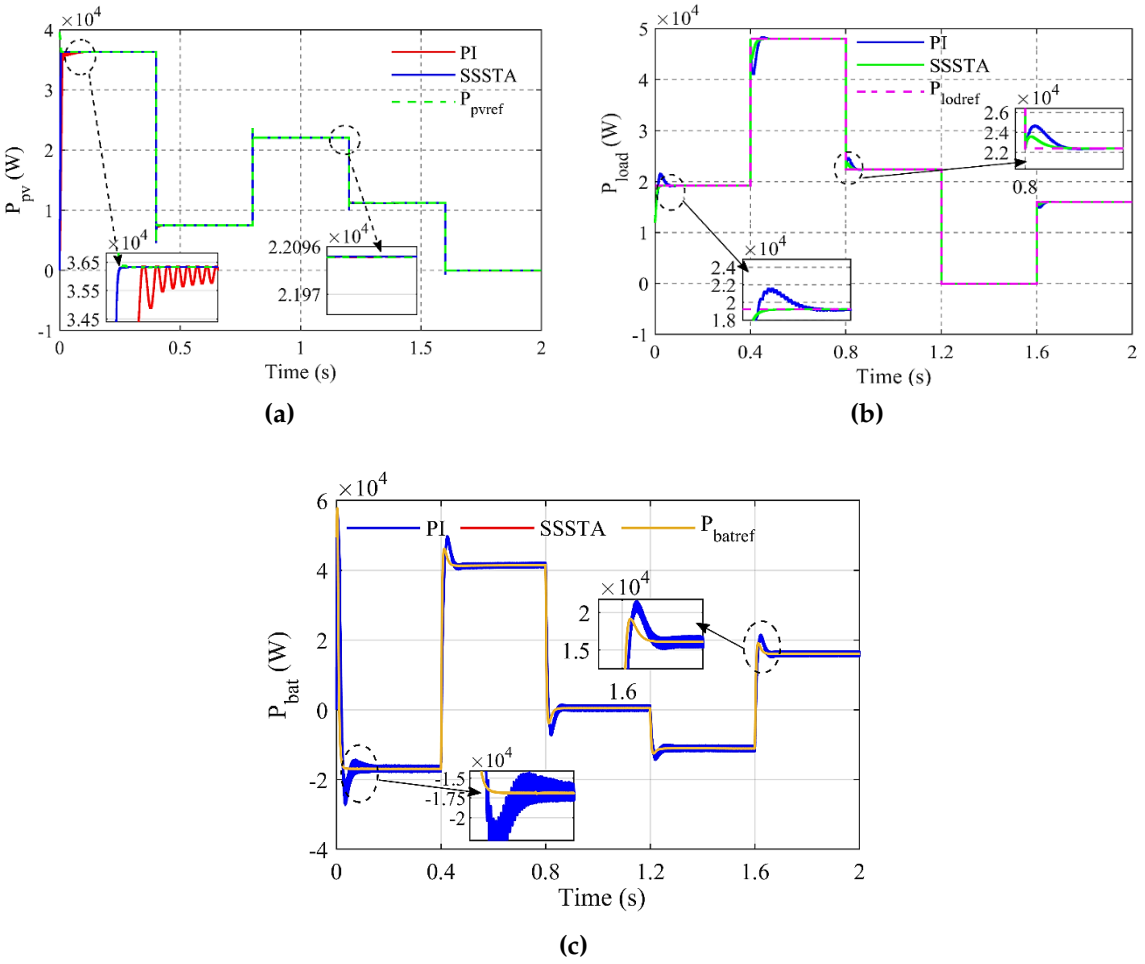

Figure 3.26 – Comparison of energy quality (a) PV array (b) DC load (c) Battery

Table 3.8 – Comparison analysis between the PI regulator and SSSTA for DC bus voltage

Methods / Performances	PI	SSSTA	**Ratios**
Settling time (s)	0.07	0.143	-51.05%
Ripple (V)	2.7 V	0.3 V	88.89%
Overshoot (V)	75 V	43 V	42.67%
Undershoots (V)	113 V	55 V	51.33%

The numerical results of this test are listed in Tables 3.8 and 3.9. Table 3.8 represents the values and reduction of the ripples, settling time, overshoot, and Undershoots of the DC bus voltage in the case of using two controls. From this table, it is noted that the approach provided satisfactory results for both fluctuations, undershoot, and overshoot compared to the PI regulator. The proposed approach reduced the ripples, overshoot, and undershoot of DC link voltage by estimated ratios of 88.89%, 42.67%, and 51.33%, respectably compared to the PI command. However, the proposed SSSTA approach provided unsatisfactory results for the settling time of DC link voltage compared to the traditional PI. The PI approach gave a better value for settling time than the SSSTA

Table 3.9 – Comparison analysis between the PI regulator and SSSTA for PV power

Methods / Performances	PI	SSSTA	**Ratios**
Settling time (s)	0.012	0.0059	50.83%
Ripple (%)	123 W	1.5 W	98.78%
Overshoot (W)	62 W	2.3 W	96.29%
Undershoots (W)	113 W	7.5 W	93.36%

approach by an estimated rate of 51.05%. This negativity can be attributed to the values of the gains, as this negativity can be avoided by using smart optimization approaches.

Table 3.9 represents the values and percentages of reduction for each of the ripples, undershoot, settling time, and overshoot of PV power. From this table, it is noted that the SSSTA approach significantly outperforms the proposed SSSTA approach in terms of providing lower values for each of the fluctuations, undershoot, settling time, and overshoot, and this superiority appears in high reduction ratios. This superiority can be attributed to its strength, durability, high competence, and great effectiveness in improving energy features and quality. Accordingly, the proposed SSSTA approach reduces the values of settling time, ripples, overshoot, and undershoot by ratios estimated at 50.83%, 98.78%, 96.29%, and 93.36%, respectively, compared to the PI approach. These high ratios will make this approach a promising and reliable solution for controlling systems.

3.4 Integration of ZSI in stand-alone PV system

In the stand-alone PV system topology, the Z-source inverter (ZSI) can provide two different and complementary functions, replacing the traditional separate boost and inversion stages. The first is to improve the energy efficiency of the PVG by controlling the shoot-through state. This function can only be implemented when the zero states are reached. The second function is similar to that of the traditional VSI. Using a bidirectional DC/DC converter, the BESS is connected to the common DC bus, corresponding to one of the ZSI capacitors, whose voltage regulation aims to balance the power between the PVG and the AC load.

3.4.1 ZSVPWM control strategy for ZSI

For the ZSI, many pulse-width modulation (PWM) control methods have been developed and used to provide the duty cycle of the shoot-through state. These techniques are performed by introducing the shoot-through within the zero states without affecting the active states. The proposed control strategies are based on modified conventional carrier PWM such as simple boost control (SBC), maximum boost control, constant boost control (MBC), and maximum constant boost control (MCBC). Meanwhile, several modified space vector pulse-width modulations (ZSVPWM) techniques have been introduced in the literature according to the number of shoot-through distributions such as four-ZSVPWM

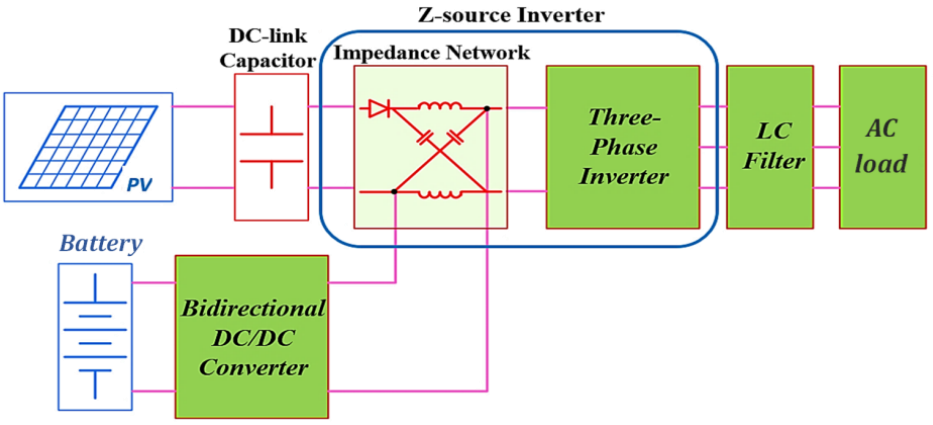

Figure 3.27 – Structure of stand-alone ZSI PV system

(4-ZSVPWM) and six-ZSVPWM (6-ZSVPWM) [158]. Afterward, different discontinuous ZSVPWM (D-ZSVPWM) techniques are proposed to enhance ZSI performance in terms of reducing power losses during switching while ensuring maximum power transfer. This is achieved by eliminating one of the zero states V0(000) or V7(111). Among these techniques, improved dis continuous ZSVPWM (ID-ZSVPWM) has emerged as one of the most effective control strategies for ZSI, being highly appreciated for its capability to improve the output waveform and reduce total harmonic distortions (THD), conduction, and switching losses [159]. In ID-ZSVPWM, each 60° sector is divided into two subsectors, resulting in 12 equal sectors of 30° instead of 6 sectors of 60° in the ($\alpha\beta$) frame. Despite its high performance, ID-ZSVPWM still suffers from a limited boost factor, significant inductance current ripple, high voltage stress, and low voltage gain. Recently, the latter strategy has been investigated under a modified reference (MR), to be called ID-ZSVPWM-MR where the magnitude of the reference voltage takes the form of a hexagon in the space vector [160]. ID-ZSVPWM-MR has proven superior in overcoming the above drawbacks compared to ID ZSVPWM but with more complexity in its implementation due to the shape of its voltage reference.

3.4.2 ZSI Control of stand-alone PV system based on PR controller

Due to the superior ability of the PR controller to handle harmonic distortions and ensure accurate tracking of sinusoidal references effectively mitigating harmonic distortions regardless of the load type, linear or nonlinear [161], it is used for the AC bus control of the ZSI inverter in a stand-alone PV system. Unlike conventional PI controllers, which struggle to properly regulate the AC signal, the robust PR controller introduces a resonant term at the fundamental frequency, providing high gain for accurate tracking and selective harmonic compensation. This improves power quality, reduces THD, and ensures stable and efficient system operation regardless of the load type [162].

The PR controller adopted for the regulation of the AC output voltage with less possible harmonics can be presented by the following expression :

$$G_v(s) = k_{pv} + \frac{k_{rv}s}{s^2 + \omega_c s + \omega_o^2} + \sum_{h=3,5,7} \frac{k_{hv}s}{s^2 + h\omega_c s + (h\omega_o)^2} \tag{3.63}$$

where k_{pv}, k_{rv} and k_{hv} are the proportional gain, the resonant gain at the fundamental frequency, and the resonant gain at the h-harmonic, respectively. ω_o is the fundamental frequency and ω_c is the resonant bandwidth that is used to avoid the instability problems associated with the infinite gain.

As for the DC side control, a cascade PI-IP controller is designed to achieve the cascade voltage oriented MPPT process and stabilize the common DC bus. The MPPT of the GPV is ensured by controlling the shoot-through state of the ZS network, while the DC bus stabilization is ensured by regulating the bidirectional converter which connects the BESS in parallel to one of the ZSI capacitors.

Thanks to its integral term, the PI controller can make the steady-state error zero. However, it may take a long time with a large overshoot to accomplish this. To improve the dynamic performance of the transient state and considerably minimize overshoot, an advanced form of the PI controller called the IP controller has been introduced. In this controller, only the integral term is kept in the feed-forward path, while the proportional term is displaced to the feedback path as shown in Figure. 3.28. Generally, this controller is used in electrical systems to reduce transient overcurrents that can deteriorate overall performance.

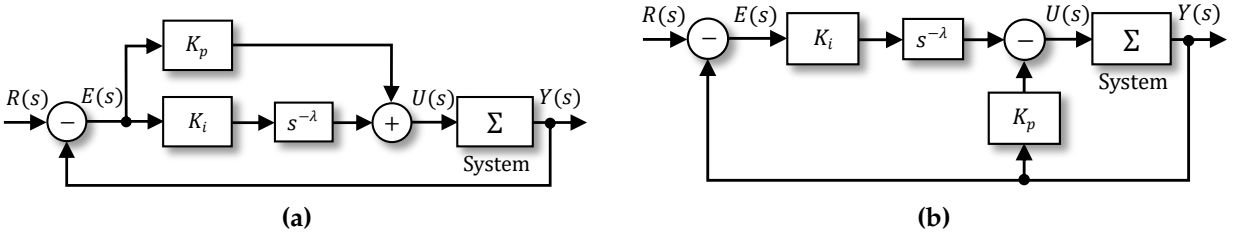

Figure 3.28 – (a) PI (b) IP Controller structure

The overall control scheme of stand-alone PV system based on ZSI is shown in Figure. 3.29.

Considering the objective function given by Equation 3.35, the optimal parameters of the PI-IP controller used for DC-side command are calculated using the PSO algorithm, where the parameters vector is given by $\theta = [k_p, k_i]^T$.

For the PR controller of the AC-side control, the parameter vector is given by : $\theta = [\omega_c, k_{pv}, k_{rv}, k_{3v}, k_{5v}, k_{7v}, k_{pi}]^T$, and the objective function is presented as follows :

$$F_{PR}(\theta) = \sum_{k=0}^{N} \left[\left(v^k_{\text{ref}_a} - v^k_{c_a}(\theta) \right)^2 + \left(v^k_{\text{ref}_b} - v^k_{c_b}(\theta) \right)^2 + \left(v^k_{\text{ref}_c} - v^k_{c_c}(\theta) \right)^2 \right] \tag{3.64}$$

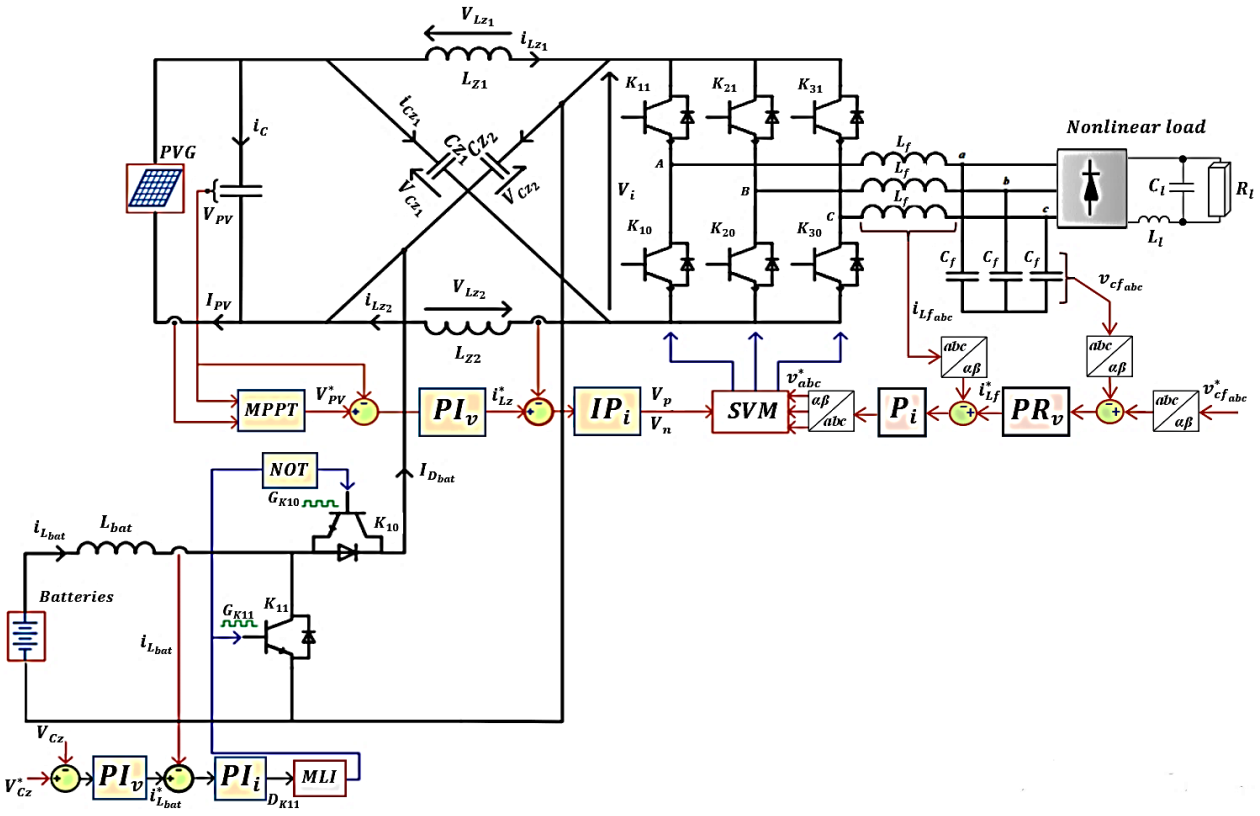

Figure 3.29 – Control of a stand-alone Z-source PV system

Results and discussion

To validate the control strategy, simulations are performed under different scenarios : variation of the irradiance and the load, as shown in Figure. 3.30. The BESS consists of 50 batteries, each one has 12V and a capacity of 100Ah. The 6-ZSVPWM is used as a control strategy of ZSI, while a simple PWM for the bidirectional converter. The switching frequency used for both control strategies is fixed at 5 kHz. The rest of physical parameters are listed in Table 3.10 and the optimal control parameters in Table 3.11.

Table 3.10 – Physical parameters of stand-alone Z-source PV system using PR control

P_{pv}(STD)	C_z	L_z	L_{bat}	C_f	L_f	C_l	L_l
4860 W	4.5 mF	10 mH	10 mH	80 μF	10 mH	490 μF	90 μH

According to Figure. 3.31a, it can be seen that the power of the PVG tracks the irradiance profile, which is ensured by the MPPT command and by exploiting the shoot-through state of ZSI. The two operating modes of the battery are illustrated through the shape of its power curve, such that the negative power indicates that the battery is in charge mode, and it is in discharge mode when the power is positive. The balance of power between the source and the load can also be observed.

The Z-inductance current depends only on the irradiation variation. Figure. 3.31b depicts the DC chain voltage V_i and the Z-inductance current, showing the presence of the zero state of the inverter regardless of the load variation, consequently, the active states are

Table 3.11 – Optimal control parameters for the PR controller

PI-IP Controller

Parameters	k_{pv}	k_{iv}	k_{pi}	k_{ii}
Z-source DC-Side	0.295	0	24.13	416.6
Bidirectional DC-DC converter	1.175	0	5	500

PR Controller

k_{pr}	k_r	k_{r3}	k_{r5}	k_{r7}	w_c	k_{pi}
0.635	77.708	27.901	19.567	15.088	3.304	71.265

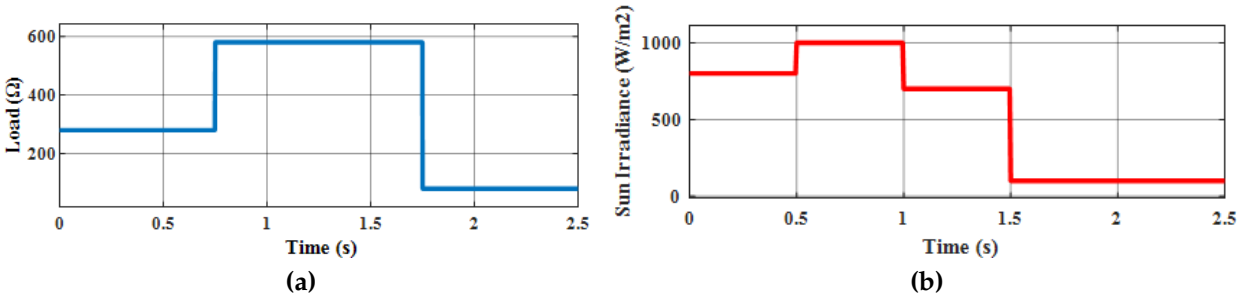

Figure 3.30 – (a) Load variation (b) Solar irradiance variation

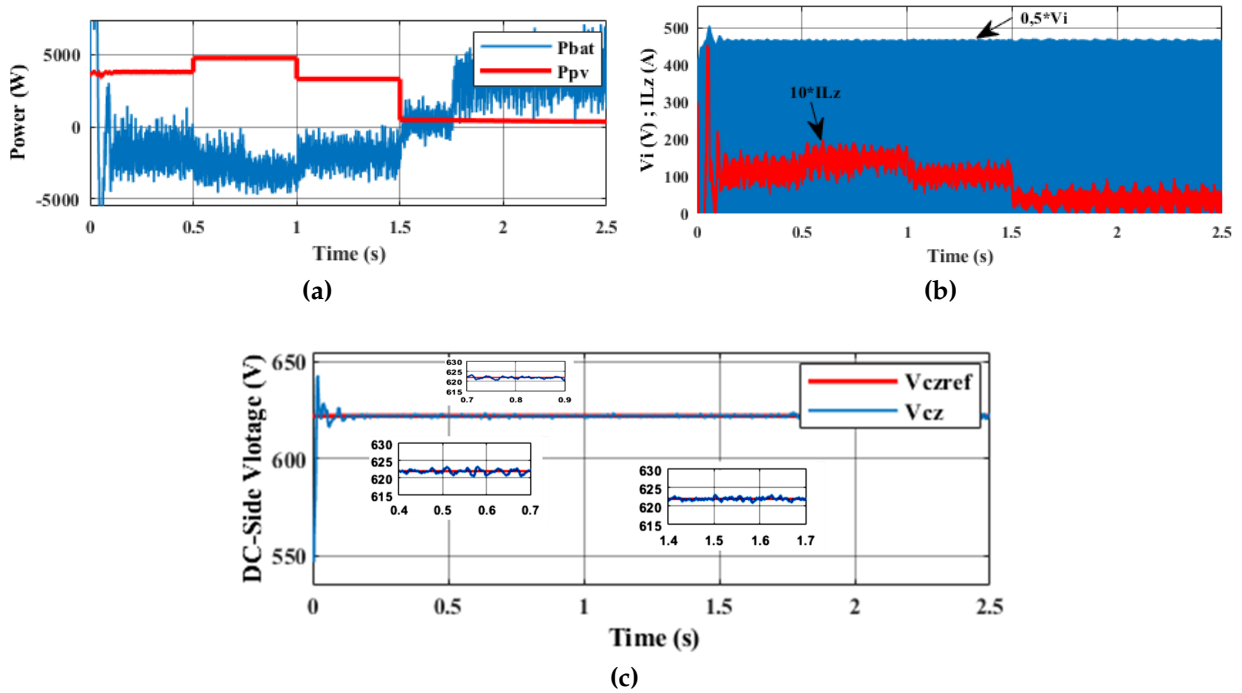

Figure 3.31 – (a) Power balance (b) Z-inductance current and ZS-DC chain voltage (c) Z-capacitor voltage

not affected by optimizing the energy efficiency of PVG through the Z-source inverter. The capacitor voltage V_{Cz} successfully tracks its reference V_{Czref} with minimum oscillations as shown in Figure. 3.31c. This result validates the performance of the bidirectional converter control.

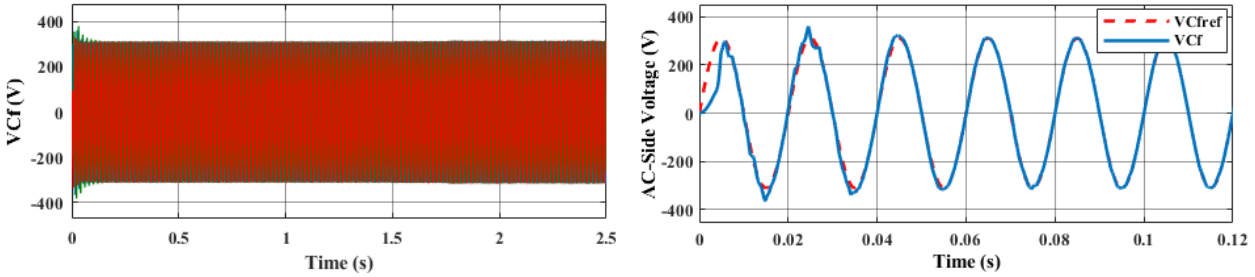

Figure 3.32 – ZSI Output voltage

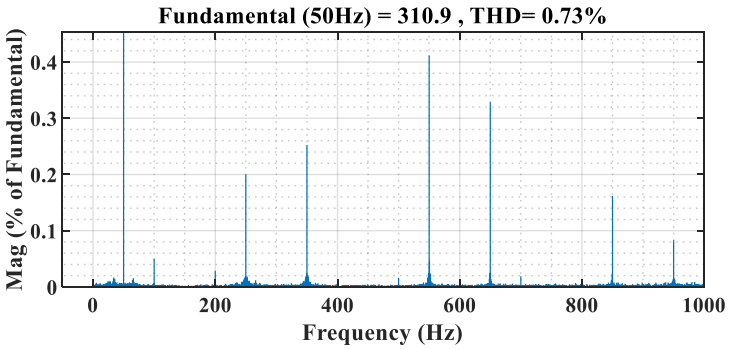

Figure 3.33 – Output voltage harmonic analysis

The designed PR controller is investigated under a local nonlinear load. From Figure. 3.32, the output voltage is successfully regulated along its reference during steady-state flow as well as transient flow (Load variations). As we can see in Figure. 3.33, the AC output voltage has a low total harmonic distortion (THD). These results verify that the PR controller can handle the system dynamics by providing perfect and fast disturbance rejection.

3.4.3 Control of stand-alone PV/ZSI system based on STA control

The super-twisting algorithm (STA) is an advanced type of sliding mode control (SMC). It has been introduced in the literature as a powerful tool to ensure the finite-time convergence of the origin of sliding variables and especially to generate a continuous control signal, which helps to reduce the overall chattering phenomenon [163, 164]. Without requiring knowledge of the mathematical model, the STA strategy is proposed for the three control stages of the stand-alone PV-ZSI system : MPPT, common DC bus stabilization and output AC bus control.

As shown in Figure. 3.34, the control circuit primarily consists of five loops : ZSI network-based MPPT control, ZSI AC side control loops, and bidirectional DC/DC converter-based DC link voltage control loop.

In this study, we have opted for the STA for all control stages due to its distinct advantages. As concluded in the literature, the STA approach is an advanced type of sliding mode control (SMC), characterized by simplicity, high robustness, great efficiency, low cost, fast dynamic response, and ease of implementation where the knowledge of the

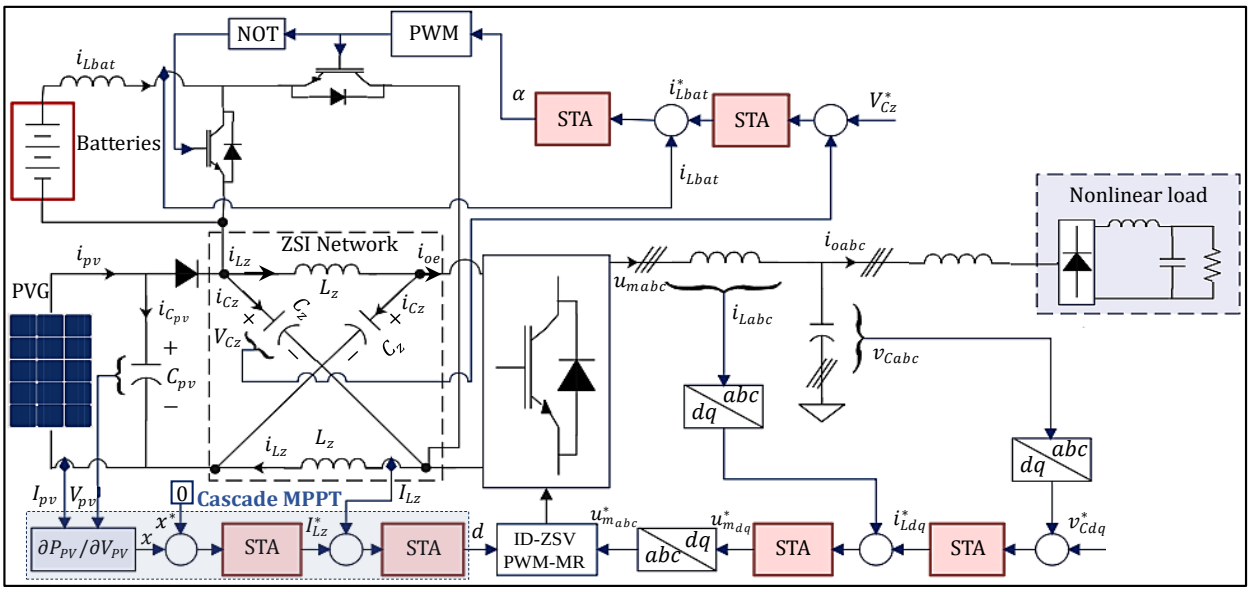

Figure 3.34 – Overall control structure based on STA

mathematical model of the studied system is not required. The law consistent with the STA approach is introduced as follows :

$$\begin{cases} u_n = -k\sqrt{|S|}\,\mathrm{sign}(S) + u_1 \\ \dot{u}_1 = -\beta\,\mathrm{sign}(S) \end{cases} \tag{3.65}$$

where $S = y^* - y$, the linear sliding surface and β, k positive coefficients. x and y^* are the signal to be controlled and its reference, respectively.

Cascade STA-based voltage-oriented MPPT

A nonlinear STA is used in the PV current and voltage loops to extract maximum and consistent power from the PV system. The first STA loop guarantees the MPP position and produces the reference current for the inductor, while the second STA loop regulates the inductor current and determines the duty cycle of the shoot-through state for the ZSVPWM block. Being x and x^* are the output to be controlled and its reference, respectively, where x represents the PV power derivative, the first linear sliding surface for PV power can be expressed as follows :

$$S_{P_{pv}} = x - x* \tag{3.66}$$

where

$$x = V_{pv} \times \frac{\partial i_{pv}}{\partial V_{pv}} + i_{pv} \tag{3.67}$$

And x^* is set to zero to keep the PV system operating point at the MPP position.

The STA control law of the PV power outer loop can be given as follows :

$$i^*_{C_{pv}} = -k_{P_{pv}}\sqrt{|S_{P_{pv}}|}\,\mathrm{sign}(S_{P_{pv}}) - \beta_{P_{pv}}\int \mathrm{sign}(S_{P_{pv}})\,d\tau \tag{3.68}$$

Therefore, using the first equation from the system 1.10, we can obtain the reference current for the inner loop as follows :

$$i^*_{Lz} = i_{pv} - i_{Cz} - \left[-k_{P_{pv}}\sqrt{|S_{P_{pv}}|}\,\mathrm{sign}(S_{P_{pv}}) - \beta_{P_{pv}}\int \mathrm{sign}(S_{P_{pv}})\,d\tau\right] \tag{3.69}$$

The second linear sliding surface for the Z-inductor current can be written as :

$$S_{i_{Lz}} = i_{Lz} - i^*_{Lz} \tag{3.70}$$

The STA approach law for Z-inductor stream regulator can be given as :

$$V^*_{Lz} = -k_{i_{Lz}}\sqrt{|S_{i_{Lz}}|}\,\mathrm{sign}(S_{i_{Lz}}) - \beta_{i_{Lz}}\int \mathrm{sign}(S_{i_{Lz}})\,d\tau \tag{3.71}$$

The control loop for Z-inductor current (i_{Lz}) provides the duty cycle of the ZSI impedance network. Using the second equation from the system 1.10 we can obtain :

$$d = 1 - \frac{1}{V_{pv} - 2V_{Cz}}\left[-k_{i_{Lz}}\sqrt{|S_{i_{Lz}}|}\,\mathrm{sign}(S_{i_{Lz}}) - \beta_{i_{Lz}}\int \mathrm{sign}(S_{i_{Lz}})\,d\tau\right] \tag{3.72}$$

STA-based ZSI AC side control with ID-ZSVPWM-MR

This section aims to regulate the output voltage of the ZSI to its references under the load nonlinearity and its changes. For this purpose, a cascade voltage/current STA controller is adopted to establish reference voltages u^*_m for the PWM block responsible for generating the gate-switching pulses (Sa, Sb, and Sc).

The first linear sliding surface for the ZSI AC side voltage can be expressed as follows :

$$S_{v_{C,dq}} = v_{C,dq} - v^*_{C,dq} \tag{3.73}$$

The STA outer control law of the AC output voltage is given as follows :

$$i^*_{C,dq} = -k_{v_C}\sqrt{|S_{v_{C,dq}}|}\,\mathrm{sign}(S_{v_{C,dq}}) - \beta_{v_C}\int \mathrm{sign}(S_{v_{C,dq}})\,d\tau \tag{3.74}$$

Because the ZSI AC side is similar to the traditional VSI, therefore, according to the first and the second equations from the system 1.9, we can obtain the reference current for the inner loop as follows :

$$i^*_{Ld} = \left[-k_{v_C}\sqrt{|S_{v_{Cd}}|}\,\mathrm{sign}(S_{v_{Cd}}) - \beta_{v_C}\int \mathrm{sign}(S_{v_{Cd}})\,d\tau\right] + i_{od} - \omega C_f v_{Cq} \tag{3.75}$$

$$i^*_{Lq} = \left[-k_{v_C}\sqrt{|S_{v_{Cq}}|}\,\mathrm{sign}(S_{v_{Cq}}) - \beta_{v_C}\int \mathrm{sign}(S_{v_{Cq}})\,d\tau\right] + i_{oq} + \omega C_f v_{Cd} \tag{3.76}$$

The second linear sliding surface for the filter inductor current can be written as

$$S_{i_{L,dq}} = i_{L,dq} - i^*_{L,dq} \tag{3.77}$$

The inner STA control law for the inductor current regulator is given as :

$$v^*_{L,dq} = -k_{i_L}\sqrt{|S_{i_{L,dq}}|}\,\text{sign}(S_{i_{L,dq}}) - \beta_{v_C}\int \text{sign}(S_{i_{L,dq}})\,d\tau \tag{3.78}$$

Because the ZSI AC side is similar to the traditional VSI, therefore, according to the first and the second equations from the system 1.9, we can obtain the reference current for the inner loop as follows :

$$u^*_{md} = \left[-k_{i_L}\sqrt{|S_{i_{Ld}}|}\,\text{sign}(S_{i_{Ld}}) - \beta_{i_L}\int \text{sign}(S_{i_{Ld}})\,d\tau\right] + v_{Cd} - \omega L_f i_{Lq} \tag{3.79}$$

$$u^*_{mq} = \left[-k_{i_L}\sqrt{|S_{i_{Lq}}|}\,\text{sign}(S_{i_{Lq}}) - \beta_{i_L}\int \text{sign}(S_{i_{Lq}})\,d\tau\right] + v_{Cq} + \omega L_f i_{Ld} \tag{3.80}$$

The inverse Park transform was used to convert the time-domain direct and quadrature (dq) references to the three-phase (abc) reference frame. This transform preserves the active and reactive powers with the system's powers in the rotating reference frame.

STA-based DC/DC bidirectional converter control

The STA control strategy is implemented in the bidirectional DC/DC converter to ensure optimal management of the stand-alone PV system. Two STA controllers are employed : one to regulate the DC bus voltage and the other to manage the battery current. The voltage control process adjusts the DC bus voltage of the bidirectional DC/DC converter to follow its reference. The output of the voltage loop regulator provides the reference for the battery current to the internal loop current regulator. Ultimately, the current control loop determines the duty cycle of the bidirectional DC/DC converter.

the first linear sliding surface for the ZSI capacitor voltage can be expressed as follows :

$$S_{V_{Cz}} = V_{Cz} - V_{Cz}* \tag{3.81}$$

The STA outer control law of the DC bus voltage of the is given as follows :

$$i^*_{Cz} = -k_{V_{Cz}}\sqrt{|S_{V_{Cz}}|}\,\text{sign}(S_{V_{Cz}}) - \beta_{V_{Cz}}\int \text{sign}(S_{V_{Cz}})\,d\tau \tag{3.82}$$

According to the first equation from the system Equation 1.5, we can obtain the reference current for the inner loop as follows :

$$i^*_{batt} = \frac{VCz}{V_{bat}}\left[-k_{V_{Cz}}\sqrt{|S_{V_{Cz}}|}\,\text{sign}(S_{V_{Cz}}) - \beta_{V_{Cz}}\int \text{sign}(S_{V_{Cz}})\,d\tau - i_{Lz} + ioe\right] \tag{3.83}$$

The second linear sliding surface for the battery inductor current is written as :

$$S_{i_{batt}} = i_{batt} - i^*_{batt} \tag{3.84}$$

The inner STA control law for the inductor current regulator is given as :

$$V^*_{bat} = -k_{i_{batt}} \sqrt{|S_{i_{batt}}|}\, \text{sign}(S_{i_{batt}}) - \beta_{i_{batt}} \int \text{sign}(S_{i_{batt}})\, d\tau \tag{3.85}$$

The control loop for filter current (i_{batt}) provides the duty cycle α of the bidirectional DC/DC converter. Using the second equation from the system 1.5 we can obtain :

$$\alpha = 1 - \frac{1}{V_{Cz}} \left[-k_{i_{batt}} \sqrt{|S_{i_{batt}}|}\, \text{sign}(S_{i_{batt}}) - \beta_{i_{batt}} \int \text{sign}(S_{i_{batt}})\, d\tau - V_{bat} \right] \tag{3.86}$$

Results and Discussion

In this test, the metaheuristic algorithm called self-learning particle swarm optimizer (SLPSO) proposed in [48] is used to adjust the optimal controller parameters taking into account the objective functions given by Equation 3.35 and Equation 3.64. The parameters vector is given by $\theta = [k, \beta]^T$.

The values of the physical parameters of the overall PV battery system are presented in Table 3.12.

Table 3.12 – Physical parameters of stand-alone Z-source PV system using STA control

C_z	L_z	L_{bat}	C_f	L_f	C_L	L_l
4.5 mF	10 mH	10 mH	80 μF	10 mH	490 μF	90 μH

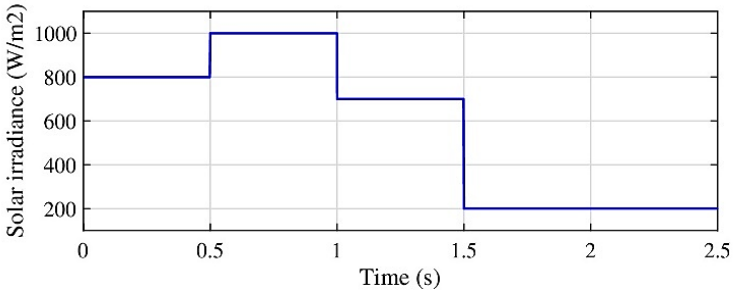

Figure 3.35 – Irradiation profile

Figure. 3.36 shows that the PV power controller achieves the MPPT in both algorithms, PI and STA. The voltage varies slightly, contrary to the PV current, which changes following irradiation to reach the MPP position. The increase in irradiation implies an increase in PV current and the corresponding power created, and vice versa. In contrast, the STA approach presents more precision and response time advantages. In the transient response, it follows the reference variation more quickly and it reduces the static errors in the steady state better. However, the conventional PI regulator introduces undesirable transient response and ripples to reach the MPP point which is considered a serious

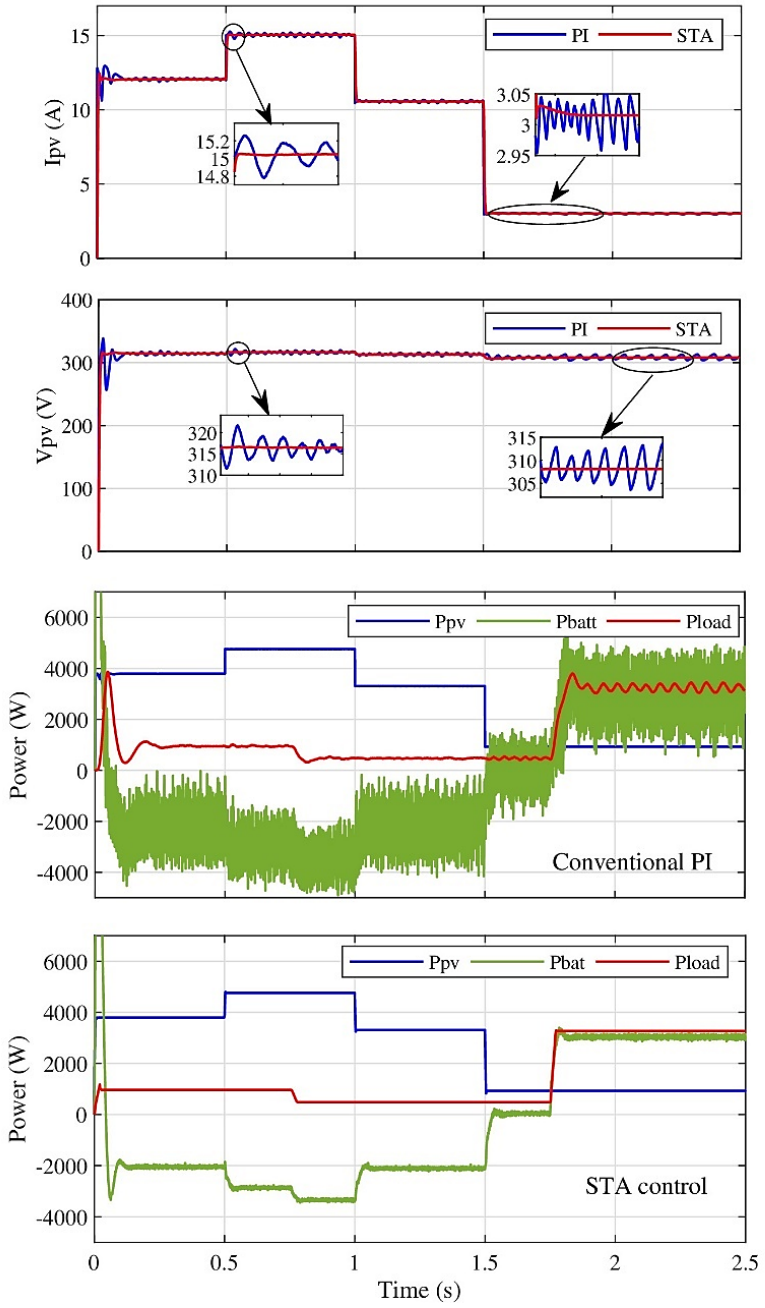

Figure 3.36 – Performance of the STA compared to the conventional PI under fast radiation changes

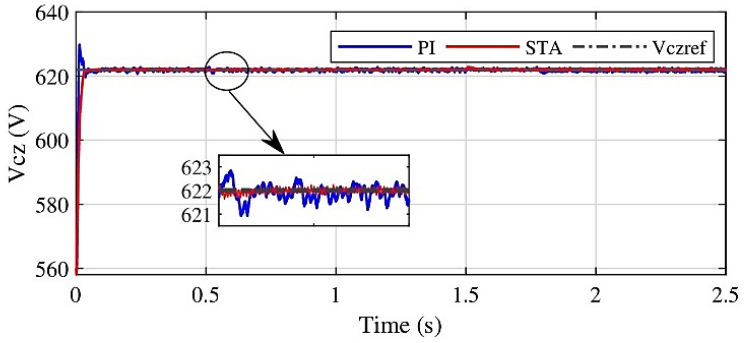

Figure 3.37 – DC bus voltage (Z-capacitor voltage)

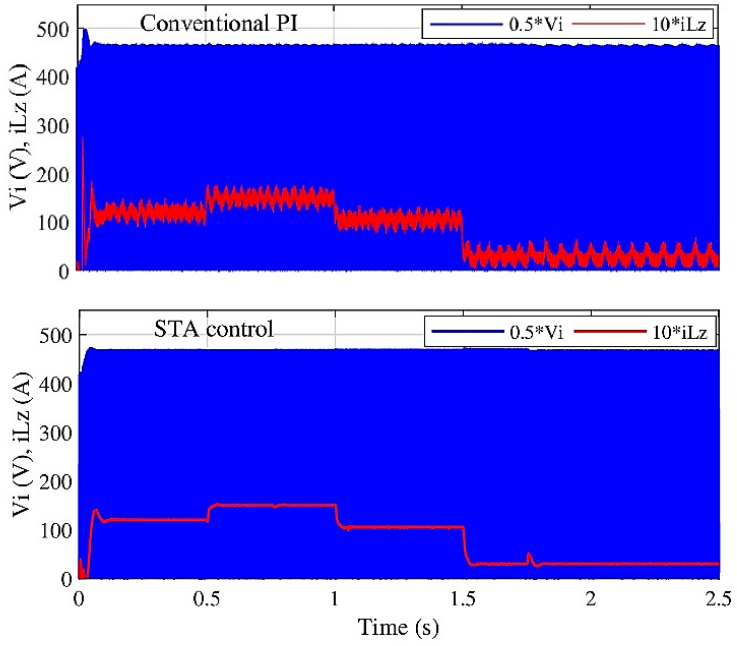

Figure 3.38 – Z-inductance current and DC chain voltage of the ZSI

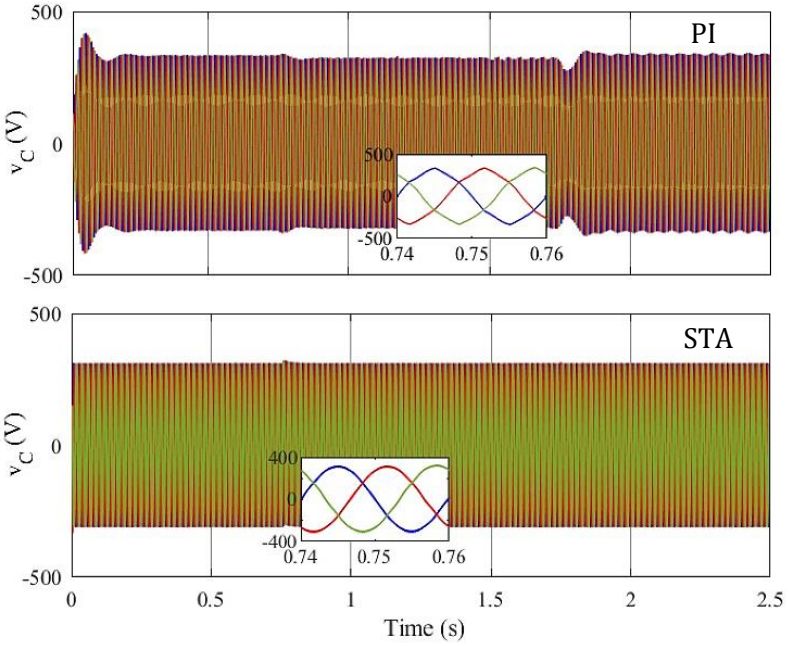

Figure 3.39 – Output voltage under conventional and STA controller

drawback of the PV system, while the STA delivers faster and higher quality MPP tracking, lower overshoot, and ignored ripples which make its dynamic performance better than that of PI in terms of competence, quality and durability.

Although both the STA and PI control units are capable of ensuring the power balance between the PV source, battery, and load by handling DC bus stability represented by the Z-capacitor voltage, obvious oscillations, and large overshoot can be observed under PI compared to the STA, which provides a fast response and ideal power quality in terms of tracking accuracy, reducing ripples and overshoot (see .Figure. 3.37 and Figure. 3.38).

For the AC side, the nonlinear STA control strategy is investigated with a local nonlinear load and compared to the conventional PI controller. From Figure. 3.39, the STA controller yields an output voltage that closely approximates a pure sine wave, whereas the PI controller's output shows significant harmonic distortion and reduced waveform quality. These results verify that the optimized STA can handle the system dynamics by providing perfect and fast disturbance rejection.

3.4.4 Control of stand-alone PV/qZSI system based on FOPID controller

Despite many modern control techniques developed in the literature, the classical PID regulator is still the most widely used to control power electronic converters due to its ease of understanding, simple implementation, and relatively good performance. Currently, the FOPID controller, generalized to the PID controller, has proven effective in improving performance even in critical operating modes [128]. For this reason, considering the changes in irradiation conditions and unbalanced nonlinear load, the FOPID is adopted for the three control stages of a stand-alone PV system based on qZSI shown in Figure. 3.40.

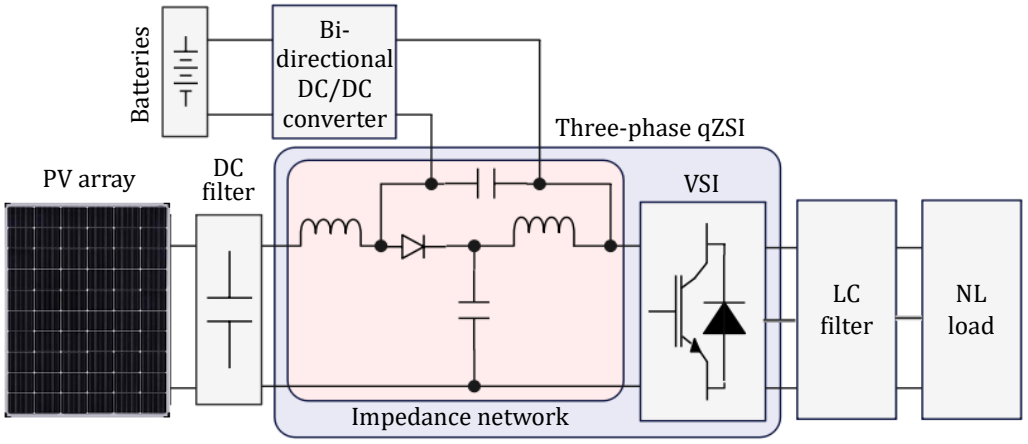

Figure 3.40 – Structure of stand-alone qZSI PV system

The transfer function of the classical PID can be presented as follows :

$$PID(s) = \frac{U(s)}{E(s)} = K_p + \frac{K_i}{s} + K_d s \tag{3.87}$$

where K_p, K_i and K_d are the proportional, integral, and derivative controller parameters, respectively. $U(s)$ is the control signal and $E(s)$ is the error between the desired signal and the measured signal to be regulated.

Using extra non-integer parameters λ and μ respectively as the order of the integral and derivative operators, the general PID model called the FOPID regulator, can be given by the following transfer function :

$$FOPID(s) = \frac{U(s)}{E(s)} = K_p + \frac{K_i}{s^\lambda} + K_d s^\mu \tag{3.88}$$

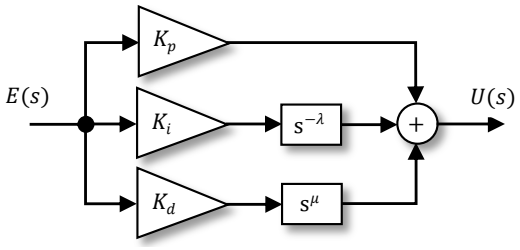

Figure 3.41 – FOPID controller structure

where

$$\{\lambda, \mu \in \mathbb{R}^+ / \ 0 < \lambda, \mu < 2\} \tag{3.89}$$

The transfer function 3.88 corresponds in the time domain to the following fractional order differential equation :

$$u(t) = K_p e(t) + K_i D_t^{-\lambda} e(t) + K_d D_t^{\mu} e(t) \tag{3.90}$$

where $D_t^{-\lambda}$ and D_t^{μ} are respectively the operators of integration and derivative of non-integer order λ and μ.

As shown in Figure. 3.42, the fractional PID controller ($PI^{\gamma}D^{\mu}$) generalizes the classic PID controller and extends it from a point to the plane. This extension provides more flexibility in the design of PID control.

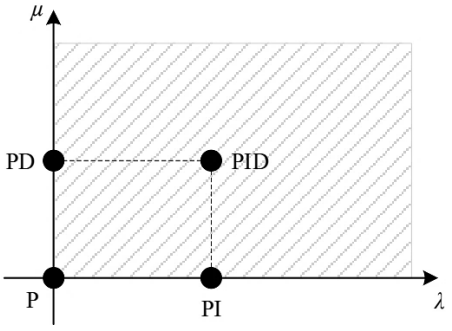

Figure 3.42 – The different PID controllers

Fractional Order Calculs Theory

The fractional order operator is the general form of integration and differentiation operations. There are several definitions in the literature for the fractional operator. But in fact, the most widely recognized definitions are :

Grunwald-Litnikov Definition :

$${}_aD_t^{\alpha} f(t) = \lim_{h \to 0} \frac{1}{h^{\alpha}} \sum_{k=1}^{\frac{t-a}{h}} (-1)^k \binom{n}{k} f(t - kh) \tag{3.91}$$

Riemann & Liouville Definition :

$$ {}_aD_t^{\alpha} f(t) = \frac{1}{\Gamma(n-\alpha)} \left(\frac{d}{dt}\right) \int_a^t \frac{f(\tau)}{(t-\tau)^{\alpha-n+1}} d\tau \tag{3.92} $$

M. Caputo Definition :

$$ {}_aD_t^{\alpha} f(t) = \frac{1}{\Gamma(n-\alpha)} \int_a^t \frac{f^n(\tau)}{(t-\tau)^{\alpha-n+1}} d\tau \tag{3.93} $$

where h is the step time, $(n-1) < \alpha < n$ and Γ stands for the well-known Euler's gamma function, and it is given by

$$ \Gamma(x) = \int_0^{\infty} t^{x-1} e^{-t} dt \tag{3.94} $$

However, due to the inability to numerically implement the above-mentioned fractional differential definitions, the dominant Oustaloup filter is used to approximate the Laplace transform of the fractional derivative operator s^{α}. It is determined by the following rational function :

$$ s^{\alpha} \approx \omega_h^{\alpha} \prod_{k=-N}^{N} \frac{s+\omega_k'}{s+\omega_k} \tag{3.95} $$

The specific parameters of (3.95), poles and zeros are given by :

$$ \begin{aligned} \omega_k &= \omega_b (\omega_h/\omega_b)^{\left(k+N+\frac{1+\alpha}{2}\right)/(2N+1)} \\ \omega_k' &= \omega_b (\omega_h/\omega_b)^{\left(k+N+\frac{1-\alpha}{2}\right)/(2N+1)} \end{aligned} \tag{3.96} $$

where $(2N+1)$ stands for the order of the filter, $\{\omega_b, \omega_h\}$ is the frequency range of the approximation. In the present study, 5^{th} order is chosen for the Oustaloup filter. The low and high frequencies of the approximation range are 10^{-4} and 10^4, respectively.

Results and discussion

The simulation results of qZSI-based stand-alone PV microgrid shown in Figure. 3.43 are presented using MATLAB/Simulink. For this purpose, the FOPID controller is evaluated for the three different control stages : qZSI network-based MPPT control, qZSI AC-side control and bidirectional DC link voltage stabilization, considering the load and the irradiation changes. The optimization problem of the FOPID controller design stands for determining the parameter vector $\theta = [K_p K_i K_d \lambda \mu]^T$. In this study, the parameters of the overall control structure based on FOPID are set using the new yellow saddle goatfish algorithm (YSGA). To converge toward optimal parameters, the YSGA algorithm must be guided by an appropriate objective function to be minimized. In the present study, the objective function 3.35 is used for both DC bus controllers, MPPT and bidirectional converter controllers, while the expression 3.64 is used for the AC bus controller.

Using the physical parameters presented in Table 3.13, the optimal control parameters are calculated and given in Table 3.14.

The simulation results are verified under different irradiation and load demand levels,

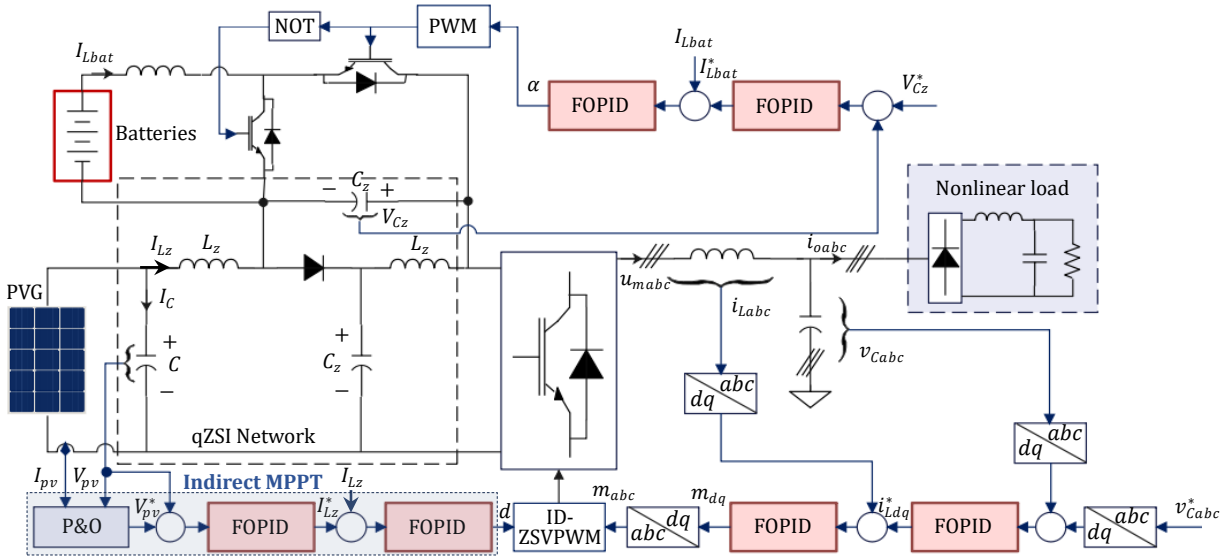

Figure 3.43 – Overall control structure

Table 3.13 – Physical Parameters of stand-alone PV/qZSI system

L_z	C_z	L_{bat}	L_f	C_f	L_l	C_l	R_l
$1.2mH$	$0.35mF$	$0.7mH$	$10mH$	$80\mu F$	$80\mu H$	$490\mu F$	$150/80\Omega$

Table 3.14 – Optimal parameters of FOPID controller

Control stage	FOPID controller parameters				
	K_p	K_i	K_d	λ	μ
qZSI DC-side MPPT $\begin{bmatrix} V_{pv} \\ I_{pv} \end{bmatrix}$	0.529	15.022	$1.87e^{-4}$	0.82	–
	28.21	194.4	$1.87e^{-4}$	1.43	–
qZSI AC-side control $\begin{bmatrix} V_C \\ I_L \end{bmatrix}$	138.45	86.74	8.82	1.02	1.3
	187.15	216.77	6.36	0.71	0.52
Bi DC/DC converter $\begin{bmatrix} V_{Cz} \\ I_{Lbat} \end{bmatrix}$	0.535	15.022	18.7	0.82	0.94
	28.21	194.4	35.25	1.43	1.02

with a sudden change after every 0.5s. The load demand is increased at t = 1s. Against the above changes the performance of the studied optimized FOPID technique is illustrated in Figure. 3.44. The results show that the optimized FOPID-based MPPT algorithm regularly determines the optimal voltage and current values to reach maximum power. The MPP moves proportionally to the irradiation change. The PV current varies after each irradiation step, while the change in voltage value is slight. From the findings, we can observe that the FOPID MPPT controller provides fast and high-quality tracking of the MPP position with low overshoot and negligible ripples compared to the conventional PID command, which proves the robust dynamic performance of the FOPID in terms of efficiency, quality, and durability.

During $t = 0 - 1s$, the findings show that the power produced by the PV generator is greater than the load consumption ($1845W$). Thus, the battery charges the excess power. During $t = 1 - 2s$, the load demand increases to $3380W$, thus imposing a discharge mode

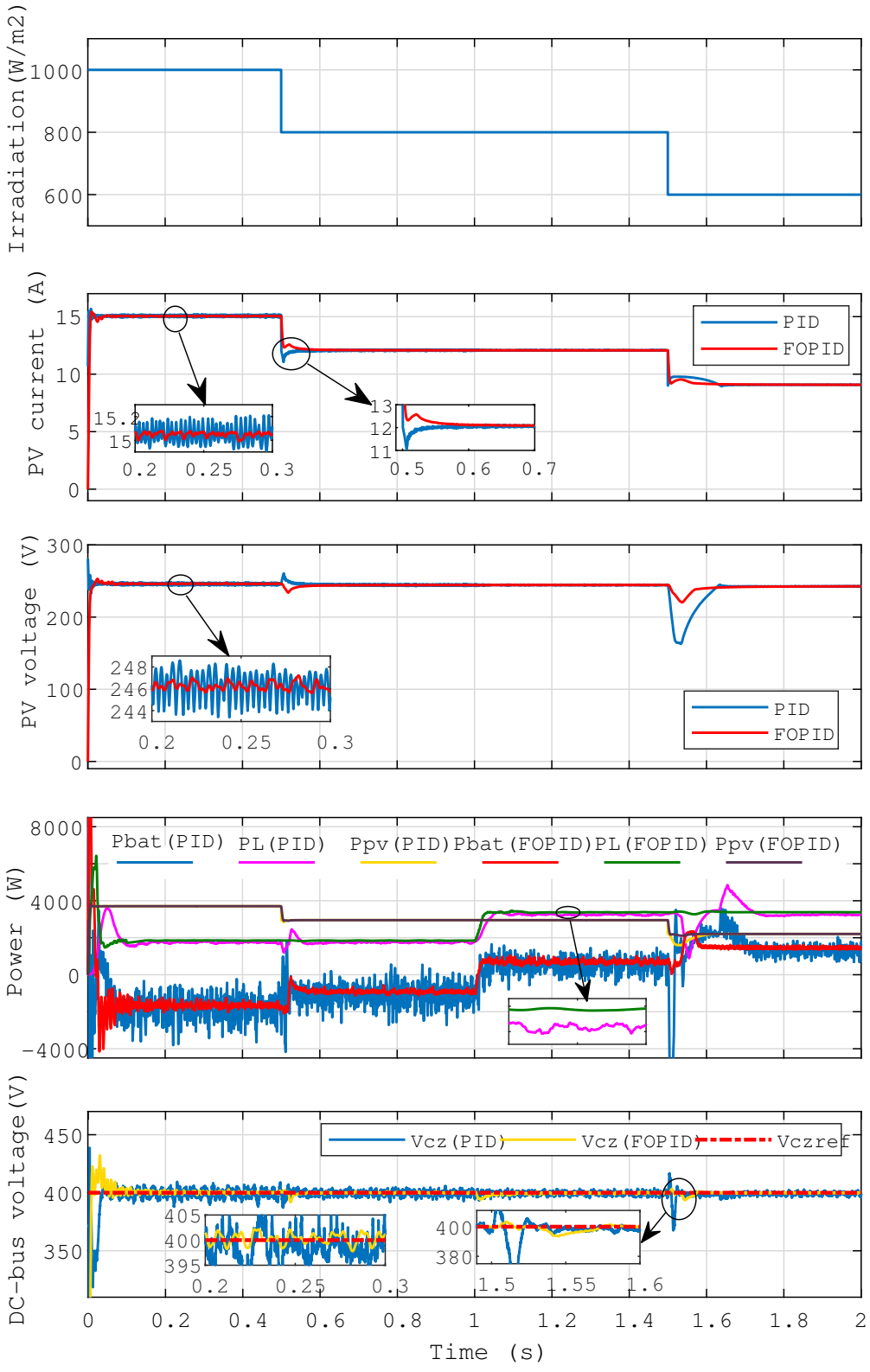

Figure 3.44 – Performance of the FOPID controller compared to the conventional PID controller under varying fluctuations of climatic and load conditions

on the battery to compensate for the missed demand, because the PV generator provides lower power than that of the load. This is what ensures the control of power flow between the different components of the chain with high performance. Likewise, we can clearly

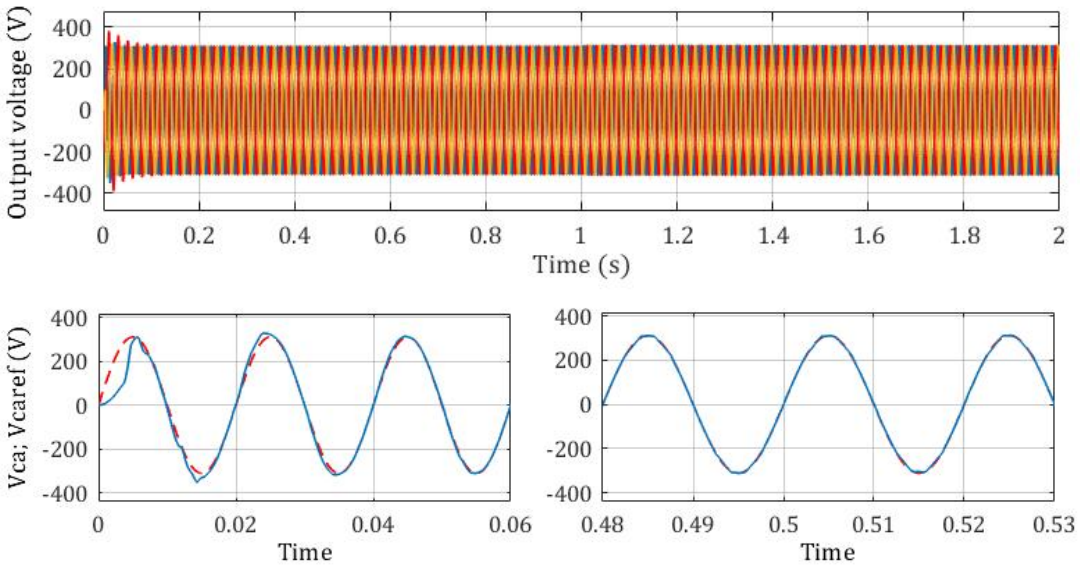

Figure 3.45 – Output AC voltage harmonic analysis

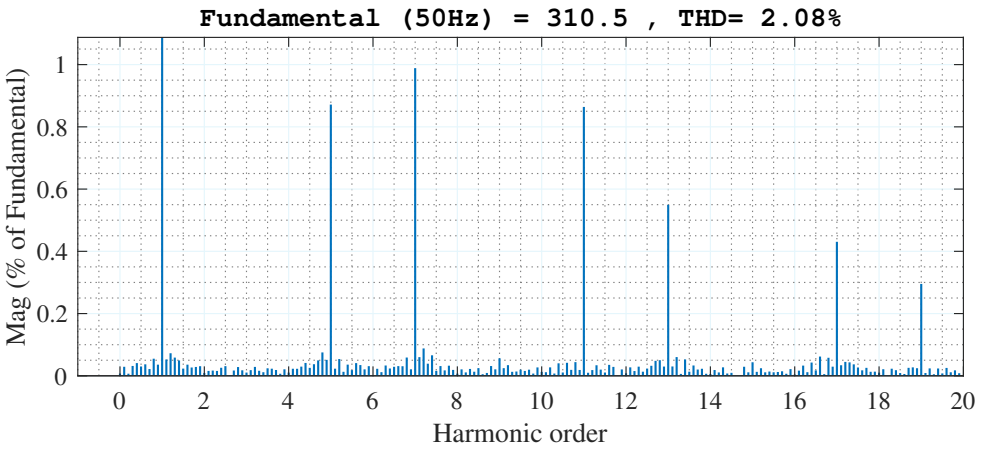

Figure 3.46 – Output AC voltage harmonic analysis

see that the DC bus voltage represented by the qZSI capacitor voltage is rapidly regulated to its imposed reference value. This is what demonstrates the high performance of the FOPID-based bidirectional DC/DC converter controller.

Again, the optimized AC side control based on the FOPID controller proves its reference tracking capability despite the load non-linearity, irradiation fluctuations, and demand changes (see Figure. 3.45). From the output voltage spectral analysis shown in Figure. 3.46, we can see that the FOPID controller can achieve low total harmonic distortion (THD), respecting the standard recommended by IEC and IEEE (less than 5%). This demonstrates that the FOPID controller can handle the stand-alone PV system dynamics by providing perfect and fast disturbance rejection.

3.5 Conclusion

In conclusion, this chapter focuses on the control strategies for distributed renewable energy generation, with particular emphasis on photovoltaic (PV) systems, both grid-connected and stand-alone. Advanced control techniques are developed to ensure efficient energy extraction, stable operation, and reliable integration with the electrical grid or local loads.

The first part addresses grid-connected PV systems, introducing a fractional-order terminal supertwisting algorithm (FOTSTA)-based MPPT, robust PV power control, and advanced voltage-source inverter (VSI) regulation, including P-DPC-SVM and anti-windup PI controllers. Stability analyses and simulation results demonstrate the effectiveness of these approaches.

The second part investigates stand-alone PV systems, where power management, operational modes, and control of boost and bidirectional converters for battery energy storage systems (BESS) are presented. Synergetic simplified supertwisting algorithms (SSSTA) are employed to achieve efficient maximum power point tracking and energy balancing.

Finally, the chapter explores the integration of impedance-source inverters (ISI)s, specifically ZSI and qZSI, in stand-alone PV systems, proposing control strategies based on PR, STA, and fractional-order PID controllers. These methods enhance system flexibility, improve voltage and power regulation, and allow seamless coordination between PV generation, storage, and AC loads.

The integration of metaheuristic optimization techniques has played a crucial role in optimizing control performance, allowing the calculation of control parameters to ensure a robust response under varying conditions.

Through systematic modeling, control design, and results discussion, this chapter demonstrates the potential of modern control techniques to optimize distributed renewable energy generation for both grid-connected and autonomous applications.

Chapter 4

Hierarchical control for parallel distributed generation in microgrids

4.1 Introduction

Microgrids represent a critical component of modern energy systems, offering enhanced flexibility, resilience, and integration of distributed generation (DG) resources. Efficient operation of a microgrid, particularly in both grid-connected and islanded modes, necessitates a structured control approach to ensure stable, reliable, and optimal performance. This chapter delves into the hierarchical control architecture for microgrids, with a focus on the integration of key control strategies designed to achieve voltage and frequency stability, power-sharing, and grid synchronization. The hierarchical control framework for microgrids is typically structured into three layers : inner control, primary control, and secondary control. At the foundation lies the **inner control**, which is responsible for implementing cascade control of DG voltage and current. This layer ensures the fast dynamic response of the power converters and provides robust regulation of the local system variables.

Building upon the inner control, the **primary control** layer employs droop controllers to facilitate decentralized power-sharing among DG units. This droop-based mechanism dynamically adjusts output power based on frequency and voltage variations, enabling seamless load power sharing among DG inverters that are connected in parallel, but on the conditions that they have the same output impedance. Furthermore, the scheduled active and reactive power is injected when the microgrid is connected to the main grid. The decentralized structure of the droop control technique offers desirable properties such as extensibility, modularity, and flexibility. This is what encourages researchers to develop it to overcome challenges and improve its performance, to be robust and more flexible during various operating modes. In [43], a robust controller called universal droop control (UDC) is developed to operate in islanded mode regardless of the output impedance of the DG inverters. On the other hand, although the UDC can also operate in grid-connected mode as in islanded mode, it remains unable to transfer its operating mode from islanded to grid-connected operation due to the lack of synchronization between microgrid and utility grid voltages. For this reason, the UDC is improved it by

introducing a derivative term to enhance the transition response and a hybrid term to distinguish between different mode of operation.

The **secondary control** layer enhances system performance by restoring voltage and frequency to nominal values after deviations introduced by primary control. Additionally, it manages synchronization with the grid voltage when the microgrid operates in a grid-connected mode or transitions from islanded operation. Through secondary control, the microgrid achieves a balance between decentralized operation and coordinated restoration of global system parameters. In order to maintain the stability and improve the flexibility of the microgrid, a simple management strategy is proposed as a **tertiary control** layer dedicated to the secondary control loops : restoration and synchronization loops, as well as to the static switch (SS).

This chapter provides a detailed analysis of each hierarchical layer, outlining the principles, methodologies, and practical considerations for their implementation. Special emphasis is placed on the interplay between control layers to ensure overall system stability and performance. By integrating advanced control techniques, this hierarchical framework enables microgrids to operate as robust, adaptable, and efficient systems in the evolving energy landscape.

4.2 Decentralized primary control

The main objective of the primary control is to achieve accurate power sharing between the islanded parallel DG inverters and scheduled power injection from them when they operate in grid connected mode, ensuring a smooth transition between different mode of operation [45, 46].

4.2.1 Fractional order universal droop controller

Modern control techniques allow improving the control systems performance and robustness such as the fractional order control. The primary control implemented in this chapter is based on the universal droop mechanism improved by introducing a fractional-order derivative term [46]. the extra term is used to enhance the transient dynamic performance of the microgrid.

Since the conventional UDC can be expressed as follows [43] :

$$\dot{E} = K_e(E^*_{MG} - V_{pcc}) - n(P - P^*) \tag{4.1}$$

$$\omega = \omega^* + m(Q - Q^*) \tag{4.2}$$

The improved UDC can be described by the following expressions [107] :

$$\dot{E} = K_e(E^*_{MG} - V_{pcc}) - n(P - P^*) - n_d D_t^{\mu_1}(P - P^*) \tag{4.3}$$

$$\omega = \omega^* + m(Q - Q^*) + m_d D_t^{\mu_2}(Q - Q^*) \tag{4.4}$$

where E is the calculated magnitude (RMS) value of the output voltage of VSI. ω and ω^*

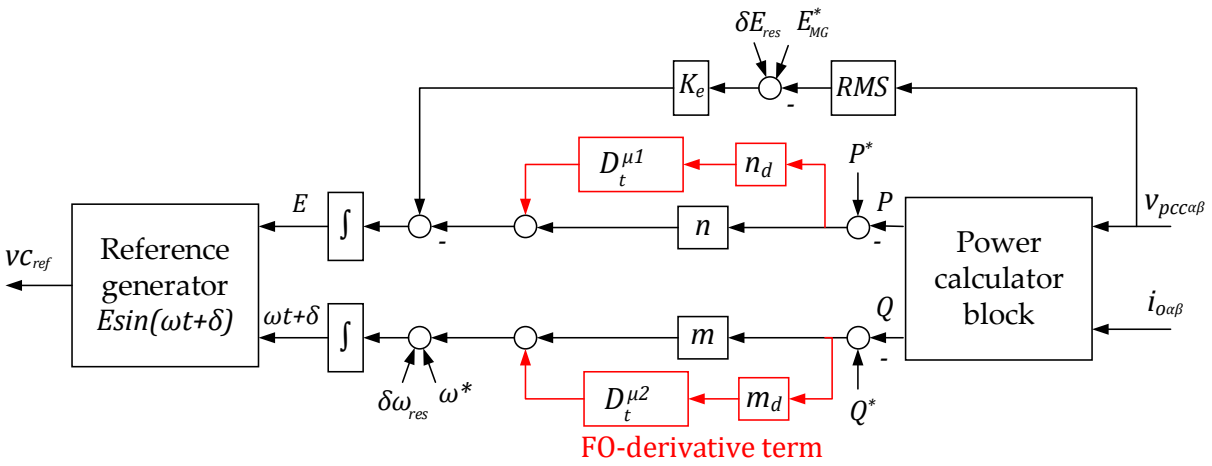

Figure 4.1 – Schematic diagram of the improved primary control in $\alpha\beta$-coordinates

are the calculated and nominal values of its frequency. V_{pcc} and E^*_{MG} are the actual RMS and the nominal value of the PCC voltage. P and Q are the actual active and reactive power of the VSI. P^* and Q^* are their desired values to be injected when the microgrid operates in grid-connected mode. K_e is a positive gain. n and m are the proportional droop coefficients which are related to the desired droop ratio $nS^*/K_eE^*_{MG}$ and frequency boost ratio mS^*/ω^*, respectively. n_d and m_d are respectively the fractional-derivative coefficients. $D_t^{\mu_{1,2}}$ is the non-integer $\mu^{th}_{1,2}$ order derivative operator where $\{\mu_{1,2} \in \mathbb{R}^+ / \ 0 < \ \mu_{1,2} < 2\}$.

The fractional calculus was detailed in Section 3.4.4, and will not be addressed in this chapter. The quantities E and ω generated by the improved UDC represent the magnitude and the frequency of the reference signal to be tracked by the output voltage of the DG inverter in the inner control level at the inner control level discussed in Chapter 3.

Based on $\alpha\beta$ frame, the instantaneous active and reactive power can be expressed as follows :

$$p(t) = v_{pcc,\alpha} i_{o,\alpha} + v_{pcc,\beta} i_{o,\beta} \tag{4.5}$$

$$q(t) = v_{pcc,\beta} i_{o,\alpha} - v_{pcc,\alpha} i_{o,\beta} \tag{4.6}$$

where v_{pcc} is the PCC voltage, i_o is the line current.

On the other hand, depending on the average power P and Q, the instantaneous power can also be described as :

$$p(t) = P + \tilde{p}(t) \tag{4.7}$$

$$q(t) = Q + \tilde{q}(t) \tag{4.8}$$

where $\tilde{p}$ and $\tilde{q}$ are the oscillating components.

The instantaneous power is integrated over one fundamental cycle T in order to obtain the average power P and Q as follows [165] :

$$P = \frac{1}{T} \int_t^{t-T} p(t) dt \tag{4.9}$$

$$Q = \frac{1}{T} \int_t^{t-T} q(t) dt \tag{4.10}$$

Which can be rewritten as :

$$P = F(s).p(s) \tag{4.11}$$

$$Q = F(s).q(s) \tag{4.12}$$

where the integration filter $F(s)$ is given by the following transfer function :

$$F(s) = \frac{1 - e^{-Ts}}{Ts} \tag{4.13}$$

4.3 Centralized secondary control

Central secondary control, often referred to as the central control system, plays a pivotal role in maintaining the operational stability and quality of power in microgrids. Its primary functions include ensuring power quality, mitigating long-term deviations in microgrid voltage and frequency during islanded operations, and aligning the phase angle between the grid and the connected microgrid voltages. Unlike primary control, which operates at a faster time scale to handle immediate stability concerns, central secondary control works on a slower time frame [45, 46]. This decoupling of secondary and primary control processes is intentional, as it reduces interference between the two layers and minimizes the communication bandwidth required for system operation. By determining optimal set points for the primary control, the central secondary control system ensures coordinated and efficient microgrid performance.

4.3.1 Islanded voltage and frequency restoration

By using the UDC method in the primary control, a compensator is required to mitigate the frequency and voltage magnitude deviations created by the droop power-sharing characteristics in the VC-VSIs as shown in Figure. 4.2. Based on the PI controller, both voltage and frequency restoration control laws can be expressed, respectively, as :

$$\delta E_{res} = k_{pE}\,(E^*_{MG} - V_{pcc}) + k_{iE}\int (E^*_{MG} - V_{pcc})\,dt \tag{4.14}$$

$$\delta \omega_{res} = k_{p\omega}\,(\omega^*_{MG} - \omega_{MG}) + k_{i\omega}\int (\omega^*_{MG} - \omega_{MG})\,dt \tag{4.15}$$

where k_{pE} and $k_{p\omega}$ are the proportional controllers parameters, k_{iE} and $k_{i\omega}$ their integral ones.

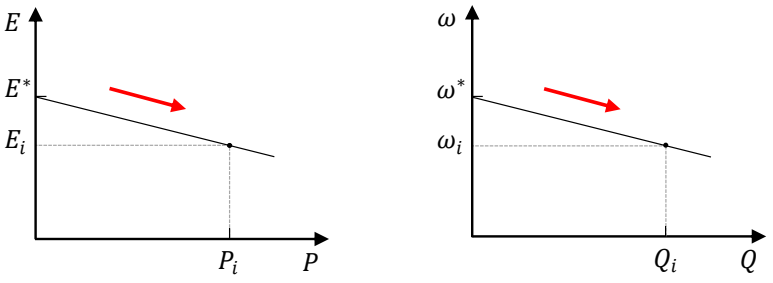

Figure 4.2 – $P - E$ and $Q - \omega$ of droop control characteristics

4.3.2 Synchronization process for smooth transition

In islanded mode, the microgrid may need to reconnect to the main grid to either import power when local demand exceeds the capacity of the paralleled DG inverters or export surplus power. While the amplitude and frequency of the PCC voltage are assumed to be restored to their nominal values, the mismatch in phase angles remains a challenge to ensure a seamless transition. An unplanned or abrupt reconnection could lead to significant circulating currents between the grid and the paralleled DGs. To prevent this, the microgrid voltage must first be synchronized with the grid voltage before activating the SS and transitioning to grid-connected mode [107].

The synchronization controller is given by using $\alpha\beta$ components variables of the PCC and the grid voltages where the following equation must be satisfied :

$$\langle v_{MG\alpha} v_{g\beta} - v_{MG\beta} v_{g\alpha} \rangle = 0 \tag{4.16}$$

For this end, a PI-type command is used for correcting the phase error, where the control law is given as follows :

$$\omega_s = \left(v_{MG\alpha} v_{g\beta} - v_{MG\beta} v_{g\alpha} \right) G_{LPF}(s) G_{syn}(s) \tag{4.17}$$

where :

$$G_{syn}(s) = \frac{k_p s + k_i}{s} \tag{4.18}$$

$$G_{LPF}(s) = \frac{\omega_{LPF} + s}{\omega_{LPF}} \tag{4.19}$$

where k_p and k_i are the PI coefficients, ω_s is the output of the synchronization loop. G_{LPF} is a low-pass filter that is used for low-bandwidth communications to all VSIs operating in parallel. The cutoff frequency is selected as $\omega_o/10$, i.e., one decade below the nominal frequency, to attenuate fast dynamics and high-frequency disturbances while preserving the fundamental phase information.

4.4 Tertiary control

This control level enhances the flexibility of the microgrid and guarantees its stability [46, 107]. A management framework dedicated to both secondary control loops and the static switch (SS) is adopted to allow them to operate autonomously and smoothly during different operating modes. A simple logic sequential algorithm is presented where the logical variables : SC, SYN, and SS are combined and used to activate/ deactivate the restoration loop, the synchronization loop, and the SS switching, respectively.

In order to maintain the stability of the whole system, the primary control must have a faster dynamic than that of the secondary control. In other words, the restoration process can be activated only when the voltage tracking error $e = V_{ref} - V_{pcc}$ has a constant and non-null value with a variation $\delta e = de/dt$ almost zero. ones the tracking error converges

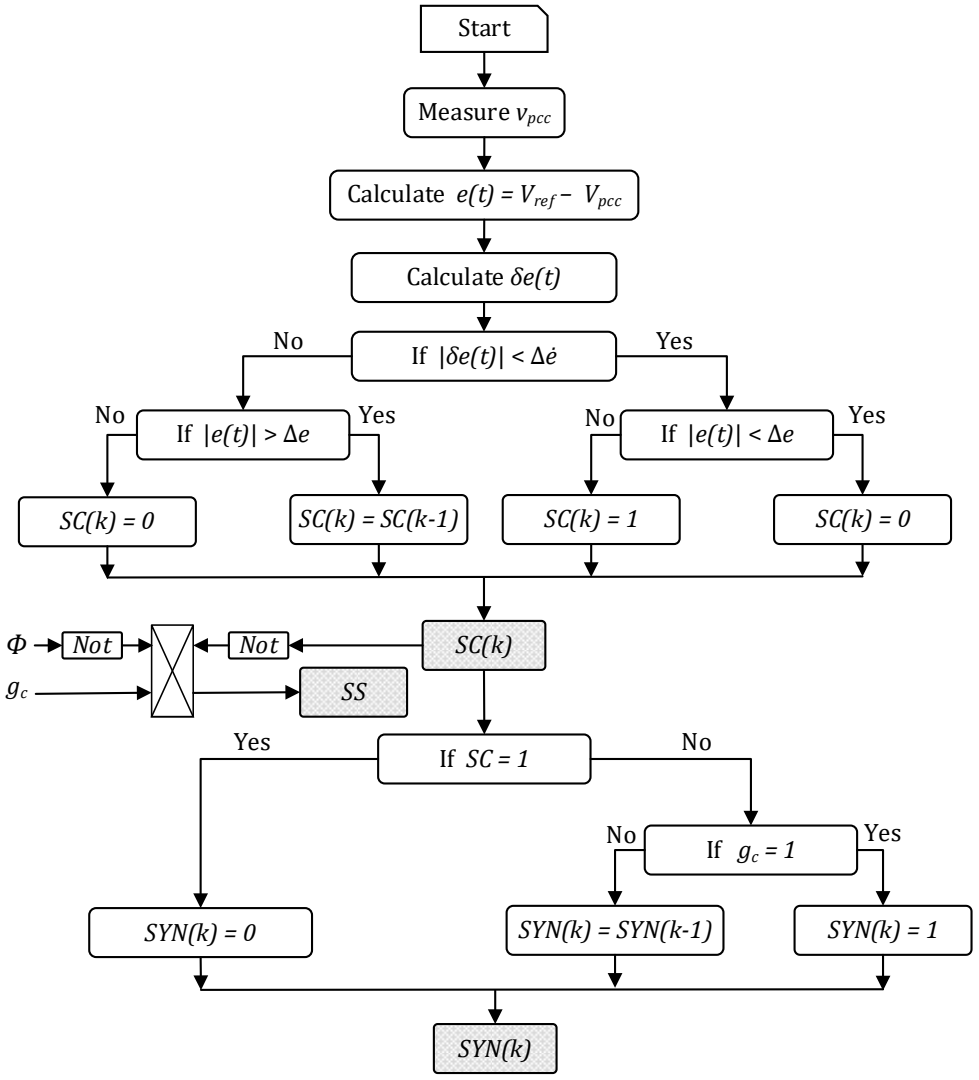

Figure 4.3 – Flowchart showing the tertiary control strategy

to zero (i.e., $e \leq e$), the restoration process is deactivated.

After giving the command to connect the microgrid to the main grid through the binary on/off signal g_c, the corrector of the phase error $\epsilon = \phi_g - \phi_{pcc}$ is turned ON to synchronize the microgrid voltage v_{pcc} with the grid voltage v_g before switching on the connection mode, but under the condition that the restoration process is out of order. Once the voltages are synchronized, the switch SS can be turned ON to connect the microgrid to the grid, where :

$$\Phi = \begin{cases} 0 & \text{if } |\varepsilon| < \Delta\varepsilon \\ 1 & \text{Else} \end{cases} \tag{4.20}$$

The control algorithm of the tertiary level strategy can be summarized by the flowchart given in Figure. 4.3.

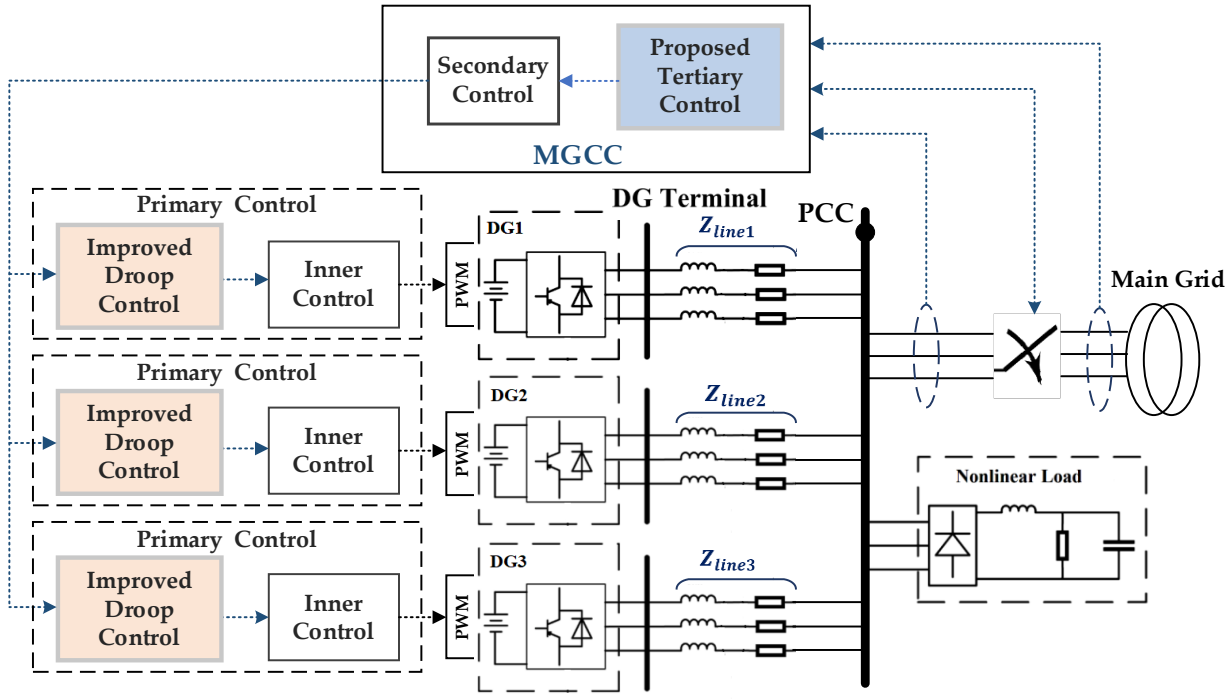

Figure 4.4 – Block diagram of the microgrid hierarchical control

Table 4.1 – Physical parameters of AC Microgrid with three parallel VSIs

Electrical system parameters

Parameter	Symbol	Value	Unit
Rated voltage	E^*	220	V
Nominal frequency	ω^*	$2\pi 50$	rad/s
Load inductance	L_l	84	μH
Load capacitance	C_l	500	μC
Load	R_l	100/140/145/60/150	Ω

VSIs parameters

Parameter	Symbol	Value	Unit
DC voltage	V_{dc}	650	V
Filter inductor	$L_{f1,2}; r_{1,2}$	1.8 ; 0.03	mH ; Ω
Filter capacitor	$C_{f1,2}$	35	μC
PWM frequency	f_s	10	kHz
Output impedance	Z_o	Z_{o1} : 2.8 ; 0.7 Z_{o2} : 1.7 ; 0.5 Z_{o3} : 1.6 ; 0.8	mH ; Ω mH ; Ω mH ; Ω
Apparent power rating	S	1250/2000/2500	VA

4.5 Simulation results

Simulations are performed by using FOMCON Toolbox and MATLAB/Simulink for the AC Microgrid illustrated in Figure. 4.4 in order to test the feasibility of the proposed four-level hierarchical control and compare its performance with the conventional three-

Table 4.2 – Hierarchical control parameters

Inner control

	ω_c	k_p	k_r	k_3	k_5	k_7
G_{PR_r}	0.0016	0.25	200.94	26.3	22.56	67.11
G_{PR_i}	0.0016	0.1925	221.02	40.29	98.17	61.04

Conventional droop control ($\mu_1 = \mu_2 = 1$)

	K_e	k_{pP}	k_{pQ}	k_{dP}	k_{dQ}	n_g	m_g
VSI_1	11.6	0.2890	2.5×10^{-4}	0.0019	2.8×10^{-6}	0.03	5.1
VSI_2	11.6	0.1089	1.6×10^{-4}	0.0039	3.3×10^{-6}	0.03	5.1
VSI_3	11.6	0.0871	1.3×10^{-4}	0.0046	1.7×10^{-6}	0.03	5.1

Fractional order droop control

	K_e	k_{fpP}	k_{fpQ}	k_{fdP}	k_{fdQ}	μ_1	μ_2
VSI_1	13	0.3222	2.5×10^{-4}	0.0025	7.18×10^{-7}	1.135	1.35
VSI_2	13	0.2014	1.6×10^{-4}	0.0014	9.05×10^{-6}	1.154	0.88
VSI_3	13	0.1611	1.3×10^{-4}	0.0038	7.89×10^{-6}	0.961	0.97

Secondary control

	Voltage loop	Frequency loop	Synchronization
k_p	1.8815	2.2586	3.8
k_i	4.2972	7.708	0

level control scheme proposed in [45]. The test microgrid consists of three VSI-based DG units connected in parallel to a local nonlinear load through a LCL filter and an output impedance Z_o [107].

The hierarchical control's optimal parameters are calculated using the metaheuristic self-learning particle swarm optimizer (SLPSO) algorithm, which is based on the minimization of the selected objective function. The optimization problem of the control design stands for determining the parameter vector of :

— The proposed FO-UDC : $\theta = [K_e, n_d, m_d, \mu_1, \mu_2]^T$
— The PI controller-based secondary control $\theta = [k_p, k_i]^T$

In order to increase the robust performance such as the overshoot limitation, the recent objective function proposed in [45] is used for the proposed droop control and secondary control, where :

$$OF = \sum_{k=0}^{N} k|e_k(\theta)| \left[1 + \eta - \eta sign(e_k(\theta) + OS.y_{ref}\right] \tag{4.21}$$

where e_k is the error of k^{th} sample between the reference and the measured value of the controlled signal $(e = y_{ref} - y)$, θ is the controller parameters, OS is the desired overshoot and the constant η is used to limit the oscillations.

Using the physical parameters presented in Table 4.1, the optimal control parameters are calculated and given in Table 4.2, where $\eta = 50$, $\delta = 0.2V$, $\delta\dot{e} = 4V/s$, $N = 2$ and $[\omega_b, \omega_h] = [10^{-2}, 10^3]$.

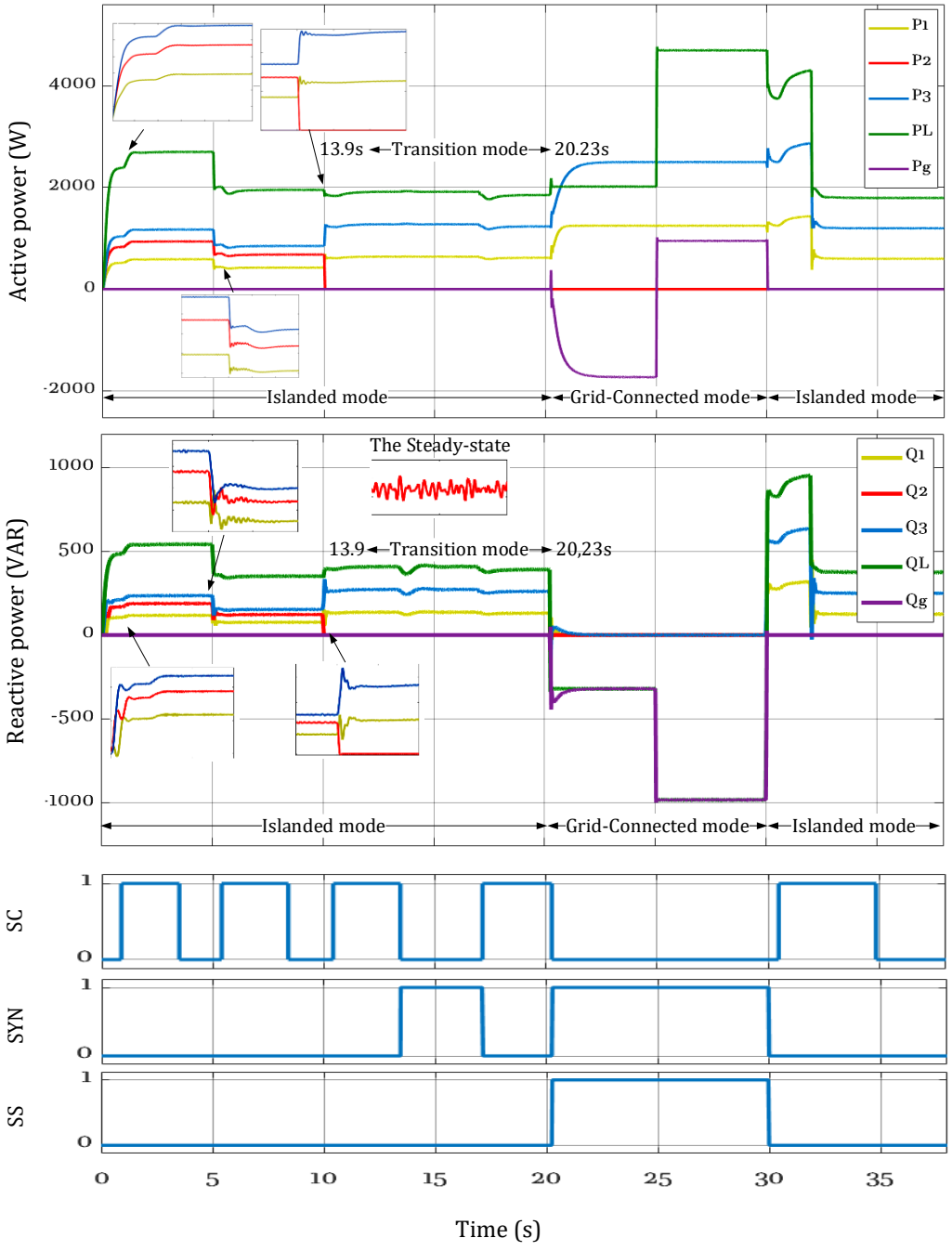

Figure 4.5 – Performance of the conventional power sharing

In order to validate the improved droop control presented in this section, as well as the tertiary-level strategy, different scenarios are simulated. After the islanded microgrid starts operating, the load demand decreases at $t = 5s$, leading to a reduction in the power supplied by the three connected DGs. The disconnection of the second DG (VSI_2), at $t = 10s$ is also simulated. For a smooth transition from islanded mode to grid-connected mode, the binary signal g_c is transmitted to the tertiary control at $t = 12s$ to activate the synchronization process in order to eliminate the phase error between the PCC and main grid voltages. However, by according to the strategy proposed in the tertiary level, the synchronization process only works when the PCC voltage is restored, at $t = 13.9s$ by

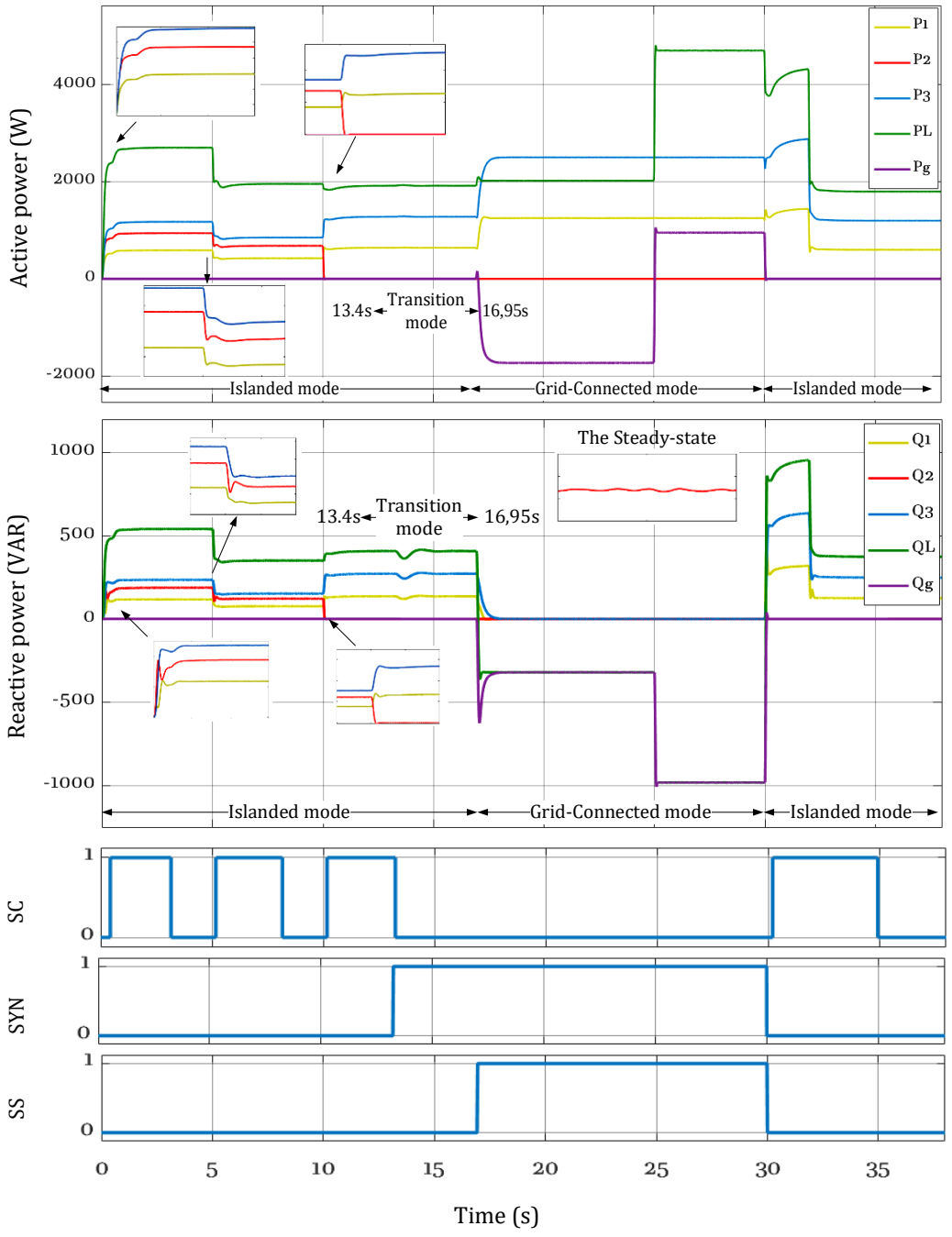

Figure 4.6 – Performance of the proposed fractional order power sharing

using the classical droop control and at $t = 13.4s$ by using the order-fractional one.

In Figure. 4.5, it is shown that by using the classical droop control, another load variation test is simulated at $t = 17s$, which makes the synchronization loop out of order, to complete the restoration of the PCC voltage. While, the non-integer order droop control, thanks to its rapidity compared with the classical one, allows the microgrid to connect to the main grid before load variation at t=16.95s (see Figure. 4.5 and Figure. 4.6).

The simulation results demonstrate that, during each transient state, the proposed primary control with a fractional order derivative performs better than the one with the integer order in terms of time response, overshoot, and steady-state oscillations, namely

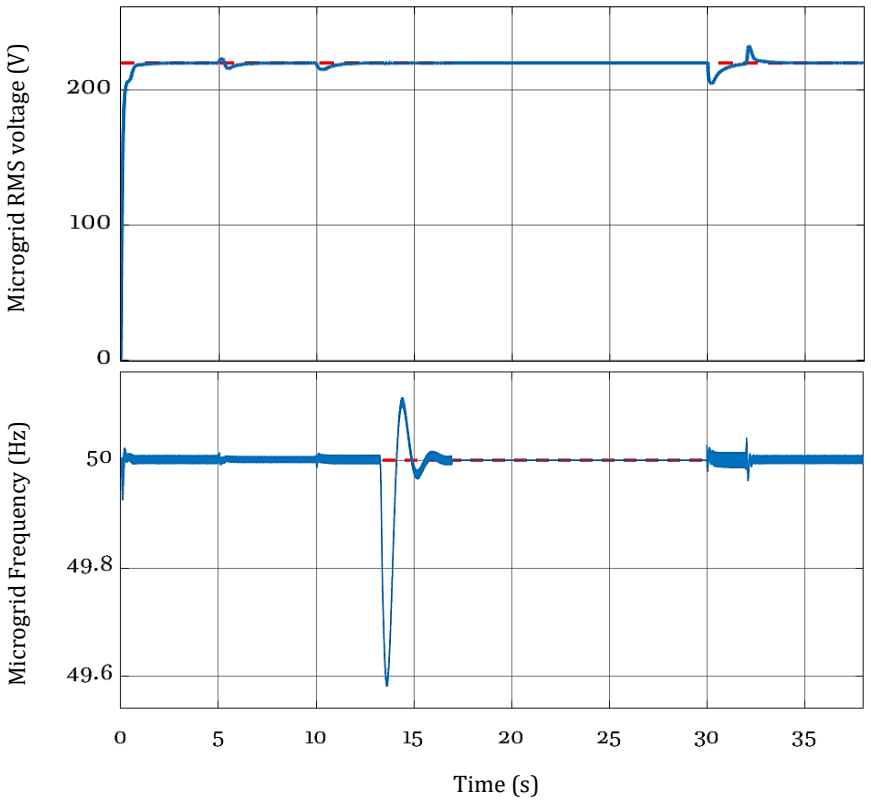

Figure 4.7 – Voltage and frequency of the microgrid voltage

for the reactive power.

The performance of the binary sequential management strategy proposed for the tertiary level is illustrated in Figure. 4.5 and Figure. 4.6. This strategy proves its efficiency to make the secondary controller loops work autonomously, as well as the switch (SS). The restoration controller is started only when the droop control outputs are in steady state. Also, for a smooth transition to the connected-grid mode, the synchronization loop doesn't work until the restoration process is not completed. The switch SS is activated once the PCC and the main grid voltages are synchronized as shown in Figure. 4.6.

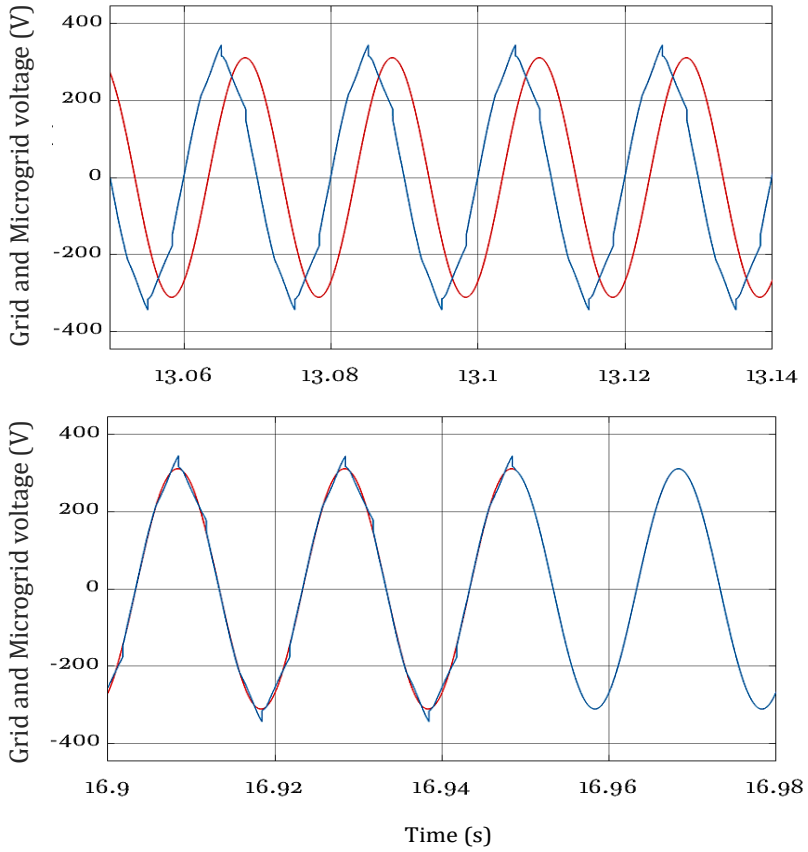

Figure 4.8 – Synchronization process

4.6 Application for a flexible PV/battery Microgrid based on parallel ZSIs

In this section, the optimized hierarchical control structure is investigated for flexible microgrids, including renewable energy resources, energy storage, and local nonlinear load to supply reliable and high-quality during the islanded operating mode and ensure a good power exchange with the main grid during the grid-connected mode [107]. Figure. 4.9 illustrates the topology of the proposed microgrid, where a PV-battery system is used by considering the practical renewable power generation and energy storage instead of a constant power supply as the subgrid DC input. Each subgrid is powered by a PV energy source via a Z-source type inverter, and Its DC bus imaged by the ZSI capacitor is connected in parallel to the BESS via a bidirectional DC/DC converter.

Figure. 4.10 shows the overall control diagram, considering inner control, decentralized power-sharing controllers, and secondary and tertiary central control levels.

In this application, the parameters of the overall control structure are set using the grey wolf optimizer (GWO). The overall system parameters are listed in Table 4.3.

After smoothing the PV output and stabilizing the DC bus voltage at each DG using FO-PI-IP (shown in Figure. 4.11), the performance of the power-sharing strategy with the proposed FO-PI-IP-based AC bus control scheme will be evaluated against a highly nonlinear load considering different microgrid operating modes. As shown in Figure.

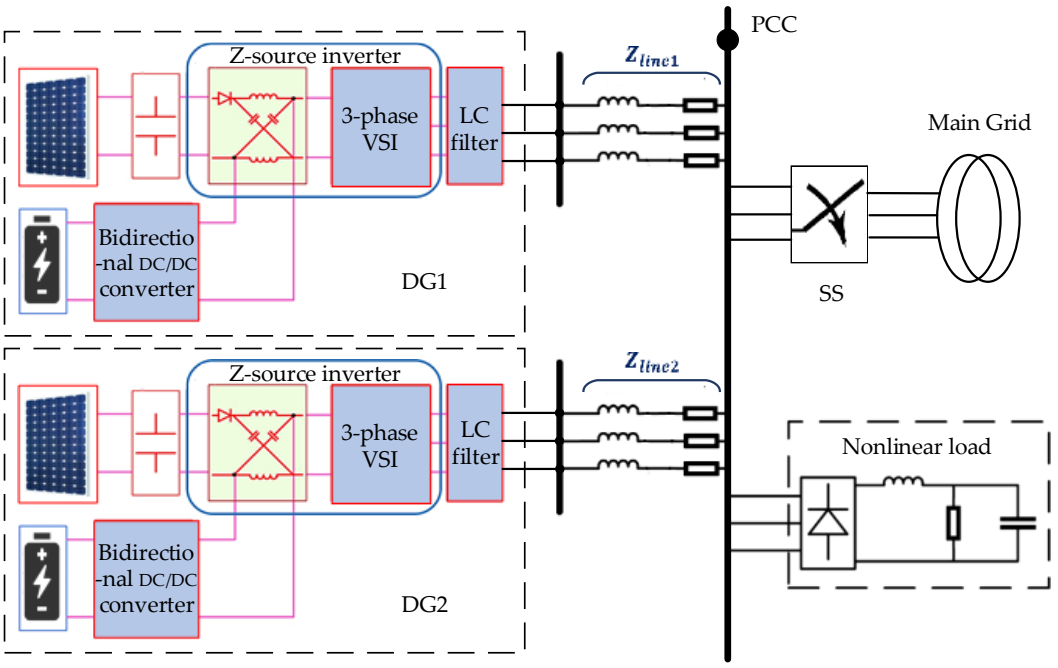

Figure 4.9 – Structure of PV-battery microgrid based on parallel ZSIs

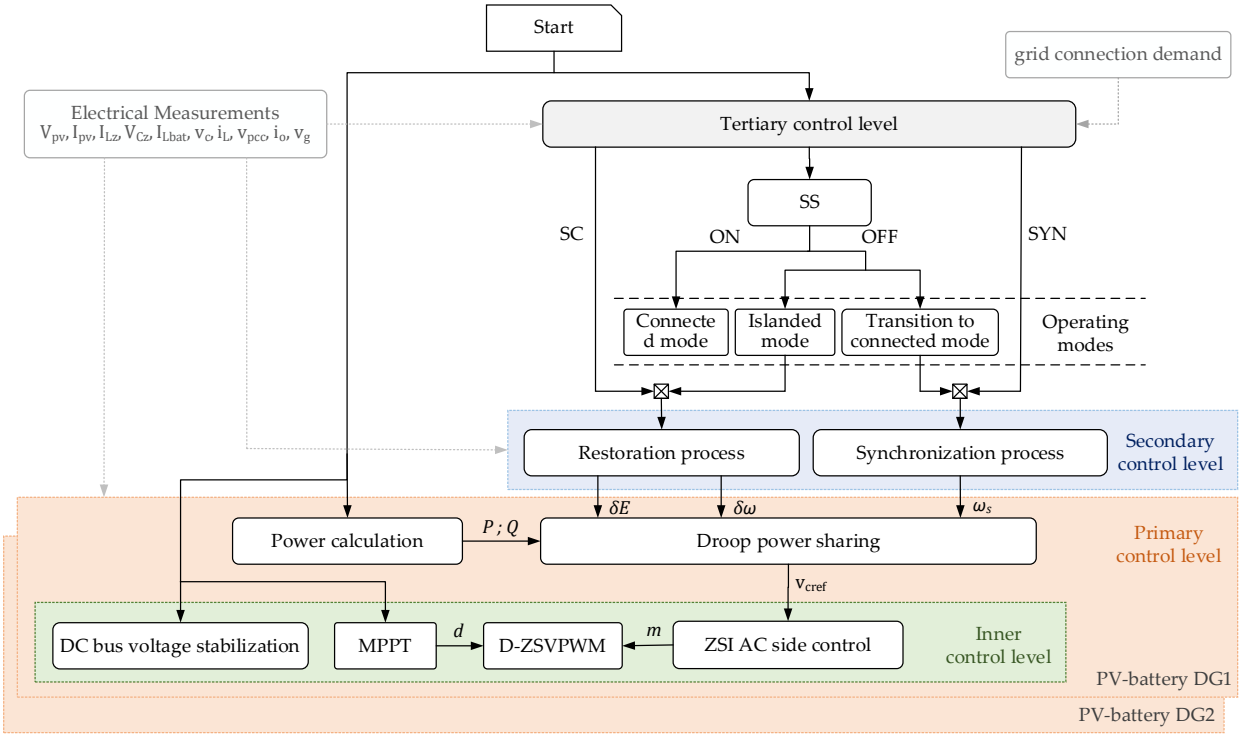

Figure 4.10 – The hierarchical control structure of PV-Battery Microgrid based on ZSIs

4.12, after the black start is successful, the microgrid operates in the islanded mode and both DGs share the local load demand, and then at t=4s, the demand suddenly decreases, which requires reducing the power supply from the parallel PV-Battery DGs. This is why the battery changes its operating mode from discharging mode to charging mode to receive the excess PV power as shown in Figure. 4.11. During the islanded mode, once

Table 4.3 – System parameters of AC Microgrid with two parallel ZSI PV-Battery system

Description	Value
Solar PV	SolarWorld SW135, 4700W (STD)
Battery	Lithium-Ion, 300V, 5kAh
DC rated voltage	V_{CZref}=622V
ZSI DC side	L_z= 10mH, C_z= 4.8mF, f_s= 12kHz
DC-DC converter	L_{bat}= 10mH, f_s= 5kHz
AC rated voltage	E^*=220V
Nominal frequency	$\omega^* = 2\pi 50 \text{rad/s}$
AC bus LC filter	R= 1Ω, L= 10mH, C= 80μF
Output impedance	$Z_{1,2} = \{1.7, 0.8\}$; $\{1.9, 0.5\}$ mH,Ω
Nonlinear load	L_l=80μH, C_l=0.5nF, R_l=35/125/60Ω
Apparent power	$S_{1,2} = 0.82 \times P_{pv_{max}}$
Power sharing	K_e = 13, $n_d = 1.4e^{-3}$, $m_d = 9.05e^{-6}$ μ_1=1.15, μ_2= 0.8
MPPT	K_{p_v}= 0.25, K_{i_v}= 14.711, λ_v= 0.9 K_{p_i}= 364.4, K_{i_i}= 17.5, λ_i= 1.2
AC side control	K_{p_v}= 33.58, K_{i_v}= 194.41, λ_v= 1.1 K_{p_i}= 86.025, K_{i_i}= 9.126, λ_i= 1.05
DC voltage control	K_{p_v}= 1.61, K_{i_v}= 18.54, λ_v= 1.02 K_{p_i}= 26.34, K_{i_i}= 161.5, λ_i= 1.3
Restoration loop	G_E : K_p= 2.018, K_i= 3.981 G_ω : K_p= 1.9902, K_i= 8.102
Synchronization loop	K_p= 5.14, K_i= 0.656

the primary control loop is stabilized, the tertiary control sends the logical command signal SC to activate the restoration loop included in the secondary control level as shown in Figure. 4.13 and Figure. 4.14. The restoration process is deactivated when the static deviations produced by the primary droop control are removed and the voltage is restored, letting only the sharing control operating.

To transfer the microgrid to grid-connected mode, the binary signal gc is sent to the tertiary algorithm at $t = 6s$ to activate the synchronization process, eliminating the phase error between the microgrid and the grid and achieving a smooth transition. However, the synchronization process remains disabled (SYN=0) until the PCC voltage is restored, i.e., SC=0, at $t = 7.8s$. Figure. 4.15 shows the phase error between the microgrid and the grid voltage before and after synchronization. From the findings, the islanded mode can be transferred to the grid-connected mode after a few seconds (about 3s) from the beginning to the end of the synchronization process. Returning to Figure. 4.14. the synchronization process leads to a deviation of the frequency, but the maximum of this deviation is still far from the maximum allowed under Nordel's grid requirements, guaranteeing a smooth transition from islanded to grid-connected mode.

Once the SS is turned on to connect the microgrid to the main grid, the system quickly responds to incremental changes in the DG active and reactive power outputs to be

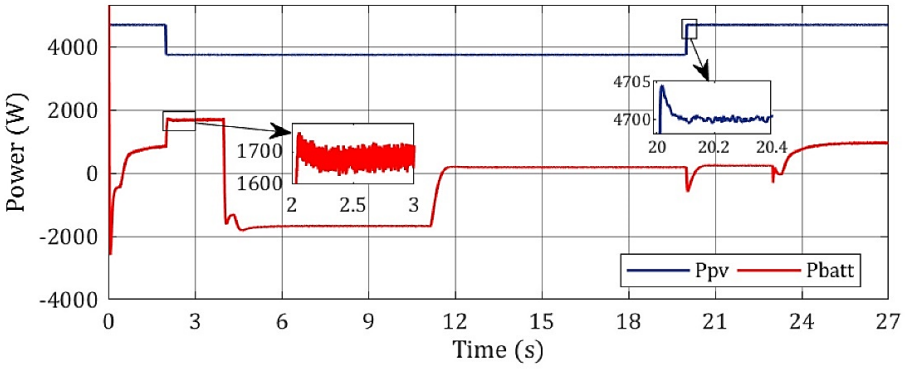

(a)

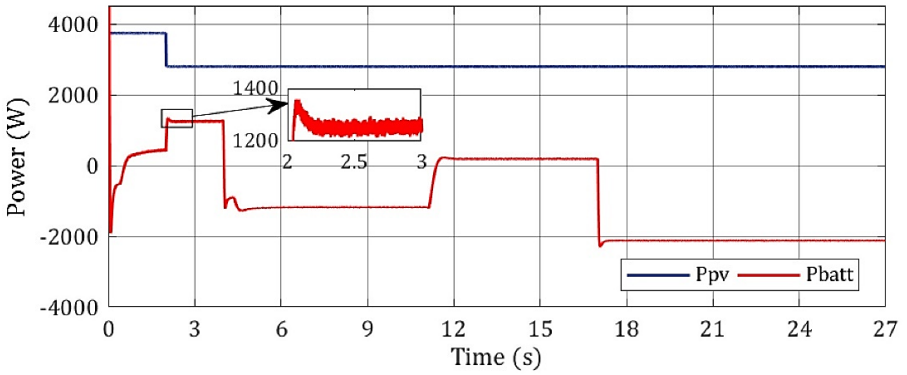

(b)

Figure 4.11 – Power balancing for PV-Battery (a) DG1 (b) DG2

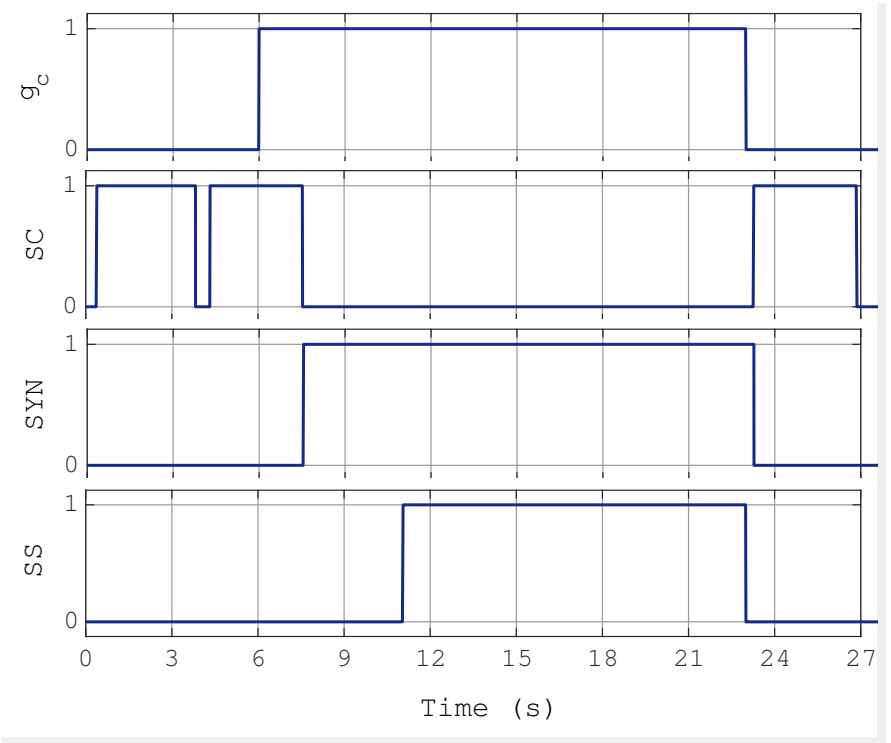

Figure 4.12 – Performance of the tertiary control strategy

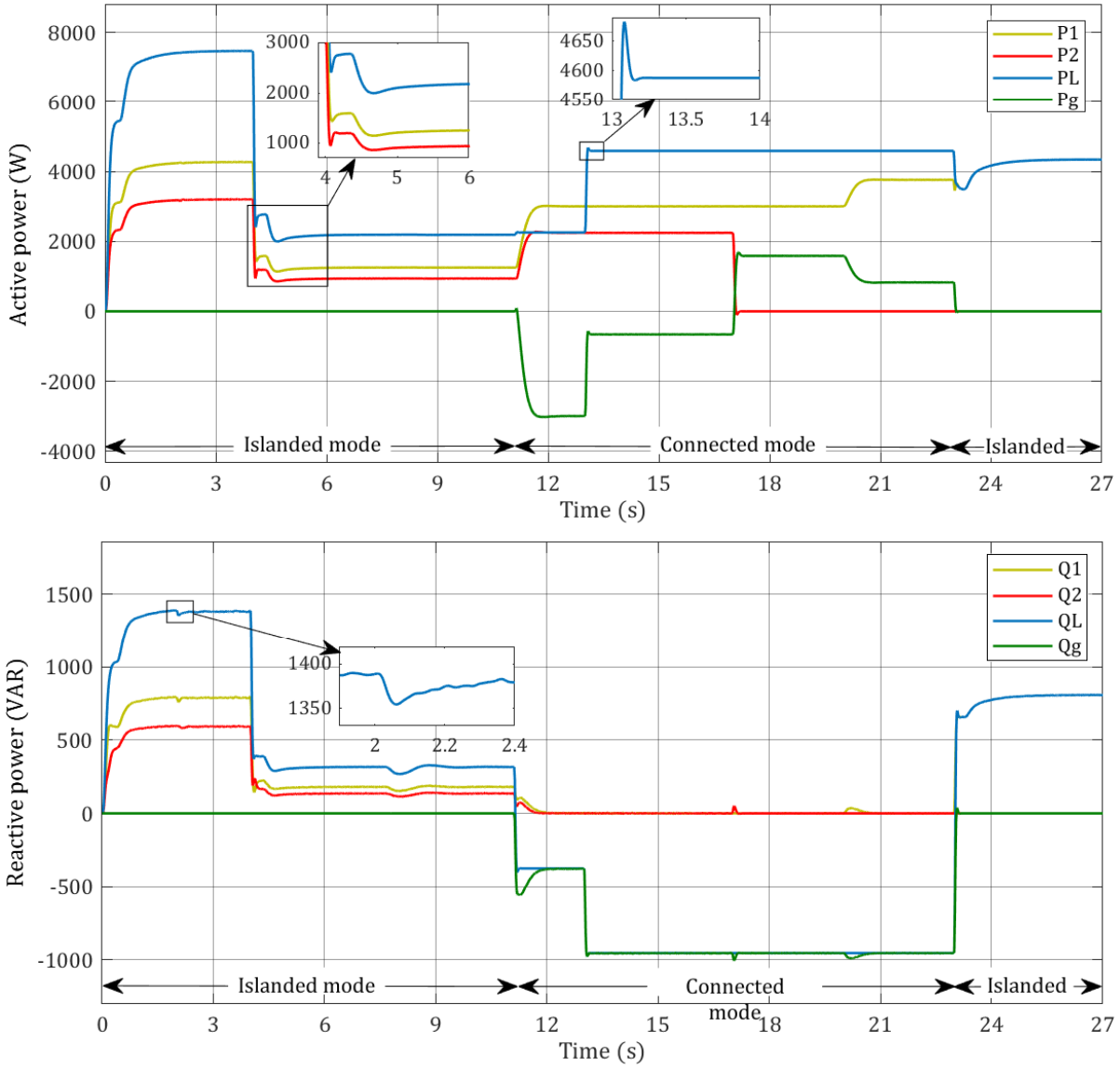

Figure 4.13 – Active and reactive power of the microgrid during different modes of operation

around the desired values P^* and Q^*. In order to inject the maximum possible PV power into the microgrid, the desired active and reactive powers are set at $P^* = 0.82 P_{pv_{max}}(W)$ and $Q^* = 0(VAR)$, respectively, where 0.82 represents the power efficiency of the used ID-ZSVPWM. This is why the power exchange with the battery is stopped in both PV-Battery DGs as shown in Figure. 4.11. In this case, since the power supplied by both DGs together is greater than the power required by the load, the main grid receives excess power. At $t = 13s$, the active power exported to the grid decreases as the local demand increases, while the reactive power of the grid remains at the same rate as that of the load. Then, according to the disconnection of the second DG at $t = 17s$, the direction of the grid power flow changes to meet the missed power since the demand exceeds the power injected from the first DG. The disconnected DG2's battery returns to charging mode to import all the power generated by the PV panel. Afterward, as the generated PV power in the connected DG1 increases at $t = 20s$, following the irradiation behavior, the active power imported from the grid decreases.

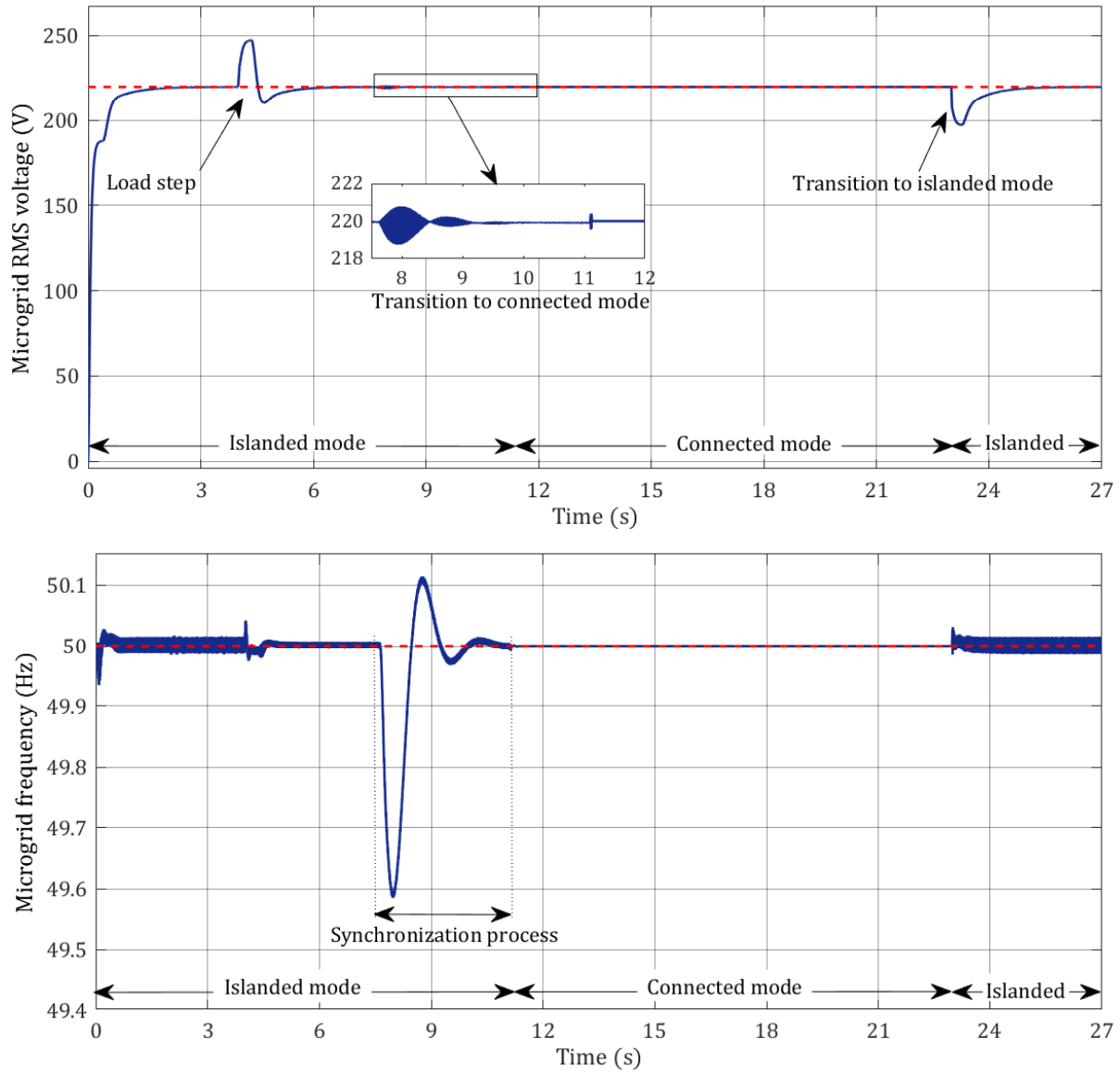

Figure 4.14 – Amplitude and frequency of the Microgrid voltage

At $t = 23s$, the SS is turned off under an external command ($g_c = 0$). The microgrid is disconnected from the main grid and returns to the islanded mode. DG1 changes its power outputs to inject the power demand of the nonlinear load individually, and DG2 is still out of operation. Here comes the role of the DG1 battery to compensate for the difference between the demand and the generated PV power. The restoration process is reactivated (SC=1) after the PCC bus stabilizes to correct the deviation in the amplitude and frequency of its voltage.

Overall, the results reveal a great performance in power-sharing ability during different operating modes. With the proposed control scheme, the major dynamic process of the outpower is rapidly completed with only minimum oscillations, and minimum steady-state power fluctuations can be observed after any change step. The tertiary strategy proves its effectiveness in managing secondary control loops, as well as switching (SS), ensuring the overall stability of the microgrid. The islanded voltage shown in Figure. 4.15

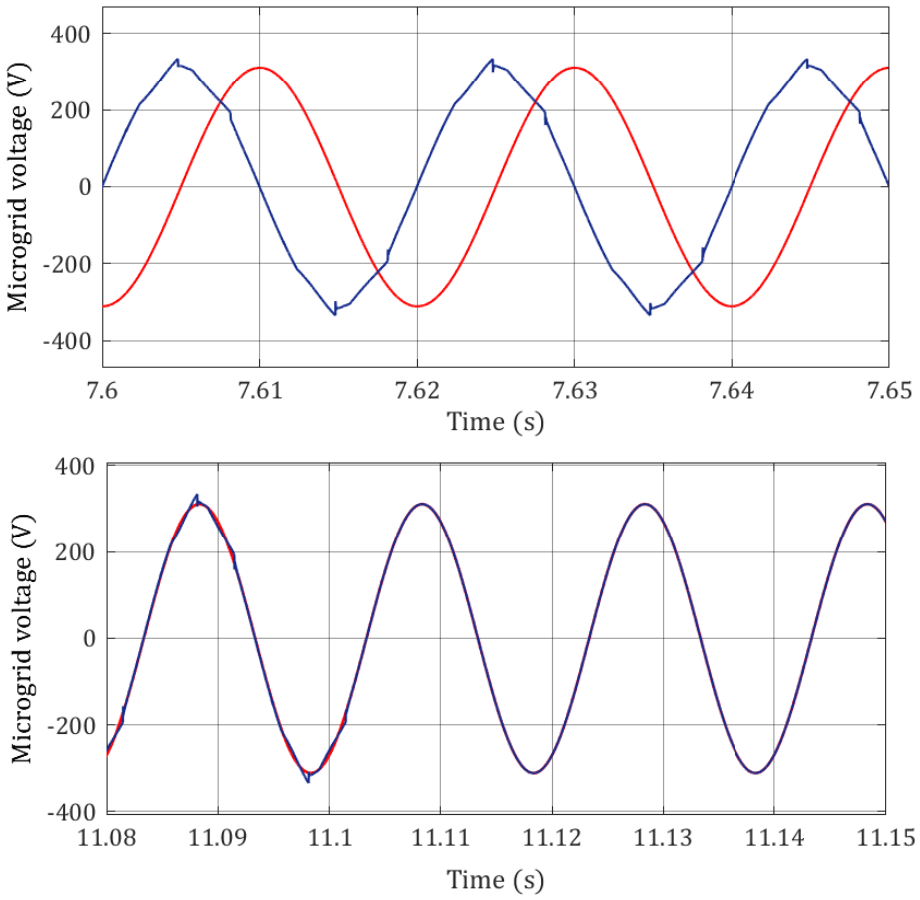

Figure 4.15 – Synchronization process

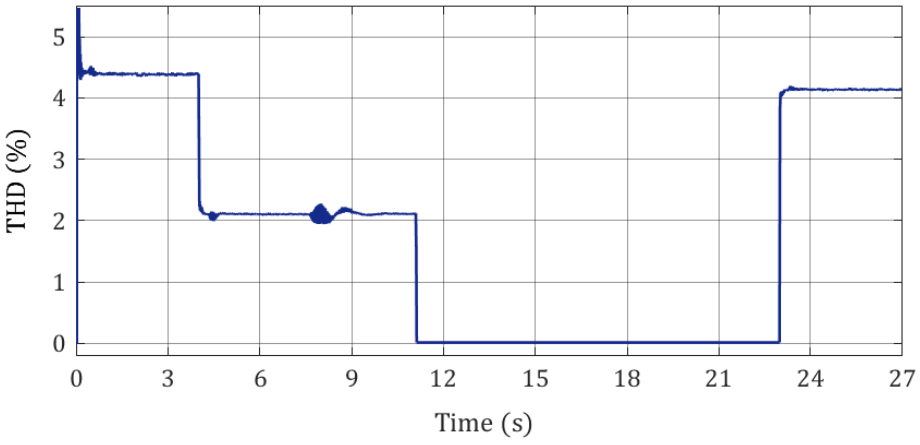

Figure 4.16 – The THD of the PCC voltage

is nearly a pure sine wave, while the connected microgrid voltage is identical to the grid voltage. FFT analysis in Figure. 4.16 confirms the compensation of harmonic components. Throughout the simulation run, where various scenarios have been tested, the last result reveals that the proposed control scheme provides good THD values for the PCC voltage, which remain below 5% as recommended by IEC 61000 and IEEE 519.

4.7 Conclusion

In this chapter, a four-level hierarchical control structure with fractional-order droop control is proposed for a flexible microgrid based on parallel distributed generators (DGs). **The first level**, referred to as the primary control, is based on an improved universal droop control incorporating a fractional-order derivative operator. This level enables accurate load-demand sharing among islanded DGs according to their power ratings. The same power-sharing strategy is maintained during grid-connected operation to inject rated power from the DGs and allow power exchange with the main grid.

The output of the first level serves as the reference voltage for the inner control layer (**zero level**), which is dedicated to cascaded voltage and current control of the VSI through capacitor voltage and inductor current regulation. **The second level** corresponds to the secondary control, where a restoration process compensates for voltage deviations caused by the droop mechanism in islanded mode. In addition, a synchronization process is integrated at this level to ensure seamless transitions between islanded and grid-connected modes.

The third level introduces a management framework that supervises the restoration and synchronization loops as well as the static switch (SS), ensuring overall microgrid stability under different operating conditions. Simulation studies based on metaheuristic optimization algorithms, namely SLPSO and GWO, are conducted to evaluate the proposed control scheme. The results demonstrate outstanding performance, highlighting the strong potential of the proposed approach for practical and flexible microgrids with intermittent renewable sources and varying load demands.

Chapter 5

Decentralized control for parallel distributed generation in microgrids

5.1 Introduction

By using the hierarchical control structure, a MGCC with low-bandwidth communication lines are required to achieve the secondary control functionality. Hence, the price to pay is that this control level may suffer from the inherent characteristics of communication technology such as delays or even data loss which can lead to the breakdown of the whole system. Therefore, to overcome these challenges, a proposed decentralized controller based on a modified UDC is described in this section. Depending on the self-restoration and self-synchronization mechanisms, the proposed controller can handle various operating modes without needing a MGCC unit [166].

5.2 Self-restoration mechanism

During the islanded mode, according to the Equations 4.1, 4.2, 4.14 and 4.15, we can write the combination between the UDC and the secondary control's restoration as follows :

$$\dot{E} = K_e \left(E^*_{MG} - V_{pcc} + \delta E_{res}\right) - nP \tag{5.1}$$

$$\omega = \omega^* + \delta\omega_{res} + mQ \tag{5.2}$$

Laplace transformation of 4.14 and 4.15 gives :

$$\delta E_{res} = \left(k_{pE} + \frac{k_{iE}}{s}\right)\left(E^*_{MG} - V_{pcc}\right) \tag{5.3}$$

$$\delta\omega_{res} = \left(k_{p\omega} + \frac{k_{i\omega}}{s}\right)\left(\omega^*_{MG} - \omega_{MG}\right) \tag{5.4}$$

Substituting 5.3 into 5.1 gives :

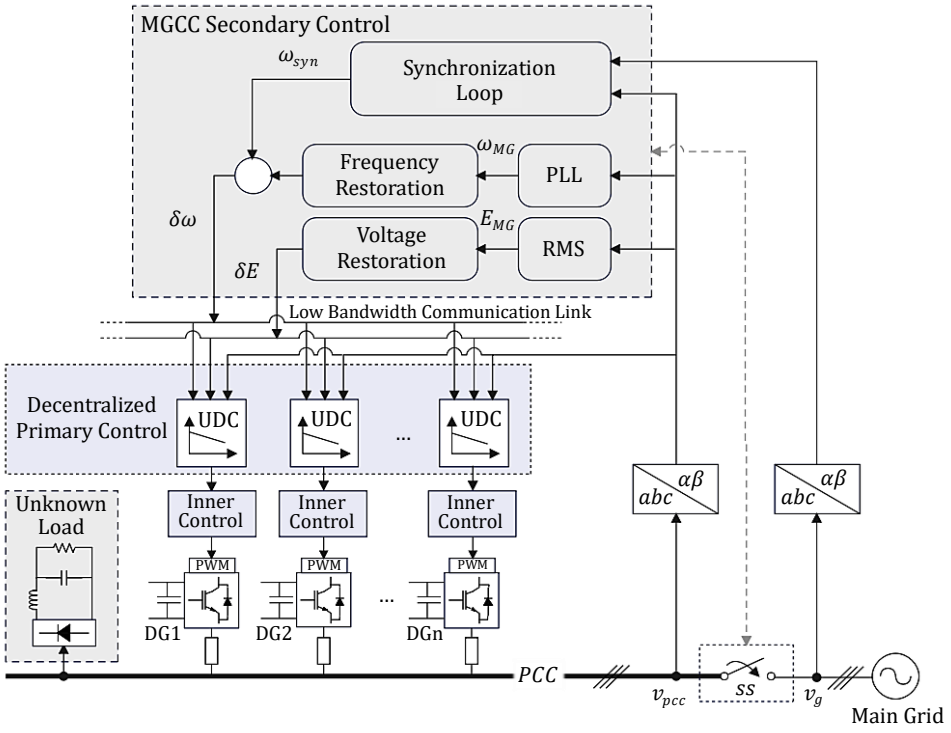

Figure 5.1 – Hierarchical Control Structure of a Microgrid

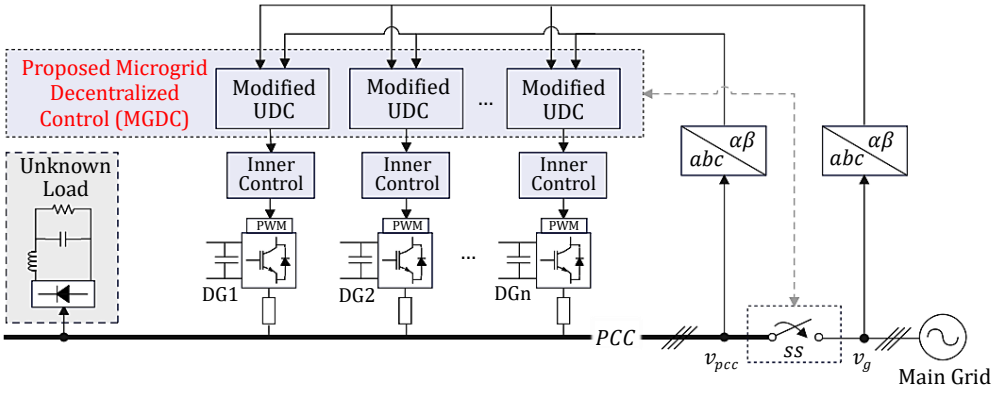

Figure 5.2 – Proposed Microgrid Decentralized Control Structure

$$\dot{E} = K_e \left((1 + k_{pE}) + \frac{k_{iE}}{s} \right) (E^*_{MG} - V_{pcc}) - nP \tag{5.5}$$

As for frequency, as a global quantity in the microgrid, it remains unchanged regardless of where it is measured or changed [167]. Therefore, by substituting 5.4 into 5.2, we can write :

$$\omega = \omega^* + \frac{s}{(1 + k_{p\omega})s + k_{i\omega}} mQ \tag{5.6}$$

Considering $k_{pP} = 1 + k_{pE}$, $k_{iP} = k_{iE}$, $k_Q = 1/k_{i\omega}$, and ignoring the proportional parameter $k_{p\omega}$ ($k_{p\omega} = 0$), the universal droop power sharing control with self-restoration and self-synchronization can be expressed as follows :

$$\dot{E} = K_e G_E(s)(E^*_{MG} - V_{pcc}) - nP \tag{5.7}$$

$$\omega = \omega^* + G_\omega(s)mQ \tag{5.8}$$

where :

$$G_E(s) = k_{pP} + \frac{k_{iP}}{s} \tag{5.9}$$

$$G_\omega(s) = \frac{k_Q s}{k_Q s + 1} \tag{5.10}$$

Compared to 4.1 and 4.2 equations, 5.7 and 5.8 contain extra components $G_E(s)$ and $G_\omega(s)$. These exactly represent the transfer functions of a PI controller and a typical washout filter, respectively [166]. By passing the transient component while blocking the DC component, the washout filter, known as a high-pass filter, can increase the robustness of the power sharing in the face of uncertain parameters [168].

5.3 Fuzzy logic-based self-synchronization mechanism

When the microgrid is in islanded mode operation, it may be necessary to tie into the main grid to export surplus power or to import power if the parallel DG power sources are insufficient to meet the local demand. In order to achieve a smooth transition in the general case, the microgrid voltage vpcc must be synchronized with the grid voltage vg by eliminating the error between them including not only the phase error as 4.16 but also the RMS error value before starting the grid-connected mode, i.e.,

$$\phi_{MG} = \phi_G \quad \text{and} \quad V_{pcc} = V_G \tag{5.11}$$

In order to force the self-synchronization mechanism to start working, according to the voltage error $v_{pcc} - v_g$, a virtual impedance $z_v = Ls + R$ is introduced to generate a virtual current which can be described as follows :

$$i_v = \frac{v_{pcc} - v_g}{Ls + R} \tag{5.12}$$

Being Z_v et ϕ_v magnitude and phase angle of the virtual impedance, the active and reactive powers created through the virtual current i_v can be presented as follows [47] :

$$\begin{bmatrix} P_v \\ Q_v \end{bmatrix} = \begin{bmatrix} \cos\phi_v & \sin\phi_v \\ \sin\phi_v & -\cos\phi_v \end{bmatrix} \begin{bmatrix} \frac{V_{pcc}V_G}{Z_v}\cos(\phi_{MG} - \phi_G) - \frac{V^2_{pcc}}{Z_v} \\ \frac{V_{pcc}V_G}{Z_v}\sin(\phi_{MG} - \phi_G) \end{bmatrix} \tag{5.13}$$

Depending on the used VSI control method, the virtual impedance is usually chosen to be inductive or resistive. Note that the UDC utilized in this study is configured as a droop controller for R-inverters [43], which implies that the impedance is dominantly

Table 5.1 – Table of fuzzy rules for Δk_r

I_v	δI_v		
	Z	S	B
Z	Z	PS	PS
S	Z	PB	PB
B	Z	NS	NB

resistive in nature. Therefore, the virtual impedance is dominantly resistive type, i.e., $\phi_v \approx 0$. Hence, we can rewrite 5.13 as follow :

$$\begin{bmatrix} P_v \\ Q_v \end{bmatrix} = \begin{bmatrix} \frac{V_{pcc}V_G}{Z_v}\cos(\phi_{MG}-\phi_G) - \frac{V_{pcc}^2}{Z_v} \\ -\frac{V_{pcc}V_G}{Z_v}\sin(\phi_{MG}-\phi_G) \end{bmatrix} \tag{5.14}$$

According to 5.14, we can note that the synchronization condition 5.11 can only be achieved when both virtual powers P_v and Q_v are driven to zero. In other words, the current generated through the virtual impedance must be regulated to zero by exploiting the VSI controller.

The total active and reactive powers can be described as :

$$P = P_i + P_v \tag{5.15}$$

$$Q = Q_i + Q_v \tag{5.16}$$

where P_i and Q_i are respectively the actual active and reactive powers delivered by the VSI which are calculated by using the voltage v_{pcc} and the output current i_o of the VSI while the virtual active and reactive powers P_v and Q_v are calculated by using the virtual current i_v.

During the self-synchronization mode, the static switch SS that connects the microgrid to the main grid is still in OFF. Therefore, by using the total current $i_t = i_o + i_v$ as shown in Figure. 5.3, the VSI controller i.e., UDC regulates the virtual current i_v to be zero. This is because there is no power exchange between the microgrid and the grid. Once the current i_v becomes equal to zero, the switch SS can be turned ON to connect the microgrid to the main grid.

Considering that the magnitude error may not be significant, the phase error can lead to a virtual current magnitude that exceeds the rated current several times [48]. This may cause instability in the VSI controller. In this sense, we have enhanced the virtual current by introducing a fuzzy gain k_r varied between $[0, 1]$ depending on its RMS [166]. The RMS current I_v and its derivation δI_v are selected as the inputs of the fuzzy logic controller and Δk_r its output, where :

$$k_r(t) = k_r(t-1) + \Delta k_r \tag{5.17}$$

The fuzzy rules are given in Table 5.1, where Δk_r is calculated by using the following

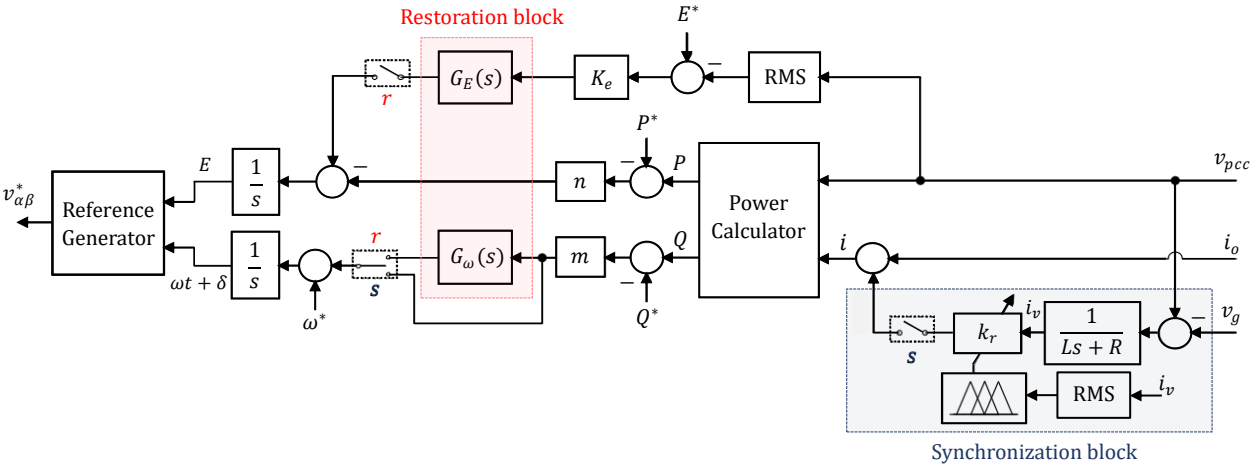

Figure 5.3 – Modified universal droop control

expression [169] :

$$\Delta k_r = \frac{\Sigma_{i=1}^{n} \Delta k_{r,i} w_i}{\Sigma_{i=1}^{n} w_i} \tag{5.18}$$

w_i is the weighting factor, $\Delta k_{r,i}$ is the corresponding value of Δk_r, where :

- **Negative Big (NB) :** Represents a large negative adjustment to significantly decrease the gain
- **Negative Small (NS) :** Represents a small negative adjustment to slightly reduce the gain
- **Zero (Z) :** No adjustment, meaning the gain remains unchanged
- **Positive Small (PS) :** Represents a small positive adjustment to slightly increase the gain
- **Positive Big (PB) :** Represents a large positive adjustment to significantly increase the gain

The fuzzy logic mechanism in the proposed algorithm provides adaptative control, allowing real-time adjustment of the gain k_r to enhance synchronization performance and maintain system stability, ensuring a smooth transition with fast and robust dynamics while offering simplicity and flexibility. Based on the amplitude of the virtual current (I_v) and its variation (δI_v), the gain (k_r) is dynamically adjusted as follows [166] :

- When the virtual current amplitude is very small ($I_v = Z$) and its variation is either small or large ($\delta I_v = S$ or $\delta I_v = B$) (indicating the final phase of synchronization), the value of (k_r) is slightly increased ($\Delta k_r = PS$) to accelerate the completion of the synchronization process
- When the virtual current amplitude is small ($I_v = S$), any variation in its amplitude requires a rapid increase in k_r , i.e., ($\Delta k_r = PB$) to give greater consideration to the virtual current, thereby accelerating the synchronization process
- When the virtual current amplitude is large ($I_v = B$), there is a potential risk of system instability. To mitigate this, the value of (k_r) must be reduced to decrease the influence of the virtual current. If the variation in amplitude is small, (k_r) is slightly reduced ($\Delta k_r = NS$), whereas a large variation requires a rapid reduction

Table 5.2 – Proposed MGDC vs. Recent droop control methods

Refs	Objectives			Features			
	Power sharing	Voltage restoration	Synchroniza-tion process	Hierarchical model	Communication technology	Dynamic speed	Design com-plexity
[43, 170, 171]	✓	✗	✗	✗	✗	↑	↓
[45, 46]	✓	✓	✓	✓	✓	↓	↑
[172, 173]	✓	✓	✗	✓	✗	↓	↑
[167, 174]	✓	✓	✗	✗	✗	↑	↓
[48, 175]	✓	✗	✓	✗	✗	↑	↓
Proposed	✓	✓	✓	✗	✗	↑	↓

✓ : Included / Supported ; ✗ : Not included ; ↑ : High ; ↓ : Low

($\Delta k_r = NB$) to promptly stabilize the system

5.4 Overall decentralized control strategy of flexible Microgrid

Based on the UDC, the proposed decentralized control approach is designed to enable the microgrid to operate seamlessly either in islanded mode with restored microgrid voltages or in connected mode with a smooth transition between both modes. These features can be achieved by integrating both self-restoration and self-synchronization processes with UDC into a single control unit as shown in Figure. 5.3.

According to the previous results, the proposed control strategy for the flexible microgrid can be introduced as follows :

$$\dot{E} = K_e \left(S_r G_E(s) + (1 - S_r)\right) \left(E^*_{MG} - V_{pcc}\right) - n(P - S_G P^*) \tag{5.19}$$

$$\omega = \omega^* + m(Q - S_G Q^*) \left(S_r G_\omega(s) + (1 - S_r)\right) \tag{5.20}$$

where S_r and S_s are the switching states that are used to enable or disable the restoration and the synchronization processes, respectively. The hybrid variable S_G is added to indicate ON/OFF the switch SS, i.e.,

$$\begin{cases} S_r = 1 \; if \text{ self-restoration mode is enabled} \\ S_r = 0 \text{ Else} \end{cases} \tag{5.21}$$

$$\begin{cases} S_s = 1 \;\; if \text{ self-synchronization mode is enabled} \\ S_s = 0 \;\; \text{Else} \end{cases} \tag{5.22}$$

$$\begin{cases} S_G = 1 \;\; if \; SS \text{ is turned ON (Grid-connected mode)} \\ S_G = 0 \;\; \text{Else} \end{cases} \tag{5.23}$$

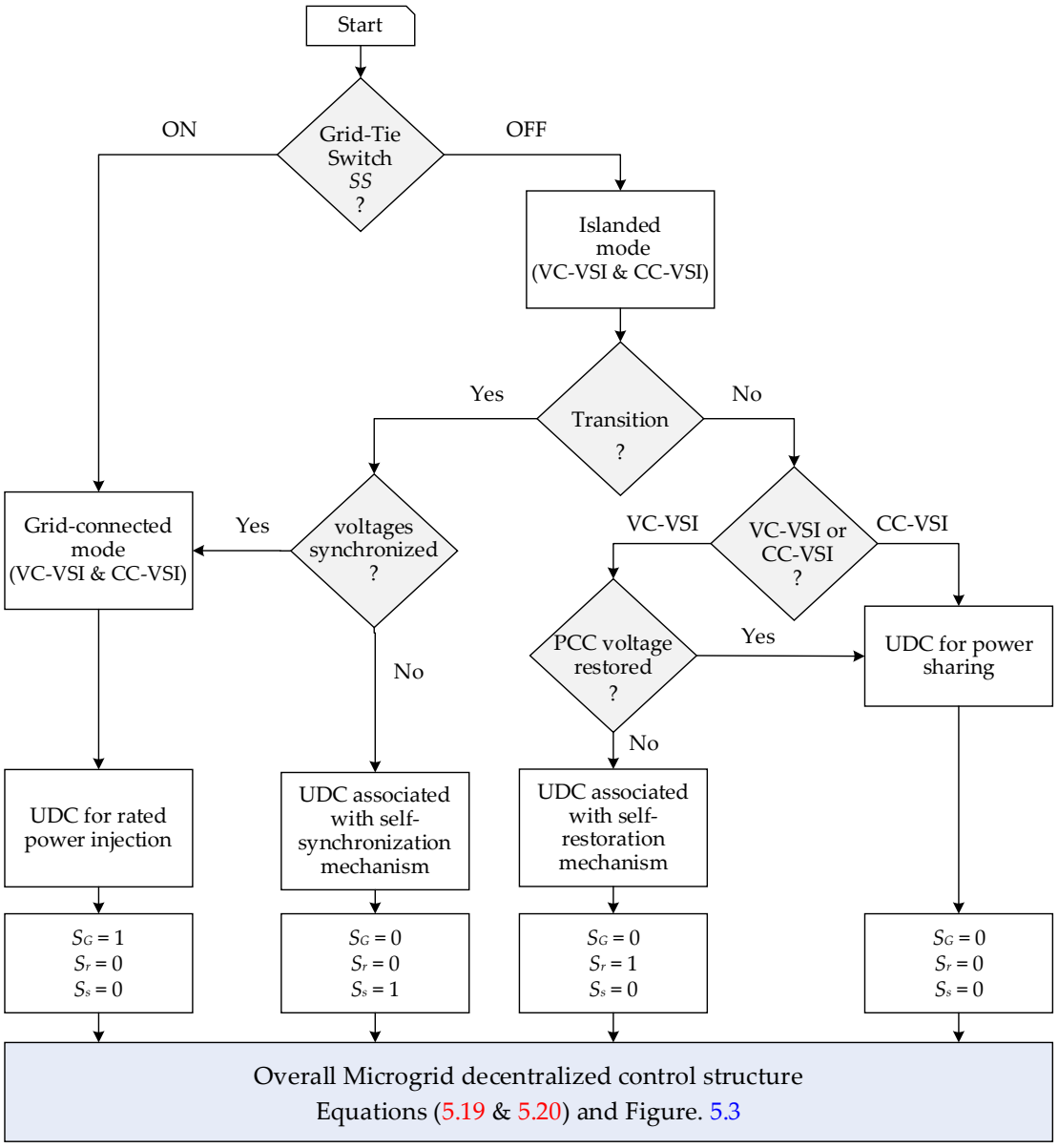

Figure 5.4 – Presentation of the proposed MGDC structure

The block diagram presented in Figure. 5.4 summarizes the proposed MGDC method. From Table 5.2 and Figure. 5.4, it can be inferred that the proposed control scheme outperforms all other power-sharing algorithms. Due to its efficiency and simple design, which does not require communication lines, the proposed control structure provides an effective solution for accurate power sharing, voltage regulation, and synchronization process, guaranteeing a smooth transition, even under various DG-VSI configurations and external disturbances such as input power variation, load demand fluctuations, plug-and-play scenarios, and uncertainties.

Considering the unknown load which can be nonlinear, the second-order generalized integrator (SOGI) is used in the power calculation unit. As shown in Figure. 5.5, the SOGI can be operated as a band-pass filter (BPF) to remove the harmonics produced particularly in islanded mode by the nonlinear load, and obtain the fundamental current of the VSI, using the frequency delivered by the parallel VSI controller and an appropriate damping factor [176, 177].

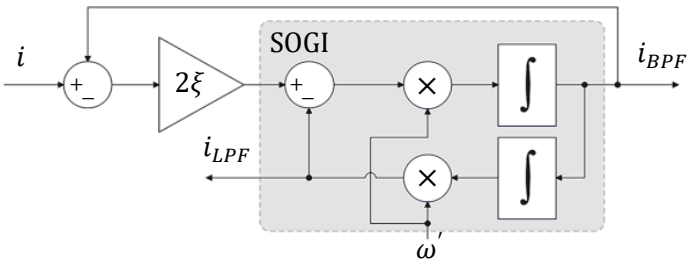

Figure 5.5 – SOGI filter structure

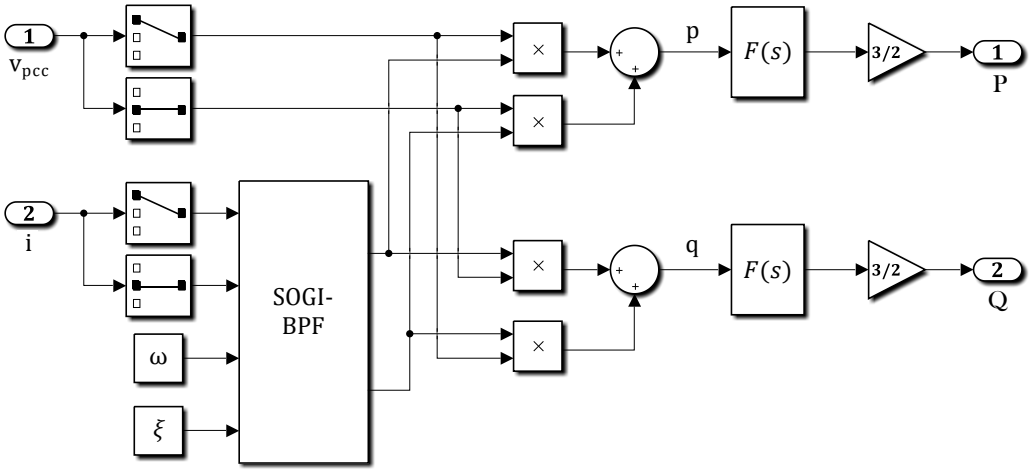

Figure 5.6 – Diagram of power calculator

Based on $\alpha\beta$ frame, the instantaneous active and reactive power can be expressed as follows :

$$p(t) = v_{pcc,\alpha}\hat{i}_{\alpha} + v_{pcc,\beta}\hat{i}_{\beta} \tag{5.24}$$

$$q(t) = v_{pcc,\beta}\hat{i}_{\alpha} - v_{pcc,\alpha}\hat{i}_{\beta} \tag{5.25}$$

where v_{pcc} is the PCC voltage, $\hat{i}$ is the fundamental component of the line current i obtained using SOGI-BPF.

Depending on the average power P and Q used in Figure. 5.3, the instantaneous power can also be described as :

$$p(t) = P + \tilde{p}(t) \tag{5.26}$$

$$q(t) = Q + \tilde{q}(t) \tag{5.27}$$

where $\tilde{p}$ and $\tilde{q}$ are the oscillating components.

From the simulink diagram of Figure. 5.6, the instantaneous power is integrated over one fundamental cycle T in order to obtain the average power P and Q as follows [165] :

$$P = \frac{1}{T}\int_{t}^{t-T} p(t)dt \tag{5.28}$$

$$Q = \frac{1}{T}\int_{t}^{t-T} q(t)dt \tag{5.29}$$

which can be rewritten as :

$$P = F(s).p(s) \tag{5.30}$$

$$Q = F(s).q(s) \tag{5.31}$$

where the integration filter $F(s)$ is given by the following transfer function :

$$F(s) = \frac{1 - e^{-Ts}}{Ts} \tag{5.32}$$

5.5 Application for hybridization between VC-VSI and CC-VSI based on qZSI/PV generator

In this section, the system illustrated in Figure. 5.7 is simulated by using MATLAB/Simulink environment to demonstrate the performance and the robustness of the proposed control strategy. The test microgrid consists of two VC-VSIs and a CC-VSI connected in parallel to a local nonlinear load through a LC filter and an output impedance Z. The CC-VSI is used to exploit the maximum power of the PV generator via qZSI. The latter can operate for the both DC-DC conversion and inversion stages, respectively. The first one is used to achieve the MPPT for extracting the maximum available power from the PVG under variable conditions. As discussed in the literature, the temperature has a non-significant effect on the maximum power position of the PVG. In contrast, the irradiation level changes have an important impact on its performance. For this reason, the proposed control scheme including MPPT IC-FOPID is verified under suddenly varying irradiation before and after the CC-VSI connection to the microgrid. The performance of the IC-FOPID can be evaluated from the simulation results shown in Figure. 5.8.

In order to improve system performance as much as possible, the optimization problem is designed to tune the controller parameters by using an appropriate objective function. The objective function is a quantitative measure of the system performance, where the objective is to find the parameter values that minimize this function. In the case of multi-objective optimization, it is necessary to choose a suitable objective function that takes into account all the performance criteria simultaneously. The linear weighting method is a frequently used approach for formulating a multi-objective optimization problem [178]. This method allows to combine the different performance criteria using normalized weighting coefficients.

The objective function adopted in this study is defined by the following expression :

$$OF = \sum_{k=0}^{N}\sum_{i=1}^{M} \gamma_i k|e_k^i(\theta)|[1 + A - Asign(e_k^i(\theta) + OS^i y_d^i] \tag{5.33}$$

where e_k^i is the error of k^{th} sample between the desired and the measured value of the

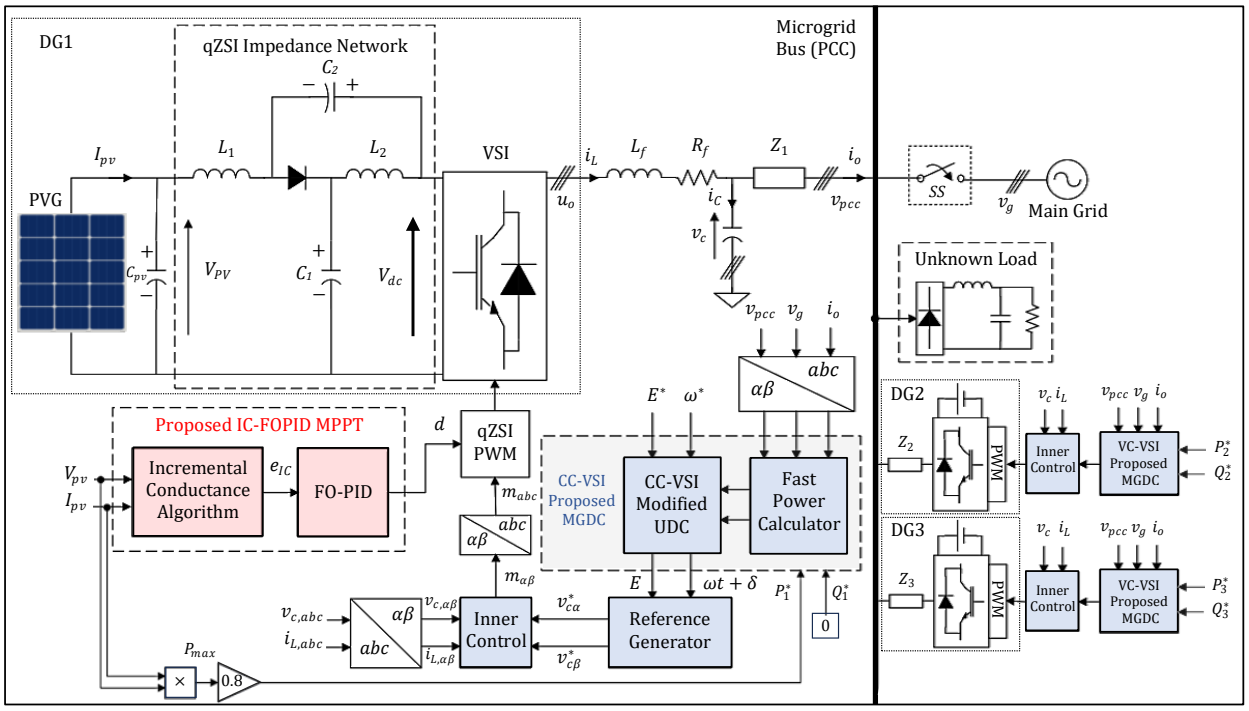

Figure 5.7 – Block diagram of complete microgrid system including CC-VSI

Table 5.3 – Physical parameters of AC Microgrid with parallel VC-VSIs and CC-VSI

Electrical system parameters

Parameter	Symbol	Value
Rated voltage	$E^*(V)$	220
Nominal frequency	$\omega^*(rad/s)$	$2\pi 50$
Load inductor	$L_l(\mu H)$	82
Load capacitor	$C_l(\mu C)$	470
Load	$R_l(\Omega)$	100/160/110

DGs parameters

Parameter	Symbol	CC-VSI	VC-VSI$_1$	VC-VSI$_2$
DC voltage source	$V_{dc}(V)$	246.4 $(2kW/STC)$	650	650
Filter inductor	$L_{lf}(mH)$	8.8	1.8	1.8
Filter capacitor	$C_{lf}(\mu F)$	60	35	35
PWM frequency	$f_s(kHz)$	5	10	10
Output impedance	$Z(mH,\Omega)$	3.4, 0.8	4.4, 0.7	3.7, 0.6
Virtual impedance	$Z_v(mH,\Omega)$	0.9, 5.5	0.9, 5.5	0.9, 5.5
Apparent power rating	$S(kVA)$	$0.8 * P_{pv_{max}}$	1.25	2
qZSI capacitor	$C_{1,2}(\mu F)$	350	-	-
qZSI inductor	$L_{1,2}(mH)$	1.2	-	-
DC filter capacitor	$C(mF)$	4.7	-	-

Table 5.4 – Optimal parameters of MGDC strategy

DGs	MGDC parameters					
	K_e	n	m	k_{pP}	k_{iP}	k_Q
CC-VSI	12.9	0.2014	$1.87e^{-4}$	–	–	–
VC-VSI$_1$	12.9	0.3511	$2.71e^{-4}$	2.7	4.2968	0.2906
VC-VSI$_2$	12.9	0.2007	$2.02e^{-4}$	1.9905	5.1087	0.3201

IC-FOPID MPPT parameters				
K_p	K_i	K_d	λ	μ
32.044	355.44	2.55	0.5	0.2

i^{th} controlled signal, θ is the controller parameters, OS^i is the desired overshoot and the constant A is used to limit the oscillations. The parameter vectors of the modified UDC and the IC-FOPID MPPT process are $\theta = [K_e, k_{pP}, k_{iP}, k_Q]^T$ and $\theta = [K_p, K_i, K_d, \lambda, \mu]^T$, respectively.

By using normalized weighting coefficients γ_i to combine the various i objectives and criteria, the approach used effectively balances power, voltage, and frequency across the proposed MGDC. This ensures minimal errors, overshoot, and oscillation while maintaining precise, reliable, and balanced performance.

The selection of the optimization algorithm is another challenge for calculating the optimal controller parameters, particularly when dealing with complex and multimodal fitness landscapes. In this context, the C-YSGA heuristic algorithm was employed to adjust the controller parameters, guided by the objective function defined in 5.33. As presented in Chapter 2, the C-YSGA combines YSGA with chaotic logistic mapping to improve optimization efficiency. By using chaotic logistic mapping for population initialization, it accelerates convergence compared to conventional metaheuristic algorithms such as PSO and GWO, offering a superior balance between exploration and exploitation, resulting in faster and more reliable convergence.

Using the physical parameters presented in Table 5.3, the optimal control parameters are calculated and given in Table 5.4.

Considering the step load, step irradiation and DG connection/disconnection operation, the four operating modes identified by IEEE Std 1547 are tested : (a) islanded operation mode, (b) islanded to grid-connected transition mode, (b) grid-connected operation mode, (c) grid-connected to islanded transition mode. In order to visualize the performance of the improved UDC, A simulation was carried out for these four different stages and the simulation results are presented in Figure. 5.9 and Figure. 5.10. The DGs outputs active and reactive power can be seen in Figure. 5.9 and the corresponding PCC voltage magnitude and frequency in Figure. 5.10.

5.5.1 Islanded operation mode

In the first stage, different scenarios are considered to evaluate the performance of the proposed control structure during the islanded mode. Initially, the microgrid starts

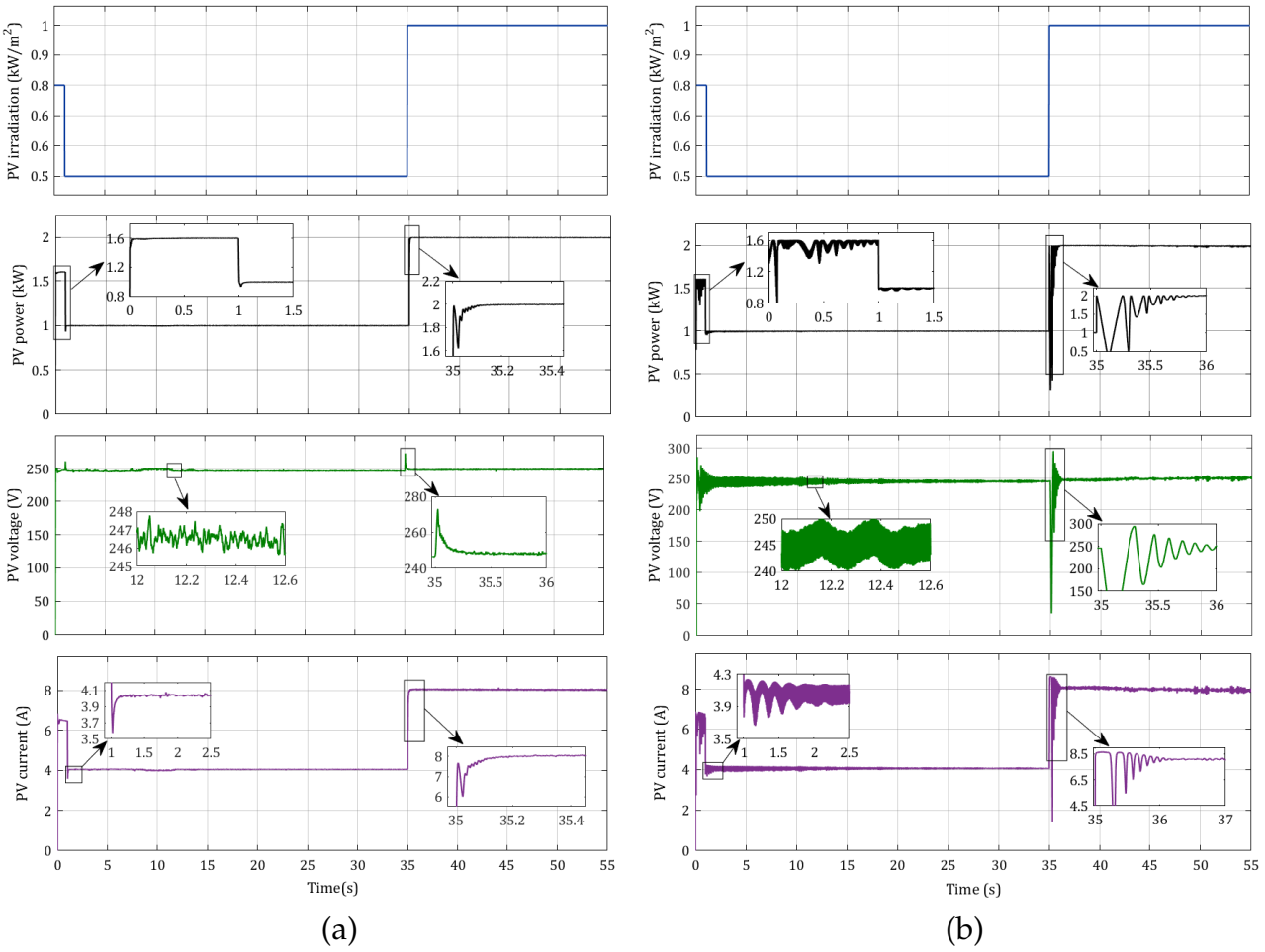

Figure 5.8 – Comparison of MPPT performance under variation of irradiation (a) proposed IC-FOPID technique (b) conventional integral regulator-based IC technique

operating with two VC-VSIs connected in parallel and capable of supplying a local nonlinear load. According to the simulation results shown in Figure. 5.9, both VC-VSIs share the active and reactive power required by the local load depending on the power capacity ratio.

In order to illustrate the mode of the CC-VSI operation of the proposed control scheme, the finding demonstrates the system performance when CC-VSI is connected to the microgrid at $t = 5s$. For the first level of control, the dynamic performance of the MPPT technique based on C-YSGA IC-FOPID is depicted in Figure. 5.8. From the results, the proposed MPPT controller offers outstanding performance in terms of tracking speed, accuracy, and robustness. From the literature, the power efficiency of the used SVPWM is about 0.8. This is why we set $P^* = 0.8 * P_{pv_{max}}$ (W) and $Q^* = 0$(VAR) for the CC-VSI. Therefore, the power factor can be considered unitary which guarantees the injection of the maximum possible PV power into the microgrid. In order to maintain the amount of power demanded from the load, the active power of both pre-connected VC-VSIs is reduced due to the additional power injected by the CC VSI while their steady-state reactive power is not affected as shown in Figure. 5.9. At $t = 10s$, the load demand is decreased which makes the outputs of both VC VSIs behave proportionally to this

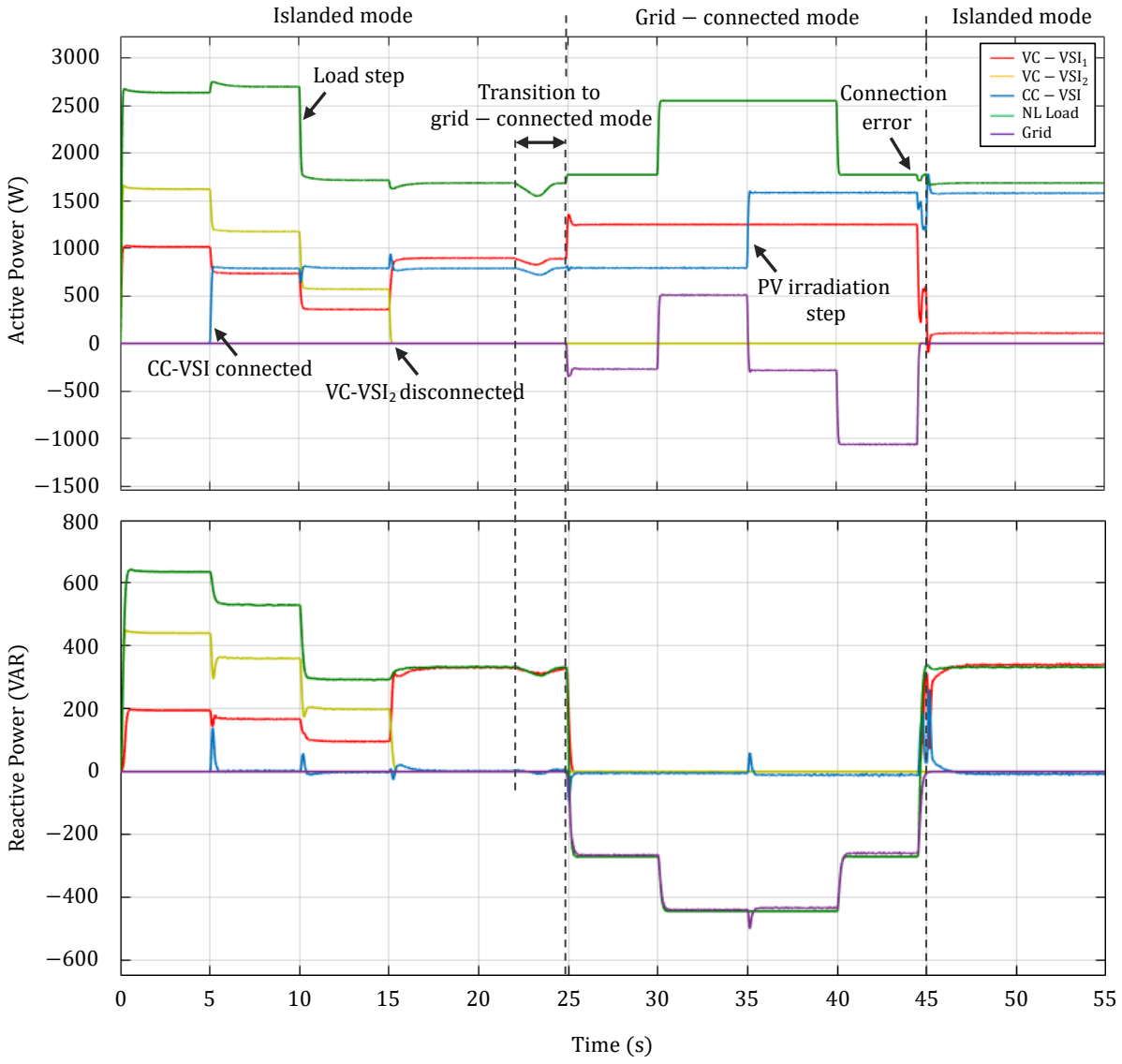

Figure 5.9 – Active and reactive power of the microgrid during different modes of operation

reduction. Then, the microgrid topology is changed by disconnecting VC-VSI2 at $t = 15s$ and letting only VC-VSI1 and CC-VSI support the power demand of the local nonlinear load. The results show that right after the outage of VC-VSI2, VC-VSI1 immediately increases its active and reactive power output to compensate for the power originally injected by VC-VSI2. Despite the last changes, the CC-VSI output remains unaffected and continuous to inject the maximum possible power generated by the PV panel into the microgrid.

On the other hand, the developed power-sharing controller clearly operates with self-restoration where the load demand is perfectly shared even after every change with very fast local compensation for deviation in either the magnitude or frequency of the PCC voltage as shown in Figure. 5.10. This is what demonstrates the effectiveness of the proposed decentralized control strategy during this stage and its ability to overcome the droop control drawback. Once the sharing dynamic stabilizes, the self-restoration process is disabled.

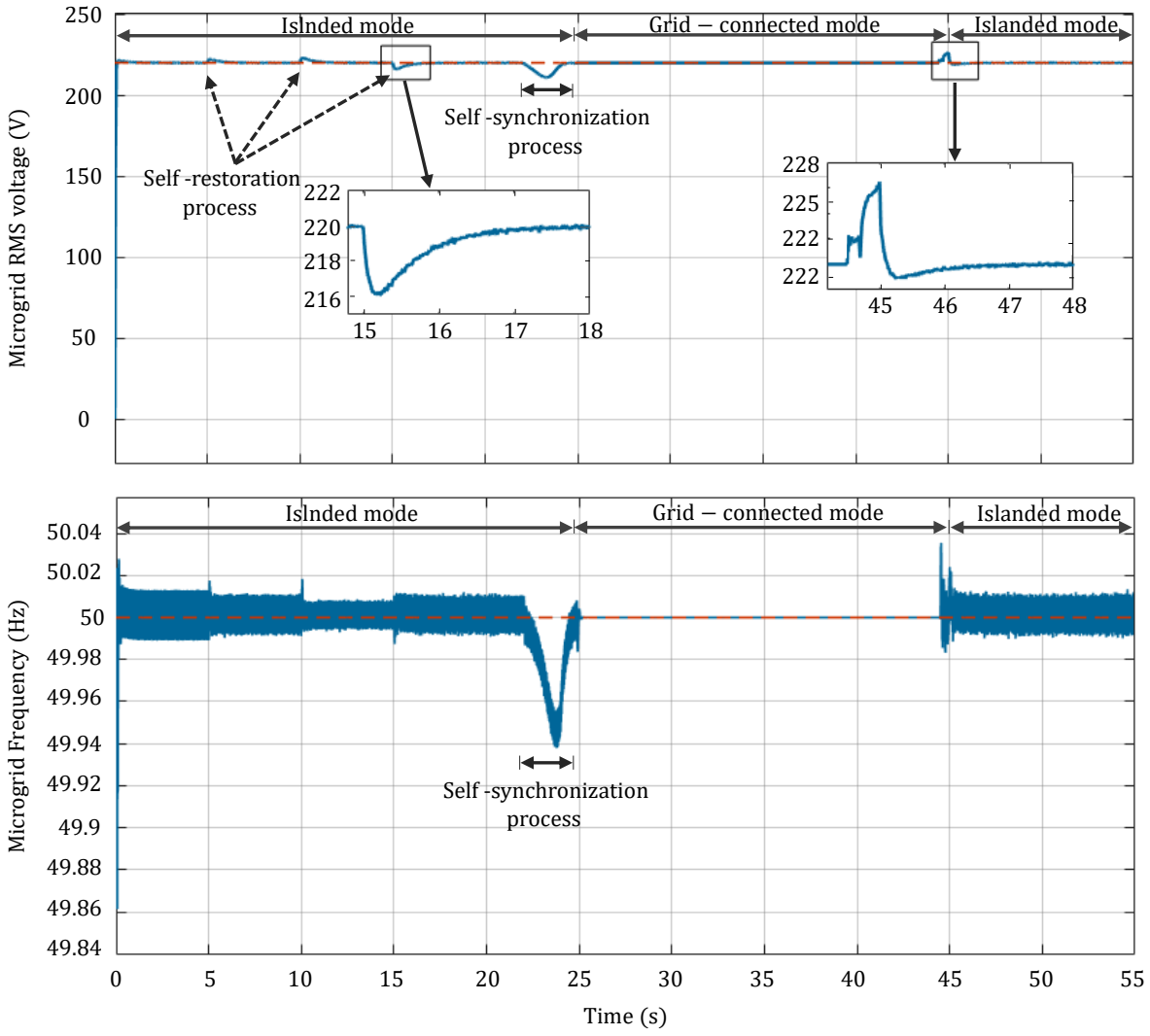

Figure 5.10 – Simulation of self-restoration and self-synchronization process of the proposed decentralized control

5.5.2 Islanded to grid-connected transition mode

In order to ensure a smooth transition to the grid-connected mode, the self-synchronization process of the modified UDC starts at $t = 22s$ to reduce the voltage error between the microgrid and the grid, making the PCC voltage able to track the main grid. Figure. 5.11 shows the synchronization process between the microgrid voltage and the grid voltage where the voltage error is represented by a phase difference. As can be seen from the findings, the islanded mode can be transferred to the grid-connected mode after only a few seconds from when the self-synchronization has been started as long as both voltages are synchronized, despite the harmonics present in the PCC voltage caused by the nonlinear load.

It is clearly observed that the improved UDC is handling well the synchronization with a fast response and a decentralized manner. However, if we take a quick look at the voltage frequency of the microgrid shown in Figure. 5.10 while reducing the voltage error, we can observe that the synchronization process leads to a deviation of the frequency but

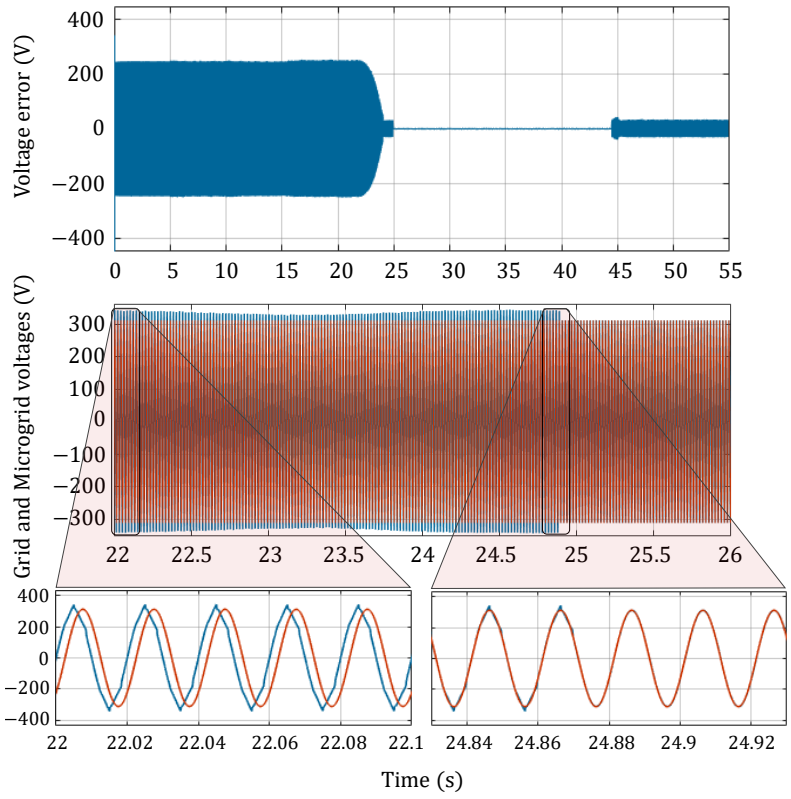

Figure 5.11 – Phase voltage error between the microgrid and the grid during the transition to grid-connected mode

the maximum of this deviation is still far from the maximum allowed under Nordel's grid requirements. These results ensure maintaining the stability of the system and a seamless transition from the islanded mode to the grid-connected mode with no transient overcurrent as shown in Figure. 5.12. At $t = 24.87s$, the SS is turned ON to connect smoothly the microgrid to the main grid without any undesirable transient, and both the active and reactive power sent are maintained.

5.5.3 Grid-connected mode

When the microgrid is connected to the main grid, the system responds quickly to step changes of the VC-VSI1 active and reactive power outputs to be around their desired values P^* and Q^* while the VC-VSI2 is still out of operation. In order to ensure extreme efficiency, the power factor is set to unity where a maximum active power is delivered by the grid-connected VC VSI1. Its desired active power is therefore set to 1250W and the corresponding reactive power is set to zero. On the other hand, the CC-VSI maintains the same operating conditions of islanded mode to inject the maximum possible PV power into the microgrid where its outputs remain constant at $P^* = 0.8 * P_{pv_{max}}$ (W) and $Q^* = 0$(VAR) . After closing the SS until $t = 30s$, we can see that the sum of power supplied by both connected DGs is greater than the power demanded by the local load. Here comes the role of the main grid to receive excess power as shown in Figure. 5.9. The demand is then increased at $t = 30s$, surpassing the power injected from connected VC-VSI1 and CC-VSI. That is why we see that the grid's active power becomes positive,

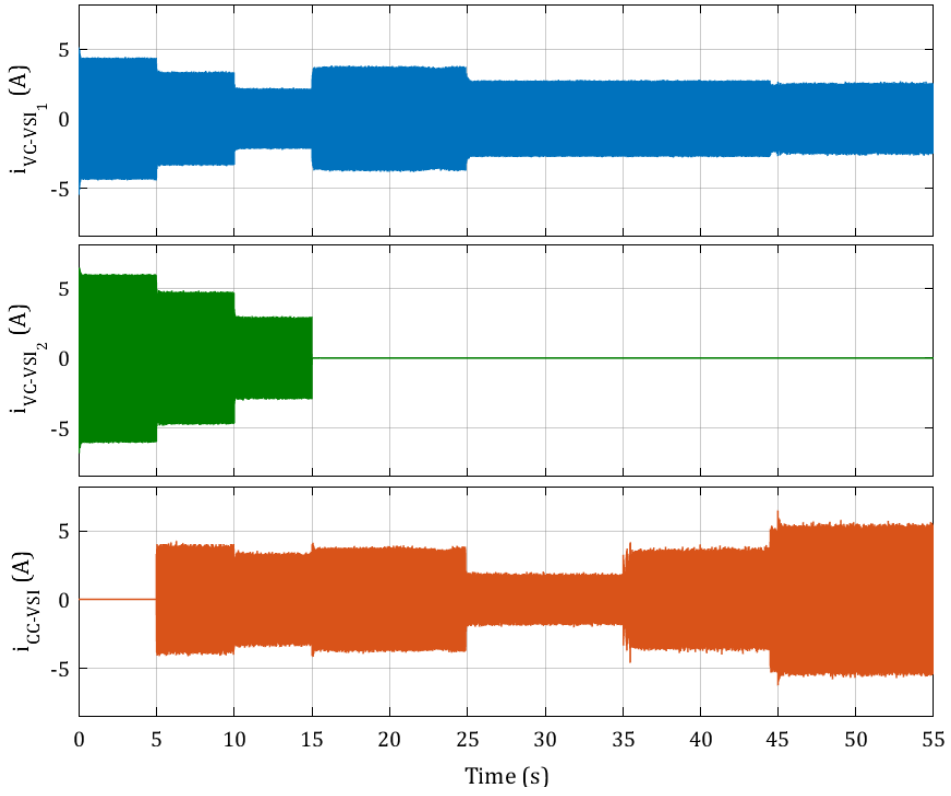

Figure 5.12 – Inverter output currents

after being negative, which means that the power flow changes its direction to satisfy the missed demand from the grid.

At $t = 35s$, once the irradiation is increased to $1000(W/m^2)$, the MPP moves correctly to reach the new maximum point corresponding to the irradiation change thanks to the MPPT IC-FOPID algorithm as shown in Figure. 5.8. Hence, the power delivered by the DGs together again becomes greater than the demand due to the increase in power generated by the PV panel, i.e., the CC-VSI. Consequently, the microgrid re-exports the excess power to the grid. After excluding the additive load demand at $t = 40s$, the amount of power exported to the grid increases without affecting the outputs of both DGs. Thanks to the robust performance of the proposed control scheme, all results of this phase demonstrate the flexibility of the microgrid, the bidirectional power flow to/from the main grid, and the ability to achieve demand balancing.

5.5.4 Grid-connected to islanded transition mode

At $t = 44.5s$, a sudden error is detected due to loss of connection to the main grid. Under these circumstances, the SS should be turned OFF to isolate the microgrid from the grid at $t = 45s$. Thus, the grid-connected mode is directly transferred to the islanded mode to maintain the stability of the microgrid and share the load demand between the connected DGs as shown in Figure. 5.9. The CC-VSI remains unaffected by this transition and continues to inject the maximum possible PV power into the microgrid, while the VC-VSI1 changes its active and reactive power outputs to inject the remaining power demand of the nonlinear load. The self-restoration process is reactivated simultaneously

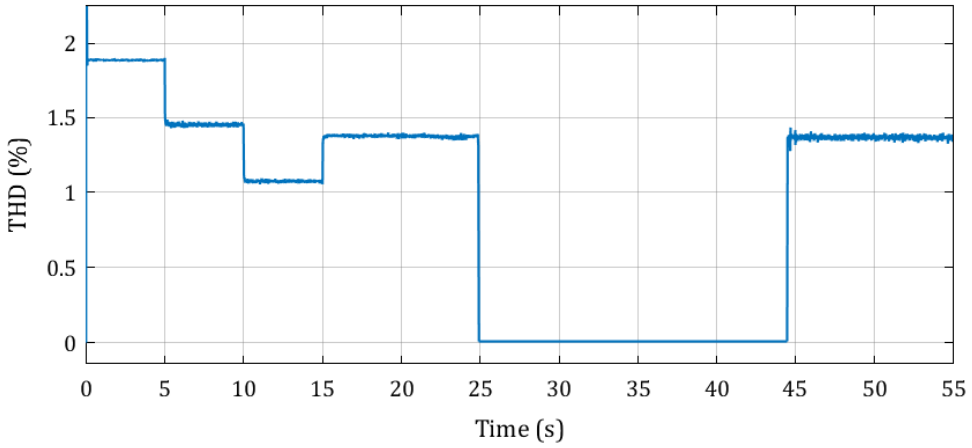

Figure 5.13 – The THD of the PCC voltage

to avoid drooping of the magnitude and frequency of the PCC voltage.

Throughout the simulation run, Figure. 5.13 reveals that the MGDC provides good THD values for the PCC voltage, which remain well below 5% as recommended by IEC 61000 and IEEE 519.

5.6 Conclusion

The widely recognized conventional droop controllers have several drawbacks, most notably the low power-sharing accuracy caused by voltage deviations during islanded mode and the poor dynamic of the transition to grid-connected mode. In this case, a secondary control based on a centralized structure with low-bandwidth communication lines is needed for deviation correction and smooth transition.

In this section, a new decentralized control structure based on the universal droop controller is proposed, handling different operating modes of the microgrid effectively, avoiding the drawbacks of centralized secondary control. During the islanded mode, the proposed controller allows proper sharing of active and reactive power demand among DGs connected to the microgrid. At the same time, voltage and frequency deviations are simultaneously corrected thanks to the self-restoration mechanism. A Fuzzy logic-based synchronization mechanism is integrated into the proposed controller to ensure a seamless mode transfer from islanded mode to grid-connected mode where the microgrid voltage is synchronized with the main grid in a decentralized manner. In this study, both different functionalities VC-VSI and CC-VSI are considered for the DGs. The CC-VSI injects the maximum possible power of a PV generator via qZSI. FO-PID controller-based MPPT method is used to enhance the efficiency of the PVG. Moreover, a metaheuristic algorithm called the chaotic yellow saddle goatfish algorithm (C-YSGA) was used for tuning the optimal parameters. The effectiveness of the proposed control strategy was evaluated by simulations in the presence of nonlinear load taking into account the variation of load and PV irradiation as well as the topology change of the microgrid. The extracted results for different scenarios demonstrate the high dynamic performance and the robustness of the proposed decentralized control scheme for the flexible microgrid.

General Conclusion

The research presented in this thesis focuses on the development of modern control techniques for multi-source energy conversion systems integrated in microgrids. The study covers both hierarchical and decentralized control strategies, aiming at improving the stability, efficiency and flexibility of microgrid operations. Through extensive literature searches, the main challenges associated with the regulation of distributed generation and microgrid management have been identified. The proposed contributions address these challenges by introducing advanced control methods for grid-connected and stand-alone PV systems, as well as for parallel distributed generation in microgrids. The developed approaches have been validated by various simulation applications in multi-source and flexible microgrids.

The overall contributions can be summarized as follows :

— A control strategy for grid-connected PV systems has been developed, integrating FOTSTA-based MPPT and P–DPC–SVM-based VSI control. Simulation results demonstrate improved energy harvesting efficiency and improved grid stability.
— For stand-alone PV systems, advanced energy management strategies and control methods such as SSSTA have been implemented, optimizing the operating modes to ensure stable and reliable energy supply.
— The integration of impedance-source inverters (ZSI/qZSI) into stand-alone PV systems has been studied, with various control strategies proposed, including PR controllers, STA-based control, and FOPID controllers. Simulation results confirm the effectiveness of these techniques in improving system performance and robustness.
— A hierarchical control framework for parallel distributed generation in microgrids has been designed, comprising a decentralized primary control with a universal fractional-order droop controller, a centralized secondary control for voltage and frequency restoration, and a tertiary control for overall system optimization. These approaches facilitate smooth grid transitions and improve energy management.
— A decentralized control strategy for microgrids has been developed, with self-restoration mechanisms and fuzzy logic-based self-synchronization. This strategy improves system resilience and ensures stable operation under variable conditions.
— Based on specific criteria, recent solvers of the optimized problem to find the optimal parameters of the developed control structures have been used. The

solvers are based on metaheuristic algorithms such as PSO, SLPSO, GWO and YSGA optimizers.

— Applications have been explored, especially for flexible and multi-source microgrids, including renewable sources, storage systems and hybrid VSI configurations, demonstrating the feasibility and benefits of the proposed control techniques in real-world scenarios.

The results of this research contribute to the advancement of control strategies for multi-source energy conversion systems, paving the way for more efficient, resilient and flexible microgrid architectures. Future work could focus on further experimental validation, real-time implementation and integration of artificial intelligence-based control methods to improve adaptability and predictive capabilities in dynamic energy environments.

References

[1] Vaclav Smil. Distributed generation and megacities : Are renewables the answer ? 17(2) :37–41, 2019.

[2] Mohammadamin Shirkhani, Jafar Tavoosi, Saeed Danyali, Amirhossein Khosravi Sarvenoee, Ali Abdali, Ardashir Mohammadzadeh, and Chunwei Zhang. A review on microgrid decentralized energy/voltage control structures and methods. 10 :368–380, 2023.

[3] IAEA. *Non-baseload Operation in Nuclear Power Plants*. Number v.NP-T-3.23 in IAEA Nuclear Energy Series No. NP-T-3.23. IAEA, 2018.

[4] Adel Choudar, Djamel Boukhetala, Said Barkat, and Jean-Michel Brucker. A local energy management of a hybrid PV-storage based distributed generation for microgrids. 90 :21–33, 2015.

[5] Julia Schulz, Valerie M. Scharmer, and Michael F. Zaeh. Energy self-sufficient manufacturing systems – integration of renewable and decentralized energy generation systems. 43 :40–47, 2020.

[6] Felix Kienast, Nica Huber, Rico Hergert, Janine Bolliger, Lorena Segura Moran, and Anna M. Hersperger. Conflicts between decentralized renewable electricity production and landscape services – a spatially-explicit quantitative assessment for switzerland. 67 :397–407, 2017.

[7] Salar Moradi, Gibran David Agundis Tinajero, Juan C. Vasquez, Gaetano Zizzo, Josep M. Guerrero, and Eleonora Riva Sanseverino. Hierarchical-power-flow-based energy management for alternative/direct current hybrid microgrids. 38 :101384, 2024.

[8] Razieh Darshi, Saeed Shamaghdari, Aliakbar Jalali, and Hamidreza Arasteh. Decentralized reinforcement learning approach for microgrid energy management in stochastic environment. 2023 :1–15, 2023.

[9] Adam Hirsch, Yael Parag, and Josep Guerrero. Microgrids : A review of technologies, key drivers, and outstanding issues. 90 :402–411, 2018.

[10] Feras Alasali, Saad M. Saad, Abdelaziz Salah Saidi, Awni Itradat, William Holderbaum, Naser El-Naily, and Fatima F. Elkuwafi. Powering up microgrids : A comprehensive review of innovative and intelligent protection approaches for enhanced reliability. 10 :1899–1924, 2023.

[11] Mariya Soshinskaya, Wina H.J. Crijns-Graus, Josep M. Guerrero, and Juan C. Vasquez. Microgrids : Experiences, barriers and success factors. 40 :659–672, 2014.

[12] Muhammad Yasir Ali Khan, Haoming Liu, Yuquan Zhang, and Jian Wang. Hybrid AC/DC microgrid : Systematic evaluation of interlinking converters, control strategies, and protection schemes : A review. 12 :160097–160132, 2024.

[13] Alexander Micallef, Maurice Apap, Cyril Spiteri-Staines, and Josep M. Guerrero. Single-phase microgrid with seamless transition capabilities between modes of operation. 6(6) :2736–2745, 2015.

[14] Fang Zheng Peng. Z-source inverter. 39(2) :504–510, 2003.

[15] Yuan Li, Shuai Jiang, Jorge G. Cintron-Rivera, and Fang Zheng Peng. Modeling and control of quasi-z-source inverter for distributed generation applications. 60(4) :1532–1541, 2013.

[16] Zhiye Lu, Lishu Wang, and Panbao Wang. Review of voltage control strategies for DC microgrids. 16(17) :6158, 2023.

[17] Abu Bakar Siddique, Md. Shahin Munsi, Subrata K. Sarker, Sajal K. Das, and Md. Rabiul Islam. Voltage and current control augmentation of islanded microgrid using multifunction model reference modified adaptive PID controller. 113 :492–501, 2019.

[18] Maniza Armin, Priyo Nath Roy, Subroto K. Sarkar, and Sajal K. Das. LMI-based robust PID controller design for voltage control of islanded microgrid. 20(5) :2014–2025, 2018.

[19] Fathi Alremali, Ersagun Yaylaci, and İhsan Uluer. Optimization of proportional-integral controllers of grid-connected wind energy conversion system using grey wolf optimizer based on artificial neural network for power quality improvement. 16(3) :295–305, 2022.

[20] Particle Swarm Optimization based Fuzzy Logic MPPT Inverter Controller for Grid Connected Wind Turbine. *International Journal of Renewable Energy Research*, (v9i1), 2019.

[21] V. Chamundeeswari and R. Seyezhai. Design and implementation of fuzzy sliding mode control (FSMC) approach for a modified negative output luo DC-DC converter with its comparative analysis. 65(1) :45–57, 2024.

[22] Zehan Li, Gunawan Dewantoro, Tuohan Xiao, and Akshya Swain. A Comparative Analysis of Fuzzy Logic Control and Model Predictive Control in Photovoltaic Maximum Power Point Tracking. *Electronics*, 14(5) :1009, 2025.

[23] Buddhadeva Sahoo, Subhransu Ranjan Samantaray, and Mohammed M. Alhaider. Advanced control scheme for harmonic mitigation and performance improvement in DC-AC microgrid with parallel voltage source inverter. 15(1) :7051, 2025.

[24] Jing He, Runzhong Tang, Qiuwei Wu, Changfan Zhang, Gongping Wu, and Shoudao Huang. Robust predictive current control of permanent magnet synchronous motor using voltage coefficient matrix update. 159 :109999, 2024.

[25] Mohamed A. Ebrahim, Beshoy Abdou Aziz, Maged N. F. Nashed, and Fawzy A. Osman. Optimal design of proportional-resonant controller and its harmonic compensators for grid-integrated renewable energy sources based three-phase voltage source inverters. *IET Generation, Transmission & Distribution*, 15(8) :1371–1386, 2021.

[26] Amina Mseddi, Ahmed Abid, Omar Naifar, Mohamed Rhaima, Abdellatif Ben Makhlouf, and Lassaad Mchiri. Investigation of the Robust Fractional Order Control Approach Associated with the Online Analytic Unity Magnitude Shaper : The Case of Wind Energy Systems. *Fractal and Fractional*, 8(4) :187, 2024.

[27] Yuxin He, Aixiang Ma, Yuehui Wang, Xinyi Tian, and Sihai Zhao. FOPID controller design for pneumatic control valves with ultra-low overshoot, rapid response and enhanced robustness. *Scientific Reports*, 15(1) :4541, 2025.

[28] Hamid Chojaa, Aziz Derouich, Seif Eddine Chehaidia, Othmane Zamzoum, Mohammed Taoussi, and Hasnae Elouatouat. Integral sliding mode control for DFIG based WECS with MPPT based on artificial neural network under a real wind profile. *Energy Reports*, 7 :4809–4824, 2021.

[29] Yigeng Huangfu, Shengrong Zhuo, Akshay Rathore, Elena Breaz, Babak Nahid-Mobarakeh, and Fei Gao. Super-twisting differentiator-based high order sliding mode voltage control design for DC-DC buck converters. 9(7) :494, 2016.

[30] Rui Ma, Yu Wu, Elena Breaz, Yigeng Huangfu, Pascal Briois, and Fei Gao. High-order sliding mode control of DC-DC converter for PEM fuel cell applications. In *2018 IEEE Industry Applications Society Annual Meeting (IAS)*, pages 1–7. IEEE, 2018.

[31] Marius Ulla Hatlehol and Mehdi Zadeh. Super-twisting algorithm second-order sliding mode control of a bidirectional DC-to-DC converter supplying a constant power load. 55(31) :287–294, 2022.

[32] Yasser S. Abdalla, Naghmash Ali, Abdulaziz Alanazi, Mohana Alanazi, Hammad Armghan, Mohamed A. Sharaf, Anis R. Boudabbous, and Ammar Armghan. Fast reaching law based integral terminal sliding mode controller for photovoltaic-fuel cell-battery-super capacitor based direct-current microgrid. 56 :105915, 2022.

[33] Yundi Chu, Shili Fu, Shixi Hou, and Juntao Fei. Intelligent terminal sliding mode control of active power filters by self-evolving emotional neural network. 19(4) :6138–6149, 2023.

[34] Maloth Ramesh, Anil Kumar Yadav, Pawan Kumar Pathak, and Ch Hussaian Basha. A novel fuzzy assisted sliding mode control approach for frequency regulation of wind-supported autonomous microgrid. 14(1) :31526, 2024.

[35] He Jiang, Yan Zhao, Hanguang Su, and Yuzhong Wang. Design of fuzzy sliding mode controller for islanded AC/DC hybrid microgrid with cyber-attacks. 18(16) :2142–2154, 2024.

[36] Sarra Adiche, Mhamed Larbi, Djilali Toumi, Riyadh Bouddou, Mohit Bajaj, Nasreddine Bouchikhi, Abdallah Belabbes, and Ievgen Zaitsev. Advanced control strategy for AC microgrids : a hybrid ANN-based adaptive PI controller with droop control and virtual impedance technique. 14(1) :31057, 2024.

[37] Ahmed M. Nassef, Mohammad Ali Abdelkareem, Hussein M. Maghrabie, and Ahmad Baroutaji. Review of metaheuristic optimization algorithms for power systems problems. 15(12) :9434, 2023.

[38] Afifa Akter, Ehsanul Islam Zafir, Nazia Hasan Dana, Rahul Joysoyal, Subrata K. Sarker, Li Li, S M Muyeen, Sajal K. Das, and Innocent Kamwa. A review on microgrid optimization with meta-heuristic techniques : Scopes, trends and recommendation. 51 :101298, 2024.

[39] Akanksha Sinha and Kartick Chandra Jana. Comprehensive review on control strategies of parallel-interfaced voltage source inverters for distributed power generation system. 14(13) :2297–2314, 2020.

[40] Jean De Dieu Iyakaremye, George N. Nyakoe, Cyrus W. Wekessa, and PAUSTI-Kenya. MPC-based droop control of parallel inverters for voltage and frequency stabilization in autonomous AC microgrid. V9(4) :IJERTV9IS040072, 2020.

[41] Jiefeng Hu, Yinghao Shan, Ka Wai Cheng, and Syed Islam. Overview of power converter control in microgrids—challenges, advances, and future trends. 37(8) :9907–9922, 2022.

[42] Seydali Ferahtia, Azeddine Houari, Tudor Cioara, Mohammed Bouznit, Hegazy Rezk, and Ali Djerioui. Recent advances on energy management and control of direct current microgrid for smart cities and industry : A survey. 368 :123501, 2024.

[43] Qing-Chang Zhong and Yu Zeng. Universal Droop Control of Inverters With Different Types of Output Impedance. *IEEE Access*, 4 :702–712, 2016.

[44] Usman Bashir Tayab, Mohd Azrik Bin Roslan, Leong Jenn Hwai, and Muhammad Kashif. A review of droop control techniques for microgrid. 76 :717–727, 2017.

[45] Islam Ziouani, Djamel Boukhetala, Abdel-Moumen Darcherif, Bilal Amghar, and Ikram El Abbassi. Hierarchical control for flexible microgrid based on three-phase voltage source inverters operated in parallel. 95 :188–201, 2018.

[46] **Fatma-Zohra Hadjaidji**, **Djamel Boukhetala**, and **Jean-Pierre Barbot**. Optimized fractional order based droop control with improving the flexibility of a microgrid. 353 :02001, 2022.

[47] Qing-Chang Zhong, Wen-Long Ming, and Yu Zeng. Self-synchronized universal droop controller. 4 :7145–7153, 2016.

[48] Mohammad Amin and Qing-Chang Zhong. Resynchronization of distributed generation based on the universal droop controller for seamless transfer between operation modes. 67(9) :7574–7582, 2020.

[49] Sulman Shahzad, Muhammad Abbas Abbasi, Hassan Ali, Muhammad Iqbal, Rania Munir, and Heybet Kilic. Possibilities, challenges, and future opportunities of microgrids : A review. 15(8) :6366, 2023.

[50] Muhammad Khalid. Smart grids and renewable energy systems : Perspectives and grid integration challenges. 51 :101299, 2024.

[51] Aboubakr El Hammoumi, Smail Chtita, Saad Motahhir, and Abdelaziz El Ghzizal. Solar PV energy : From material to use, and the most commonly used techniques to maximize the power output of PV systems : A focus on solar trackers and floating solar panels. 8 :11992–12010, 2022.

[52] Athil S. Al-Ezzi and Mohamed Nainar M. Ansari. Photovoltaic solar cells : A review. 5(4) :67, 2022.

[53] Toshihisa Funabashi. Integration of distributed energy resources in power systems—chapter 1 : Introduction. In *Integration of Distributed Energy Resources in Power Systems*, pages 1–14. Elsevier, 2016.

[54] Bhavna Jain, Shailendra Jain, and R.K. Nema. Control strategies of grid interfaced wind energy conversion system : An overview. 47 :983–996, 2015.

[55] Arash Farnoosh. Power generation from coal, oil, gas, and biofuels. In Manfred Hafner and Giacomo Luciani, editors, *The Palgrave Handbook of International Energy Economics*, pages 111–130. Springer International Publishing, 2022.

[56] Salvatore Musumeci. Energy conversion using electronic power converters : Technologies and applications. 16(8) :3590, 2023.

[57] Vijaychandra Joddumahanthi, ukasz Knypiński, Yatindra Gopal, and Kacper Kasprzak. Review of power electronics technologies in the integration of renewable energy systems. 15(8) :4523, 2025.

[58] Giovanni De Carne, S. Masoome Maroufi, Hamzeh Beiranvand, Valerio De Angelis, Salvatore D'Arco, Vahan Gevorgian, Simon Waczowicz, Barry Mather, Marco Liserre, and Veit Hagenmeyer. The role of energy storage systems for a secure energy supply : A comprehensive review of system needs and technology solutions. 236 :110963, 2024.

[59] K Hemmes, J Zachariahwolf, M Geidl, and G Andersson. Towards multi-source multi-product energy systems. 32(10) :1332–1338, 2007.

[60] Qusay Hassan, Sameer Algburi, Aws Zuhair Sameen, Hayder M. Salman, and Marek Jaszczur. A review of hybrid renewable energy systems : Solar and wind-powered solutions : Challenges, opportunities, and policy implications. 20 :101621, 2023.

[61] Jie Ji, Yinqi Xie, Yibai Wang, Jia Xiao, Wenchao Wen, Cong Zhang, Na Sun, Hui Huang, and Chu Zhang. Holistic optimization of grid-connected multi-energy systems : Biomass and flexible storage integration. 327 :119558, 2025.

[62] T. Adefarati and R.C. Bansal. Integration of renewable distributed generators into the distribution system : a review. 10(7) :873–884, 2016.

[63] Talha Bin Nadeem, Mubashir Siddiqui, Muhammad Khalid, and Muhammad Asif. Distributed energy systems : A review of classification, technologies, applications, and policies. 48 :101096, 2023.

[64] Gianfranco Chicco and Pierluigi Mancarella. Distributed multi-generation : A comprehensive view. 13(3) :535–551, 2009.

[65] Fahad Saleh Al-Ismail. DC microgrid planning, operation, and control : A comprehensive review. 9 :36154–36172, 2021.

[66] T.S. Basso and R. DeBlasio. IEEE 1547 series of standards : Interconnection issues. 19(5) :1159–1162, 2004.

[67] IEEE Recommended Practice and Requirements for Harmonic Control in Electric Power Systems, 2016. ISBN : 9780738190051.

[68] Dinesh Kumar, Firuz Zare, and Arindam Ghosh. DC microgrid technology : System architectures, AC grid interfaces, grounding schemes, power quality, communication networks, applications, and standardizations aspects. 5 :12230–12256, 2017.

[69] Muhammad Yasir Ali Khan, Haoming Liu, Yuquan Zhang, and Jian Wang. Hybrid AC/DC microgrid : Systematic evaluation of interlinking converters, control strategies, and protection schemes : A review. 12 :160097–160132, 2024.

[70] Adel Merabet, Labib Labib, Amer M.Y.M. Ghias, Ahmed Aldurra, and Mahdi Debbouza. Dual-mode operation based second-order sliding mode control for grid-connected solar photovoltaic energy system. 111 :459–474, 2019.

[71] Pragya Gawhade and Amit Ojha. Recent advances in synchronization techniques for grid-tied PV system : A review. 7 :6581–6599, 2021.

[72] Tamer Khatib, Azah Mohamed, and K. Sopian. A review of photovoltaic systems size optimization techniques. 22 :454–465, 2013.

[73] Sonali Goel and Renu Sharma. Performance evaluation of stand alone, grid connected and hybrid renewable energy systems for rural application : A comparative review. 78 :1378–1389, 2017.

[74] Adel A. Elbaset, Saad Awad Mohamed Abdelwahab, Hamed Anwer Ibrahim, and Mohammed Abdelmowgoud Elsayed Eid. *Introduction. In : Performance Analysis of Photovoltaic Systems with Energy Storage Systems*, pages 1–10. Springer International Publishing, 2019.

[75] Vikrant Sharma and S.S. Chandel. Performance and degradation analysis for long term reliability of solar photovoltaic systems : A review. 27 :753–767, 2013.

[76] Vun Jack Chin, Zainal Salam, and Kashif Ishaque. Cell modelling and model parameters estimation techniques for photovoltaic simulator application : A review. 154 :500–519, 2015.

[77] R Chenni, M Makhlouf, T Kerbache, and A Bouzid. A detailed modeling method for photovoltaic cells. *Energy*, 32(9) :1724–1730, 2007.

[78] Hanane Yatimi and Elhassan Aroudam. Assessment and control of a photovoltaic energy storage system based on the robust sliding mode MPPT controller. 139 :557–568, 2016.

[79] Madhav Kumar, Kaibalya Prasad Panda, Julio Cesar Rosas-Caro, Antonio Valderrabano-Gonzalez, and Gayadhar Panda. Comprehensive review of conventional and emerging maximum power point tracking algorithms for uniformly and partially shaded solar photovoltaic systems. 11 :31778–31812, 2023.

[80] Mingxuan Mao, Lichuang Cui, Qianjin Zhang, Ke Guo, Lin Zhou, and Han Huang. Classification and summarization of solar photovoltaic MPPT techniques : A review based on traditional and intelligent control strategies. 6 :1312–1327, 2020.

[81] Nabil Karami, Nazih Moubayed, and Rachid Outbib. General review and classification of different MPPT techniques. 68 :1–18, 2017.

[82] Riaz Ahmad, Ali F Murtaza, and Hadeed Ahmed Sher. Power tracking techniques for efficient operation of photovoltaic array in solar applications–a review. *Renewable and Sustainable Energy Reviews*, 101 :82–102, 2019.

[83] Cherrelle Eid, Paul Codani, Yannick Perez, Javier Reneses, and Rudi Hakvoort. Managing electric flexibility from distributed energy resources : A review of incentives for market design. 64 :237–247, 2016.

[84] Ahmed Mohammed Saleh, Istvan Vokony, Muhammad Waseem, Muhammad Adnan Khan, and Ahmed Al-Areqi. Power system stability with high integration of RESs and EVs : Benefits, challenges, tools, and solutions. 13 :2637–2663, 2025.

[85] Debani Prasad Mishra, Rudranarayan Senapati, and Surender Reddy Salkuti. Comparison of DC-DC converters for solar power conversion system. 26(2) :648, 2022.

[86] Sergio Coelho, Vitor Monteiro, and Joao L. Afonso. Topological advances in isolated DC–DC converters : High-efficiency design for renewable energy integration. 17(6) :2336, 2025.

[87] Fabrizio Marignetti, Roberto Luigi Di Stefano, Guido Rubino, and Roberto Giacomobono. Current source inverter (CSI) power converters in photovoltaic systems : A comprehensive review of performance, control, and integration. 16(21) :7319, 2023.

[88] Christian Buzzio, Yamil S. Poloni, Germán G. Oggier, and Guillermo O. García. A current-source DC-AC converter and control strategy for grid-connected PV applications. 154 :109399, 2023.

[89] Judith Stammers. *Solar Energy*, pages 132–156. Macmillan Education UK, 1985.

[90] Joakim Widén. *Solar Radiation Theory*. Uppsala University, 1 edition, 2019. Medium : Elektronisk resurs.

[91] Christopher J. Rhodes. Solar energy : Principles and possibilities. 93(1) :37–112, 2010.

[92] C. Lupangu and R.C. Bansal. A review of technical issues on the development of solar photovoltaic systems. 73 :950–965, 2017.

[93] Jancarle L. Santos, Fernando Antunes, Anis Chehab, and Cícero Cruz. A maximum power point tracker for PV systems using a high performance boost converter. 80(7) :772–778, 2006.

[94] Rohit Nandi, Manoj Tripathy, and Chandra Prakash Gupta. Coordination of BESS and PV system with bidirectional power control strategy in AC microgrid. 34 :101029, 2023.

[95] Tushar Kanti Roy, Subarto Kumar Ghosh, and Sajeeb Saha. Stability enhancement of battery energy storage and renewable energy-based hybrid AC/DC microgrids using terminal sliding mode backstepping control approaches. 142 :40–56, 2023.

[96] Xuemei Zheng, Zongxuan Liu, Xingyu Zhang, and Josep M. Guerrero. Robust control for PV and battery DC microgrid system based on passive and sliding mode. 19(1) :e70033, 2025.

[97] David Cortes-Vega and Hussain Alazki. Robust maximum power point tracking scheme for PV systems based on attractive ellipsoid method. 25 :100410, 2021.

[98] Saeed Sepasi, Celia Talichet, and Abrar Shahriar Pramanik. Power quality in microgrids : A critical review of fundamentals, standards, and case studies. *IEEE Access*, 11 :108493–108531, 2023.

[99] Shuang Xu, Yaosuo Xue, and Liuchen Chang. Review of power system support functions for inverter-based distributed energy resources-standards, control algorithms, and trends. *IEEE open journal of Power electronics*, 2 :88–105, 2021.

[100] David Rebollal, Miguel Carpintero-Rentería, David Santos-Martín, and Mónica Chinchilla. Microgrid and distributed energy resources standards and guidelines review : Grid connection and operation technical requirements. *Energies*, 14(3) :523, 2021.

[101] Ieee standard for the specification of microgrid controllers. *IEEE Std 2030.7-2017*, pages 1–43, 2018.

[102] Frank W Bohn, Joseph J Vitale, Blane CT Wilson, David O Teicher, Thomas F Podlesak, Darren Z Stephens, Michael L Gonzalez, Stefan G Siegfried, Bradley J Stanley, and Jaclyn A Lynch. Hybrid energy storage system for tactical microgrids.

[103] Md Hossain, Hemanshu Pota, Walid Issa, and Md Hossain. Overview of AC microgrid controls with inverter-interfaced generations. 10(9) :1300, 2017.

[104] Hamid Saeed Khan and Attaullah Y. Memon. Active and reactive power control of the voltage source inverter in an AC microgrid. 15(2) :1621, 2023.

[105] Bibhudatta Mishra and Monalisa Pattnaik. A modified droop-based decentralized control strategy for accurate power sharing in a PV-based islanded AC microgrid. 153 :467–481, 2024.

[106] Kunyu Zuo and Lei Wu. A review of decentralized and distributed control approaches for islanded microgrids : Novel designs, current trends, and emerging challenges. 35(5) :107138, 2022.

[107] **Fatma-Zohra Hadjaidji**, Asma Behlouli, Fares Baatouche, **Djamel Boukhetala**, **Jean-Pierre Barbot**, and El-Madjid Berkouk. Hierarchical control for flexible pv-battery microgrid based on z-source inverters operated in parallel. *ENP Engineering Science Journal*, "Under review".

[108] Octavio Ramos-Figueroa, Marcela Quiroz-Castellanos, Efrén Mezura-Montes, and Oliver Schütze. Metaheuristics to solve grouping problems : A review and a case study. 53 :100643, 2020.

[109] Essam H. Houssein, Mahmoud Khalaf Saeed, Gang Hu, and Mustafa M. Al-Sayed. Metaheuristics for solving global and engineering optimization problems : Review, applications, open issues and challenges. 31(8) :4485–4519, 2024.

[110] Xin-She Yang. *Nature-inspired metaheuristic algorithms*. Luniver Press, 2. ed edition, 2010.

[111] El-Ghazali Talbi. *Metaheuristics : from design to implementation*. John Wiley & Sons, 2009.

[112] Iztok Fister, Xin-She Yang, Janez Brest, and Dušan Fister. A brief review of nature-inspired algorithms for optimization. 2013. Publisher : arXiv Version Number : 1.

[113] Ahmed M. Nassef, Mohammad Ali Abdelkareem, Hussein M. Maghrabie, and Ahmad Baroutaji. Review of metaheuristic optimization algorithms for power systems problems. 15(12) :9434, 2023.

[114] Daniel Molina, Javier Poyatos, Javier Del Ser, Salvador García, Amir Hussain, and Francisco Herrera. Comprehensive taxonomies of nature- and bio-inspired optimization : Inspiration versus algorithmic behavior, critical analysis and recommendations (from 2020 to 2024). 2020. Publisher : arXiv Version Number : 5.

[115] Xuexia Zhang, Weirong Chen, and Chaohua Dai. Application of oriented search algorithm in reactive power optimization of power system. In *2008 Third International Conference on Electric Utility Deregulation and Restructuring and Power Technologies*, pages 2856–2861, Nanjing, China, 2008. IEEE.

[116] Kanchan Rajwar, Kusum Deep, and Swagatam Das. An exhaustive review of the metaheuristic algorithms for search and optimization : taxonomy, applications, and open challenges. 56(11) :13187–13257, 2023.

[117] Xavier Gandibleux, Marc Sevaux, Kenneth Sörensen, Vincent T'kindt, G. Fandel, and W. Trockel, editors. *Metaheuristics for Multiobjective Optimisation*, volume 535 of *Lecture Notes in Economics and Mathematical Systems*. Springer Berlin Heidelberg, Berlin, Heidelberg, 2004.

[118] Zhenan He, Gary G. Yen, and Jiancheng Lv. Evolutionary Multiobjective Optimization With Robustness Enhancement. *IEEE Transactions on Evolutionary Computation*, 24(3) :494–507, 2020.

[119] Yudong Zhang, Shuihua Wang, and Genlin Ji. A comprehensive survey on particle swarm optimization algorithm and its applications. 2015 :1–38, 2015.

[120] J. Kennedy and R. Eberhart. Particle swarm optimization. In *Proceedings of ICNN'95 - International Conference on Neural Networks*, volume 4, pages 1942–1948. IEEE, 1995.

[121] Ahmed G. Gad. Particle swarm optimization algorithm and its applications : A systematic review. 29(5) :2531–2561, 2022.

[122] Kashif Ishaque, Zainal Salam, Muhammad Amjad, and Saad Mekhilef. An improved particle swarm optimization (PSO)–based MPPT for PV with reduced steady-state oscillation. 27(8) :3627–3638, 2012.

[123] Karim Kaced, Cherif Larbes, Salah Mohamed Ait-Chikh, Moussaab Bounabi, and Zine Elabadine Dahmane. FPGA implementation of PSO based MPPT for PV systems under partial shading conditions. In *2017 6th International Conference on Systems and Control (ICSC)*, pages 150–155. IEEE, 2017.

[124] Seyedali Mirjalili, Seyed Mohammad Mirjalili, and Andrew Lewis. Grey wolf optimizer. 69 :46–61, 2014.

[125] Qi Liu, Hong Lu, Heisei Yonezawa, Ansei Yonezawa, Itsuro Kajiwara, and Ben Wang. Grey-wolf-optimization-algorithm-based tuned p-PI cascade controller for dual-ball-screw feed drive systems. 11(10) :2259, 2023.

[126] Yunyun Liu, Azizan As'arry, Hesham Ahmed, Abdul Aziz Hairuddin, Mohd Khair Hassan, Mohd Zakimi Zakaria, and Shuai Yang. Online optimal tuning of fuzzy PID controller using grey wolf optimizer for quarter car semi-active suspension system. 16(2) :16878132231219620, 2024.

[127] Hadjer Azli, Sabrina Titri, Cherif Larbes, Karim Kaced, and Karima Femmam. Novel yellow saddle goatfish algorithm for improving performance and efficiency of PV system under partial shading conditions. 247 :295–307, 2022.

[128] Mihailo Micev, Martin Ćalasan, and Diego Oliva. Fractional order PID controller design for an AVR system using chaotic yellow saddle goatfish algorithm. 8(7) :1182, 2020.

[129] Piotr Oziablo, Dorota Mozyrska, and Małgorzata Wyrwas. Fractional-variable-order digital controller design tuned with the chaotic yellow saddle goatfish algorithm for the AVR system. 125 :260–267, 2022.

[130] Radhwan A. A. Saleh, Yunes Alqudsi, Murat Makaraci, and Huseyin Metin Ertunc. Integration of robust control and multi-objective metaheuristic optimization for improved stability and tracking performance of WIP systems. 46(3) :1135–1153, 2025.

[131] Manish Kumar Pandey, Ram Niwash Mahia, Sukriti Tiwari, and Om Prakash Mahela. Robust and metaheuristic load frequency control techniques for renewable energy-based power system : comprehensive review and comparative analysis. 46(1) :2474150, 2025.

[132] Changhe Li, Shengxiang Yang, and Trung Thanh Nguyen. A self-learning particle swarm optimizer for global optimization problems. 42(3) :627–646, 2012.

[133] Daniel Zaldívar, Bernardo Morales, Alma Rodríguez, Arturo Valdivia-G, Erik Cuevas, and Marco Pérez-Cisneros. A novel bio-inspired optimization model based on yellow saddle goatfish behavior. 174 :1–21, 2018.

[134] Bilal Alatas. Chaotic harmony search algorithms. 216(9) :2687–2699, 2010.

[135] Leandro Dos Santos Coelho. A quantum particle swarm optimizer with chaotic mutation operator. 37(5) :1409–1418, 2008.

[136] L. Dos Santos Coelho and P. Alotto. Multiobjective electromagnetic optimization based on a nondominated sorting genetic approach with a chaotic crossover operator. 44(6) :1078–1081, 2008.

[137] Implementation and analysis of a fuzzy logic and sliding mode controller on a boost DC/DC converter in a PV array. 2023.

[138] Akshaya K. Pati and N.C. Sahoo. Adaptive super-twisting sliding mode control for a three-phase single-stage grid-connected differential boost inverter based photovoltaic system. 69 :296–306, 2017.

[139] **Fatma-Zohra Hadjaidji**, **Djamel Boukhetala**, Naamane Debdouche, Habib Benbouhenni, **Jean-Pierre Barbot**, and Laid Zarour. Performance evaluation of nonlinear control approaches for grid-connected PV systems includes a novel fractional-order terminal-super twisting approach. 12 :5024–5043, 2024.

[140] F Wang, Z Zhang, X Mei, J Rodriguez, and R Kennel. Advanced control strategies of electrical drives : Field oriented control, direct torque control and model predictive control. *Energies*, 2017.

[141] Jose Rodriguez and Patricio Cortes. *Predictive control of power converters and electrical drives*. John Wiley & Sons, 2012.

[142] Sabir Ouchen, Achour Betka, Jean-Paul Gaubert, and Sabrina Abdeddaim. Simulation and real time implementation of predictive direct power control for three phase shunt active power filter using robust phase-locked loop. *Simulation Modelling Practice and Theory*, 78 :1–17, 2017.

[143] Yingying Zhao, Aimin An, Yifan Xu, Qianqian Wang, and Minmin Wang. Model predictive control of grid-connected pv power generation system considering optimal mppt control of pv modules. *Protection and Control of Modern Power Systems*, 6 :1–12, 2021.

[144] Jose Rodriguez, Cristian Garcia, Andres Mora, Freddy Flores-Bahamonde, Pablo Acuna, Mateja Novak, Yongchang Zhang, Luca Tarisciotti, S Alireza Davari, Zhenbin Zhang, et al. Latest advances of model predictive control in electrical drives—part i : Basic concepts and advanced strategies. *IEEE Transactions on Power Electronics*, 37(4) :3927–3942, 2021.

[145] Xiaotao Chen, Weimin Wu, Ning Gao, Henry Shu-Hung Chung, Marco Liserre, and Frede Blaabjerg. Finite control set model predictive control for lcl-filtered grid-tied inverter with minimum sensors. *IEEE Transactions on Industrial Electronics*, 67(12) :9980–9990, 2020.

[146] Abdelbasset Krama, Laid Zellouma, Boualaga Rabhi, Shady S. Refaat, and Mansour Bouzidi. Real-time implementation of high performance control scheme for grid-tied PV system for power quality enhancement based on MPPC-SVM optimized by PSO algorithm. 11(12) :3516, 2018.

[147] Abdelbaset Laib, Fateh Krim, Billel Talbi, and Abdeslem Sahli. A predictive control scheme for large-scale grid-connected pv system using high-level npc inverter. *Arabian Journal for Science and Engineering*, 45 :1685–1701, 2020.

[148] Mohamed said Adouairi, Badre Bossoufi, Saad Motahhir, and Ikram Saady. Application of fuzzy sliding mode control on a single-stage grid-connected pv system based on the voltage-oriented control strategy. *Results in Engineering*, 17 :100822, 2023.

[149] Naamane Debdouche, Laid Zarour, Habib Benbouhenni, Fateh Mehazzem, and Brahim Deffaf. Robust integral backstepping control microgrid connected photovoltaic system with battery energy storage through multi-functional voltage source inverter using direct power control svm strategies. *Energy Reports*, 10 :565–580, 2023.

[150] Debdouche Naamane, Zarour Laid, and Mehazzem Fateh. Power quality improvement based on third-order sliding mode direct power control of microgrid-connected photovoltaic system with battery storage and nonlinear load. *Iranian Journal of Science and Technology, Transactions of Electrical Engineering*, 47(4) :1473–1490, 2023.

[151] AP Srivishnupriya, M Mohamed Thameem Ansari, and NJ Vinoth Kumar. Automatic generation control of three area hybrid power system by sine cosine optimized dual mode fractional order controller. *International Journal of Renewable Energy Research (IJRER)*, 12(3) :1414–1426, 2022.

[152] Ahsene Boubakir, Sid-Ahmed Touil, Salim Labiod, and Nasserdine Boudjerda. A robust model-free controller for a three-phase grid-connected photovoltaic system based on ultra-local model. *Protection and Control of Modern Power Systems*, 6 :1–13, 2021.

[153] Pedro J. Dos Santos Neto, Tárcio A.S. Barros, Joao P.C. Silveira, Ernesto Ruppert Filho, Juan C. Vasquez, and Josep M. Guerrero. Power management techniques for grid-connected DC microgrids : A comparative evaluation. 269 :115057, 2020.

[154] Naamane Debdouche, Ali Chebabhi, Habib Benbouhenni, **Fatma-Zohra Hadjaidji**, ZMS Elbarbary, and Saad F Al-Gahtani. Synergetic simplified super-twisting algorithm control for stability enhancement of pv/bess-based dc microgrid. *Scientific Reports*, 15(1) :7392, 2025.

[155] Naamane Debdouche, Brahim Deffaf, Habib Benbouhenni, Zarour Laid, and Mohamed I. Mosaad. Direct power control for three-level multifunctional voltage source inverter of PV systems using a simplified super-twisting algorithm. 16(10) :4103, 2023.

[156] Brahim Deffaf, Hamoudi Farid, Habib Benbouhenni, Slimane Medjmadj, and Naamane Debdouche. Synergetic control for three-level voltage source inverter-based shunt active power filter to improve power quality. 10 :1013–1027, 2023.

[157] Habib Benbouhenni, Hamza Gasmi, Ilhami Colak, Nicu Bizon, and Phatiphat Thounthong. Synergetic-PI controller based on genetic algorithm for DPC-PWM strategy of a multi-rotor wind power system. 13(1) :13570, 2023.

[158] Chaib Ibtissam, Behlouli Asma, **Hdjaidji Fatma Zahra**, Benkouider Ouarda, and Berkouk El-Madjid. Comparative study between diffirent control strategy of the z-source inverter. In *2017 5th International Conference on Electrical Engineering-Boumerdes (ICEE-B)*, pages 1–6. IEEE, 2017.

[159] Ibtissam Chaib, El Madjid Berkouk, Jean-Paul Gaubert, Mostefa Kermadi, Nassereddine Sabeur, and Saad Mekhilef. An improved discontinuous space vector modulation for z-source inverter with reduced power losses. *IEEE Journal of Emerging and Selected Topics in Power Electronics*, 9(3) :3479–3488, 2020.

[160] Moufek Khelifi, Omar Benzineb, El Madjid Berkouk, Asma Behlouli, and Fares Baatouche. An improved discontinuous space vector modulation for a three-phase z-source inverter with a modified reference. *IEEE Journal of Emerging and Selected Topics in Power Electronics*, 10(3) :3207–3218, 2021.

[161] **Fatma-Zohra Hadjaidji**, **Djamel Boukhetala**, **Jean-Pierre Barbot**, and El-Madjid Berkouk. Optimized z-source inverter control of hybrid PV/battery system based on proportional resonant controller. In *2022 2nd International Conference on Advanced Electrical Engineering (ICAEE)*, pages 1–6. IEEE, 2022.

[162] Ayman Ayad, Mohamed Hashem, Christoph Hackl, and Ralph Kennel. Proportional-resonant controller design for quasi-z-source inverters with LC filters. In *IECON 2016 - 42nd Annual Conference of the IEEE Industrial Electronics Society*, pages 3558–3563. IEEE, 2016.

[163] Saban Ozdemir, Necmi Altin, Ibrahim Sefa, Zhen Zhang, and Hasan Komurcugil. Super twisting sliding mode control of three-phase grid-tied neutral point clamped inverters. 125 :547–559, 2022.

[164] Shahzad Ahmed, Hafiz Mian Muhammad Adil, Iftikhar Ahmad, Muhammad Kashif Azeem, Zil E Huma, and Safdar Abbas Khan. Supertwisting sliding mode algorithm based nonlinear MPPT control for a solar PV system with artificial neural networks based reference generation. 13(14) :3695, 2020.

[165] Mohammad A Abusara, Suleiman M Sharkh, and Josep M Guerrero. Improved droop control strategy for grid-connected inverters. *Sustainable energy, grids and networks*, 1 :10–19, 2015.

[166] **Fatma-Zohra Hadjaidji**, **Djamel Boukhetala**, and **Jean-Pierre Barbot**. Decentralized control for parallel distributed generation units in flexible microgrid integrating PV quasi-Z-source inverter. *Electric Power Systems Research*, 247 :111711, 2025.

[167] Yinghao Shan, Jiefeng Hu, Ming Liu, Jianguo Zhu, and Josep M. Guerrero. Model predictive voltage and power control of islanded PV-battery microgrids with washout-filter-based power sharing strategy. 35(2) :1227–1238, 2020.

[168] Munther A Hassouneh, Hsien-Chiarn Lee, and Eyad H Abed. Washout filters in feedback control : Benefits, limitations and extensions. In *Proceedings of the 2004 American control conference*, volume 5, pages 3950–3955. IEEE, 2004.

[169] Li-Xin Wang. *A course in fuzzy systems and control*. Prentice-Hall, Inc., 1996.

[170] Qing-Chang Zhong, Yeqin Wang, and Beibei Ren. Ude-based robust droop control of inverters in parallel operation. *IEEE Transactions on Industrial Electronics*, 64(9) :7552–7562, 2017.

[171] Hui Wang, Chengdong Yang, Xu Liao, Jiarui Wang, Weichao Zhou, and Xiu Ji. Artificial neural network-based virtual synchronous generator dual droop control for microgrid systems. *Computers and Electrical Engineering*, 111 :108930, 2023.

[172] Xiangyu Wu, Chen Shen, and Reza Iravani. A distributed, cooperative frequency and voltage control for microgrids. *IEEE Transactions on Smart Grid*, 9(4) :2764–2776, 2016.

[173] Manoja Kumar Behera and Lalit Chandra Saikia. An improved voltage and frequency control for islanded microgrid using bpf based droop control and optimal third harmonic injection pwm scheme. *IEEE Transactions on Industry Applications*, 58(2) :2483–2496, 2021.

[174] Min Ding, Zili Tao, Bo Hu, Shengji Tan, and Ryuichi Yokoyama. Parallel operation strategy of inverters based on an improved adaptive droop control and equivalent input disturbance approach. *Electronics*, 13(3) :486, 2024.

[175] Soham Chakraborty, Sourav Patel, Govind Saraswat, Atif Maqsood, and Murti V Salapaka. Seamless transition of critical infrastructures using droop-controlled grid-forming inverters. *IEEE Transactions on Industrial Electronics*, 71(2) :1535–1546, 2023.

[176] Mingshen Li, Jose Matas, Jorge El Mariachet, Carlos Gustavo C Branco, and Josep M Guerrero. A fast power calculation algorithm for three-phase droop-controlled-inverters using combined sogi filters and considering nonlinear loads. *Energies*, 15(19) :7360, 2022.

[177] Jorge El Mariachet, Jose Matas, Helena Martín, Mingshen Li, Yajuan Guan, and Josep M Guerrero. A power calculation algorithm for single-phase droop-operated-inverters considering linear and nonlinear loads hil-assessed. *Electronics*, 8(11) :1366, 2019.

[178] R Timothy Marler and Jasbir S Arora. The weighted sum method for multi-objective optimization : new insights. *Structural and multidisciplinary optimization*, 41 :853–862, 2010.

Scientific Production

Publications in International Journals

1. **F.-Z. Hadjaidji**, D. Boukhetala, N. Debdouche, H. Benbouhenni, J.-P. Barbot, and L. Zarour, "Performance evaluation of nonlinear control approaches for grid-connected PV systems includes a novel fractional-order terminal-super twisting approach," *Energy Reports*, vol. 12, pp. 5024–5043, Dec. 2024. **DOI :** `10.1016/j.egyr.2024.10.059`, **ELSEVIER, Impact Factor = 5.1**.
2. **F.-Z. Hadjaidji**, D. Boukhetala, and J.-P. Barbot,"Decentralized control for parallel distributed generation units in flexible microgrid integrating PV quasi-Z-source inverter," *Electric Power Systems Research*, vol. 247, p. 111711, Oct. 2025. **DOI :** `10.1016/j.epsr.2025.111711`, **ELSEVIER, Impact Factor = 4.2**.
3. N. Debdouche, A. Chebabhi, H. Benbouhenni, **F.-Z. Hadjaidji**, Z. M. S. Elbarbary, and S. F. Al-Gahtani, "Synergetic simplified super-twisting algorithm control for stability enhancement of PV/BESS-based DC microgrid," *Scientific Reports*, vol. 15, no. 1, p. 7392, Mar. 2025. **DOI :** `10.1038/s41598-025-92042-4`, **Springer, Impact Factor = 3.8**.

Publications in National Journals

1. **F.-Z. Hadjaidji**, A. Behlouli, F. Baatouche, D. Boukhetala, J.-P. Barbot, and E.-M. Berkouk, "Hierarchical Control for Flexible PV-Battery Microgrid based on Z-Source Inverters Operated in Parallel," *The ENP Engineering Science Journal (ENPESJ)*, Under Review.

International Conference Proceedings

1. **F.-Z. Hadjaidji**, D. Boukhetala, and J.-P. Barbot, "Optimized Fractional Order PID Controller Design for Stand-alone PV System Based on Quasi-Z-Source Inverter," in *Proceedings of the 6th International Conference on Electrical Engineering and Control Applications (ICEECA 2024)*, Khenchela, Algeria : Springer.
2. **F.-Z. Hadjaidji**, D. Boukhetala, and J.-P. Barbot, "Optimized Fractional Order Based Droop Control with Improving the Flexibility of a Microgrid," *E3S Web of Conferences*, vol. 353, p. 02001, 2022. **DOI :** `10.1051/e3sconf/202235302001`.
3. **F.-Z. Hadjaidji**, D. Boukhetala, J.-P. Barbot, and E.-M. Berkouk, "Optimized Z-Source Inverter Control of Hybrid PV/Battery System Based on Proportional Resonant Controller," in *2022 2nd International Conference on Advanced Electrical Engineering (ICAEE)*, Constantine, Algeria : IEEE, Oct. 2022, pp. 1–6. **DOI :** `10.1109/ICAEE53772.2022.9962132`.
4. I. Chaib, A. Behlouli, **F.-Z. Hadjaidji**, O. Benkouider, and E.-M. Berkouk, "Comparative Study Between Different Control Strategies of the Z-Source Inverter ," in *International Conference ICEE*, Boumerdes, Algeria, 2017. **DOI :** `10.1109/ICEE-B.2017.8192064`.